ADVANCED STEEL CONSTRUCTION

An International Journal

Volume 20 Number 2

June 2024

CONTENTS

Website: *http://www.hkisc.org*
ISSN 1816-112X
Science Citation Index Expanded, Materials Science Citation Index and ISI Alerting
Cover: Niushou Mountain Scenic Spot in Nanjing, China. Photo @ Yang Yuhua
e-copy of IJASC is free to download at "www.ascjournal.com" in internet and mobile apps.

ADVANCED STEEL CONSTRUCTION

VOL.20, NO.2 (2024)

ADVANCED STEEL CONSTRUCTION

an International Journal

ISSN 1816-112X

Volume 20 Number 2 *June 2024*

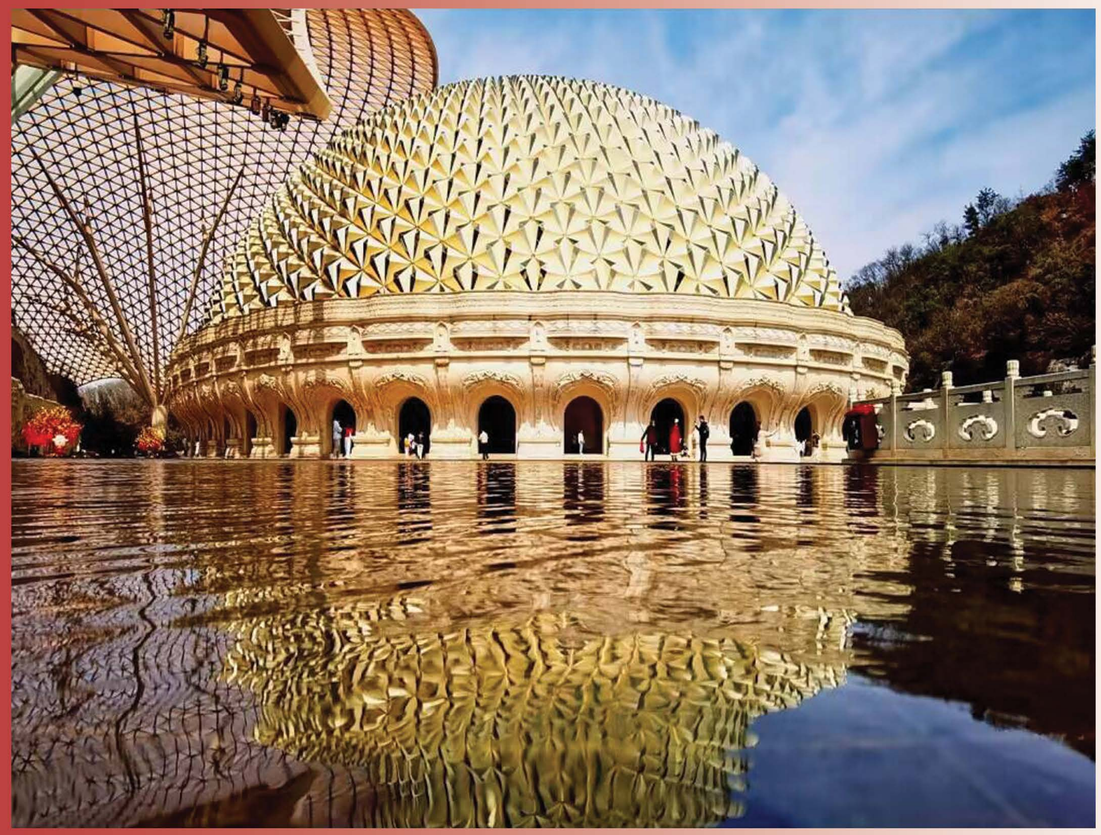

ISSN 1816-112X

Science Citation Index Expanded, Materials Science Citation Index and ISI Alerting

Advanced Steel Construction
an international journal

Cover: Niushou Mountain Scenic Spot in Nanjing, China. Photo @ Yang Yuhua
e-copy of IJASC is free to download at "www.ascjournal.com" in internet and mobile apps.

General Information
Advanced Steel Construction, an international journal

Aims and scope

The International Journal of Advanced Steel Construction provides a platform for the publication and rapid dissemination of original and up-to-date research and technological developments in steel construction, design and analysis. Scope of research papers published in this journal includes but is not limited to theoretical and experimental research on elements, assemblages, systems, material, design philosophy and codification, standards, fabrication, projects of innovative nature and computer techniques. The journal is specifically tailored to channel the exchange of technological know-how between researchers and practitioners. Contributions from all aspects related to the recent developments of advanced steel construction are welcome.

Subscription inquiries and change of address. Address all subscription inquiries and correspondence to Member Records, IJASC. Notify an address change as soon as possible. All communications should include both old and new addresses with zip codes and be accompanied by a mailing label from a recent issue. Allow six weeks for all changes to become effective.

The Hong Kong Institute of Steel Construction
HKISC
c/o Prof. SL Chan,
Unit 209B, Photonics Centre, No. 2 Science Park East Avenue,
Hong Kong Science Park, Shatin, N.T., Hong Kong, China.
Tel: 852- 3595 6150 Fax: 852- 3619 7238
Email: ceslchan@connect.polyu.hk Website: *http://www.hkisc.org/*
ISSN 1816-112X
Science Citation Index Expanded, Materials Science Citation Index and ISI Alerting

ISSN 1816-112X

Science Citation Index Expanded, Materials Science Citation Index and ISI Alerting

Advanced Steel Construction
an international journal

VOLUME 20 NUMBER 2 **June 2024**

Technical Papers

Advanced Steel Construction – Vol. 20 No. 2 (2024) 105–110
DOI:10.18057/IJASC.2024.20.2.1
(Special Issue: *11st International Conference on Advances in Steel Structures, ICASS'2023, Kuching, Sarawak, Malaysia*)

INFLUENCE OF THERMAL HISTORY ASSUMING FIRE DAMAGE ON MECHANICAL PROPERTIES OF STEELS FOR BRIDGE HIGH PERFORMANCE STRUCTURE

Koki Matsubara, Mikihito Hirohata * and Ayato Hamada

Graduate School of Engineering, Osaka University, Suita, Japan
** (Corresponding author: E-mail: hirohata@civil.eng.osaka-u.ac.jp)*

ABSTRACT

Many cases of bridge fires have been reported in Japan and overseas. When bridges are taken out of service due to fire, it is feared that economic activities will be greatly affected. Therefore, fire-damaged bridges must be recovered to service as soon as possible. It is important to accurately diagnose the degree of fire damage by estimating the thermal history of the damaged members and inspecting the external appearance of the bridge during a detailed investigation. Although data on mechanical properties of fire-affected steel materials is being accumulated, the mechanical properties after fire heating for newly developed high-performance steel materials are unknown. This study aims to investigate the influence of thermal history assuming fire damage on the mechanical properties of Steels for Bridge High Performance Structure (SBHS), standardized by JIS in 2008. A series of experiments were conducted to clarify the change in mechanical properties of SBHS400 and SBHS500 by heating and cooling. The heating up to 600℃ and cooling after that kept the mechanical properties of SBHS within the JIS standard. The heating up to 900℃ and cooling after that changed the mechanical properties of SBHS significantly. Furthermore, a method by using a portable hardness tester for estimating the change in mechanical properties after heating and cooling was proposed. The results indicated the possibility of quick investigation on after-fire site.

ARTICLE HISTORY

Received: 8 April 2024
Revised: 28 April 2024
Accepted: 5 June 2024

KEYWORDS

Bridge;
Fire;
SBHS;
Mechanical properties;
Leeb hardness test

1. Introduction

Many cases of bridge fires caused by traffic accidents and lost fires have been reported [1-5]. Regardless of the cause of the fire, bridges may be taken out of service for a long time depending on the degree of damage. In this case, there is concern that transportation networks and logistics will be interrupted and economic activities will be greatly affected. Therefore, it is important to aim for the early resumption of service when bridges are damaged by fire.

In order to quickly and safely put bridges damaged by fire back into service, it is necessary to clarify the process of surveying the damage, diagnosis, and judgement for necessity of repair. In 2015, the Japan Society of Civil Engineers (JSCE) presented the "Guidelines for Diagnosis and Repair Method of Steel Bridge exposed to Fire" [6], which systematically outlines the process required to put fire-affected steel bridges back into service. According to this guideline, it is important to accurately diagnose the degree of fire damage by conducting visual inspections of the external appearance such as deformation and estimating the temperature of members in the fire-affected steel bridge. For steel members, the temperature of member by fire is often estimated from the damage to the coating film. If it is determined that the temperature has exceeded a predetermined acceptance level, material tests may be conducted by extracting samples from the fire-affected area to directly investigate the change in mechanical properties. In previous studies [7, 8], it has been reported that no change in mechanical properties occurs after heating up to 600℃ and cooling for structural steels such as SS400, SM490, SM570, and high-strength bolts. In contrast, the above-mentioned guideline [6] defines 400℃ as the standard with safety margin for the temperature of member at which fire-affected bridges can be put back into service without the need for a detailed investigation. Since there are some materials among the members of steel bridges that have not been the subject of previous studies [7, 8], data on the change in mechanical properties of various steel materials after heating and cooling assuming fire are being accumulated [9, 10]. However, the mechanical properties after fire heating for newly developed high-performance steel materials are unknown. In particular, Steels for Bridge High Performance Structure (SBHS), which has been JIS-standardized since 2008, lacks data on the change in mechanical properties after fire heating. SBHS is a steel material with high strength, excellent weldability, workability, and toughness achieved by the application of Thermo-Mechanical Control Process (TMCP). It is supposed to be important to clarify how the mechanical properties of SBHS change when subjected to unintended thermal history due to fire and extinguishing. In order to expand the application of SBHS to steel structures, it will be useful to clarify the change in mechanical properties of SBHS subjected to heating and cooling history from the viewpoint of guaranteeing the performance of steel after fire. In addition, tensile test is the most basic and obvious method for investigating the material performance of fire-affected steel, but it takes time and effort to extract the steel from fire-damaged areas and process test specimens. Therefore, for early resumption of service, it is desirable to establish an investigation method that is easier to conduct than tensile test and can quickly estimate the change in mechanical properties due to fire.

This study aims to investigate the influence of thermal history assuming fire damage on the mechanical properties of SBHS. Heating and cooling experiments and various material tests were conducted to clarify the change in mechanical properties of SBHS400 and SBHS500 by heating and cooling. It was also investigated whether the change in mechanical properties of SBHS could be estimated by the Leeb hardness test with a portable device.

2. Steel specimen

The chemical composition and mechanical properties (mill test report) of SBHS400 and SBHS500 used in this study are shown in Tables 1 and 2. As shown in Fig. 1, all specimens were 12 mm thick, and they were cut into 300 mm × 200 mm pieces for the heating and cooling experiments.

Table 1
Chemical composition of steel specimen (mass%, mill test report)

	C	Si	Mn	P	S	N
SBHS400	0.12	0.36	1.44	0.009	0.001	0.005
JIS standards	<0.15	<0.55	<2.00	<0.020	<0.006	<0.006
SBHS500	0.10	0.22	1.53	0.009	0.002	0.0025
JIS standards	<0.11	<0.55	<2.00	<0.020	<0.006	<0.006

Table 2
Mechanical properties of steel specimen (mill test report)

	Yield stress (N/mm^2)	Tensile strength (N/mm^2)	Elongation (%)
SBHS400	473	550	25
JIS standards	>400	490 - 640	>15
SBHS500	587	679	30
JIS standards	>500	570 - 720	>19

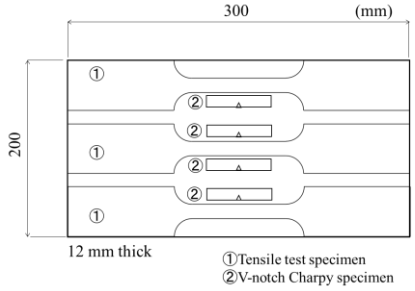

Fig. 1 Geometry of steel specimen

3. Heating and cooling experiments

3.1. Experimental method

Heating and cooling experiments were conducted to subject the specimens to a thermal history assuming fire. This method was basically the same as the conditions in previous studies [9, 10], for the purpose of comparison and examination with other steels.

The heating temperatures were based on 600℃ and 900℃. The former has been frequently reported as the upper limit of the temperature of members in steel bridge fire cases [1-5]. The latter was assumed to be the temperature of members in a large-scale fire. These also mean lower and higher temperature than the A_1 transformation temperature (about 727℃) at which microstructural changes occur in steel. The specimens were heated up to 600℃ or 900℃ in an electric furnace to heat them uniformly. Once the target temperature was reached, the steel was held for a sufficient time (approximately 12 hours) until the temperature of the steel became uniform. After heating, the steel was cooled by two different methods of air cooling and water cooling. In the case of air cooling, the heated steel was taken out from the furnace and left in the air. In the case of water cooling, the heated steel was immersed in a container filled with water at room temperature immediately after being taken out from the furnace. Water cooling is assumed fire extinguishing activities.

The steel of the same dimensions as the specimens was prepared for temperature measurement. They were dummy specimens. A hole was made in the center of the side surface that reached to the center of the steel. A thermocouple was inserted into the hole, and heated and cooled together with the specimens. Since temperature differences are expected to occur depending on the position of the steel in the furnace, the temperature history was measured by placing the specimens between two dummy specimens, as shown in Fig. 2. When the temperature of the dummy specimens reached the target temperature, it was assumed that the specimens between them also reached the same temperature. In the case of 600℃ heating, the temperature of the dummy specimens was between 620℃ to 630℃. In the case of 900℃ heating, the temperature was between 920℃ to 940℃. After confirming that the target temperature was reached, the specimens were cooled.

3.2. Experimental results

Fig. 3 shows the temperature history of each steel during the heating and cooling processes. The metallurgical structures of steel used in heating and cooling experiments were observed under an optical microscope (400x magnification), and the results are shown in Fig. 4.

Without heating and cooling, a layered ferrite-pearlite microstructure was observed in SBHS400, while like a bainite microstructure was observed in SBHS500. After heating up to 600℃ and air and water cooling, the pearlite structure disappeared in SBHS400. However, no significant changes in the metallurgical structure were observed for any of the steel or cooling conditions. This is thought to be due to the fact that the heating temperature was lower than the A_1 transformation temperature at which the metallurgical structure changes.

When heated up to 900℃, a ferrite-pearlite microstructure was observed in both steels when air cooling, while a bainitic microstructure was observed when water cooling. For both steels, the ferrite-pearlite microstructure became coarser when the steels were heated up to 900℃ and then air cooling than that without heating and cooling. The microstructure that appeared to be bainite in water cooling was coarser crystal grains than that of SBHS500 without heating and cooling. For SBHS400, after heating up to 900℃ and water cooling, a fine martensite-like structure was observed in some parts. Furthermore, the microstructures were slightly different between the surface and inside of the steel in water cooling. In both cooling methods, the fine metallurgical structure of SBHS adjusted in steelmaking might be changed by heating at temperature higher than the A_1 and A_3 transformation temperatures (about 911℃).

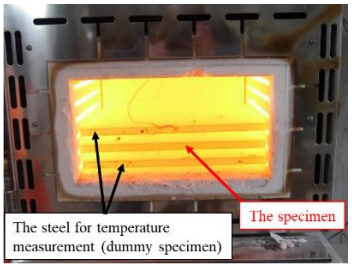

Fig. 2 Condition inside an electric furnace (heating up to 900℃)

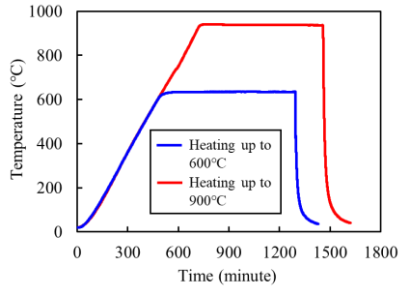

a) Air cooling

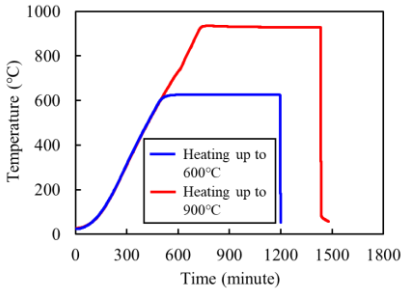

b) Water cooling

Fig. 3 Temperature histories obtained from heating and cooling experiments

Steel	Without heating and cooling	Heating up to 600℃		Heating up to 900℃		
		Air cooling	Water cooling	Air cooling	Water cooling (surface)	Water cooling (inside)
SBHS400	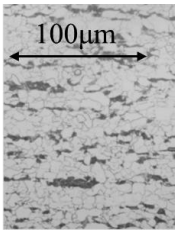	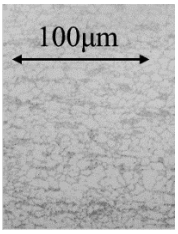	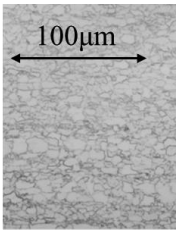	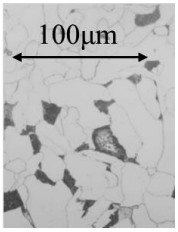	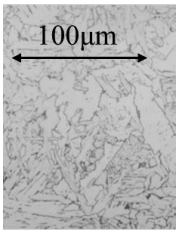	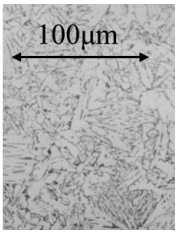
SBHS500	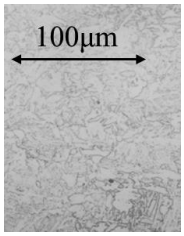	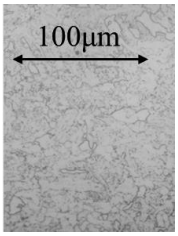	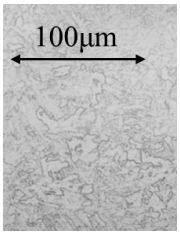	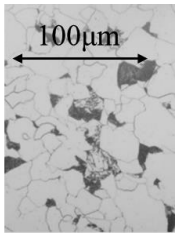	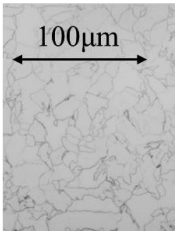	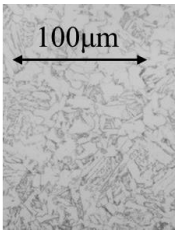

Fig. 4 Results of metallographic observation (400x magnification)

4. Mechanical properties of SBHS subjected to thermal history

4.1. Tensile test

4.1.1. Test method

Three specimens of JIS Z 2241, No. 14B were extracted from each steel used in the heating and cooling experiments, and tensile tests were conducted. Strain gauges were attached to the front and back surfaces of the mid span of the specimens. Young's modulus was determined from the strain gauge values in the elastic region. The displacement was measured with a clip-type displacement transducer attached between the reference points. In cases where the yield shelf did not clearly appear, the 0.2% proof stress was defined as the yield stress. The data obtained from the tensile tests were used to calculate nominal stress and nominal strain, and stress-strain curves were illustrated.

4.1.2. Test results

The stress-strain curves of SBHS400 and SBHS500 obtained from the tensile tests for each heating and cooling condition are shown in Figs. 5 and 6. The stress-strain curves were similar for the same three specimens, so the one of them was extracted. The results for yield stress, tensile strength, Young's modulus, and elongation at break are shown in Figs. 7 and 8, along with the JIS standards. The figure shows the average and standard deviation of the data obtained from three specimens.

For SBHS400, the heating up to 600℃ and cooling after that showed no change in Young's modulus and elongation, but yield stress and tensile strength decreased by 4-8% and 3-8%. Yield shelf appeared in SBHS500 caused the decrease in tensile strength by 6-8% and the increase in Young's modulus by 5%. In addition, elongation increased by around 15%. However, the values of yield stress, tensile strength, Young's modulus, and elongation were almost the same compared to the mechanical properties without heating and cooling. The yield stress, tensile strength, and elongation of both steel satisfied the standard values specified by JIS.

The yield stress and tensile strength of SBHS400 were 30% and 15% lower than those without heating and cooling in heating up to 900℃ and air cooling. The elongation decreased by 6%, and Young's modulus was unchanged. Water cooling caused the decrease in yield stress by 17% and the increase in tensile strength by 14%, and the decrease in elongation by 24%. Young's modulus did not change. When SBHS400 was heated up to 900℃ and then air-cooled, the yield stress and tensile strength did not satisfy the JIS specification. When the specimens were water-cooled, the yield stress was equal to the JIS standard value, and the tensile strength increased. For SBHS500, heating up to 900℃ and air cooling caused the decrease in yield stress by 38% and the decrease in tensile strength by 30% compared to the case without heating and cooling. This result was significantly lower than the specified values by JIS. Young's modulus increased by 6% and the elongation increased by 52%. When water cooling, the yield stress decreased by 33% and did not satisfy the specification by JIS. Although the tensile strength decreased by about 7%, it was within the range specified by JIS. Young's modulus and the elongation were almost the same as those without heating and cooling.

4.2. Charpy impact test

4.2.1. Test method

V-notch specimens of 55 mm × 10 mm × 10 mm, as specified in JIS Z 2242, were extracted from both steels used in the heating and cooling experiments. Charpy impact tests were conducted at 0℃ for SBHS400 and -5℃ for SBHS500 as test temperature specified by JIS. The number of specimens was basically three, but up to six specimens were tested for those with large variations in test results. For SBHS400, four specimens were used when air cooling after heating up to 900℃, and six specimens were used when water cooling after heating up to 900℃. For SBHS500, six specimens were used when water cooling after heating up to 600℃ and 900℃. Charpy absorbed energy was evaluated by the average value of all specimens used in the test.

4.2.2. Test results

The Charpy absorbed energy values obtained from the test under each condition are shown in Fig. 9, along with the JIS standards. The figure shows the average and standard deviation of the test results. The fracture patterns of each steel after the test are shown in Fig. 10. For SBHS400, the absorbed energy decreased by about 16 J when air-cooled after heating up to 600℃ and by about 34 J when water-cooled. The energy decreased from the case without heating and cooling was about 10% at maximum. For SBHS500, the energy increased about 95 J when air-cooled and about 72 J when water-cooled. Absorbed energy increased by more than 30% compared to that without heating and cooling. This was a different trend from SBHS400.

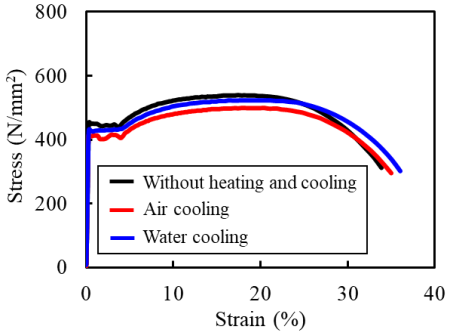

a) Heating up to 600℃

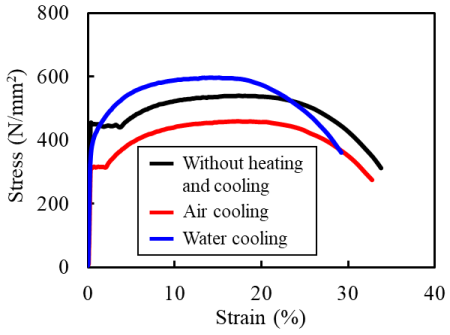

b) Heating up to 900℃

Fig. 5 Stress-strain curves of SBHS400

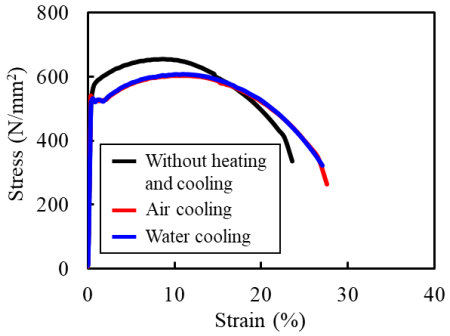

a) Heating up to 600℃

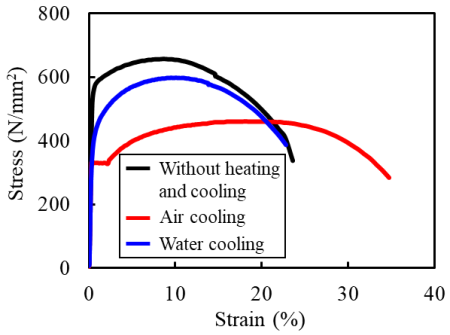

b) Heating up to 900℃

Fig. 6 Stress-strain curves of SBHS500

Observation of the fracture surface showed that both steels had the ductile fracture in the cases without heating and cooling, air cooling after heating up to 600℃, and water cooling.

When SBHS400 was heated up to 900℃ and then air-cooled, there was almost no change in absorbed energy compared to the case without heating and cooling, while that of SBHS500 increased by 47%. When water-cooled, that decreased by 67% for SBHS400 and 41% for SBHS500, and the values were close to JIS value. Observation of the fracture surface as in the 600℃ case showed that a ductile fracture was dominant in both steels in air cooling after heating up to 900℃. Water cooling after heating up to 900℃ resulted in brittle fracture with the brittle fracture surface ratio of about 70%. Therefore, the toughness of SBHS might be decreased.

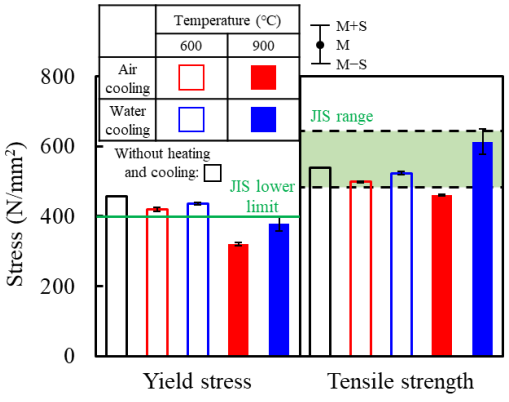

a) Yield stress and tensile strength

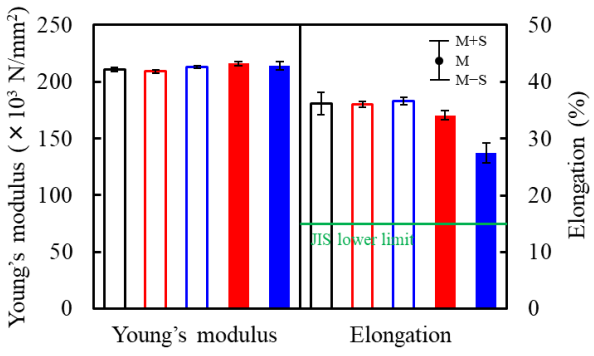

b) Young's modulus and elongation

Fig. 7 Tensile test results of SBHS400

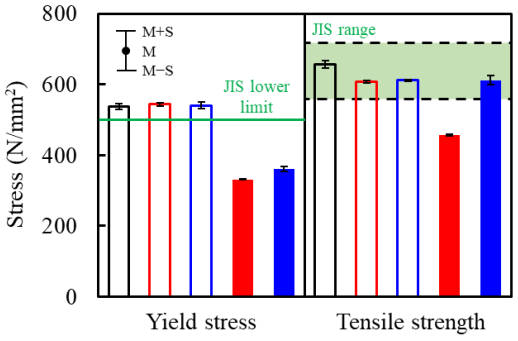

a) Yield stress and tensile strength

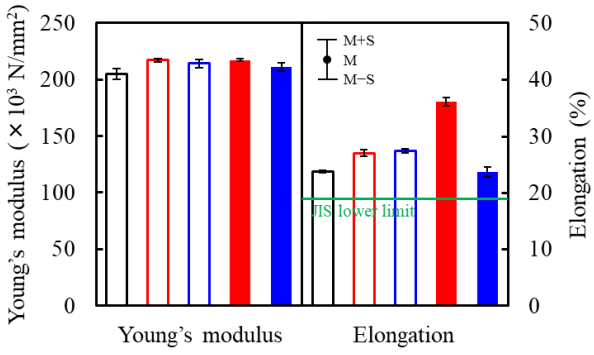

b) Young's modulus and elongation

Fig. 8 Tensile test results of SBHS500

5. Estimation of changes in mechanical properties of SBHS by Leeb hardness test

5.1. Estimation method

It is known experimentally that there is a correspondence between the hardness and tensile strength of steel [11]. Based on this, the Leeb hardness test was conducted with the intention of using hardness to estimate the mechanical properties of steel subjected to fire heating. The Leeb hardness tester in this study and the test situation are shown in Fig. 11. The tester is approximately 150 mm long, 45 mm wide, and 150 g in weight, making it compact and lightweight. In the test, a small hammer inside the tester is driven into the steel surface. As shown in equation (1), the Leeb hardness *HL* is calculated by the ratio of the velocity v_i when the hammer is launched and the velocity v_r after the rebound.

$$HL = v_r/v_i \times 1000 \quad (1)$$

As shown in Fig. 12, 18 measurement points were set on the specimen at which the surface was smoothed with a grinder. The test was conducted with grease applied between the surface plate and the steel to keep the air gap tight. The average and standard deviation were calculated from five measurements of the Leeb hardness at each measuring point of the specimen.

5.2. Relationship between Leeb hardness and mechanical properties of SBHS

It was investigated whether the change in mechanical properties of SBHS could be estimated by the Leeb hardness. The relationship between the Leeb hardness and the mechanical properties of SBHS400 and SBHS500 under each condition is shown in Fig. 13. The figure shows the average and standard deviation of each test value. The red graph shows the results for SBHS400, and the blue one shows the results for SBHS500. The figure also shows the regression line by the least-squares method and its coefficient of determination (R^2 value). The yield stresses of both SBHS400 and SBHS500 showed a correspondence with the Leeb hardness. The R^2 value of the regression line was also greater than 0.9. In contrast, for tensile strength, there were points (heating up to 900°C and water cooling) which deviated significantly from the regression line, and the R^2 became small. Although the relationship was less clear than that of yield stress, a tendency for tensile strength to increase with increase in Leeb hardness was observed.

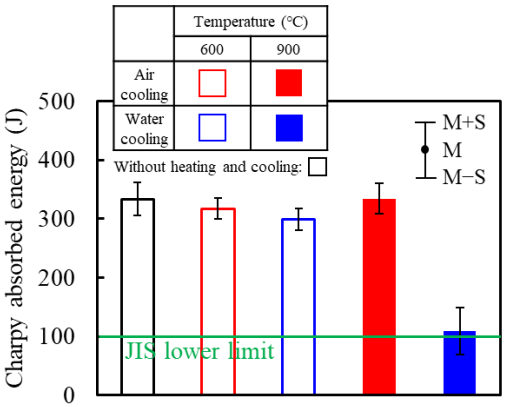

a) SBHS400

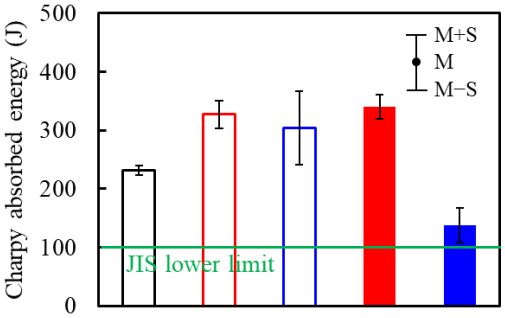

b) SBHS500

Fig. 9 Charpy impact test results

6. Discussions

When SBHS400 and SBHS500 were heated up to 600°C, changes in mechanical properties were small under both air and water cooling conditions. For SBHS500, the yield shelf appeared in the stress-strain relationship and there were some changes in mechanical properties, but these were within the range specified by JIS. The fracture behavior in the Charpy impact test was ductile

Steel	Without heating and cooling	Heating up to 600℃		Heating up to 900℃	
		Air cooling	Water cooling	Air cooling	Water cooling
SBHS400	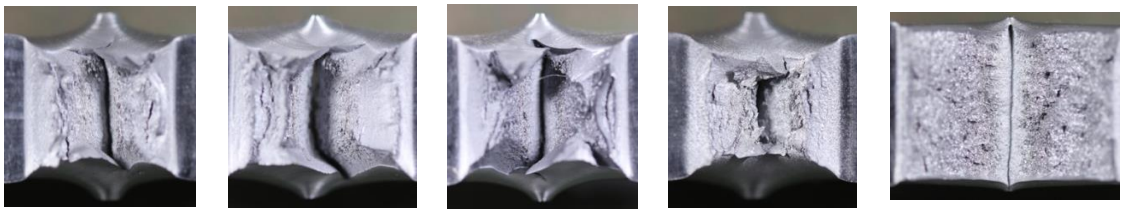				
SBHS500	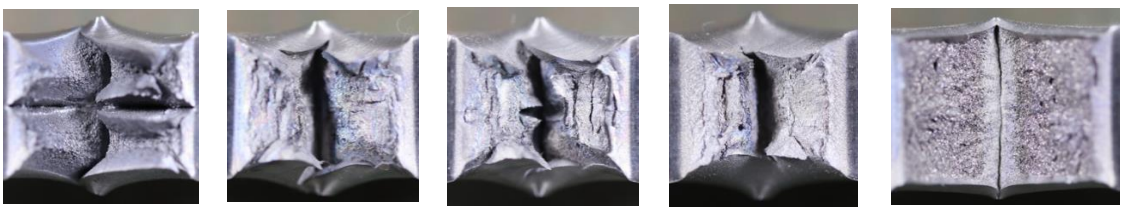				

Fig. 10 Fracture patterns of Charpy impact test specimens

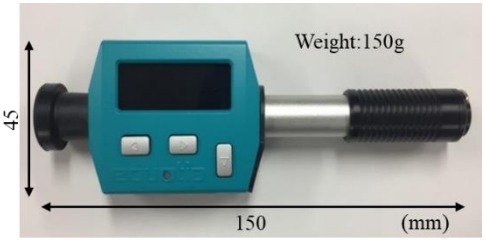

a) Test device

b) Test situation

Fig. 11 Leeb hardness test device and test situation

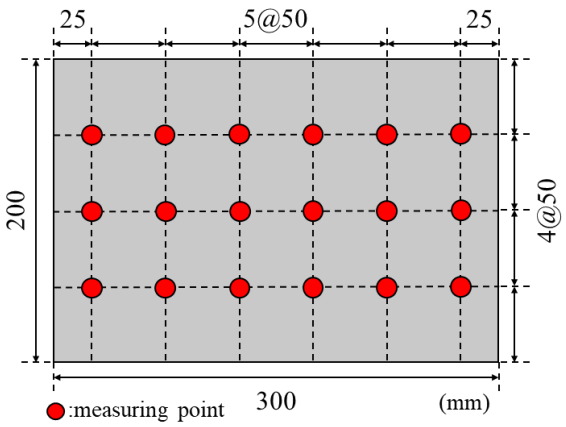

Fig. 12 Measuring point of Leeb hardness test

and there was no decrease in absorbed energy. As shown in Fig. 4, this can be explained by the fact that the metallurgical structure of SBHS did not change significantly when heated below the A_1 transformation temperature. The "Guidelines for Diagnosis and Repair Method of Steel Bridge exposed to Fire" [6] stipulates that a detailed investigations are not required if the temperature of member is less than 400℃. Therefore, it was shown that the stipulations may be applicable to SBHS as well as to general structural steel.

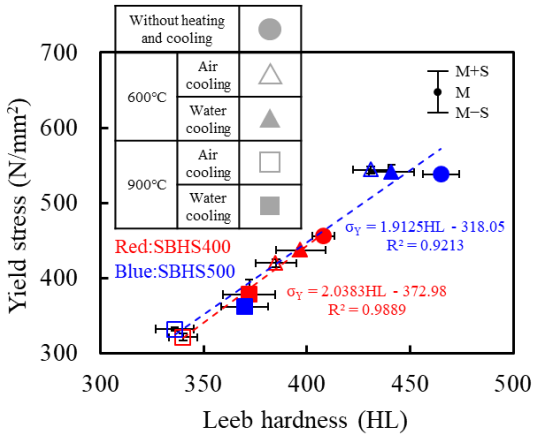

a) Yield stress

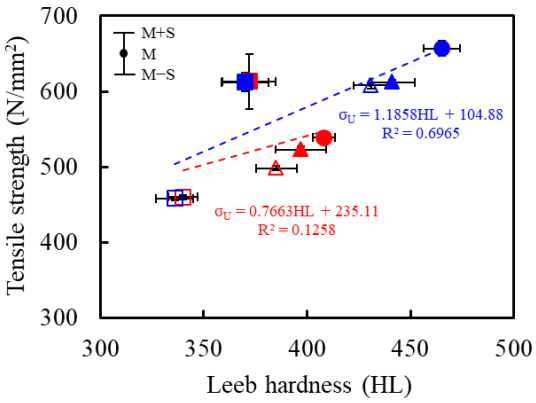

b) Tensile strength

Fig. 13 Relationship between Leeb hardness and mechanical properties of SBHS

On the other hand, when SBHS400 and SBHS500 were heated up to 900℃ and then air-cooled, the microstructures of both steels coarsened and softened. When SBHS400 was heated up to 900℃ and then water-cooled, the martensite-like microstructure was observed in part due to quenching, resulting in the increase in tensile strength. The metallurgical structure of SBHS500 was coarser and tensile strength did not increase. The yield stress of both SBHS400 and SBHS500 was lower than that of the case without heating. This trend was different from that observed for general structural steel heated up to 900℃ and then water-cooled. In general steel, it was confirmed that the effect of quenching increased the yield stress and tensile strength [9]. Unlike general steel, the mechanical properties of SBHS are adjusted by strictly controlling the temperature in each process during steelmaking. Under the 900℃ heating conditions of this

experiment, the steel was heated up to 920-940℃. This is above the A_3 transformation temperature (about 911℃) at which the metallurgical structure of the steel is completely transformed to a soft austenite structure. Therefore, the cooling from this situation invalidated the microstructure adjusted in steelmaking of SBHS, caused the decrease in strength. If there is a large fire in which the temperature of members exceeds the A_3 transformation one, the experimental results in this study suggest that the yield stress and tensile strength may be significantly decreased in SBHS.

Regarding the estimation of mechanical properties using the Leeb hardness, the case in which the specimens were heated up to 900℃ and then water-cooled showed the significant deviation from the regression line. As shown in Fig. 4, the microstructural states differed between the steel surface and the inside during water cooling after heating up to 900℃. The reason might be the difference in cooling rate affecting the formation of microstructure between the surface and the inside of the steel by rapid cooling with water. In addition, the hardness is strongly influenced by the microstructural condition of the steel surface. Therefore, it is suggested that the estimation accuracy based on the Leeb hardness may decrease during water cooling after heating up to 900℃ due to differences in the microstructural state.

7. Conclusions

A series of material tests were conducted to clarify the influence of thermal history assuming fire on the mechanical properties of SBHS. It was examined whether the change in mechanical properties of SBHS due to fire could be estimated by the Leeb hardness test. The obtained main results in this study are as follows.

(1) When SBHS400 and SBHS500 were heated up to 600℃ and then cooled, the mechanical properties were almost the same as those without heating and cooling. In the case of a fire on a steel bridge with SBHS, 400℃ might be applicable as the temperature criterion for determining whether detailed investigations are required or not. This criterion is the same for general steel.

(2) When SBHS400 and SBHS500 were heated up to 900℃ and then air-cooled, there was almost no change in Charpy absorbed energy for SBHS400. The increase in Charpy absorbed energy by 47% was observed in SBHS500 compared to the case without heating and cooling. In contrast, the yield stress was 30% lower for SBHS400 and 38% lower for SBHS500, and the tensile strength was 15% lower for SBHS400 and 30% lower for SBHS500. As a result, the standard values specified in JIS were not satisfied.

(3) When SBHS400 and SBHS500 were heated up to 900℃ and then water-cooled, Charpy absorbed energy was 67% lower for SBHS400 and 41% lower for SBHS500 than that without heating and cooling. The fracture patterns of these cases were brittle. The yield stress was 17% lower for SBHS400 and 33% lower for SBHS500. The tensile strength increased by 14% for SBHS400, but decreased by 7% for SBHS500. No effect of quenching was observed in SBHS with high strength provided by TMCP. This trend was different from that of general steel.

(4) Except for the case of water cooling after heating up to 900℃, the average value of the Leeb hardness measured at several points on the steel surface is possible to be used to accurately estimate the changes in yield stress and tensile strength. Although there is room for improvement in accuracy and applicable range, the Leeb hardness test has shown the potential for use in quickly estimating the mechanical properties of SBHS subjected to thermal history assuming fire.

In the future, similar studies will be conducted for latest steel such as SBHS700. SBHS700 has not yet been investigated in previous studies. Research and evaluation will be continued to accumulate data on mechanical properties of steel in bridge fires.

References

[1] Oyama, O., Imagawa, Y., Kurita, A., “Damage examples of bridge caused by fire”, *Bridge and Foundation Engineering*, 42, 35-39, Japan, 2008. (in Japanese)

[2] Kuwano, T., Masui, T., Suzuki, H., Yoda, K., “Restoration of urban expressway viaducts damaged by severe fire accident”, *Bridge and Foundation Engineering*, 43, 13-18, Japan, 2009. (in Japanese)

[3] Bridge and Foundation Engineering, Overseas Literature Research Group., “The collapse and reconstruction of the Macarthur Maze”, *Bridge and Foundation Engineering*, 44, 48-49, Japan, 2010. (in Japanese)

[4] Yanagisawa, N. et al. “An analysis of failure mechanism due to fire for 9 mile road overpass in USA”, *Bridge and Foundation Engineering*, 48, 26-30, Japan, 2014. (in Japanese)

[5] Godart, B. et al. “Diagnosis, assessment and repair of the Mathilde Bridge close to collapse during a fire”, *Structural Engineering International*, 331-338, France, 2015.

[6] Japan Society of Civil Engineers., “Steel structure series No.24, Guidelines for Diagnosis and Repair Method of Steel Bridge exposed to Fire”, Japan, 2015. (in Japanese)

[7] Japanese Society of Steel Construction, Technical Committee, Safety Subcommittee, Fire Resistance Subcommittee, High Temperature Strength Group., “Mechanical properties of structural steels at and after heating”, *JSSC Vol.4*, No.33, Japan, 1968. (in Japanese)

[8] Architectural Institute of Japan., “Guide Book for Fire-Resistive Performance of Structural Materials”, *Archi Books*, Japan, 2009. (in Japanese)

[9] Hirohata, M., Kitane, Y., Itoh, Y., “Effect of heating and cooling process assuming fire of steel bridges on characteristics of welded joints of structural steel”, *Journal of Steel Construction*, Vol.21, No.84, 67-78, Japan, 2014. (in Japanese)

[10] Hirohata, M., Nezu, K., Nakayama, T., Matsui, S., “Effect of heating and cooling processes simulating fire damage on mechanical properties of steels used in aged bridges”, *Journal of Steel Construction*, Vol.24, No.95, 49-57, Japan, 2017. (in Japanese)

[11] Zhang, P., Li, S.X., Zhang, Z.F., “General relationship between strength and hardness”, *Materials Science and Engineering A*, 529, 62-73, China, 2011.

Advanced Steel Construction – Vol. 20 No. 2 (2024) 111–119
DOI:10.18057/IJASC.2024.20.2.2
(Special Issue: *11st International Conference on Advances in Steel Structures, ICASS'2023, Kuching, Sarawak, Malaysia*)

STUDY ON THE IMPACT CUSHIONING PERFORMANCE AND STRUCTURAL OPTIMIZATION OF A MODULAR COMPOSITE BUFFERING STRUCTURE

Yun-Tao Jin [1, 3] and Zhi-Xiang Yu [1, 2, 3, *]

[1] *School of Civil Engineering, Southwest Jiaotong University, Chengdu 610031, China*
[2] *National Engineering Laboratory for prevention and control of geological disasters in land transportation, Chengdu 611756, China*
[3] *Research Center of Protection Structures Against Natural Hazards, Southwest Jiaotong University, Chengdu 610031, China*
** (Corresponding author: E-mail: yzxzrq@swjtu.edu.cn)*

ABSTRACT

The traditional concrete rockfall shed, relying on a sand cushion for impact energy absorption, suffers from limited buffering performance, long recovery cycles, and inadequate resilience in emergency disaster prevention. To address these issues, this paper proposes a modular composite buffering structure comprising a flexible steel buffer and a sand cushion. A 500kJ impact test was conducted on the structure to investigate its mechanical behavior and rockfall cushioning performance. The test revealed the energy dissipation mechanism between the flexible steel buffer and the sand. Using the LS-DYNA platform, a FEM-DEM coupled dynamic numerical model was established to compare the cushioning performance of the buffering structure with other typical cushions. Additionally, the supports under the concrete slab and the structural layout of the flexible buffer were optimized to achieve better buffering and structural perfoemance. The research demonstrates that the composite buffering structure exhibits excellent cushioning performance, remaining intact under 500 kJ impact. Compared to sand material and EPS-sand cushion, the composite buffering structure reduces impact force by 62% and 20%, respectively. After replacing the supports under the slab by buckling corrugated tubes, the composite system is able to bear 1000kJ impact and the slab's bearing capacity is improved. With its superior cushioning performance, the composite buffering structure shows great potential for engineering applications.

ARTICLE HISTORY

Received: 8 April 2024
Revised: 13 May 2024
Accepted: 5 June 2024

KEYWORDS

Steel rockfall shed;
Rockfall impact;
Flexible steel structure;
Energy absorption;
Buckling corrugated tubes

1. Introduction

Approximately two-thirds of China's main land is mountainous area[1], posing a threat to human activities, especially the normal operation of transportation arteries, due to geological hazards such as landslides, debris flows and rockfalls. Rockfall disasters refer to the phenomenon of rocks rapidly rolling down from steep cliffs or slopes to the ground[2], and they are characterized by randomness and frequent occurrences[3]. When geological hazards such as rockfalls occur in mountainous areas, it is often not feasible to directly implement protective measures on the slopes adjacent to the transportation routes due to adverse geological conditions and the high risk of recurring rockfall disasters. Therefore, rockfall sheds[4-6], as they can be directly installed on roads, have become important protective measures for emergency response to geological disasters in mountainous areas. Traditional reinforced concrete rockfall sheds (Fig. 1a) have disadvantages such as long construction periods and low energy dissipation capacity. Additionally, the cushioning layer of rockfall sheds often utilize materials such as sand and gravels[7,8], resulting in limited buffering performance. These factors affect the impact resistance and emergency response capabilities of rockfall sheds. Therefore, the development of a steel rockfall shed structure with good buffering performance and fast assembly speed holds significant practical engineering significance and application value.

The rockfall shed is a common passive protective measure used for rockfall protection at tunnel entrances, exits, or sections prone to frequent rockfall disasters. Existing shed structures mainly consist of support structures and cushioning layers. The sheds achieve energy dissipation and impact diffusion of rockfall through the cushioning layer, reducing the impact force on the support structure, and ultimately intercepting the rockfall on the shed structure or guiding it to the specific area. Currently, steel sheds can be classified into two main types[9,10]: steel frame sheds and steel flexible sheds (Fig.1b, 1c). The steel flexible sheds combine arch-shaped steel structures with flexible protective nets. The flexible nets utilize their own deformation to intercept and cushion the rockfall, embodying the concept of "flexibility overcomes rigidity" in protection. Energy dissipation devices can also be installed when necessary[11,12], enhancing buffering and energy dissipation capabilities. In comparison, steel frame sheds have relatively higher stiffness and require the installation of a cushioning layer on the roof. Regarding shed supporting structures, Wang et al. conducted full-scale impact tests on a flexible steel shed[13], demonstrating that the flexible shed successfully intercepted rockfall under a 250kJ impact and only required simple maintenance for continued use. Tan proposed a flexible buffering structure based on the cable-supported structural principle and studied its deformation characteristics and energy dissipation capacity[14]. This cushioning structure can be flexibly applied to various shed structures. Wu et al. introduced a novel energy-dissipating and shock-absorbing shed by incorporating energy-dissipating supports[10], which increased the flexibility of the structure while maintaining its buffering capacity. Chen et al.[15] presented an optimized composite steel shed, in which the roof of the shed was optimized as a sandwich steel plate and the supports were optimized as thin-walled steel tubes to achieve secondary energy dissipation. They also developed a formula to calculate the internal forces of the optimized shed structure, and the results showed a reduction of approximately 20% in the maximum bending moment of the transverse and longitudinal beams after optimization. Yu et al.[16] proposed a new piston-rod-supported flexible structure system based on flexible protective nets. The system demonstrated buffering, self-recovery, and rock ejection capabilities, with an impact force approximately 60% of that of sand and EPS cushioning layers under the same impact energy. In terms of cushioning layers for sheds, the effect of a sand cushion on reinforced concrete slabs has been studied in literature[7]. The influence of parameters such as density, thickness of sand, and rock shape effect on the impact force has also been investigated [8,17,18], but these cushion materials have high self-weight. In recent years, research on using EPS materials as cushion has gained popularity[19,20], and they have been combined with sand, geotextiles, and steel structures to achieve satisfactory buffering effects with a lower self-weight. Some scholars have even creatively used materials such as waste tires and tennis balls as cushioning layers for rockfall impact response studies[21,22], but these studies are still in the preliminary exploration stage. The aforementioned studies provide valuable insights for the selection of shed structures and cushioning layers. However, the mentioned cushions either have issues with high self-weight and insufficient buffering capacity or have compatibility issues with steel sheds. Although the piston-rod-supported flexible structure is compatible with steel sheds, controlling its deformation is challenging, and there is a risk of excessive deformation or direct collision between the rockfall and the shed roof slab after the flexible net is penetrated [23].

Therefore, this paper proposes a buffering structure that combines the flexible steel structure and sand cushion to fully utilize the superior buffering and energy dissipation performance of flexible protective structures while avoiding the problem of direct collision between rockfall and shed roof slab caused by deformation variability. A 500kJ full-scale impact test was conducted to verify the effectiveness of this combined cushioning structure. Based on the LS-DYNA explicit dynamic simulation platform, FEM-DEM coupled numerical models were established for this buffering structure and other representative cushioning layers, and the buffering effect, structural stresses, and deformations of these cushions were quantitatively compared. Finally, the structural optimization of the system especially the supporting improvement under the slab were carried out to achieve better buffering performance. The research results provide a theoretical basis for the engineering design of this type of cushioning structure.

(a) Reinforced concrete rock-shed (b) Steel frame rock-shed (c) Fexible steel rock-shed

Fig. 1 Different types of rockfall sheds

2. The composite buffering structure

2.1. Structural principles

The main focus of this paper is the buffering structure on the upper part of the steel shed. This composite buffering structure consists of a flexible steel buffer and a sand cushion, as shown in Fig. 2a. The flexible steel buffer is primarily composed of flexible interception nets, steel wire ropes, energy dissipaters, and steel supports. The steel supports include vertical supports and inclined supports to ensure the geometric integrity of the structural system. The top of the steel supports is a sliding node, allowing the steel wire ropes passing through it to slide semi-freely and dissipate energy through frictions. These steel structural components can be assembled quickly, providing strong emergency response capabilities and disaster resilience. Fig. 2b shows the front view of the assembled buffering structure with the steel shed, with space provided for vehicles underneath the steel shed. The reason for adding a layer of sand on top of the concrete slab beneath the flexible steel buffer is that it is impossible to accurately predict the deformation of such nonlinear large deformation structures in practical engineering environments due to uncertain factors such as the shape, size, impact position, and impact angle of the rockfalls. Moreover, the bullet effect[23] may cause penetrations of the flexible net. These uncertain factors can result in direct rigid collisions between the falling rocks and the shed slabs, causing significant structural damage or even structural failure.

As shown in Fig.2b, the rockfall contacts with the flexible net firstly, and the net panel drives the movement of the steel wire ropes. When the tension in the steel wire ropes reaches a threshold (the activation force of the energy dissipater), it will trigger the stretching of the connected energy dissipater. This controls the development of internal forces in the components and dissipates the impact energy. The energy dissipation in this stage occurs through the plastic deformation of the net panel, the frictional sliding of structural components, and the stretching of the energy dissipater, with the latter being the main energy dissipation approach. When the falling rock continue to move downward, it may collide with the sand cushion. At this point, the sand cushion plays a role in spreading the pressure and dissipates some of the impact energy through the internal friction of the sand particles. Throughout the entire impact process, there are various complexities such as geometric, material, and contact nonlinearities, making the mechanical behavior highly intricate. The energy control equation for this process can be determined by Eq (1), which assumes a single rockfall impact and neglects the rolling friction of the falling rock within the flexible net.

$$\int_0^{h_{max}} F(h)dh = E_{k0} + mgh_{max} = E_{ed} + E_{sld} + E_n + E_s \tag{1}$$

Where $F(h)$ represents the vertical impact force of the falling rock, h represents the vertical impact displacement, h_{max} represents the maximum impact displacement, E_{k0} represents the kinetic energy of the falling rock when it contact the net, m represents the mass of the falling rock, and g represents the gravity acceleration, which is taken as 9.81 m/s^2. E_{ed}, E_{sld}, E_n and E_s represent the energy dissipated through stretching of the energy dissipater, friction of the structural components, deformation of the net, and friction of the sand, respectively.

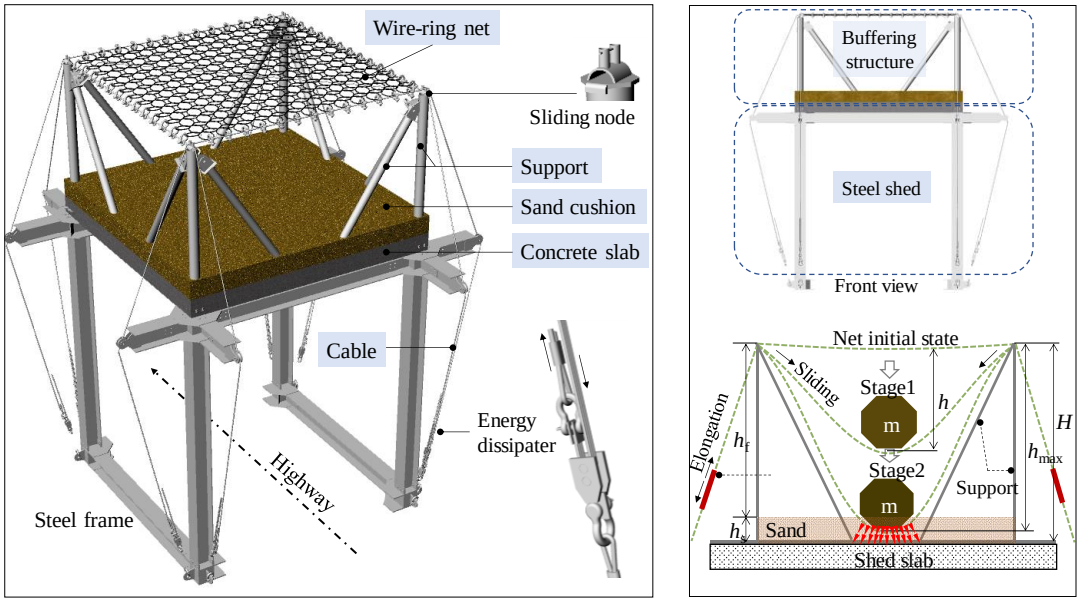

(a) Buffering structure fabricated with a steel rockfall shed (b) Front view and mechanism of the buffering structure

Fig. 2 The composition and working mechanism of the composite buffering structure

2.2. Test overview of the composite buffering structure

The full-scale impact test of the composite buffering structure was conducted at the National Engineering Laboratory for prevention and control of geological disasters in land transportation. The impact energy in the test was 500 kJ, and the test field is a comprehensive test platform with a testing capacity of up to 5000 kJ. The lifting and releasing of the impact block were achieved through a mobile crane with a maximum lifting height of 35 m (Fig. 3a). The

structural model of the test is shown in Fig.3b. It should be noted that in addition to the red triangle supports shown in the figure, there are also inclined supports, which are designed to meet the anchoring conditions of the end energy dissipaters at the test site to prevent excessive deformation caused by the extension cantilever. Otherwise it may affect the accuracy of the test results. The top of the steel support is designed to be slidable to facilitate the movement of the steel wire ropes (Fig. 3c), and the bottom of the vertical support is designed to be elastically rotatable (Fig. 3c). The impact block used in the test is a 26-faced polyhedron recommended in the European guidelines [25], with a mass of 6 tons (Fig. 3c). The bulk density of the sand cushion is 1480 kg/m^3. During the test, high-speed cameras were used to capture the impact images (Fig. 3c), and load cells were installed to measure the tension at the end of the steel wire ropes (Fig. 3c). The specifications of the components can be referred to Table 1, and other detailed test parameters can be found in the literature [24]. The test results will be compared and discussed with the numerical simulation results in Section 3.2.

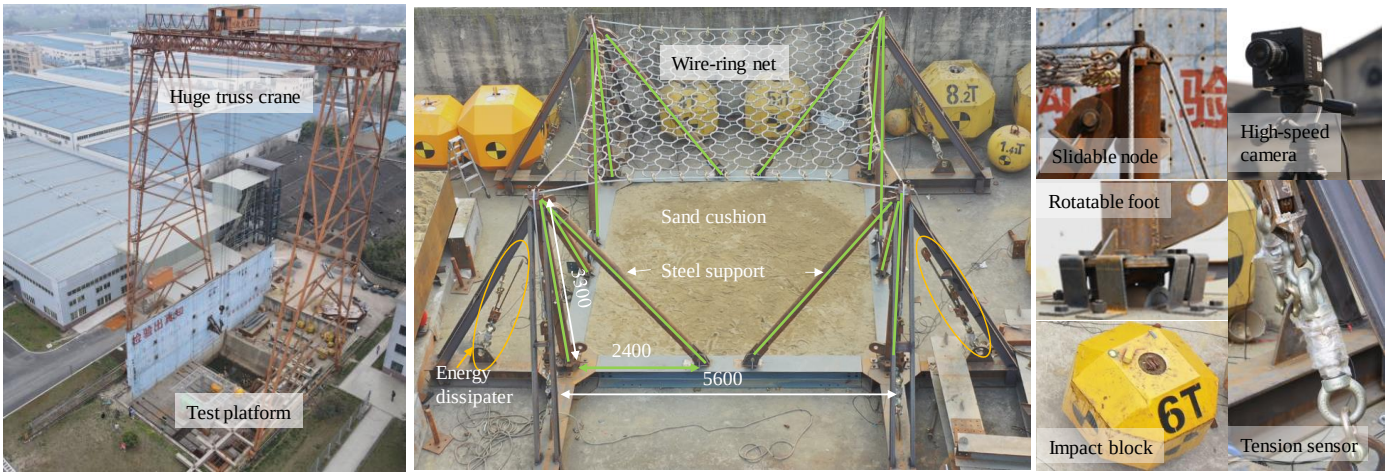

(a) Aerial view of the test field (b) Full-scale test structural model (c) Test equipments and nodes

Fig. 3 Layout of the experiment site

Table 1
Specifications of the members

Member	Specification	Material	Comment
Support	P180mm×8mm	Q235B	Tube
Wire-ring net	R19/3/300	Steel wire	1770 grade
Cable	Φ22mm	Steel wire	1770 grade
Energy dissipater	3@Φ16mm	Q235B	U-shaped
Sand	Medium sand	1480kg/m^3	4.3% water content

3. Numerical analysis of the composite buffering structure

3.1. Introduction of the numerical model

The numerical model in this study is based on the explicit dynamic analysis software LS-DYNA, utilizing the FEM - DEM coupling analysis method. This method allows for the simultaneous analysis of the dynamic responses of the falling rocks, flexible structures, sand cushion and reinforced concrete slab. The arrangement of the numerical model is shown in Fig. 4, and the dimensions of the concrete slab are 7000mm×6000mm×600mm. In the model, the falling rock and concrete slab are represented using solid elements, while the flexible net, supports, energy dissipaters, and steel rebars are represented using beam elements. The steel wire ropes are represented using cable elements, and the sand particles are represented using discrete elements with a radius of 15mm. In terms of material models, the falling rock is modeled as rigid bodies, the DEM particles are modeled as elastic materials, the flexible net and energy dissipaters are modeled using multi-linear elastoplastic material models, and the remaining steel components are modeled using ideal elastic-plastic material. The concrete is modeled using the CSCM Concrete material in LS-DYNA with a strength grade of 40 MPa. The specific parameter values are based on the literature [26]. Part of the input parameters for the materials are shown in Table 2, and the parameter values are based on the literature [27].

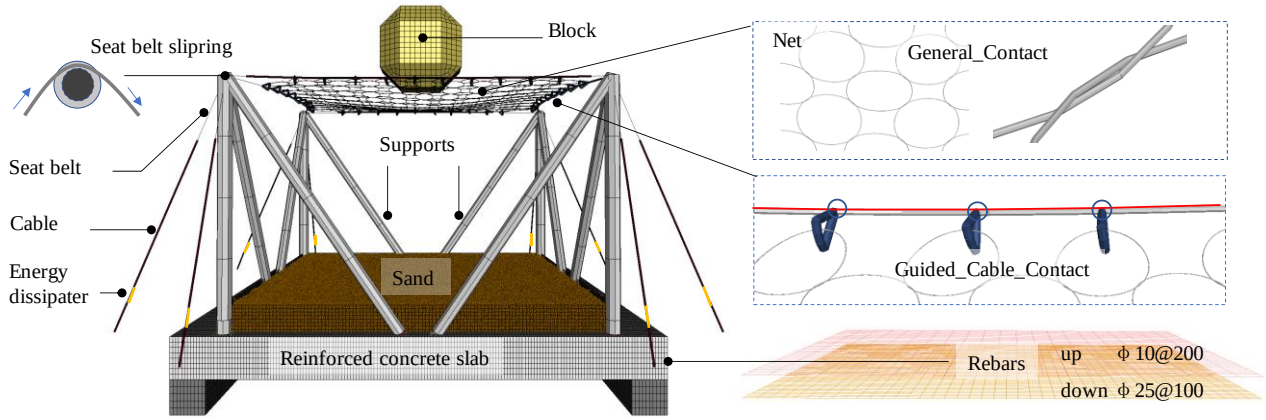

Fig. 4 Layout of the numerical mode

In this section, we specifically introduce two key steel structural components in the flexible buffer, the wire-ring net and the bar-shaped energy dissipater. As shown in Fig. 5a, the wire-ring net exhibits strong nonlinear characteristics under out-of-plane loading, with a tendency for the rings to transit from a curved shape to a straightened shape, accompanied by sliding between the rings. Influenced by geometric, material, and contact nonlinear factors, the force-displacement relationship during loading also shows a strong nonlinear correlation, which can be divided into stages dominated by flexural behavior and tensile behavior. Due to the considerations of geometric nesting relationships and actual contact conditions during modeling, the net in the model is able to reproduce the actual mechanical behaviors under impact. The energy dissipater plays a crucial role in the system by absorbing energy. As

shown in Fig. 5b, it typically remains in an elastic state before activation. When the tension in the steel wire rope exceeds the activation force, the energy dissipater starts to operate, leading to a significant energy dissipation. The bar-shaped energy dissipater used in this study is achieved by winding steel rebars around an axis pin and stretching it, utilizing its own plastic deformation and frictions between the steel bars and the axis pin for energy dissipation. In the computational model, a beam element with a special stress-strain relationship or a nonlinear elastic-plastic spring element consistent with the actual force-displacement relationship of the energy dissipater is employed to reproduce the behavior. This approach ensures efficient computation of the overall model while maintaining consistency with the mechanical behavior.

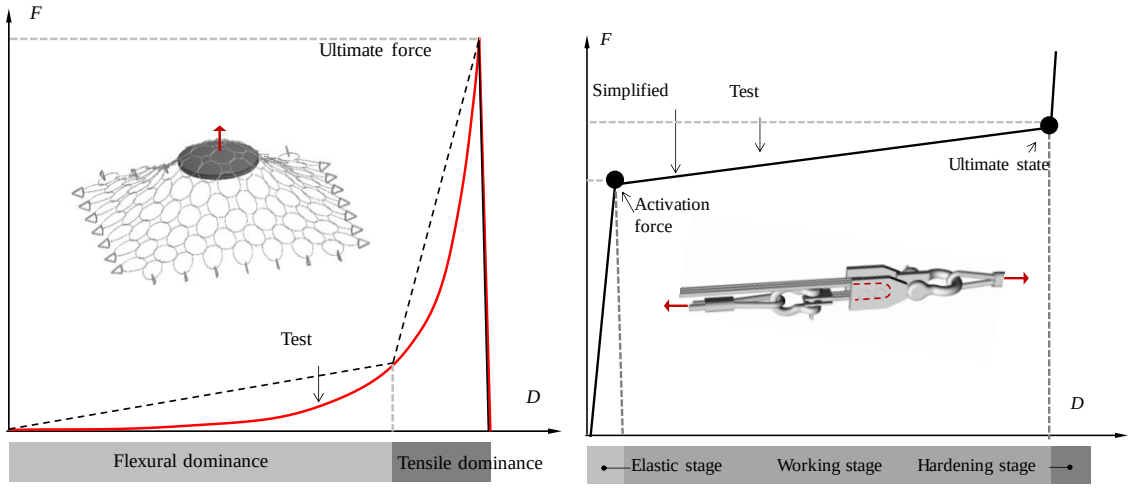

(a) Typical *F-D* curve of the wire-ring net

(b) Typical *F-D* curve of the energy dissipater

Fig. 5 Working characteristics of key components

Table 2
Parameters input of the materials

Member	Density	Elastic modulus	Poison's ratio	Yield stress	Failure strain
Wire-ring	7850kg/m^3	2.07×10^5 MPa	0.3	1488MPa	0.14
Energy dissipater	7850kg/m^3	2.06×10^5 MPa	0.25	1100MPa	1.61
Cable	7850kg/m^3	1.2×10^5 MPa	0.35	1770 MPa	0.015
Supports	7850kg/m^3	2.06×10^5 MPa	0.3	235 MPa	0.25
Block	2500kg/m^3	2.0×10^4 MPa	0.2	-	-
Bebar	7850kg/m^3	2.06×10^5 MPa	0.3	335 MPa	0.2
DEM	1480kg/m^3	2.1×10^4 MPa	0.25	-	-

3.2. Comparation analysis with the test responses

In the numerical model that is compared with the test results, all degrees of freedom of the nodes in the bottom concrete slab were fully constrained, so the boundary stiffness was consistent with the sand cushion in direct contact with the ground in the actual experiment. The images at the moment of maximum deformation for the experiment and simulation are shown in Fig. 6a and 6b, respectively. All structural components remained intact, and the deformation patterns of the flexible nets are consistent, with both coming into contact with the sand cushion. The steel supports did not undergo significant deformation, and the mesh shape of the flexible net underwent significant changes, with sliding deformation occurring along the steel wire ropes at the edge of the net. The sag of the steel wire ropes significantly increased compared to the state before the experiment, indicating that the energy dissipaters connected to the steel wire ropes underwent tension deformation. The displacement history comparison in Fig. 6c shows that the maximum displacements for the experiment and simulation are 3.493m and 3.381m, respectively. The simulated displacement is slightly smaller than the experimental value, with an error of less than 5%. One of the most important indicators for evaluating the bufferperformance of the cushion is the impact force or acceleration of falling rocks, and these two can be converted using Eq (2).

$$F = F_{fb} + F_{sl} = m(a+g) \tag{2}$$

Where F is the vertical impact force on the block. F_{fb}, F_{sl} is the vertical contact force of the flexible net and the sand on the block, and a is the acceleration of the block. The acceleration history curves of the block for the experiment and simulation are shown in Fig. 7a. The peak accelerations for the experiment and simulation are 122 m/s^2 and 133 m/s^2, respectively, with a relative error of 9%. When converted to impact forces, they are 791 kN and 857 kN, respectively. The time-history curve shows a steep peak in the impact force around t = 0.3 s, and the high-speed image during the experiment reveals that the moment of rapid increase in impact force occurs at t=0.29s, which is the instant of contact between the block and the sand cushion. The numerical simulation results indicate that at this moment, more than 90% of the energy of the falling block has already been dissipated, indicating that the energy dissipation of the sand cushion is relatively small but has a significant impact on the increase in impact force. Fig. 7b shows the comparison of the maximum tensions in the steel wire ropes between the experiment and simulation. Both the peak value and duration are consistent, and the tension is lower than the tensile strength of the 22mm-diameter steel wire rope utilizing high strength steel wires with a tension strength of 1770MPa. Fig. 7c presents the time-history results of the maximum axial force in the simulated circular beam elements. The peak tension is 24.5 kN, which is much lower than the tensile strength of the wire windings in the R19/3/300 wire-ring net[28-30].

The steel supports are made of low-carbon steel with a strength grade of 235 MPa. The stress distribution at the maximum load moment is shown in Fig. 8a, with a maximum stress of 99.4 MPa. The conservative approach was taken in selecting the cross-section values, and further optimization is considered in the following sections. The stress distribution nephogram of the wire-rings within the flexible net (Fig. 8b) indicates that the wire strands experience the maximum tension at the corners and the area in contact with the block. The main tension direction is at a 45-degree diagonal, which is different from the main tension direction in a flexible barrier [27]. This is because, in the given structural arrangement, the stiffness of the corner boundaries is slightly greater than that of the cables in the middle, which reflects the self-adaptive stiffness characteristics of the flexible structure.

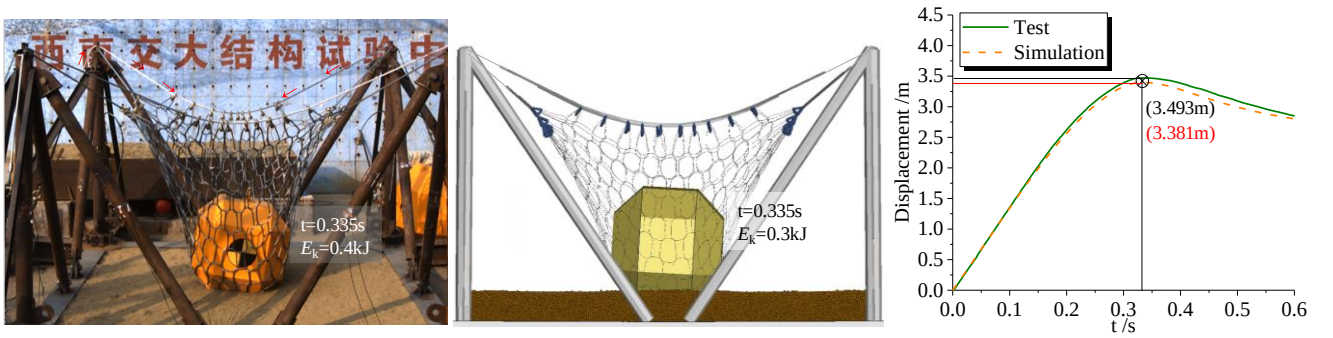

(a) The test image at maximum deformation moment (b) the simulation image at maximum deformation (c) block displacement history of the test and simulation

Fig. 6 Deformation comparation of the test and simulation result

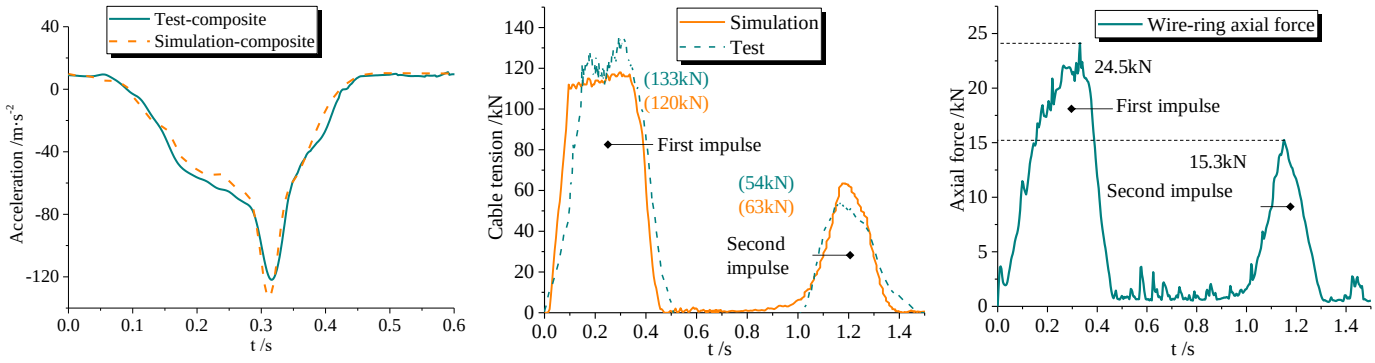

(a) The block acceleration history comparation (b) The cable tension comparison (c) The simulated wire-ring axial force history

Fig. 7 Impact responses of different parts

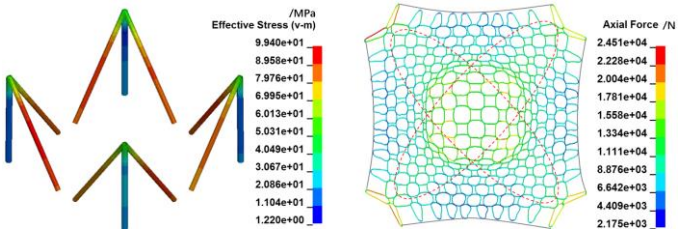

(a) Stress nephogram of the steel supports (b) Axial force nephogram of the ring net

Fig. 8 The stress state of steel components

3.3. Comparation analysis with typical cushions

In order to compare the buffering performance of the proposed composite buffering structure, numerical models of the rockfall impact on the sand cushion and EPS-sand composite cushion were also established based on the numerical approach described in Section 3.1, as shown in Fig. 9. The selected EPS material has a density of 30 kg/m^3 and a thickness of 2 m, with a sand layer thickness of 0.4 m on the top. In the model covering only with the sand cushion, the thickness of the sand cushion is 0.8 m. The EPS material model adopts a multi-linear elastoplastic material model, and specific input parameters can be referred to reference[20]. Other parameters in the model can be referred to in Section 3.1. In the three models, the impact energy when the rock bottom reaches the height of the net shown in Fig. 9c is 500 kJ. The simulation results (Fig. 10) show that among the three cushions, the proposed composite buffering structure has the smallest impact force, measuring 852 kN. The EPS-sand layer has the second smallest impact force, measuring 1055 kN. The traditional sand cushion has the largest impact force, measuring 2242 kN. The impact force of the flexible buffering structure is 62% lower than that of the traditional sand cushion and 20% lower than that of the EPS-sand cushion, indicating its superior buffering effect. In addition, from the time-history curve of the impact force in Fig.10, it shows that the flexible buffering structure also has the longest impact duration, which is beneficial for reducing the impact force according to the theorem of impulse.

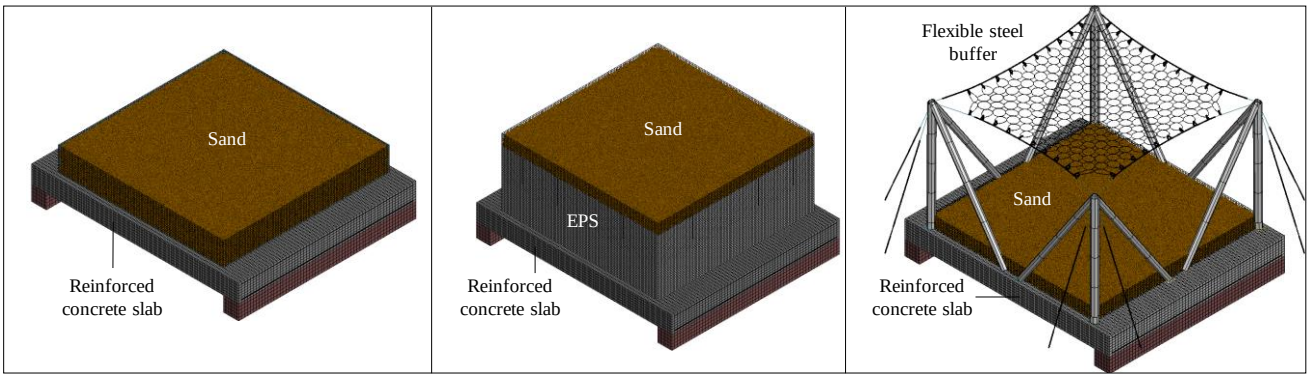

(a) 0.8m-thick sand cushion (b) 2m EPS-0.4m sand cushion (c) Composite buffering structure in this paper

Fig. 9 Three different rockfall cushions for responses comparation

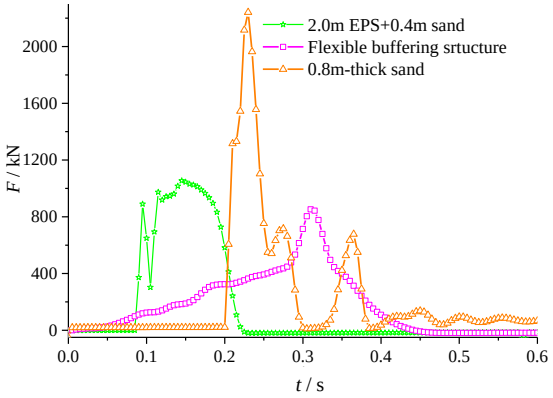

Fig. 10 Impact force history of the three different cushions

From the perspective of impact deformation, the composite buffering structure has the largest impact deformation, measuring 3382 mm (Fig.11c); the impact penetration depth of the sand cushion is the second largest, measuring 742 mm (Fig.11a); and the impact penetration depth of the EPS-sand composite cushion is the smallest, measuring 715 mm (Fig.11b). Interestingly, in combination with the results of the peak impact force mentioned above, the impact force of the EPS-sand composite cushion, which has a smaller impact deformation compared to the sand cushion, is actually smaller. This indicates that in the context of impact problems, it is not sufficient to simply compare the impact deformation to infer the relative magnitude of the impact force. The distribution of the impact force over time is also important and needs to be analyzed in conjunction with the actual situation. The distribution of compression stress in the bottom reinforced concrete slab is shown in Fig. 12. The concrete with a sand cushion has the highest compression stress, measuring 28.0 MPa. The concrete slab covered with the flexible buffering structure has the second highest stress, measuring 13.3 MPa. And the concrete slab covered with the EPS-sand composite cushion has the lowest stress, measuring 10.1 MPa. Although the impact force of the composite flexible buffering structure is the smallest according to the results in Fig. 10, the stress in the bottom concrete slab is higher than that in the EPS-sand composite cushion. This is because the arrangement of steel supports in the flexible buffering structure is not optimal. The inclined supports are located at the mid-span of the slab, resulting in a significant concentrated load at the mid-span, leading to local stress concentration and larger bending moments in the slab. This issue will be addressed and optimized in Section 3.4. The stress nephogram of the steel rebars in the concrete slab is shown in Fig. 12b. Similar to the stress state in the concrete, the maximum stress is observed in the scenario with a pure sand cushion, while the minimum stress is observed in the scenario with the EPS-sand composite cushion.

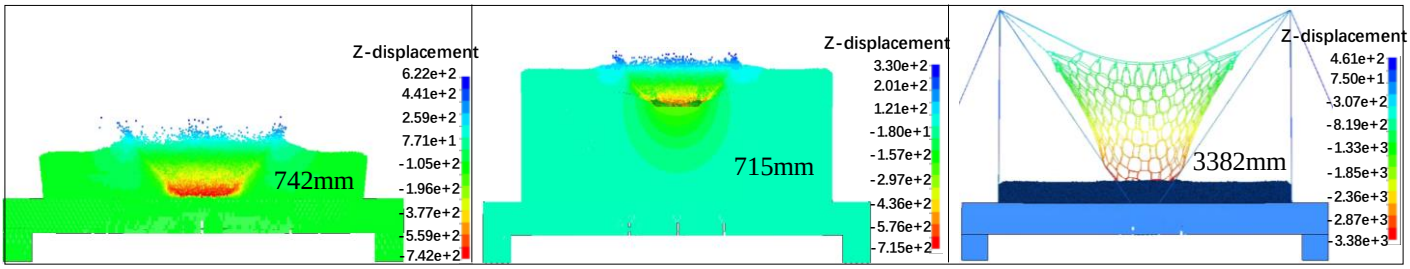

(a) 0.8m-thick sand cushion (b) 2m EPS-0.4m sand cushion (c) Composite buffering structure in this paper

Fig. 11 The maximum deformation nephogram of the cushions

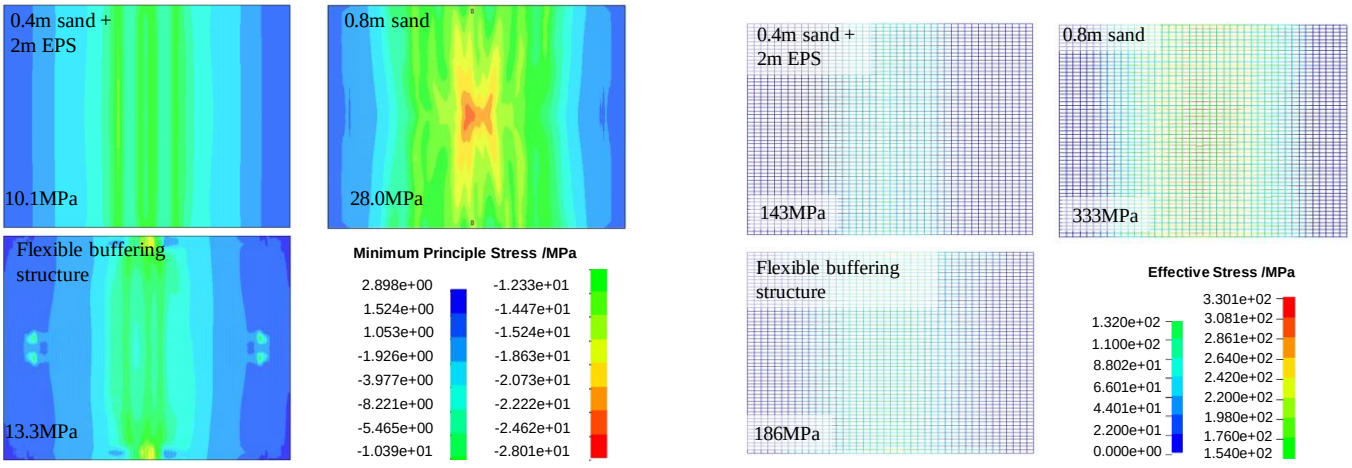

(a) Compression stress nephograms of the slabs (b) Von-Mises stress nephograms of the rebars

Fig. 12 Stress state of the reinforced concrete slab

4. Structural optimization

4.1. Optimization of the upper buffering structure

This section focuses on the layout optimization of the upper steel supports since the diagonal supports are located near the mid-span of the concrete slab and are subjected to significant compression, this results in large bending moments in the bottom slab. Therefore, an optimization of the steel supports is conducted. The specific optimization involves removing the inclined supports and using a horizontal support to connect the top of the vertical supports, along with diagonal connections using cables with diameter of 18mm. The numerical model was applied 500kJ impact with the same condition in Section 3.3. The maximum effective stress in the optimized steel supports is reduced to 89.5 MPa, which is a 10% reduction compared to the original structure (Fig.13a). More importantly, the compression stress in the concrete slab decreases to 8.05 MPa (Fig. 13b), with a reduction of 39.5%, and the stress in the bottom steel rebars decreases to 108.6 MPa (Fig. 13c), with a reduction of 41.6%. This optimization approach provides significant stress reduction for the protective object at the bottom, resolving the contradiction described in Section 3.3, where the composite buffering structure has low impact force but imposes a large load on the bottom slab. The maximum tension in the diagonal cables during impact is only 14kN，which means low internal forces in cables.

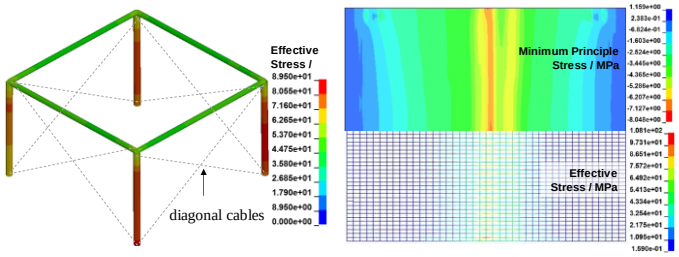

(a) Stress nephogram of the steel supports (b) Stress nephogram of the reinforced slab

Fig. 13 The stress nephogram of the structure after layout optimization

4.2. Buckling corrugated tubes for the slab supporting

To consider larger impact energy of the rockfalls, better adapt to the variability of rockfall hazards in actual field environments, and improve the impact resistance of concrete slabs under composite buffer structures during end-stage impact, a numerical analysis was conducted by replacing the supports of the slab with corrugated steel tubes. Previous studies have been carried out on similar tube supports [10,15], but the impact resistance of these corrugated tubes within the framework of this study still needs further research. The structure and dimensions of the corrugated steel tube used are shown in Fig. 14. The diameter of the corrugated tube D = 270mm, the height H = 300mm, the radius of the circular wave r = 25mm, the central angle corresponding to the arc is 60°, and the wall thickness of the metal tube t = 6mm. The material used is Q235B steel which is cost-effective in engineering application. End plates with a thickness of 10mm are welded at the upper and lower ends of the corrugated tube, and they are locked in by lock plates. The upper lock plate can be connected to a shear connector embedded into the concrete slab. The dimensions of the concrete slab in this analysis case are consistent with that in Section 3.3, with three corrugated tube supports on each side of the slab, totaling six supports.

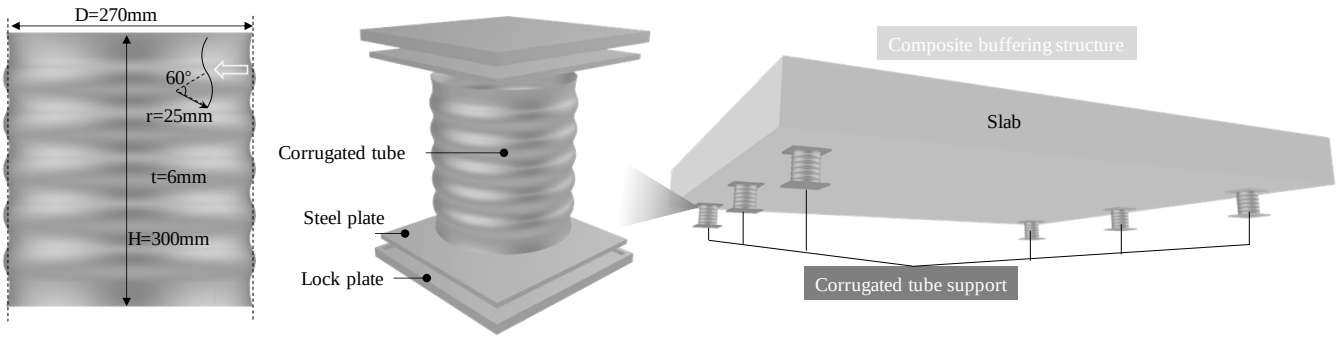

Fig. 14 Buckling corrugated tubes for supporting the shed slab

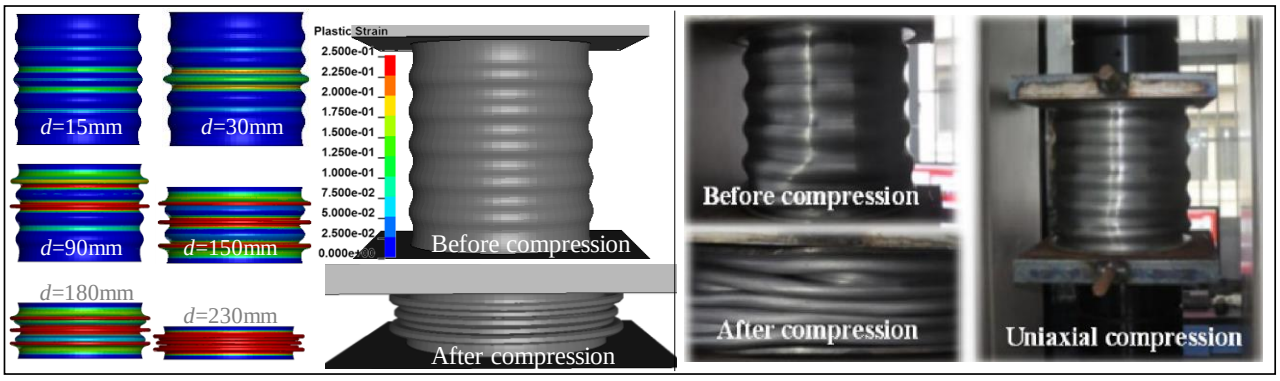

(a) Axial compression simulation of the corrugated tube (b) Axial compression test of the tube[10]

Fig. 15 Axial compression performance of the corrugated tube

Before using the corrugated tubes in the composite buffering structure and slab supporting, it is necessary to clarify its axial compression performance. Therefore, a uniaxial compression simulation of the corrugated tube was conducted, compared and verified against experimental results[10]. The compression test was modeled in LS-DYNA, with the steel tube established using shell elements. Self-contact was considered for thin-walled tubes to account for contact force transmission and stiffness evolution after bending deformation of the tube, as shown in Fig. 15a. The simulation results show significant plastic deformation occurring at the two grooves in the middle of the corrugated tube at a compression displacement of d = 15mm. At d = 30mm, plastic deformation also occurred at the convex wave between the two grooves, with further plastic deformation increases at the grooves. At d = 90mm, significant flattening occurred at the upper and middle circular areas of the tube, leading to self-contact of the tube-walls, with vertical loads being transmitted through squeezing between the tube-walls. During the compression process from d = 150mm to 230mm, more waves underwent large deformations and were flattened. The corresponding corrugated tube before and after compression in the experiment is shown in Fig. 15b, where the post-compression state aligns closely with the simulation results, forming dense compressed annular folds.

The compressive force-displacement curves of the corrugated tubes' compression process is shown in Fig. 16, where the simulated curve matches the experimental results, with buckling initiation force around 600 kN. Particularly, the simulation highly reproduced the undulations in the plateau segment of the curve, which is the stiffness evolution result of the process of corrugated tube-wall buckling, folding, and re-contacting, playing a crucial role in vertical force transmission. It shows that in the later stages of compression, the steel tube, due to the stacking of tube walls to form a contact-compression whole, exhibits a stiffening development, providing reliable support strength for the slab. The ultimate energy absorption of a single corrugated tube in simulation and experiment is 147 kJ and 134 kJ, respectively, with an error within 10%. The corrugated tube demonstrates superior buckling fuse function in static loading test and can consume considerable energy.

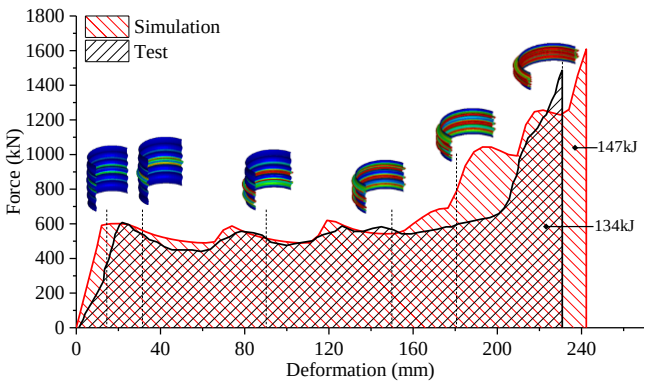

Fig. 16 F-D curves of axial compression of the corrugated tubes

After the corrugated tube was calibrated through static calculations, it was applied to the bottom supporting of the rock-shed slab under the protection of the composite buffering structure in this study to verify its buffering capacity for the slab under high kinetic energy impact exceeding the design level. The numerical model is essentially consistent with the composite buffering structure case in Section 3.3, with the only modification being the replacement of rigid supports with corrugated tube supports at the bottom of the concrete slab. A 1000 kJ rockfall impact simulation on the system was conducted, and the responses of the system under corrugated tube supporting are compared with that of rigid supporting at the same energy level. The established dynamic simulation model and its impact process are shown in Fig. 17, with the layout of the corrugated tubes in top view detailed in Fig. 17a, with a total of 6 corrugated tubes supporting on both sides. The gravity is gradually applied to 9.81 m/s^2 in the first 0.5 seconds of the calculation to achieve a stable state of system components and sand cushion under gravity, at which point the rockfall is just about to contact the flexible net. At t=0.70 s, the rock collided with the sand cushion and developed a significant impact force. At this moment, the bottom corrugated tubes are about to undergo significant buckling deformation, and the wire-ring net has experienced substantial sliding and deformation (Fig. 17b). At t=0.83 seconds, the rock has reached near the lowest point of the impact, and the supporting corrugated tubes have undergone significant buckling deformation (Fig. 17c), with compression deformations ranging from 59 mm to72 mm. The buckling deformation pattern is somewhat different from the fully symmetrical situation observed in static loading, possibly due to uneven vertical loading caused by the deflection of the concrete slab and certain horizontal shear forces acting on the tubes.

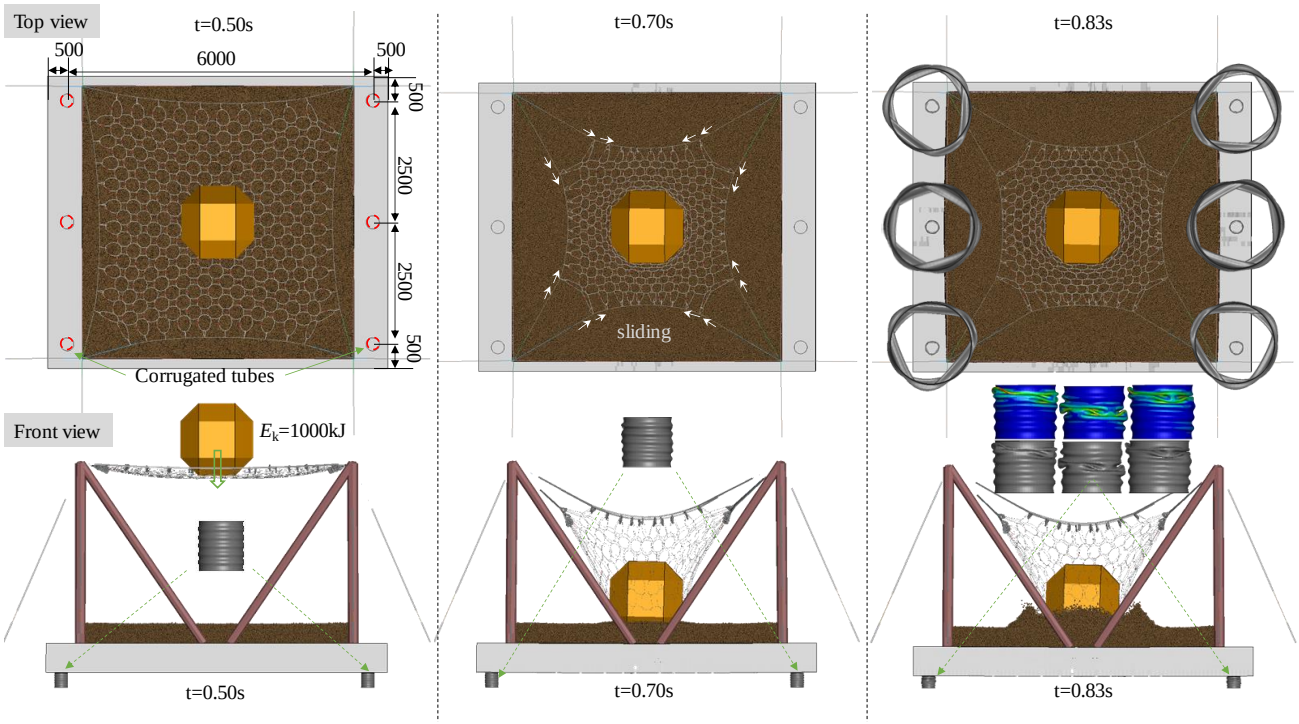

(a) t=0.50s initial state (b) t=0.70s impact state (c) t=0.83s impact state

Fig. 17 1000kJ impact process on the slab with the cushioning of composite buffering structure and the corrugated tubes supporting

Under the same 1000 kJ impact level, the impact responses of the composite buffering structure-slab with rigid supporting and corrugated tube supporting are compared as shown in Fig. 18. As observed in Fig. 18a, the maximum compressive stress of the concrete slab is reduced from 38.5 MPa under rigid supporting condition to 30.3 MPa, with a stress reduction of up to 21.3%, indicating a significant improvement. In Fig. 18b, the maximum impact reaction force can be reduced from 5351 kN under rigid supporting condition to 2505 kN, representing a reduction of 53.2%. The buffering effect is evident, and in the force-history curve under corrugated tube supporting condition, the plateau near the peak is more pronounced. This is a result of the combined action of the flexible buffering structure and corrugated tubes, with the corrugated tubes playing a key role in reducing the impact force peak when the rock collides the slab. Fig. 18b also presents the internal energy- history curve of the corrugated tubes, with a total energy absorption of 140 kJ under this calculation condition. The stress and deformation nephogram of the concrete slab under the two aforementioned supporting conditions are shown in Fig. 19. The maximum impact deflection decreases from 31.4 mm under rigid supporting to 20.6 mm, representing a reduction of 34.4%.

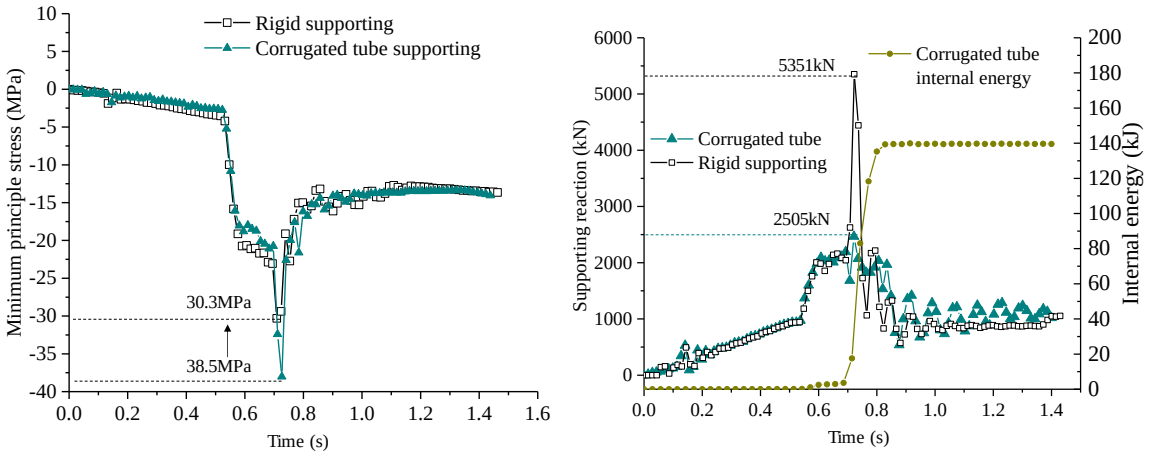

(a) Temporal maximum compression stress of slab (b) Temporal supporting reaction under the slab

Fig. 18 The concrete slab related responses using different supports

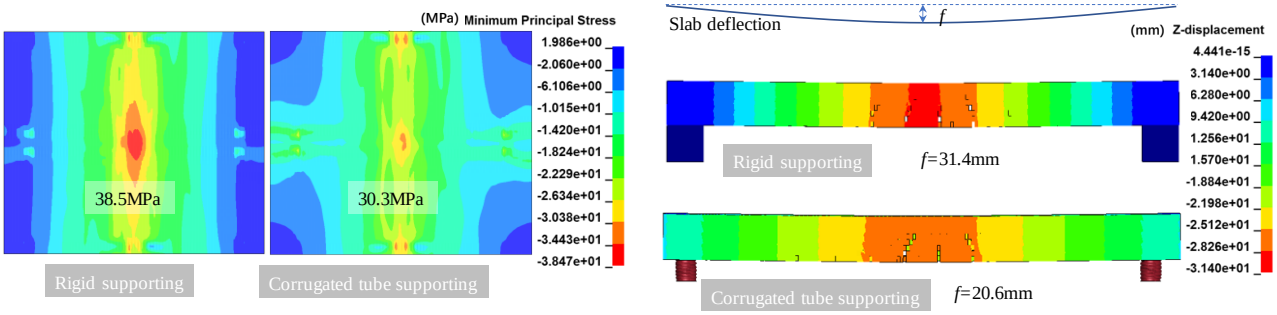

(a) Compression stress nephogram of slabs

(b) Maximum impact deflection of slabs

Fig. 19 The impact responses nephogram under the two supporting conditions

5. Conclusions

This paper proposes a composite buffering structure that combines a flexible steel buffer with a sand cushion. A full-scale 500 kJ impact test was conducted to validate the effectiveness of this type of structure. Based on the LS-DYNA explicit dynamic simulation platform, a coupled FEM-DEM numerical model was established for this buffering structure and currently typical cushioning layers. The buffering effects, structural stresses, and deformations of these cushions were quantitatively compared. Finally, structural optimizations especially the slab supporting optimization using corrugated tubes were performed, and the specific conclusions are as follows.

(1) The composite buffering structure is capable of withstanding impact energies of over 500 kJ while keeping the structure intact. The peak impact force in the experimental model was 787 kN, with the upper flexible steel buffer contributing significantly to energy dissipation and buffering, accounting for over 90% of the total energy dissipated. The sand cushion primarily serves as the second line of defense.

(2) The FEM-DEM coupled numerical model established based on the commercial code LS-DYNA effectively captures the dynamic behaviors of such structures, with errors in key responses such as impact force and displacement within 10%. Compared to the traditional sand cushion and the typical EPS-sand combination cushion, the proposed buffering structure in this paper can reduce the impact force by 62% and 20% respectively under a 500 kJ rockfall impact, demonstrating superior buffering performance.

(3) After upper structural optimization, the compression stress on the concrete slab and in the steel rebars can be reduced by 39.5% and 41.6%, respectively. When subjected to axial compression, corrugated steel tubes exhibit good buffering and energy absorption capabilities. When applied as supports for concrete slabs under the composite buffering structure, they can reduce the compressive stress on the slab by 21.3%, decrease the peak support reaction by 53.2%, and reduce the deflection of the slab by 34.4%. The proposed fast assembly composite buffering structure and the buckling corrugated-tube supports have high engineering application value.

Acknowledgements

This study is supported by the Key Research and Development Program of Sichuan Province (Grant No. 2022YFG0414), the Key Science and Technology Projects in the Transportation Industry in 2020 (Grant No. 2020-MS3-101).

References

[1] Yu Z.X., Zhao L., Liu Y.P., Zhao S.C. Xu H. and Chan S.L., Studies on flexible rockfall barriers for failure modes, mechanisms and design strategies: a case study of Western China, Landslides 16(2), 347-362, 2018.
[2] Volkwein A., Schellenberg K., Labiouse V., Agliardi F., Berger F., Bourrier, Dorren L.K.A., Gerber W. and Jaboyedoff M., Rockfall characterisation and structural protection –a review, Natural Hazards and Earth System Sciences, 11(9), 2617-2651, 2011.
[3] Luo G., Cheng Q., Shen W., Ling S., Zhang X., Zou P. and Zhao Y., Research Status and Development Trend of the High-Altitude Extremely-Energetic Rockfalls, Earth Science 47(3), 913-934, 2022.
[4] Kishi N., Konno H., Ikeda K. and Matsuoka K.G., Prototype impact tests on ultimate impact resistance of PC rock-sheds, International Journal of Impact Engineering, 27(9), 969-985, 2002.
[5] Delhomme F., Mommessin M., Mougin J.P. and Perrotin P., Behavior of a structurally dissipating rock-shed: experimental analysis and study of punching effects, International Journal of Solids and Structures, 42(14), 4204-4219, 2005.
[6] Mougin J.-P., Perrotin P., Mommessin M., Tonnelo J. and Agbossou A., Rock fall impact on reinforced concrete slab: an experimental approach, International Journal of Impact Engineering, 31(2), 169-183, 2005.
[7] Pichler B., Hellmich C. and Mang H.A., Impact of rocks onto gravel Design and evaluation of experiments, International Journal of Impact Engineering, 31(5), 559-578, 2005.
[8] Kawahara, S. Muro T., Effects of dry density and thickness of sandy soil on impact response due to rockfall, Journal of Terramechanics, 43(3), 329-340, 2006.
[9] Shi S.Q., Wang M., Peng X.Q., Yang Y.K., A new-type flexible rock-shed under the impact of rock block: initial experimental insights, Natural Hazards and Earth System Sciences, 13(12), 3329-3338, 2013.
[10] Wu Y., He S.M., Li X.P. and Wang D.P., Dynamic response and optimization of an inclined steel rock shed by the graded energy dissipating method, Journal of Mountain Science, 16(1), 138-152, 2019.
[11] Castanon-Jano L., Blanco-Fernandez E., Castro-Fresno D. and Ballester-Muñoz F., Energy Dissipating Devices in Falling Rock Protection Barriers, Rock Mechanics and Rock Engineering, 50(3), 603-619, 2016.
[12] Qi X., Xu H., Yu Z.X. and Zhao L., Meng Q.C., Dynamic mechanical property study of brake rings in flexible protective system, Engineering Mechanics, 35(09), 198-206, 2018.
[13] Wang M., Shi S., Cui L., Liu Y. and Yang Y., Experimental investigation on three-bay and single-span flexible rock-shed under impact of rockfall, China Civil Engineering Journal, 51(5), 1-11, 2018.
[14] Tan K., Flexible Multi-body Dynamics Simulation of Cable-supported structure for rockfall protection, Southwest Jiaotong University, 2018.
[15] Chen F., Chen H., Structure optimization and calculation method of combined shed-tunnel structure, The Chinese Journal of Geological Hazard and Control, 31(1), 1-10, 2020.
[16] Yu Z.X., Zhao L., Guo L.P., Liu Y.P., Yang C. and Zhao S.C., Full-Scale Impact Test and Numerical Simulation of a New-Type Resilient Rock-Shed Flexible Buffer Structure, Shock and Vibration, 1-16, 2019.
[17] Zhang Y., Xie L.Z., He B. and Zhao P., Research on the Impact Force of Rockfall Impacting Sand Cushions with Different Shapes. Applied Sciences, 122, 2022.
[18] Wang Y.S., Xu M., Yang C., Lu M.Y., Meng J., Wang Z.L. et al. Effects of elastoplastic strengthening of gravel soil on rockfall impact force and penetration depth. International Journal of Impact Engineering, 136, 2020.
[19] Ouyang C., Liu Y., Wang D. and He S., Dynamic Analysis of Rockfall Impacts on Geogrid Reinforced Soil and EPS Absorption Cushions, KSCE Journal of Civil Engineering, 23(1), 37-45, 2018.
[20] Ertugrul O.L., Kiwanuka A., Dynamic analysis of rock fall impact for a cantilever rock shed with geofoam cushion, European Journal of Environmental and Civil Engineering, 27(5), 1989-2014, 2022.
[21] Sun J., Chu Z., Liu Y., Luo W. and Wang M., Performance of Used Tire Cushion Layer under Rockfall Impact, Shock and Vibration, 1-10, 2016.
[22] Wang D.P. , Bi Y.Z. , Zhou L., Chen H., Zhou R. and Lovati M., Experimental study on physical model of waste tennis ball-sand composite shed cushion under rockfall impact, Bulletin of Engineering Geology and the Environment, 81(5), 2022.
[23] Mentani A., Giacomini A., Buzzi O., Govoni L., Gottardi G. and Fityus S., Numerical Modelling of a Low-Energy Rockfall Barrier: New Insight into the Bullet Effect, Rock Mechanics and Rock Engineering, 49(4), 1247-1262, 2015.
[24] Zou P., Design of Modular Steel Structural Flexible Shed and Research on its Anti-impact Performance, Southwest Jiaotong University, 2021.
[25] EOTA, Falling rock protection kits, European Assessment Document, 2018.
[26] Zhong H.Q., Yu Z.X., Zhang C., Lyu L. and Zhao L., Dynamic mechanical responses of reinforced concrete pier to debris avalanche impact based on the DEM-FEM coupled method, International Journal of Impact Engineering, 167, 104282, 2022.
[27] Xu H., Gentilini C., Yu Z.X., Qi X. and Zhao S.C., An energy allocation based design approach for flexible rockfall protection barriers, Engineering Structures, 173, 831-852, 2018.
[28] Yu Z.X., Liu C., Guo L.P., Zhao L. and Zhao S.C., Nonlinear Numerical Modeling of the Wire-Ring Net for Flexible Barriers, Shock and Vibration, 1-23, 2019.
[29] Jin Y.T., Yu Z.X., Guo L.P., Luo L.R., Zhang L.J. and Liao L.X., Tensile-bending stiffness coordinated model for wire-ring nets in flexible rockfall protection system, Chinese Journal of Rock Mechanics and Engineering, 42(3), 698-707, 2022.
[30] Liu C., Theory and method of discrete analysis for flexible protective structure against geological hazard on shallow Slope, Southwest Jiaotong University, 2020.

Advanced Steel Construction – Vol. 20 No. 2 (2024) 120–124
DOI:10.18057/IJASC.2024.20.2.3
(Special Issue: *11st International Conference on Advances in Steel Structures, ICASS'2023, Kuching, Sarawak, Malaysia*)

DURABILITY EVALUATION OF REPAINT-COATING ON STEEL WITH INITIAL PAINT－COATING REMOVED BY INDUCTION HEATING

Sota Inoue [1], Mikihito Hirohata [1, *] and Tomonori Nakahara [2]

[1] *Graduate School of Engineering, Osaka University, Suita, Japan*
[2] *Japan Bridge Corporation, Osaka, Japan*
* *(Corresponding author: E-mail: hirohata@civil.eng.osaka-u.ac.jp)*

ABSTRACT

Repair of damaged paint-coating is an important issue in extending the service life of steel bridges. When repainting the paint-coating, the substrate steel is subject to surface preparation for removing the deteriorated original paint-coating and rust and appropriately making the steel surfaces rough. Although blasting and power tools are used for surface preparation, dust and noise are generated during the work. Therefore, the removal of paint-coating is performed prior to the surface preparation. A new paint-coating removal method by using induction heating (IH) is noted recently. The steel is rapidly heated by IH for removing the paint-coating easily. However, there are many unknowns regarding the influence of IH paint-coating removal on the durability of repaint-coating. In this study, the influence of removing paint-coating by IH on the durability of repaint-coating was evaluated through a series of accelerated corrosion experiments. The results of the 168-day accelerated corrosion experiments showed that the removal of paint-coating by IH did not cause a loss of the durability of repaint-coating compared to the case without using IH for the paint-coating removal.

ARTICLE HISTORY

Received: 8 April 2024
Revised: 28 April 2024
Accepted: 5 June 2024

KEYWORDS

Paint-coating;
Surface preparation;
Induction heating;
Acceleration corrosion experiment

1. Introduction

Corrosion is one of the main causes of deterioration of steel bridges, therefore, appropriate corrosion protections are required [1]. In Japan, a lot of steel bridges, such as Akashi Kaikyo Bridge and Tatara Bridge, have been built in coastal areas [2] where the environment is severe in terms of corrosion. Therefore, corrosion protection is essential to keep steel bridges in service safely. There are various corrosion protection methods such as metal spraying and use of weathering steel. The most widely used corrosion protection is paint-coating. However, due to deterioration caused by UV rays and water, the life of the coating is shorter than that of the structure itself. As a result, the paint-coating need to be replaced as necessary. A surface preparation performed in the repainting process removes rust and initial paint film from the steel surface. Furthermore, it provids an appropriate degree of roughness. The surface preparation is generally performed by blasting or power tools. In these cases, noise and dust are generated during the work because the rust and paint film are grinded from the surface. In particular, the paint-coating applied under past standards may contain toxic substances such as Pb and PCBs, it is important to ensure worker's safety. It is also necessary to prevent the dust from spreading into the surrounding environment. For these reasons, the deteriorated paint-coating might be removed by various methods prior to surface preparation.

One method that has recently been attracting attention is the use of induction heating (IH) to remove paint-coating. IH paint-coating removal has some advantages that the paint-coating can be easily removed after a short time heating and that the removed paint film can be collected in a dry sheet condition. It has been applied to the repainting of steel bridges in Japan [3]. However, the influences on the repaint-coating such as the degree of paint removal and the state of remaining paint-coating after the removal have not been fully elucidated. The objective of this study is to investigate the influence of the paint removal by IH on the durability of the repaint-coating. To accomplish this, a 168-day accelerated corrosion experiment was conducted. The specimens were paint-coated steel used in an actual bridge and were repainted for the experiment. Then, the durability of the repaint-coating with and without IH paint-coating removal prior to the surface preparation was compared.

2. Experimental specimen and condition

2.1. Experimental specimen

Fig. 1 shows the procedure for preparing the experimental specimens. In this experiment, 16 mm-thick paint-coated steel extracted from a girder of an actual bridge was cut into 150×70 mm pieces, and repainted. Prior to repaint-coating, cross-sectional observation of the initial paint-coating was conducted. As shown in Fig. 2, the initial paint film consisted of a total five layers. Three different repaint-coating systems, Rc-I, Rc-II, and Rc-III were prepared with and without IH paint-coating removal applied to each. The six conditions in total were set up for repaint-coating. The number of specimens was 18, three for each condition. All repaint-coatings are C-type based on epoxy and fluorocarbon rasins, the numbers of 'I', 'II', and 'III' indicate the degree of surface preparation. The following section describes each step of the specimen preparation process.

2.1.1. IH paint-coating removal

IH paint-coating removal was performed on 9 specimens. In this experiment, the entire surface of the specimen was subjected to the paint-coating removal. Fig. 3 shows the principal of IH paint-coating removal. A high-frequency current is applied to the coil in the device. When the device is brought

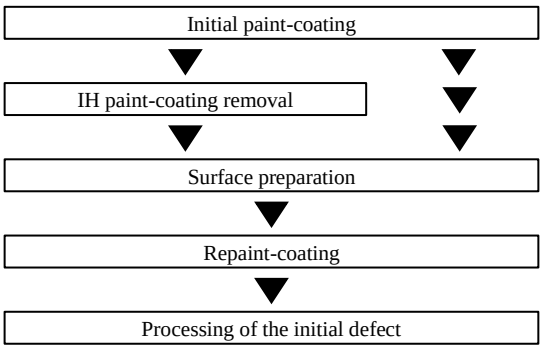

Fig. 1 Procedure for preparing specimens

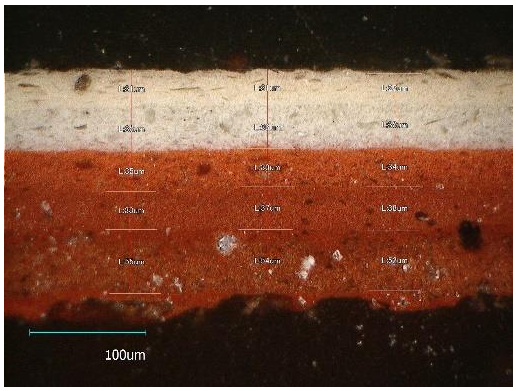

Fig. 2 Cross-section of initial paint-coating

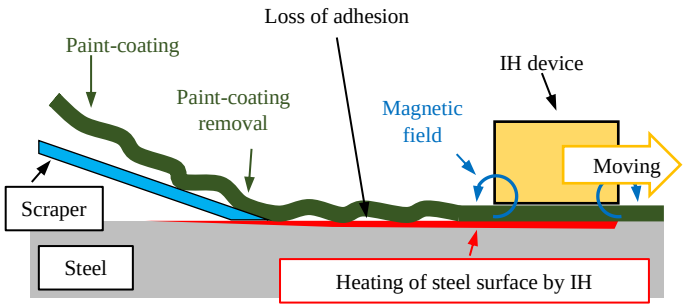

Fig. 3 Principal of IH paint-coating removal

a) Heating with IH

b) Removing by a scraper

Fig. 4 Procedure of paint-coating removal by IH

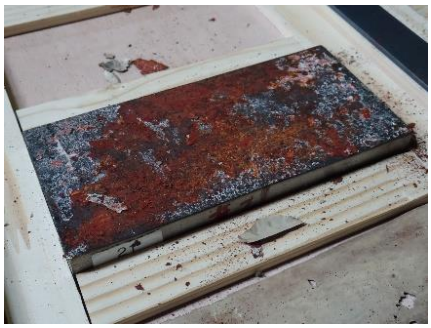

Fig. 5 Specimen after IH paint-coating removal

Table 1
Details of surface preparation

Type	Work method	Work content
Type-I	Blasting	Remove all rust and initial paint-coating
Type-II	Grinding	Remove all rust and initial paint-coating
Type-III	Grinding	Remove rust and deteriorated paint-coating

into close to the target steel surface, eddy currents are generated and the steel itself becomes a resistance and being heated. As the temperature rises to about 200 ℃, the adhesion between the paint-coating and the steel decreases. As a result, the paint-coating can be easily removed by using a scraper.

Fig. 4 shows the situation of IH paint-coating removal in this experiment. The induction heating coil manufactured by RPR Technologies was used as the heating device. When heating, the moving speed of the induction head was adjusted so that the temperature of the steel surface of specimen was 200 ℃. Fig. 5 shows an example of the specimen surface after the paint-coating removal. The black areas on the surface are the steel substrate, the white area is the primer of the initial paint-coating, and reddish-brown area is the undercoat. Although the degree of paint-coating remaining on each specimen was different, the upper layer of paint-coating could almost be removed from the undercoat. Possible reasons for the differences include variations in the heating temperature and the positions where the scraper blade attached.

a) Type-I

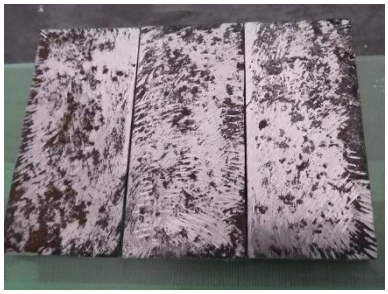

b) Type-II (IH)

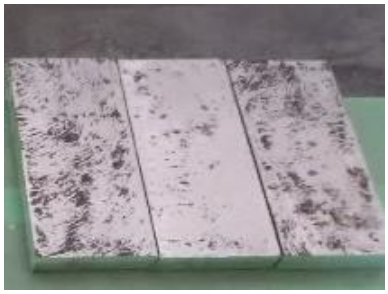

c) Type-II (non-IH)

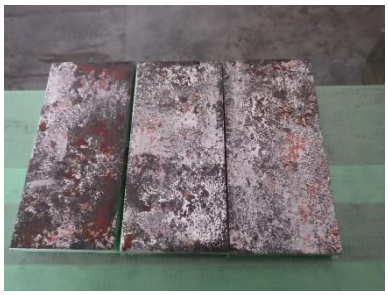

d) Type-III (IH)

e) Type-III (non-IH)

Fig. 6 Specimens after surface preparation

2.1.2. Surface preparation

Table 1 shows the details of surface preparation. Three types of surface preparation, Type-I, Type-II, and Type-III, as regulated in the specification in Japan [4], were performed. For each type, two kinds of condition were set up. The one was that IH paint-coating removal was applied before surface preparation. The other was that the surface preparation was performed from the state where the initial paint-coating was adhered. In other words, the six different conditions in total were set for the surface preparation.

Fig. 6 shows the appearance of the specimens after surface preparation. In Type-I and Type-II, whole steel surfaces are exposed by blasting or power tools. Therefore, there was no difference in the surface condition depending on whether IH paint-coating removal was applied or not. On the other hand, Type-III specifies that the paint-coating maintains sound adhesion to the steel should be left. In this experiment, the specimens with IH paint-coating removal remained some parts of the undercoat, while the specimens without IH paint-coating removal remained some parts of the topcoat which seemed to be sound.

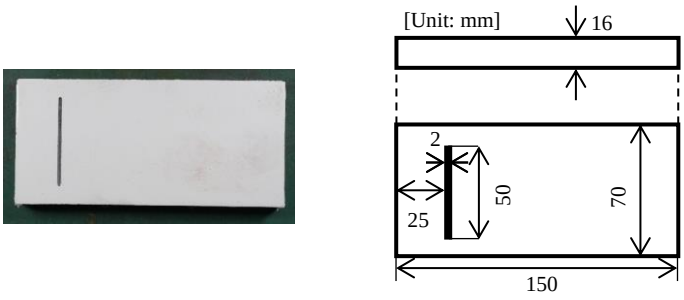

a) Appearance b) Dimensions

Fig. 7 Details of repaint-coated specimen

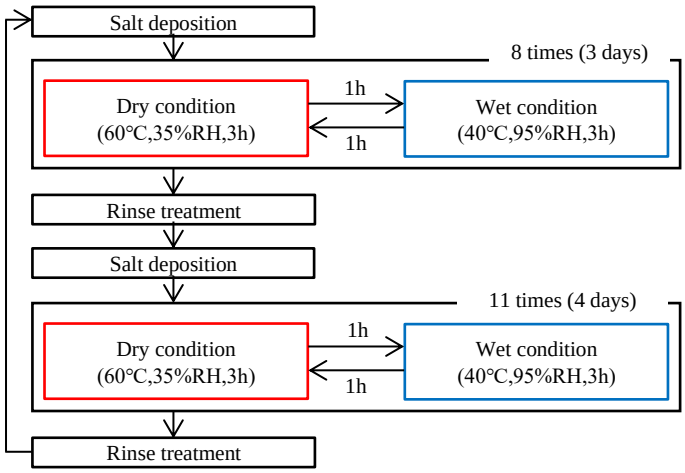

Fig. 8 Experimental condition of ISO16539-Method B

2.1.3. Repaint-coating

The specimens were repainted with Rc-I, Rc-II, and Rc-III paint-coating systems. The regulations in Japan [4] are shown in Table 2. Basically, the repaint-coating on the specimens also follows these regulations. However, for the convenience of the experiment, the paint method was changed to “spray” even if the paint method was “brush”. After the repaint was completed, the paint-coating thickness was measured and confirmed to be sufficient. After that, a linear scratch with 2 mm wide and 50 mm long reaching the steel substrate was processed as an initial defect at 25 mm from the edge of the specimen. Fig. 7 shows the appearance and dimensions of the specimen after the repainting.

Table 2
Details of repaint-coating systems [4]

Paint systems	Process	Paint type	Weight [g/m^2]	Paint method
Rc-I	Surface preparation	Type-I, ISO Sa2 1/2	-	-
	Protective underlay	Organic Zn-rich paint	600	Spray
	Undercoat	Epoxy resin	480	Spray
	Middlecoat	Fluorocarbon resin	170	Spray
	Topcoat	Fluorocarbon resin	140	Spray
Rc-II	Surface preparation	Type-II, ISO St3	-	-
	Protective underlay	Organic Zn-rich paint	240 (600)	Brush
	Undercoat	Epoxy resin	400	Brush
	Middlecoat	Fluorocarbon resin	140	Brush
	Topcoat	Fluorocarbon resin	120	Brush
Rc-III	Surface preparation	Type-III, ISO St3	-	-
	Undercoat	Epoxy resin	400 (600)	Brush
	Middlecoat	Fluorocarbon resin	140	Brush
	Topcoat	Fluorocarbon resin	120	Brush

2.2. Experimental condition

In this study, ISO16539-Method B was applied as the accelerated corrosion experiment. Fig. 8 shows the detailed condition of this experiment and Fig. 9 shows the apparatus used in the experiment. The experiment consisted of a seven-day cycle, and was based on a process of artificial seawater spraying using a salt spray apparatus, repetition of dry and wet conditions in an environmental test chamber, and rinsing of the specimen surface. To evaluate corrosion degradation, the specimen surfaces were photographed, and surface topography was measured using a laser displacement meter (Fig. 10) at 28, 84, and 168 days after the start of the experiment. The laser displacement measurement was made at intervals of 0.1 mm in longitudinal and transverse directions over an area of 50 mm × 70 mm centered on the initial defect.

a) Salt spraying apparatus b) Environmental test chamber

Fig. 9 Experimental apparatus

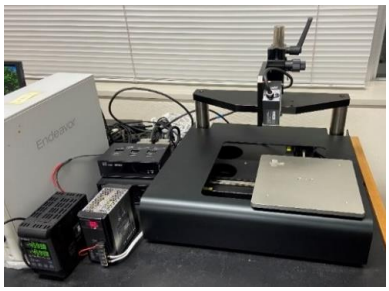

Fig. 10 Laser displacement meter

3. Experimental results ans discussions

3.1. Appearance of specimens

Fig. 11 shows the change in surface appearance of specimen during the experiment. In all paint-coating systems, there was no difference in appearance change depending on whether IH paint-coating removal was applied prior to the surface preparation or not. First, focusing on the sound areas of repaint-coating, stains due to rust fluid were observed in some areas. However, no degradation such as corrosion progress under the paint-coating, cracking or peeling of the paint-coating was observed. Next, the vicinity of the initial defect is noted. Fig. 12 shows the results of surface topography measurement by the laser displacement meter. Rust was observed at the initial defect in all specimens at 28 days after start of the experiment. Blistering was observed in the paint-coating near the initial defects, and the height and extent of the blistering tended to increase along with the experimental days. After 168 days, in some of specimens, the paint-coating were cracked or peeled off.

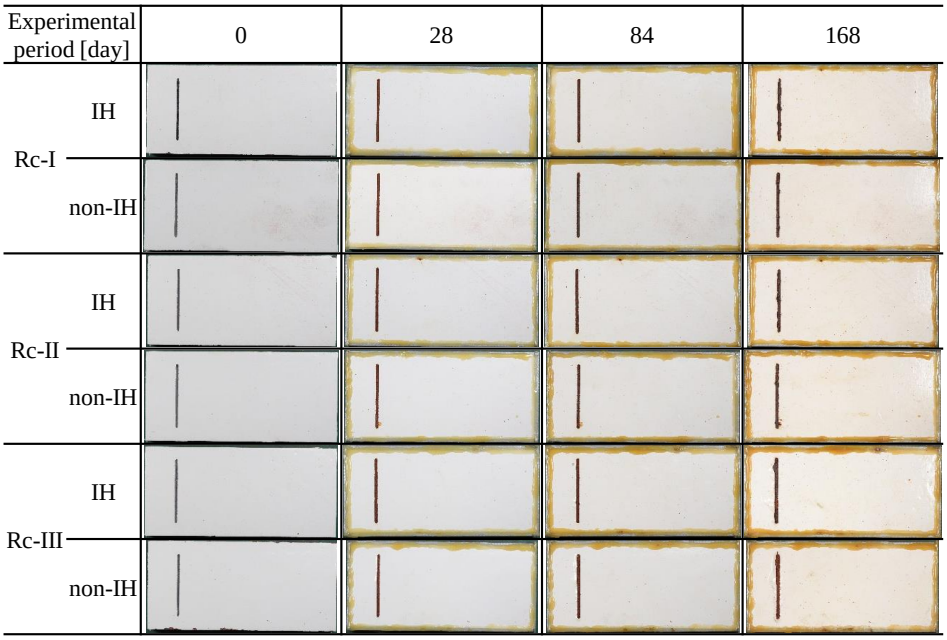

Fig. 11 Specimens after corrosion acceleration experiments

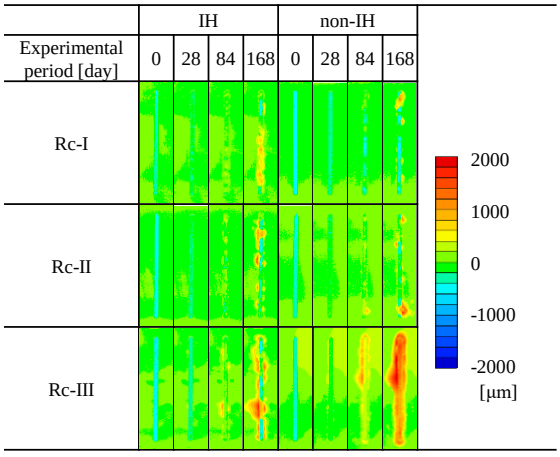

Fig. 12 Surface topography of specimens

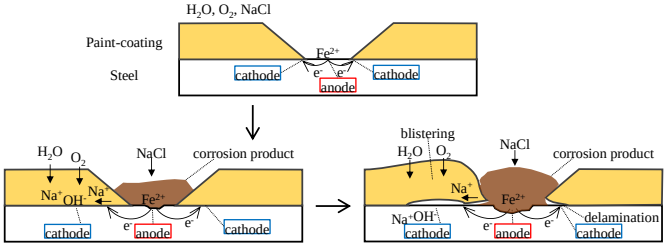

Fig. 13 Blistering mechanism [5]

3.2. Blistering area

It is known that in paint defect area reaching the steel surface, the steel just below the scratch acts as the anode and the steel under the paint-coating near the defect area acts as the cathode. Therefore, the large defects reaching the steel substrate cause blistering of the surrounding paint-coating by the mechanism shown in Fig. 13 [5]. In this experiment as well, blistering occurred near the initial defects. The height and extent of the blistering increased as the testing days progressed. This blistering might occur by the mechanism shown in Fig. 13. In this study, "blistering area" was defined as an evaluation index for paint-coating deterioration. This index indicates the area where the height of the paint film was more than 50 μm compared to the state before the experiment. The surface topography data measured by the laser displacement meter was used to calculate the blistering area.

Fig. 14 shows the transitions of blistering area. The graphs show the mean value (M) and standard deviation (S) of the results of three specimens. For all paint-coating systems, the blistering area of IH specimens was slightly smaller than that of non-IH specimens. This suggests that the application of IH paint-coating removal does not cause a decrease in the durability of the repaint-coating.

3.3. Discussions

In Rc-III paint-coating system, the difference in blistering area between IH and non-IH was larger compared to the other paint-coating systems. In Rc-I and Rc-II paint-coating systems, all rust and initial paint film were removed in the surface preparation. Therefore, there was no difference in the steel substrate after surface preparation when comparing IH and non-IH. On the other hand, Rc-III paint-coating system left the sound paint film in surface preparation. This might be the reason for the larger difference in blister area in Rc-III paint-coating system.

Therefore, the percentage of remaining paint-coating on the specimens with Rc-III paint-coating system after surface preparation was calculated using the image analysis software WinROOF 2018. The calculated area percentage of remaining paint-coating is shown in Table 3, and the picture used for the calculation is shown in Fig. 15. In Fig. 15, the areas where the paint-coating remained are extracted and colored green. The area percentage of remaining paint-coating was about 20% in IH compared to non-IH. In non-IH, the topcoat remained in some areas, while in IH, remaining paint-coating was only undercoat. Therefore, the thickness of remaining paint-coating was also different. The difference in area and thickness might be the reason for the difference in blistering area.

However, it is difficult to evaluate whether the topcoat should be removed or not. It is possible that the undercoat deteriorates even under the sound topcoat. In the case of IH, almost all of the undercoat is exposed and then the surface is prepared using a power tool, which ensures that the deteriorated undercoat is removed. On the other hand, in the case of non-IH, where the sound topcoat is left, the repaint-coating is applied on the sound topcoat. It means that the paint film thickness is increased, therefore, the corrosion factors cannot penetrate the coating and reach the surface of the steel. The validity of these discussions depends on the types of the paint-coating system and the degradation degree of the initial paint-coating. It is necessary to accumulate data using other paint-coated steels and examine other aspects such as the adhesive strength of the initial paint-coating.

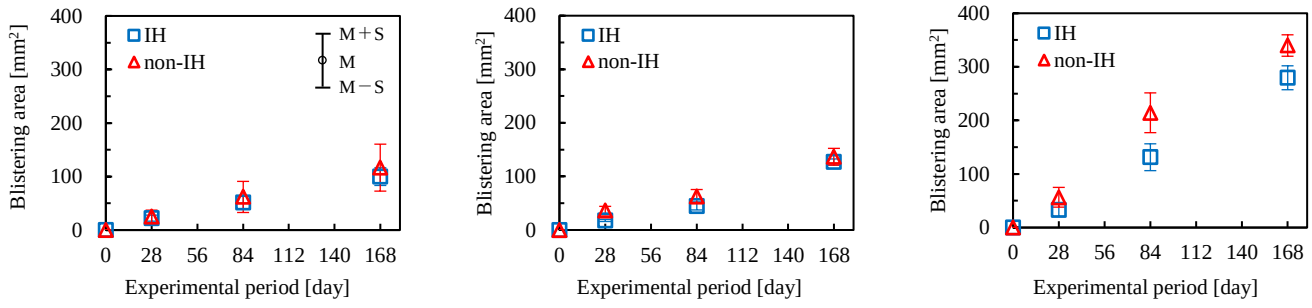

a) Rc-I b) Rc-II c) Rc-III

Fig. 14 Change in blistering area

Table 3
Percentage of remaining paint-coating

[%]	IH	non-IH
Undercoat	12.9	35.1
Topcoat	-	22.1
total	12.9	57.2

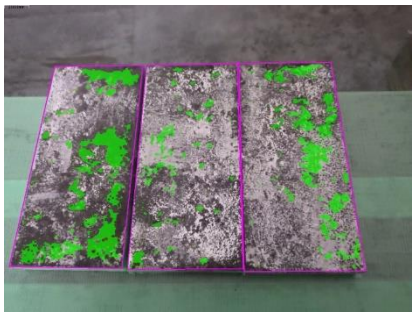

a) IH

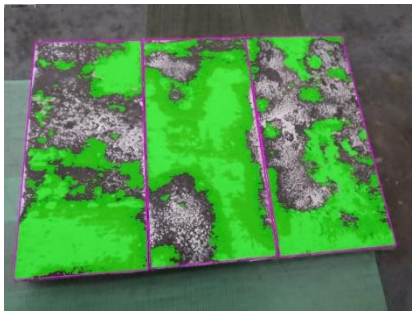

b) non-IH

Fig. 15 Remained area of paint-coating

4. Conclusions

In this study, a series of accelerated corrosion experiments was conducted to investigate the influence of the removal of paint-coating by IH on the durability of repaint-coating. The main results are as follows.

(1) IH paint-coating removal was able to remove most of the upper layer of paint-coating from the undercoat on the actual bridge.
(2) After surface preparation, the condition of the steel substrate differed depending on whether IH paint-coating was applied prior to Type-III surface preparation only removing deteriorated paint-coating. On the other hand, no difference in the steel substrate was observed in Type-I and Type-II surface preparation removing all of rust and paint-coating.
(3) After 168-day accelerated corrosion experiment, rust occurred at the initial defects of specimens, and the paint-coating in the vicinity of the defects became blistering. It was confirmed that the extent and height of the blistering increased with the passage of experimental period, regardless of the paint-coating system and the use of IH paint-coating removal.
(4) Based on the results of blistering area, IH paint-coating removal did not cause a loss of the durability of repaint-coating compared to the case without using IH.

References

[1] E. S. Kline, “Steel Bridge: Corrosion Protection for 100 Years.” *Journal of Protective Coatings & Linings*, 20-31, 2008.

[2] T. Kitada, “Considerations on recent trends in, and future prospects of, steel bridge construction in Japan”, *Journal of Constructional Steel Research*, 62 (11), 1192-1198, 2006.

[3] H. Konishi, N. Suzuki, M. Tanaka, C. Sameshima, T. Nishitani, and M. Hirohata, “Application of Induction Heating for Removal Coating in Kyoda Steel Bridges”, *Bridge and foundation engineering*, 51 (7), 14-20, 2017 (in Japanese).

[4] Japan Road association, “Steel road bridge corrosion protection handbook”, Maruzen publishing, 2014 (in Japanese).

[5] T. Nguyen, J.B. Hubbard, and J.M. Pommersheim, Unified Model for the Degradation of Organic Coatings on Steel in a Neutral Electrolyte, *Journal of Coatings Technology*, 68, No.855, 45-56, 1996.

Advanced Steel Construction – Vol. 20 No. 2 (2024) 125–134
DOI:10.18057/IJASC.2024.20.2.4
(Special Issue: *11st International Conference on Advances in Steel Structures, ICASS'2023, Kuching, Sarawak, Malaysia*)

BEHAVIOR INSIGHTS AND PLASTIC DESIGN CONSIDERATIONS OF SSTF SYSTEMS BASED ON DETAILED FINITE ELEMENT ANALYSES OF A PROPOSED SUB-STRUCTURE

Ze-Xiang Li [1], Dan Gan [1,*], Xu-Hong Zhou [2] and Xi Lu [2]

[1] *School of Civil Engineering and Geomatics, Southwest Petroleum University, Chengdu 610500, China*
[2] *School of Civil Engineering, Chongqing University, Chongqing 400045, China*
** (Corresponding author: E-mail: gandan@cqu.edu.cn)*

ABSTRACT

The steel staggered truss framing (SSTF) system has been increasingly utilized due to its large column-free spaces, high construction efficiency, and favorable economic benefits. Despite its advantages, the SSTF system has yet to be incorporated in mainstream seismic design codes and is predominantly applied in low-seismic regions. The primary obstacle hindering the wider application of the SSTF system is the limited understanding of its inelastic behaviors, particularly in regard to diaphragm actions. This study firstly introduces an SSTF sub-structure that precisely reflects the diaphragm actions and the structural behaviors of SSTF systems, facilitating experimental researches and finite element (FE) analyses. Subsequently, a detailed SSTF sub-structure FE model and a pure steel truss FE model, considering the diaphragm actions and gusset plate connections, were established based on a plastically designed prototype SSTF structure in previous study. The yielding mechanism of the chord members, inelastic behaviors of the diaphragms, lateral responses, and stress distributions of the web members were investigated. Lastly, plastic design considerations involving the classification of the rigidity of the diaphragm, rotation demand of the chord member, mechanical calculation model of the truss and amplification factor of the web members were given to facilitate achieving the expected ductile failure mode of SSTF systems.

ARTICLE HISTORY

Received: 8 April 2024
Revised: 30 April 2024
Accepted: 5 June 2024

KEYWORDS

Steel staggered truss framing system;
Diaphragm action;
Inelastic behavior;
Sub-structure;
Finite element analysis

1. Introduction

A steel staggered truss framing (SSTF) system (see Fig. 1) is mainly composed of a series of transverse story-high trusses, columns, longitudinal framing beams, and diaphragms [1]. The large-span trusses are staggered arranged at the adjacent column lines, which creates large column-free spaces for flexible layouts. In the middle of the trusses, a Vierendeel panel without diagonal web member is usually adopted to build a practical corridor and increase the ductility of the trusses [2]. The truss members and columns in a SSTF system are mainly subjected to axial forces, which are efficient in carrying loads and reducing steel consumption [3]. The columns are arranged on the perimeter of the structure only, which reduces superstructure weight and saves foundation cost. In general, SSTF systems have the advantages of large lateral stiffness, large column-free space, reduced steel consumption, low foundation cost, and quick erection, and this system is suitable for multi-story residential buildings, dormitories, hotels, and office buildings [4,5].

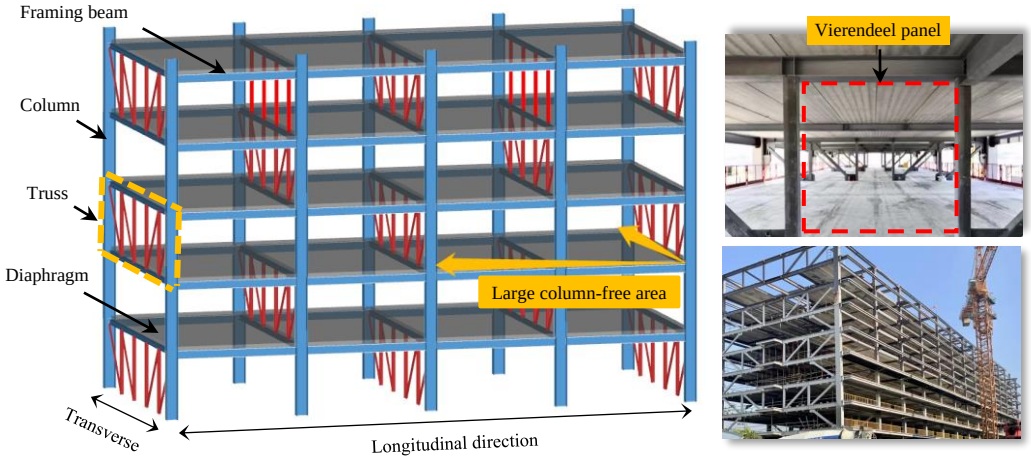

Fig. 1 SSTF systems

Since the SSTF system originated in 1960s [1], continuous researches on the load-carrying behaviors, design solutions and seismic performances were conducted. Gupta and Goel [3] conducted inelastic dynamic analyses of a SSTF system with a proposed computational analytical model. High seismic performance of the system was proved: only the chord members in the Vierendeel panels yielded when the structure was subjected to 1.5 times the ground motion of the 1940 EI Centro earthquake. Hanson and Robert [6] presented an elastic limit-ultimate strength design procedure for earthquake resistant response of multi-story SSTF buildings concentrating the inelastic activity at the chord members in the Vierendeel panels. Kim et al. [7] conducted nonlinear static analyses of SSTF buildings to identify their failure modes under seismic loads. The Design Guide 14: Staggered Truss System Framing Systems [8], published by AISC, provides an all-round process for the primary design of a SSTF system. Simasathien et al. [9] adopted additional diagonal members, multiple Vierendeel panels and horizontal trusses to enhance the seismic performance of SSTF systems. Kim et al. [10,11] introduced kinds of strategies including interior columns, vertical cables, end braces, and buckling-restrained braces to improve the seismic performance of SSTF systems and developed a performance-based seismic design method for SSTF structures equipped with friction dampers in the Vierendeel panels. Zhou et al. [12] quantified the inelastic seismic demand of a novel SSTF system showing damage-control behavior by using a probabilistic seismic demand spectral surface model.

The above studies paid extensive interest on the seismic performance of SSTF systems but, for various reasons, did not account for the influence of diaphragm actions. It should be noted that the diaphragm constitutes a vital component of the lateral load-resisting system of SSTF systems. Due to the staggered arrangement of the trusses, the diaphragms need to transmit the top-down lateral loads from the trusses. The diaphragm actions, including the out-of-plane stiffness, the inelastic behavior, and the interactions to the trusses, affect the lateral stiffness, load distribution, and failure mechanism of SSTF systems [13]. Up to now, the SSTF system is not included in the mainstream seismic design codes. The practical engineering projects of SSTF systems are mainly located in low-seismic regions. Some works still need to be done to figure out the inelastic behavior and failure mechanism of SSTF systems.

The seismology committee of the Structural Engineers Association of California (SEAOC) holds that the SSTF system is not a basic seismic-force-resisting system and more tests and analyses considering the diaphragm actions should be performed, as opposed to just the behavior of individual components [14]. Several experimental studies of SSTF systems were conducted [15–18]. However, either bare steel plate diaphragms were used or the sources of the diaphragm behavior were not given, and the tested SSTF systems exhibited relatively poor ductility due to the premature failure of the web members or column base. In addition, experimental researches or refined finite element (FE) analyses of an entire structural system induce significant costs.

To facilitate conducting in-depth experimental studies and FE analyses of SSTF systems, an SSTF sub-structure which accurately reflect the diaphragm actions and the structural behaviors of SSTF systems was proposed in this work. Subsequently, detailed FE models considering the inelastic behavior of diaphragms and the effects of the gusset plate connections were established and the behavior insights of the SSTF system were studied. Lastly, several plastic design considerations for SSTF systems to achieve the expected ductile failure mode were given.

2. Verification of the SSTF sub-structure

In an SSTF system, the diaphragms and the trusses constitute the lateral load-resisting systems in the transverse direction. Fig. 2 illustrates the smallest lateral load-transmitting element of an SSTF system. The seismic loads or the wind loads from the upper truss are transmitted by the diaphragm to the lower two trusses, and thereby to the foundation step by step. However, the boundary conditions of chord members are difficult to precisely set up due to the vertical and lateral deformation of the chord members when this element is subjected to lateral loads. In addition, the trusses are prone to suffer out-of-plane instability.

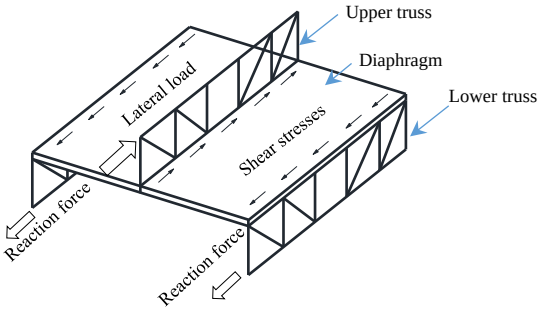

Fig. 2 The lateral load-resisting element of SSTF systems

Therefore, an SSTF sub-structure comprising a typical truss, two diaphragms, six columns, eight beams, and four side chord members is proposed herein, extracted from a prototype SSTF structure, as shown in Fig. 3. Hinged supports are set at the four exterior column bases since there is almost no bending moment at the columns while SSTF structure subjected to transverse lateral loads. Transverse sliding supports whose vertical and longitudinal degrees of freedom are constrained are set at the two interior column bases. This provides the truss with supports while allows in-plane deformation of the lower diaphragm. Lateral loads are applied at the top ends of the four exterior columns. In the sub-structure, the applied lateral loads are transmitted to the truss through the top diaphragm, and finally to the hinged supports through the bottom diaphragm. The features of the SSTF system that diaphragms transmit the shear forces between the staggered trusses and the interaction of the diaphragm and truss are thereby reflected by the sub-structure. Most importantly, the sub-structure facilitate experimental researches or FE analyses due to its simple boundary conditions. In addition, it is a stable three-dimensional spatial structure that does not require additional supports when conducting experimental research.

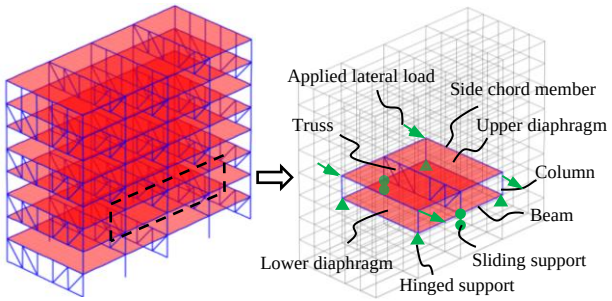

Fig. 3 A typical SSTF sub-structure

In previous study, an analysis model of an plastically designed example SSTF structure with diaphragm based on nonlinear multi-layered shell elements was established and transverse pushover analysis was conducted [13]. Based on the previous study, pushover analysis of the sub-structure extracted from the prototype SSTF structure was conducted. And then, the shear force versus lateral displacement relationships of the same truss from the prototype SSTF structure and the sub-structure were collected and compared. The horizontal force components of the chord members and the vertical web members were neglected, as shown in Fig. 4.

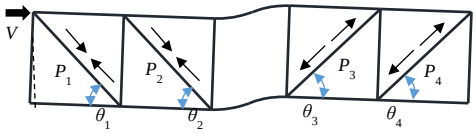

Fig. 4 Shear force of the truss

Therefore, the shear force of the truss can be calculated by accumulating the horizontal force components of the diagonal web members:

$$V = P_1\cos\theta_1 + P_2\cos\theta_2 + P_3\cos\theta_3 + P_4\cos\theta_4 \quad (1)$$

As shown in Fig. 5, the shear force versus lateral displacement relations of the trusses from the sub-structure and the prototype SSTF structure kept almost the same. Therefore, the proposed sub-structure precisely predicts lateral responses of the SSTF structure and can be used to conduct further FE analyses to explore the inelastic behavior of SSTF systems considering diaphragm actions.

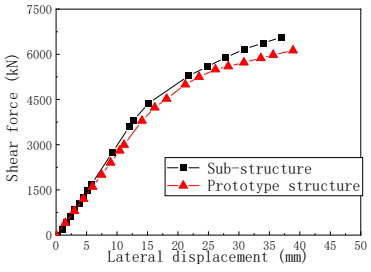

Fig. 5 The shear force versus lateral displacement curves of the trusses

3. Finite element model

3.1. Model description

A detailed FE model of an SSTF sub-structure established by the software ABAQUS [19] is shown in Fig. 6. The boundary conditions were set as mentioned above. Four-node reduced integral shell (S4R) elements were employed to model the steel members including the truss, the columns, the beams, the side chord members and the gusset plates. Eight-node incompatible solid (C3D8I) elements were employed to model the concrete floor slabs, as C3D8I elements were found to be more efficient in modelling plate components without mesh distortions, and could reduce the number of grid units and shorten

the calculation time [20]. Two-node three-dimensional truss (T3D2) elements were employed to model the reinforcements. The chord member in the Virendeel panel and the adjacent diaphragm will inevitably produce significant plasticity. To accurately capture the interaction behavior of the diaphragm and chord member at the Vierendeel panel, seven studs based on four-node shell element (S4) were set at the Vierendeel panel (plastic hinge zone), as recommended by Yin and Shi [21]. Six nodes of each stud tied with the concrete slab. Hard contact was used in the normal direction of the interfaces between the chord and the concrete in the Vierendeel panel and the tangential friction coefficient of the interfaces was taken as 0.25. In the areas outside the Vierendeel panel, the floor slabs were tied in the top flanges of beams and the chord members. The element size was taken as 15 mm for the steel members and reinforcements and 100 mm for the floor slabs after sensitivity analysis. The floor slabs were discretized into four layers of mesh through thickness. All the steel members were merged as one part. The reinforcements were embedded in the concrete floor slabs.

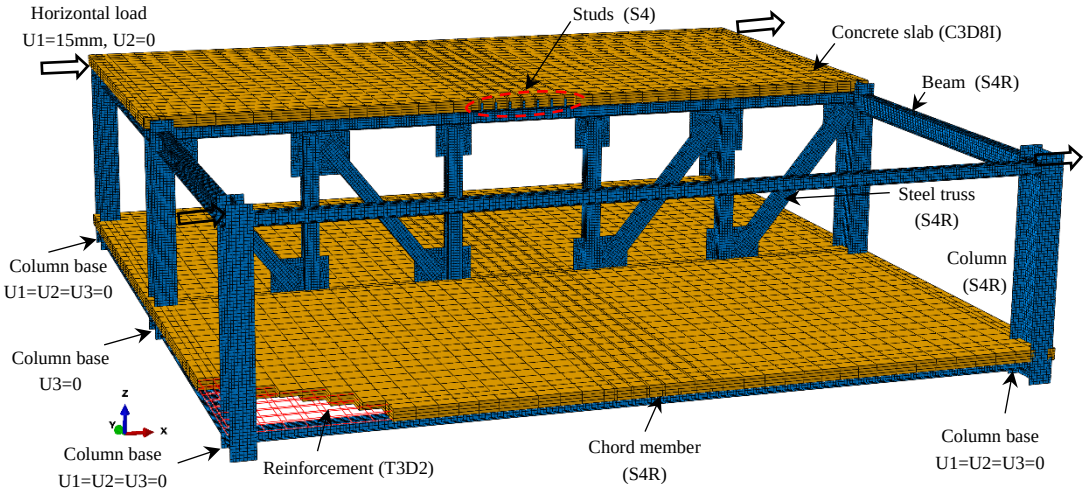

Fig. 6 FE model of the SSTF sub-structure

The prototype structure in Ref. [13] is plastically designed and realized the expected failure mode. The sub-structure model is 1/3 scaled of the prototype structure in Ref. [13], with the height of 1 m and the plane dimension of 4 m × 4 m. The detailed elevation arrangement of the truss is shown in Fig. 7. The dimensions of the steel members are listed in Table 1. The letter "H" denotes an H-section, with the subsequent four numbers signifying the section height, flange width, web thickness, and flange thickness, respectively. The letter "F" denotes a square-section, with the subsequent four numbers signifying the tube width and tube thickness, respectively. The thickness of the floor slabs was 60mm. The reinforcements were double layered and bi-directional in configuration. The diameter and spacing of the reinforcements were 8 mm and 100 mm, respectively.

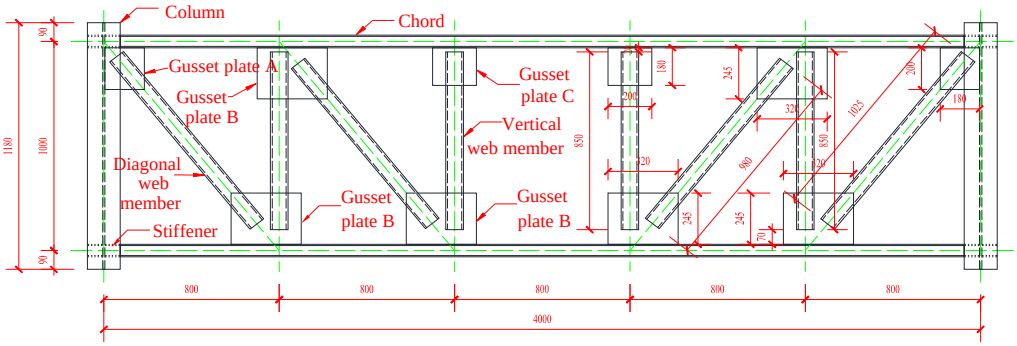

Fig. 7 Elevation of the truss (unit in mm)

Table 1
Dimensions of the steel members

Member	Sectional dimension (mm)
Column	H200×150×10×10
Beam	H100×80×6×6
Chord member	H60×60×6×6
Diagonal web member	F80×6
Vertical web member	F80×6
Gusset plate A	180×200×8
Gusset plate B	320×245×8
Gusset plate C	200×180×8

The elastic-perfectly plastic model was used for the steel members and reinforcements. The modulus of elasticity (E_s) and the Poisson's ratio of the steel members and reinforcements was taken as 200 GPa and 0.3, respectively. The steel grade of the Gusset plate was Q355 (yield strength f_y = 355 MPa) and the steel grade of the other steel members was Q235 (yield strength f_y = 235 MPa). The reinforcement grade was HRB400 (yield strength f_{yr} = 400 MPa).

The concrete grade of the floor slabs was C30 (compressive strength f_c = 24 MPa). Modulus of elasticity of concrete (E_c) was taken as $4700(f_c)^{0.5}$ [22]. The plastic damage model of concrete was adopted and the detailed parameters are shown in Table 2.

Table 2
Dimensions of the steel members

Dilation angle (ψ)	Flow potential eccentricity (e)	f_{bo}/f_c	Compressive meridian (K_c)	Viscosity parameter
31°	0.1	1.16	0.67	0.0001

where f_{bo}/f_c is the ratio of equal biaxial to uniaxial compressive strength of concrete.

The nonlinear uniaxial compressive behavior of the concrete from GB 50010 [23] was used. The stress-strain relationship was defined by Eqs. (2)–(6).

$$\sigma = (1-d_c)E_c\varepsilon \tag{2}$$

$$d_c = \begin{cases} 1-\dfrac{\rho_c n}{n-1+x^n} & (x \leqslant 1) \\ 1-\dfrac{\rho_c}{\alpha_c(x-1)^2+x} & (x>1) \end{cases} \tag{3}$$

$$\rho_c = \frac{f_c}{E_c\varepsilon_{cr}} \tag{4}$$

$$n = \frac{E_c\varepsilon_{cr}}{E_c\varepsilon_{cr}-f_c} \tag{5}$$

$$x = \frac{\varepsilon}{\varepsilon_{cr}} \tag{6}$$

where ε_{cr}=1640×10^{-6}, and α_c=1.36 when C30 concrete was used.

Fracture energy G_f was used to describe the tensile behavior of the concrete as suggested by mode specification Mode Code [24].

$$G_f = \alpha\left(0.1f_c\right)^{0.7} \tag{7}$$

where α is a parameter related to the sizes of concrete aggregate and taken as 0.03 in this investigation.

A damage variable d calculated by Eq. (8) [25] for concrete was used.

$$d = 1-\sqrt{\frac{\sigma}{E_c\varepsilon}} \tag{8}$$

A FE model of a pure steel truss was established for comparison, as shown in Fig. 8. The sizes, modelling methods and materials of the pure steel truss model were the same as the sub-structure model. Horizontal loads were applied at the top ends of the columns and hinged supports were set at the column bases. Lateral supports were set at the ends of the Vierendeel panel to prevent lateral torsion.

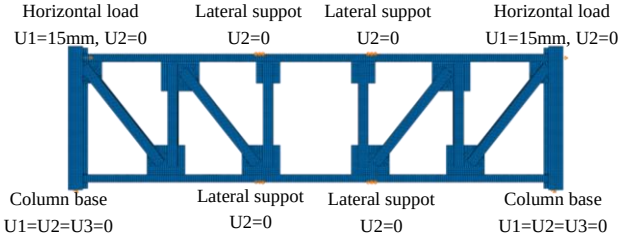

Fig. 8 FE model of the pure steel truss

3.2. Model validation

For conducting precise refined analysis of the sub-structure, the accurate prediction of the inelasicity of the Vierendeel panel of the truss and the interaction behavior between the RC concrete diaphragm and the chord member are of key importance. As mentioned above, the existing experimental results of SSTF systems are not suitable to be used to validate the FE model due to the lack of the sources of diaphragm behavior and inelasticity [15–18]. Also, there is no existing experiment of SSTF sub-structures. However, the developments of the special truss moment frames and eccentrically braced frames offer experimental sources to validate the FE model, since both of them allow a middle special segment to dissipate energy and improve the ductility of the structure, similar as SSTF structure [10,14]. Thus, available experimental results of a steel special truss moment frame with a Vierendeel panel under cyclic loads tested by Chao et al. [26] and an steel eccentrically braced frame with a floor slab under cyclic loads tested by Ciutina et al. [27] are used to validate FE model.

The elevation arrangement and test set up of the full scaled steel special truss moment frame specimen STMF1 are shown in Fig 9(a) and the counterpart FE model based on S4R elements is shown in Fig 9(b). The loading history, material properties, boundary conditions were the same as the test [26]. The double channel chord members and web members were tied with the gusset plates. Kinematic hardening rule was used in the validating.

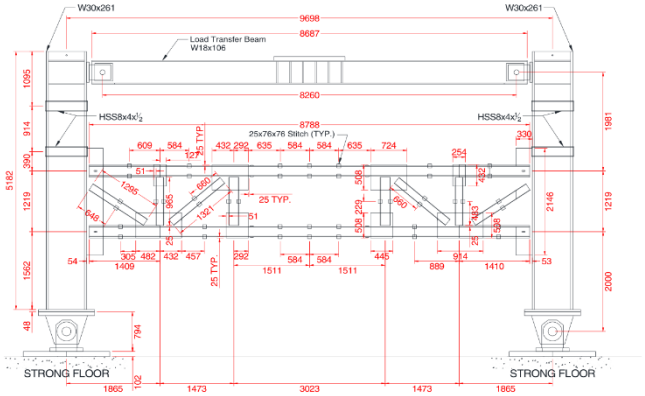

(a) Elevation arrangement and test set up (sourced from Ref. [26])

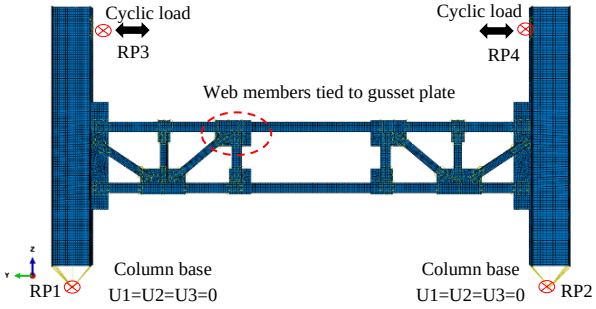

(b) FE model

Fig. 9 The special truss moment frame specimen STMF1

Only the chord member at the Vierendeel panel end yielded and the members outside kept elastic during the tests of specimen STMF1 [26]. Fig. 10(a) shows the yielding pattern of STMF1 at a story drift ratio (SDR) of 2%. It can be seen that the yielding pattern of the FE model shown in Fig. 10(b) is consistent well with the tested results.

Although considering fracture is conductive to the determination of the ultimate load-carrying capacity of the steel structural components [28,29], it is not essential to consider the cracking behavior of the chord member of the sub-structure since the current work focus on the inelastic behavior before its ultimate state. In the tests, the strength of STMF-1 started to degrade significantly at 3% SDR due to the fracture of the chord member [26]. As shown in Fig. 11, the lateral force versus displacement curve from FE analysis results coincides well with the tested results.

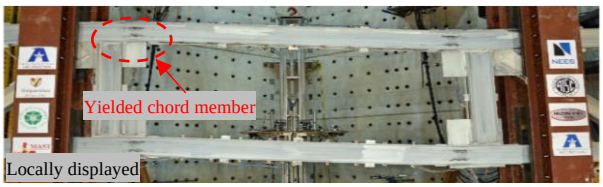

(a) Tested specimen STMF1 (sourced from Ref. [26])

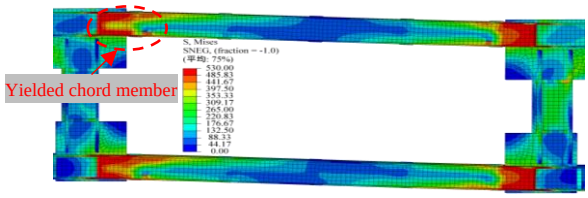

(b) FE analysis

Fig. 10 Comparison of the yielding pattern at 2% SDR

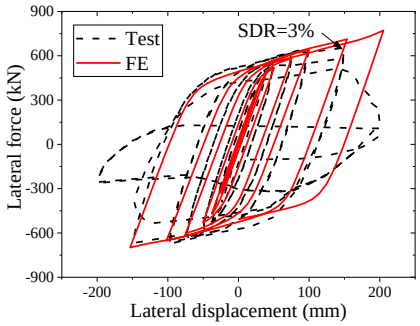

Fig. 11 Force versus displacement curves of test [26] and FE analysis

The elevation arrangement and test set up of the eccentrically braced frame specimen EBF-LF-Comp1 is shown in Fig. 12(a) and the counterpart FE model is shown in Fig. 12(b). The loading history, material properties, boundary conditions were the same as the test [27]. The modelling method of the steel members and the RC diaphragm was the same as the sub-structure descripted above. Kinematic hardening rule for the middle steel link beam was used.

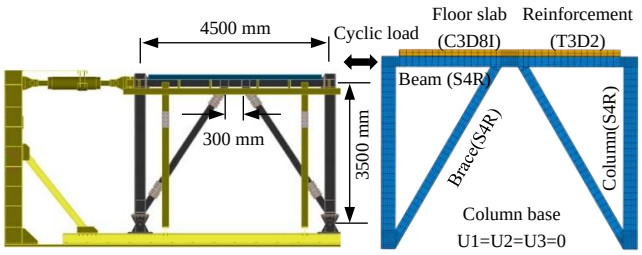

(a) Test set up (sourced from Ref. [27]) (b) FE model

Fig. 12 The eccentrically braced frame specimen EBF-LF-Comp1

The failure modes and lateral force versus displacement curves of the test specimen and the FE model are shown in Figs. 13 and 14, respectively. As seen, the FE model accurately predicts both the failure modes and the lateral responses of the tested composite eccentrically braced frame specimen before the specimen losing its load-carrying capacity due to the fracture of the link beam.

In general, the FE models acquired good predicting accuracy, including the yielding mechanism of the steel members, the inelasticity of the RC diaphragm, and the lateral behavior of the structures. Therefore, the modelling method is adequate to conduct further analysis of the SSTF sub-structure.

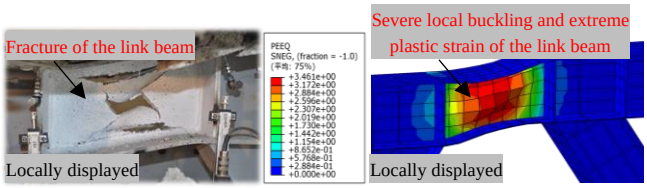

(a) steel link beam

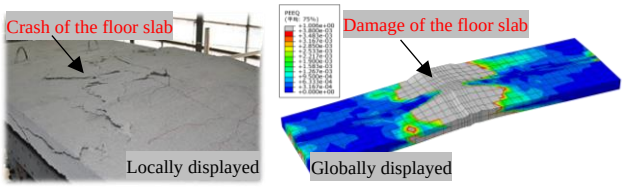

(b) floor slab

Fig. 13 Failure modes of the test [27] and FE analysis

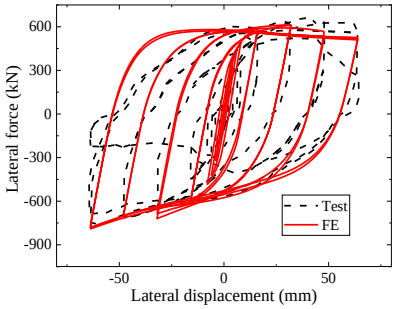

Fig. 14 Force versus displacement curves of the test [27] and FE analysis

4. Finite element analysis

4.1. Yielding patterns of the steel trusses

Fig. 15 shows the von Mises stress contour plot of the truss in the sub-structure model at the plastic SDR limit (stipulated as 1/75 by JGJ/T 329-2015 [30]). The expected yield mechanism was achieved. The chord member at the Vierendeel panel ends yielded sufficiently and the web members kept elastic.

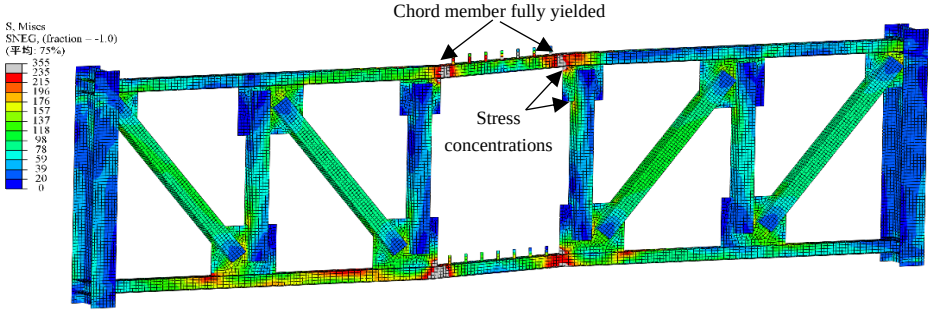

Fig. 15 Von Mises stress contour plot of the truss in the sub-structure model

However, it should be noted that there were stress concentrations near the Vierendeel panel, located at the vertical web member ends and the corners of the gusset plate C. The corners of the gusset plate C had yielded and the vertical web member ends nearly reached to the yield stress. The stresses were unevenly distributed at the vertical web members near the Vierendeel panel, which exhibited bending moment-subjecting characteristic. The stresses at the other web members were evenly distributed, which exhibited axial force-subjecting characteristic

Fig. 16 shows the von Mises stress contour plot of the pure steel truss model with the same SDR. The expected yield mechanism that the chord member at the Vierendeel panel ends yield firstly was achieved as well. It exhibited similar load-subjecting characteristics as the truss of the sub-structure. However, the stresses at the web members were much smaller than those of the sub-structure model, because the lateral stiffness of the pure truss model was much smaller than the sub-structure model (see the comparison of the skeleton curves below).

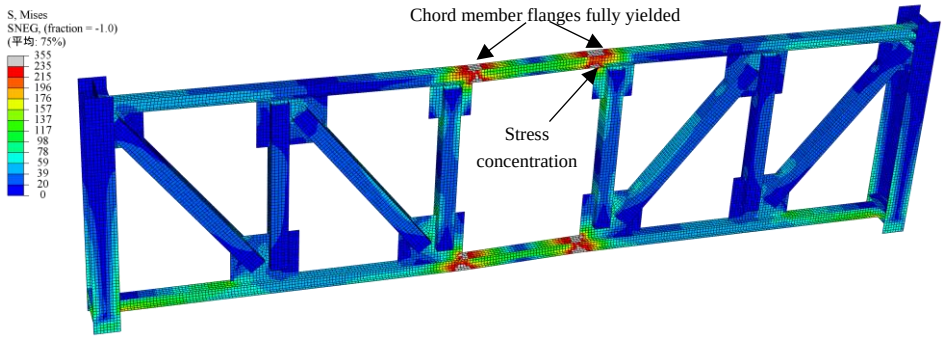

Fig. 16 Von Mises stress contour plot of the pure truss model

4.2. Behaviors of the RC diaphragms

Fig. 17 shows the equivalent plastic strain (PEEQ, defined by ABAQUS User's manual [19]) contour plots of the concrete slabs at 1/75 SDR. As seen, a damage area occurred at middle of the diaphragms while the areas else keep elastic. The stresses in the concrete slab is complicated since the diaphragms are subjected to combined in-plane and out-of-plane forces when the sub-structure is horizontal loaded, namely the shear forces transmitted to the truss and the passive moments caused by the rotation of the chord member in the Vierendeel panel. However, it is inferable that the damage at the diaphragms is a kind of ductile flexural failure caused by flexural stresses rather than brittle shear failure caused by shear stresses, which can be verified by the stress plot of the reinforcements and the hysteretic curve below. The diaphragms could still effectively transfer in-plane shear forces by the elastic concrete parts and the reinforcements at the plastic SDR limit, and thereby provides lateral stiffness of the SSTF structure for load-resisting.

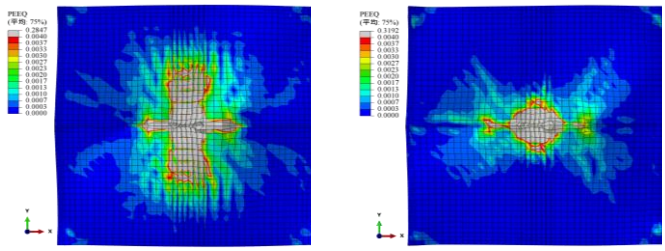

(a) Top concrete slab **(b)** Bottom concrete slab

Fig. 17 Damage of the concrete slabs

Fig. 18 shows the Von Mises stress contour plots of the reinforcements at 1/75 SDR. As seen, all the stress profiles consisted of two parts: the "X" type shear stresses penetrating the entire reinforcement mesh and the flexural stresses near the Vierendeel panel. The yielded reinforcements near the Vierendeel panel caused by passive moments coincided with the damage area of the concrete slab shown in Fig. 17.

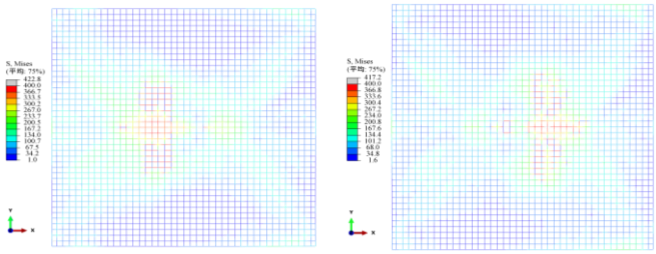

(a) Upper mesh of the upper diaphragm (b) Lower mesh of the upper diaphragm

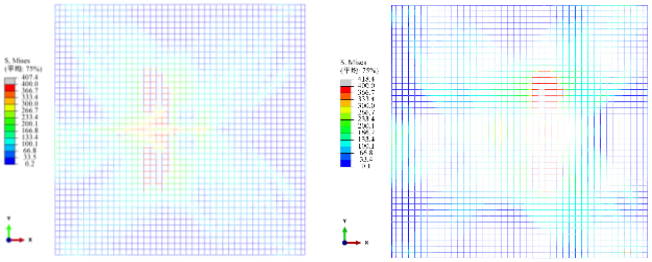

(c) Upper mesh of the lower diaphragm (d) Lower mesh of the lower diaphragm

Fig. 18 Damage of the concrete slabs

4.3. Lateral load versus displacement responses

Fig. 19 depicts the hysteretic curves of the sub-structure model and the pure truss model under lateral cyclic loads. The hysteretic curves were full due to the presence of expected failure mode, i.e., the chord members at the Vierendeel panel ends fully yielded and the web members kept elastic. After the chord member yielded, the hysteretic curve of the sub-structure model still slowly grew due to the increasing effective width of the RC diaphragms. This also supports the above argument about the failure modes of the concrete slab. Because once in-plane shear failure of the diaphragm occurred, the diaphragm would lose its function for load-transmitting and the sub-structure would lose its load-carrying capacity.

In the seismic design code GB50011-2010 [31], the elastic SDR limit for the steel structures is 1/250 and the plastic SDR limit is 1/50. In JGJ/T 329-2015 [30], the plastic SDR limit for SSTF structures in the transverse direction is tighten to 1/75 due to its relatively poor ductility while the elastic SDR is still stipulated as 1/250. As shown in Fig. 19, both the sub-structure model and the pure truss model yielded before the elastic SDR limit due to the relatively large rotation of the chord members [32,33]. In addition, the lateral stiffness of SSTF structures in the transverse direction is usually larger than the steel moment frames. Therefore, the existing elastic SDR limit of 1/250 for SSTF structures is too loose and might not fulfil the requirement of the "no damage in low-level earthquake". A stricter elastic SDR limit of 1/400 is recommended.

The diaphragms significantly enhanced the lateral stiffness and load-carrying capacity of the truss, as shown in the comparison of the skeleton curves of the two models (Fig. 20). The initial stiffness of the pure truss was 56 kN/mm, while that of the sub-structure model was 101 kN/mm (1.8 times the pure truss). The yield load was defined when the flange of the chord member yielded, i.e., the model entered inelastic stage. The yield load of the pure truss model was 149 kN, while that of the sub-structure model was 319 kN (2.1 times the pure truss). Therefore, the diaphragm actions in SSTF structures need to be considered, which is beneficial for correctly obtaining the internal force of the web members to realize the expected failure mode [13].

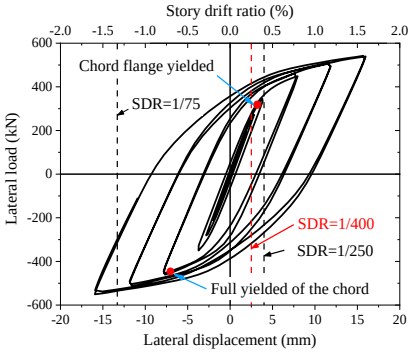

(a) Sub-structure

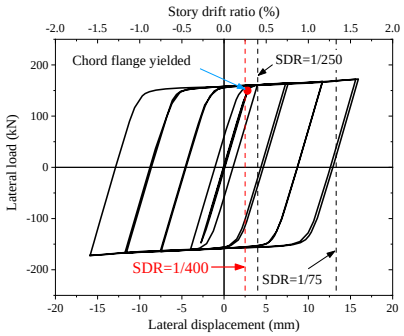

(b) Pure truss

Fig. 19 Hysteretic curves under lateral cyclic loads

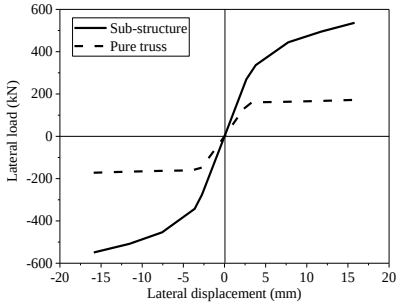

Fig. 20 Skeleton curves

4.4. Stress distributions at the web members

Longitudinal stresses at the vertical web member and the diagonal web member near the Vierendeel panel of the sub-structure model were extracted at 1/75 SDR. The positions of the extracted points are displayed in Fig. 21, located at the center and the corners of the top, middle and bottom sections of the web members.

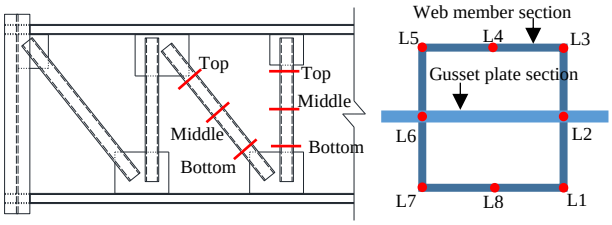

Fig. 21 The position of the extracted stresses

Fig. 22 shows the distribution of the longitudinal stresses at the vertical web member near the Vierendeel panel. Note that the positive values denote tensile stresses while the negative values denote compressive stresses. It could be seen that the stresses at the middle section were evenly distributed while the stresses at the top section and the bottom section were symmetrically distributed. Therefore, the vertical web member near the Vierendeel panel was subjected to combined axial force and moment. In addition, the vertical web member near the Vierendeel panel was predominantly subjected to moment, since the flexural stresses at the end sections caused by moment were larger than the stresses at the middle section caused by axial force.

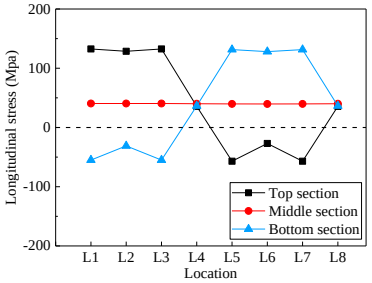

Fig. 22 Longitudinal stresses at the vertical web member

Fig. 23 shows the distribution of the longitudinal stresses at the diagonal web member near the Vierendeel panel. All the stresses were compressive stresses, ranged from -122 MPa to -79 MPa. Therefore, the vertical web member near the Vierendeel panel was subjected to axial force.

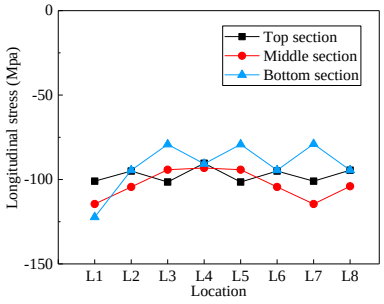

Fig. 23 Longitudinal stresses at the diagonal web member

5. Design considerations

5.1. The rigidity of the diaphragm

The classification of the in-plane rigidity of the diaphragm is required to precisely determine the lateral load on the lateral force-resisting elements and conduct an appropriate structural analysis. Diaphragms can be traditionally idealized as either “rigid”, “flexible”, or “semi-rigid” according to the relative in-plane stiffness of the diaphragms compared with the vertical elements of the lateral force-resisting system [34].

The typical RC diaphragms and concrete-filled metal decking diaphragms are idealized as rigid diaphragms provided the diaphragm span-to-depth ratio is three or less and there is no horizontal irregularity of the structure [35]. In SSTF systems, the span-to-depth ratio of the diaphragms is usually less than one, because the span of the truss is larger than the column spacing. The RC diaphragms, concrete-filled metal decking diaphragms or steel bar truss metal decking diaphragms are recommended by JGJ/T 329-2015 [30]. Therefore, in these circumstances, the diaphragms in SSTF systems are rigid.

However, the diaphragms in SSTF systems need to transfer the shear loads of the trusses due to the staggered arrangement of the trusses. In the bottom story, the diaphragms are subjected to large in-plane shear load, almost equal to the base shear of the structure. The in-plane deformation of the diaphragms need to be assessed. In addition, the diaphragm near the Vierendeel panel occurred out-of-plane damages at the plastic stage when the sub-structure subjected to lateral loads, which thereby performs like diaphragm with opening, as shown in Fig. 17.

A more explicit classification of diaphragms, as currently prescribed and as shown in Fig. 24, is based on the ratio between maximum diaphragm displacement relative to the lateral force-resisting systems (Δ_{dia}) and the corresponding average inter-story drift of the lateral force-resisting systems (Δ_{LFRS}) [35]. For rigid diaphragm behaviour this ratio (η) is expected to be less than 0.5, for flexible diaphragm behaviour greater than 2.0 and for all values in-between, the diaphragm is classified as semi-rigid [36].

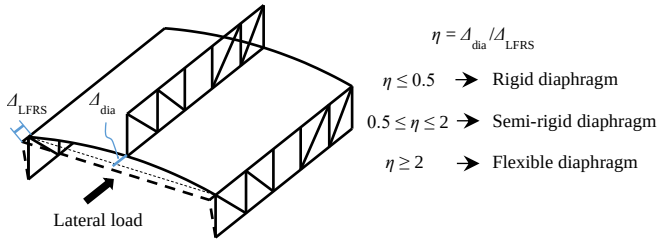

Fig. 24 Prescribed diaphragm classification

Fig. 25 depicts the transverse in-plane deformations of the diaphragms in the SSTF sub-structure model and the ratio to story drift. Though the in-plane diaphragm deformation gradually increased at the loading process, the in-plane diaphragm deformation was far less than the story drift. The ratios (η) were less than 0.13. Therefore, the RC diaphragms in SSTF systems indeed performed as a rigid plate accounting for the minor in-plane deformations. The allocation of lateral loads to each individual truss is based on the relative stiffnesses of the trusses and this principle is adopted in the Design Guide 14: Staggered Truss System Framing Systems [8] and JGJ/T 329-2015 [30]. However, it should be noted that the rigid diaphragm assumption (the out-of-plane stiffness is neglected) is not recommended for the structural analysis and design of SSTF structures. The out-of-plane stiffness of the diaphragms significantly increased the lateral stiffness of the truss and the internal forces of the web members, as discussed above. Most importantly, the use of the rigid diaphragm assumption may result in erroneous predictions of yielding mechanisms and overly underestimated predictions of base shear forces [13].

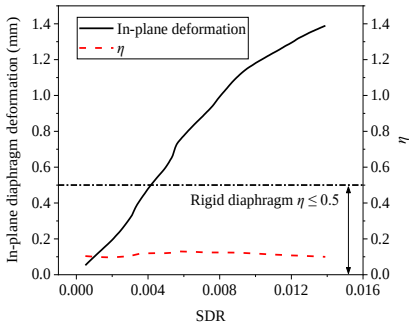

Fig. 25 In-plane deformation of the diaphragm and ratio to the story drift

5.2. The rotation demand of the chord member

As described above, the chord members of the SSTF systems are convinced of high rotation demand in order to achieve the expected ductile failure mode. As shown in Fig. 26, when the expected failure mode is achieved, the rotation of the chord member (α) is proportional to SDR (θ) [10,33].

$$\alpha = (L/s)\theta \tag{9}$$

where L and s are the truss span and the Vierendeel panel length, respectively.

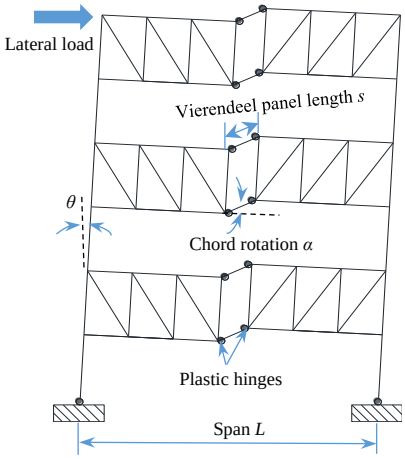

Fig. 26 Deformation configuration of a SSTF

The rotation of the chord member (α) in Eq. (9) is overvalued due to the idealized plastic hinge assumption: the flexural stiffness and length of the plastic hinge at the chord member are zero. Actually, both the steel chord member and the composite chord member with diaphragm hard to form the idealized plastic hinge. As shown in Fig. 27, the ratio of the chord member rotation to SDR of both the pure truss model and the sub-structure model were far less than the idealized ratio (L/s). For the pure truss model, the ratio was a constant value in the elastic stage. After the chord member yielded, the ratio increased with the development of the plasticity of the chord member. The ratio of the chord member rotation to SDR of the pure truss model at the plastic SDR limit was 16% lower than the idealized value. In addition, the ratio of the chord member rotation to SDR of the sub-structure model at the plastic SDR limit was 51% lower than the idealized value, because of the provided flexural stiffness of the diaphragm. The closer the actual plastic hinge is to the idealized hinge, the higher ratio (α / θ) is. A reduction factor (γ) herein is proposed to calculate the rotation demand (α_D) of the designed chord member, and γ can be taken as 0.6 when RC diaphragm or concrete-filled metal decking diaphragms are used.

$$\alpha_D \le \gamma(L/s)\theta \tag{10}$$

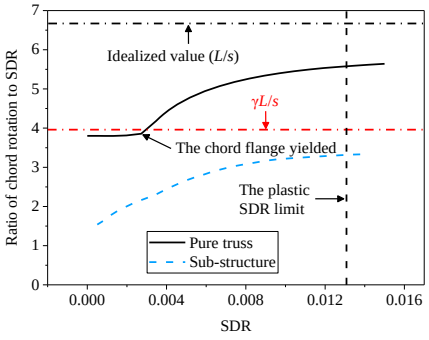

Fig. 27 The rotation of the chord member at loading process

The precise determination of the rotation demand of the chord member concerns the selecting of the section form and structural form of SSTF systems. In the reported studies, double channel sections were used for the chord member and long or multiple Vierendeel panels were used to improve the rotation capacity and reduce the rotation demand of the chord member [9,26,32,33]. However, double channel sections are inconvenient for construction and the adoption of long or multiple Vierendeel panels reduce the stiffness of the structure. Actually, the rotation demand of compact H section is sufficient for the chord members of SSTF structures with the single Vierendeel panels. For instance, the rotation of the H-sectional chord member of the sub-structure is 0.043 rad at the plastic SDR limit, approximately equal to the rotation capacity of compact H-sectional beams [37].

5.3. Mechanical calculation model

In existing studies, the vertical web members near the Vierendeel panel was commonly assumed as a two-force member. The schematic diagram of bending moment in a truss with a Vierendeel panel under horizontal load is illustrated in Fig. 28(a). There is no moment at the vertical web members. In addition, the axial forces in the vertical web member are small since the majority of the shear loads are borne by the diagonal web member when the truss is subjected to horizontal loads. In this case, the vertical web members might be designed in a relatively small size.

However, the gusset plate could transfer moments from the chord member due to its large in-plane flexural stiffness, producing stress concentrations at the vertical web member ends and the corners of the gusset plates. The schematic diagram of bending moment of a truss with fixed vertical web near the Vierendeel panel is shown in Fig. 28(b). It can be seen that the majority of the moment from the chord member is borne by the fixed vertical web member. Therefore, the web members near the Vierendeel panel should be treated as a fixed member subjected to combined axial force and moment. Unsafe designed results may be obtained when the ends of the vertical members are treated as hinged joints.

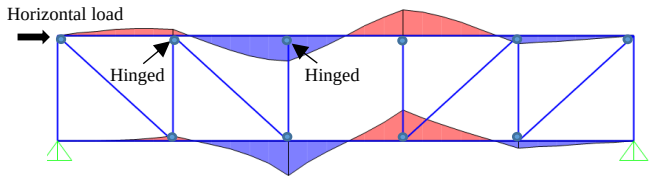

(a) with hinged vertical web near the Vierendeel panel

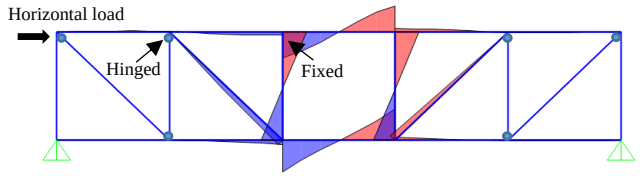

(b) with fixed vertical web near the Vierendeel panel

Fig. 28 Schematic diagram of bending moment of the truss

5.4. Amplification factor of the web members

In an SSTF system, the chord members at the Vierendeel panel are usually designed to yielded to dissipate energy and the members outside keep elastic. The maximum expected vertical shear strength of the Vierendeel panel when it is fully yielded is used to design the non-yielding members outside. The design of the web members should consider the diaphragm actions since the diaphragms significantly enhanced the strength of the Vierendeel panel by improving the flexural strength of the chord members. One practical solution is to amplify the design loads of the web members by an amplification factor when a primary design of SSTF systems was conducted. An amplification factor of 1.4 is recommended in the specification JGJ/T 329-2015 [30] to calculate the design axial load of the diagonal web member near the Vierendeel panel. However, it is an empirical value based on the findings of the premature buckling and fracture of the diagonal web members in existing tests of SSTF systems [30].

The stresses at the diagonal web member near the Vierendeel panel of the pure truss model were extracted as well, as shown in Fig. 29. The ratio of the maximum stress at the web members of the sub-structure to the pure truss was used to determine the amplification factor rather than an average value, since the web members were not permitted to yield. As seen, the ratio of the maximum stress at the diagonal web member near the Vierendeel panel of the sub-structure to the pure truss was 2.63. Therefore, a modified amplification factor of 2.7 to calculate the design axial load at the diagonal web member near the Vierendeel panel, together with the other web members, is recommended to obtain safe design results.

The flexural stresses in the web member near the Vierendeel panel of the sub-structure model shown in Fig. 30 were obtained by deducting the stresses caused by axial force (equal to the stresses at the middle section). In the same way, the flexural stresses in the web member near the Vierendeel panel of the pure truss model were obtained. The ratio of the maximum flexural stress at the vertical web member near the Vierendeel panel of the sub-structure to the pure truss was 1.57. Therefore, an amplification factor of 1.6 to calculate the design moment at the vertical web member near the Vierendeel panel is recommended.

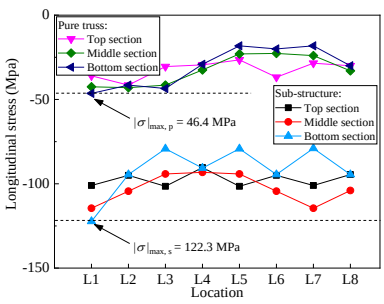

Fig. 29 Stresses at the diagonal web member near the Vierendeel panel

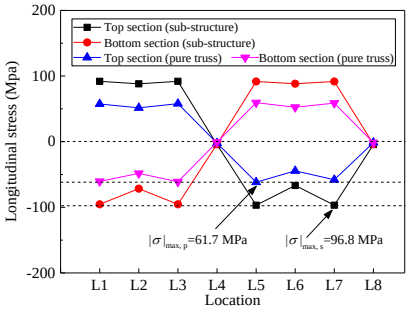

Fig. 30 Flexural stresses at the vertical web member near the Vierendeel panel

6. Conclusions

In this paper, an SSTF sub-structure for facilitating experimental research and refined FE analysis was proposed. Inelastic behavior of the proposed sub-structure was investigated by refined FE analyses. Several conclusions can be drawn.

(1) The shear force versus lateral displacement response of the truss in the sub-structure was almost the same as that in the prototype SSTF structure. The diaphragm actions in SSTF systems were well reflected by the proposed sub-structure model.

(2) The RC diaphragms increased the initial lateral stiffness and yield load of the truss by 80% and 110%, respectively. The diaphragm actions in SSTF systems should be considered when conducting structural design and analysis of SSTF systems.

(3) The RC diaphragms in SSTF systems performed as a rigid plate due to the minor in-plane deformations. The allocation of lateral loads to each individual truss of SSTF structures is based on the relative lateral stiffnesses of the trusses. The RC diaphragms can effectively transfer in-plane shear forces at the plastic SDR limit.

(4) The rotation demand of the chord member is overvalued in existing studies and H-sectional chord members is sufficient for SSTF structures with the single Vierendeel panels to realize the expected failure mode that plastic hinges only occurred in the chord members at the Vierendeel panel ends.

(5) The stresses were unevenly distributed at the vertical web members near the Vierendeel panel, exhibiting bending moment-subjecting characteristic. The web member near the Vierendeel panel should be treated as a fixed member subjected to combined axial force and moment, rather than a two-force member.

(6) A modified amplification factor of 2.7 to calculate the design axial load at the web members and an amplification factor of 1.6 to calculate the design moment at the vertical web member near the Vierendeel panel are recommended, to simply consider the diaphragm actions when conducting a primary design of SSTF systems under lateral loads.

Acknowledgements

The authors greatly appreciate the financial support provided by the National Natural Science Foundation of China (No. 52378133) and the Chongqing Natural Science Foundation of China (No. CSTB2023NSCQ-MSX0758). However, the opinions expressed in this paper are solely the authors' own

References

[1] R.J. Hansen, W.J. LeMessurier, P.J. Paul, others, New steel framing system promises major savings in high-rise apartments, Architecture Record. 139 (1966) 191–196.
[2] X. Zhou, Z. Zhou, Q. Zhou, W. Huang, W. Guo, Hysteretic behavior and design considerations of staggered truss framing systems, Journal of Building Engineering. 72 (2023) 106696. https://doi.org/10.1016/j.jobe.2023.106696.
[3] R.P. Gupta, S.C. Goel, Dynamic analysis of staggered truss framing system, Journal of the Structural Division. 98 (1972) 1475–1492.
[4] A. Brazil, Staggered truss system proves economical for hotels, Modern Steel Construction. 40 (2000) 32–39.
[5] B. Pollak, Staggered truss solution, Modern Steel Construction. 43 (2003) 38–43.
[6] R.D. Hanson, G.V. Berg, Aseismic Design of Staggered Truss Buildings, Journal of the Structural Division. 100 (1974) 175–193. https://doi.org/10.1061/JSDEAG.0003690.
[7] J. Kim, J.-H. Lee, Y.-M. Kim, Inelastic behavior of staggered truss systems, The Structural Design of Tall and Special Buildings. 16 (2007) 85–105.
[8] AISC (American Institute of Steel Construction), Steel design guide series 14: staggered truss framing systems, AISC, Chicago, IL, 2002.
[9] S. Simasathien, S. Chao, K. Moore, T. Okazaki, Modified structural layouts for staggered truss framing systems used in seismically active areas, in: Proceedings of the 10th National Conference in Earthquake Engineering, Earthquake Engineering Research Institute Anchorage, AK, 2014.
[10] J. Kim, J. Lee, B. Kim, Seismic retrofit schemes for staggered truss structures, Eng. Struct.

102 (2015) 93–107. https://doi.org/10.1016/j.engstruct.2015.08.006.
[11] J. Kim, S. Kim, Performance-based seismic design of staggered truss frames with friction dampers, Thin-Walled Struct. 111 (2017) 197–209. https://doi.org/10.1016/j.tws.2016.12.001.
[12] X. Zhou, Y. Chen, K. Ke, M.C.H. Yam, H. Li, Hybrid steel staggered truss frame (SSTF): A probabilistic spectral energy modification coefficient surface model for damage-control evaluation and performance insights, Journal of Building Engineering. 45 (2022) 103556. https://doi.org/10.1016/j.jobe.2021.103556.
[13] Z. Li, D. Gan, X. Zhou, Effects of Modeling Methods of RC Diaphragm on the Behavior of Steel Staggered Truss Framing Structures, in: G. Geng, X. Qian, L.H. Poh, S.D. Pang (Eds.), Proceedings of The 17th East Asian-Pacific Conference on Structural Engineering and Construction, 2022, Springer Nature Singapore, Singapore, 2023: pp. 1369–1381.
[14] Seismology Committee of Structural Engineers Association of California, Seismic design of staggered truss systems, Structure Magazine. (2008) 46–47.
[15] X. Zhou, Y. He, L. Xu, Q. Zhou, Experimental study and numerical analyses on seismic behaviors of staggered-truss system under low cyclic loading, Thin-Walled Struct. 47 (2009) 1343–1353. https://doi.org/10.1016/j.tws.2009.03.007.
[16] C. Chen, W. Zhang, Comparative experimental investigation on steel staggered-truss constructed with different joints in fire, Journal of Constructional Steel Research. 77 (2012) 43–53. https://doi.org/10.1016/j.jcsr.2012.05.002.
[17] C. Chen, W. Zhang, Experimental study of the mechanical behavior of steel staggered truss system under pool fire conditions, Thin-Walled Structures. 49 (2011) 1442–1451. https://doi.org/10.1016/j.tws.2011.07.004.
[18] X. Zhou, W. Huang, Q. Zhou, Z. Zhou, W. Guo, Pseudo-dynamic test and numerical analyses of staggered truss framing systems, Structures. 45 (2022) 509–522. https://doi.org/10.1016/j.istruc.2022.09.018.
[19] D.S. Simulia, ABAQUS 6.13 User's manual, Dassault Systems, Providence, RI. 305 (2013) 306.
[20] X. Qiang, F.S.K. Bijlaard, H. Kolstein, X. Jiang, Behaviour of beam-to-column high strength steel endplate connections under fire conditions – Part 2: Numerical study, Engineering Structures. 64 (2014) 39–51. https://doi.org/10.1016/j.engstruct.2014.01.034.
[21] H. Yin, G. Shi, Finite element analysis on the seismic behavior of fully prefabricated steel frames, Engineering Structures. 173 (2018) 28–51. https://doi.org/10.1016/j.engstruct.2018.06.096.
[22] ACI (American Concrete Institute), Building code requirements for structural concrete (ACI 318–19), ACI, Farmington Hills, 2019.
[23] MOHURD (Ministry of housing and urban rural development of the people's Republic of China), Code for design of concrete structures: GB50010-2010, China Construction Industry Press, Beijing, 2015.
[24] Fib Bulletins : Model Code 2010 - Final draft, Volume 1, (n.d.). https://fib-international.org/publications/fib-bulletins/model-code-2010-final-draft,-volume-1-detail.html (accessed March 23, 2023).
[25] W. Demin, H. Fukang, Investigation for plastic damage constitutive models of the concrete material, Procedia Engineering. 210 (2017) 71–78. https://doi.org/10.1016/j.proeng.2017.11.050.
[26] S.-H. Chao, C. Jiansinlapadamrong, S. Simasathien, T. Okazaki, Full-Scale Testing and Design of Special Truss Moment Frames for High-Seismic Areas, J. Struct. Eng. 146 (2020) 04019229. https://doi.org/10.1061/(ASCE)ST.1943-541X.0002541.
[27] A. Ciutina, D. Dubina, G. Danku, Influence of steel-concrete interaction in dissipative zones of frames: I–Experimental study, Steel and Composite Structures, An International Journal. 15 (2013) 299–322.
[28] Z. Tan, W. Zhong, B. Meng, Y. Zheng, S. Duan, Z. Qu, Numerical evaluation on collapse-resistant performance of steel-braced concentric frames, Journal of Constructional Steel Research. 193 (2022) 107268. https://doi.org/10.1016/j.jcsr.2022.107268.
[29] Afifi Mohamed, Tremblay Robert, Rogers Colin A., Design and Detailing Recommendations of Slotted-Hidden-Gap Connection for Square HSS Brace Members, Journal of Structural Engineering. 149 (2023) 04022249. https://doi.org/10.1061/JSENDH.STENG-11609.
[30] MOHURD (Ministry of housing and urban rural development of the people's Republic of China), Specification for design of staggered steel truss framing systems: JGJ/T 329-2015, China Construction Industry Press, Beijing, 2015.
[31] MOHURD (Ministry of housing and urban rural development of the people's Republic of China), Code for seismic design of buildings: GB50011-2010, China Construction Industry Press, Beijing, 2016.
[32] S. Simasathien, C. Jiansinlapadamrong, S.-H. Chao, Seismic behavior of special truss moment frame with double hollow structural sections as chord members, Eng. Struct. 131 (2017) 14–27. https://doi.org/10.1016/j.engstruct.2016.10.001.
[33] X. Zhou, D. Gan, J. Xi, Z. Li, K. Ke, Z. Yang, Seismic behavior analysis and energy-based design of SSTFs with multiple Vierendeel panels, Journal of Constructional Steel Research. 212 (2024) 108243. https://doi.org/10.1016/j.jcsr.2023.108243.
[34] J.P. Moehle, J.D. Hooper, D.J. Kelly, T.R. Meyer, Seismic design of cast-in-place concrete diaphragms, chords, and collectors, NIST GCR. (2010) 10–917.
[35] ASCE (American Society of Civil), Minimum Design Loads for Buildings and Other Structures: ASCE/SEI 7-16, ASCE, Reston, VA, 2016.
[36] S. Srisangeerthanan, M.J. Hashemi, P. Rajeev, E. Gad, S. Fernando, Numerical study on the effects of diaphragm stiffness and strength on the seismic response of multi-story modular buildings, Engineering Structures. 163 (2018) 25–37. https://doi.org/10.1016/j.engstruct.2018.02.048.
[37] A. Mohabeddine, Y.W. Koudri, J.A.F.O. Correia, J.M. Castro, Rotation capacity of steel members for the seismic assessment of steel buildings, Engineering Structures. 244 (2021) 112760. https://doi.org/10.1016/j.engstruct.2021.112760.

Advanced Steel Construction – Vol. 20 No. 2 (2024) 135–143
DOI:10.18057/IJASC.2024.20.2.5
(Special Issue: *11st International Conference on Advances in Steel Structures, ICASS'2023, Kuching, Sarawak, Malaysia*)

FEASIBILITY STUDY ON AN OPTICAL STRAIN GAGE BASED ON FLUORESCENCE RESPONSE OF GRAPHENE QUANTUM DOTS

Yan-Hao Sun [1], Hai-Tao Liu [1], Bo Yang [1] and Kang Chen [2, *]

[1] *School of Civil Engineering, Chongqing University, Chongqing, China*
[2] *Department of Civil Engineering, Xi'an Jiaotong-Liverpool University, Suzhou, China*
** (Corresponding author: E-mail: Kang.Chen@xjtlu.edu.cn)*

ABSTRACT

In this study, based on the excellent fluorescence properties of graphene quantum dots (GQDs) and their good response to mechanical effects, the GQDs were mixed with epoxy resin to make a coating sensor. Taking this as the research object, the film was coated on the Q235 tensile steel sample, which can dynamically monitor the stress and strain of the steel sample. By investigating the effects of the concentration of the GQDs solution, the synchronization of the film and the steel component, and the residual stress of the epoxy resin, the mechanism of the visual fluorescence signal was analyzed. The response of stress-strain of steel sample and the fluorescence intensity of coating sensor under uniaxial tension and cyclic loading were studied. The test results showed that the synthesized coating sensor had good stability and can produce very sensitive fluorescence response to the stress and strain. The fluorescence intensity of the coating sensor increased with the increase of stress and strain, and decreased with the decrease of stress and strain under cyclic loading, which had the potential to act as a new optical strain gauge. Based on the test results, the stress and strain of the GQDs-epoxy resin composites coated on tensile steel samples with different thicknesses were studied by numerical simulation.

ARTICLE HISTORY

Received: 24 May 2024
Revised: 24 May 2024
Accepted: 11 June 2024

KEYWORDS

Graphene quantum dots;
Stress-strain monitoring;
Fluorescence response;
Numerical simulation

1. Introduction

Graphene quantum dots (GQDs) are zero-dimensional structure of graphene, belonging to nanomaterials. They can produce stable and bright fluorescence under ultraviolet light irradiation, showing good water solubility, low biological toxicity, chemical inertness and other excellent characteristics [1,2]. The photoluminescence peak position and intensity of GQDs depend on or are independent of excitation wavelength, PH value, solvent, boundary and size of GQDs. Due to its unique characteristics, it has broad application prospects in biosensing [3], bioimaging [4], fluorescent probes [5], optical sensing [6] and so on.

For steel structures, stress and strain monitoring is particularly important. Whether in the basic experimental process or in the specific parts of the actual structure, stress and strain monitoring is required. Especially in harsh environments, it is very valuable to develop a sensor with low cost, good stability, high real-time performance and remote monitoring of stress and strain. The problem of creep strain accumulation of steel structure can not be ignored. At present, there are many methods of strain measurement, including resistance strain gauge [7], optical fiber sensor [8], DIC [9] and so on. Although these methods are currently mature, they are still limited by response time, sample destruction, and cost issues. The quantum dots fluorescence sensor is based on the optical response characteristics of fluorescent quantum dots, which can alleviate the limitations of these problems to some extent.

Liu et al. [10] studied the pressure-induced optical response of InP/ZnS nanocrystals. During the full pressure cycle of 0-2.5 GPa, the photoluminescence blue shift is completely reversible, and the emission color range is from orange to green with a slight intensity enhancement. Wang [11] found that CuInS2/ZnS quantum dots not only showed high photoluminescence intensity, but also showed a reliable and simple relationship between photoluminescence emission peak energy and external pressure. Yin et al. [12] developed a quantum dot-based composite composed of the CdSe@ZnS core-shell quantum dots and bisphenol A epoxy resin. The photoluminescence intensity will change significantly for large engineering strain. Zhao et al. [13] explored a technical means to track the crack propagation of metal materials in real time by using the fluorescence characteristics of quantum dots. It was revealed that the minimum width of the crack that can be detected was 7 μm, which showed a significant improvement compared with the limit that the existing non-destructive testing technology can reach. Zhang et al. [14] found that the luminescence of semiconductor quantum dots can be adjusted by piezoelectric effect. Small mechanical force can cause significant changes in the emission spectrum. Existing studies have found that the photoluminescence properties (fluorescence) of quantum dots do have a more sensitive response to mechanical forces. Therefore, it is very potential to use the fluorescence response characteristics of GQDs to monitor the stress and strain of steel structures.

In this study, the GQDs were uniformly embedded in epoxy resin, and the fluorescence response of the GQDs fluorescence sensor to uniaxial tensile load and cyclic loading was studied. The response mechanism of the GQDs fluorescence sensor was clarified from the influence of factors such as the change of the GQDs solution concentration, the synchronization of sensor and steel sample, and the residual stress inside epoxy resin.

2. Preparation of the GQDs fluorescence sensor

2.1. Selection of the GQDs

According to the preliminary work of the laboratory, three batches of GQDs were synthesized by a similar 'top-down' method [15]. The fluorescence color and fluorescence effect are shown in Fig. 1. The fluorescence colors are blue, green and light blue, respectively. The fluorescence spectra of three batches of the GQDs with different production processes were measured by fluorescence fiber spectrometer (Ocean Insight, FLAME-S-XR1). As shown in Fig. 1, The fluorescence wavelength of the GQDs1 is 501 nm, the fluorescence intensity is 51713 Counts, the fluorescence spectrum is smooth and has only one fluorescence peak. The fluorescence wavelength of GQDs2 is 483 nm, and the fluorescence intensity is 51303 Counts. Although the fluorescence intensity is good, its fluorescence spectrum has two peaks, which is not conducive to the development of later sensors. The fluorescence wavelength of GQDs3 is 486 nm. Although the fluorescence spectrum is smooth, its fluorescence intensity is only 38075 Counts, and the fluorescence effect is poor.

After comparing the fluorescence spectra and fluorescence intensity of the above three batches of GQDs, GQDs1 was used to develop a fluorescence sensor.

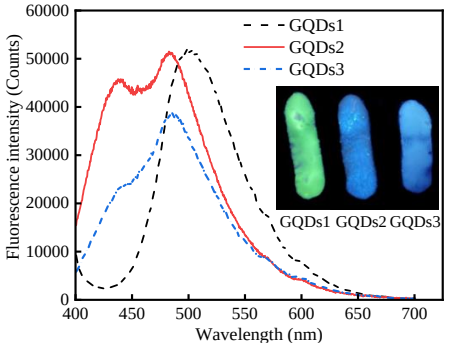

Fig. 1 Fluorescence spectra and fluorescence effect of three batches of GQDs

2.2. Selection of the GQDs carrier matrix

Considering the characteristics of GQDs, it is difficult to be directly used for actual monitoring, so it is necessary to select a suitable bearing matrix, which can not only protect GQDs, but also meet the practical application without affecting its fluorescence characteristics. The epoxy resin is easy to cure and has high strength, which can well protect GQDs from oxidation. And it has good light transmittance, and the fluorescence of GQDs can be well transmitted and almost no attenuation. In addition, the epoxy resin has good adhesion and can be firmly bonded to the structural surface in specific applications.

Considering the need to fully disperse the GQDs into epoxy resin, so epoxy resin must have a small viscosity and good fluidity. After screening and investigation, two epoxy resins were selected, which were 6002-type epoxy resin with 572-type curing agent as well as 664-type diluent, and high transparent epoxy resin with matching curing agent. The ratio test of two epoxy resins was carried out.

For the 6002-type epoxy resin, it belongs to thermosetting epoxy resin. The reference curing volume ratio is: epoxy resin : curing agent : diluent = 1 : 1 : 0.2. The curing temperature and time are : 90 °C 2h + 160 °C 2h + 180 °C 4h. Fig. 2 shows the curing conditions of three different ratios of epoxy resin. The volume ratios from left to right are (epoxy resin：curing agent：diluent) 3：3：1, 3：1：1 and 1：1 (without diluent). The group without diluent was basically uncured. Although the first two groups were cured, the curing effect was poor and the surface was not smooth. According to the curing effect, the shortcomings of this epoxy resin were obvious. The high curing temperature, long curing time and poor curing effect were not conducive to the practical application of the later sensor.

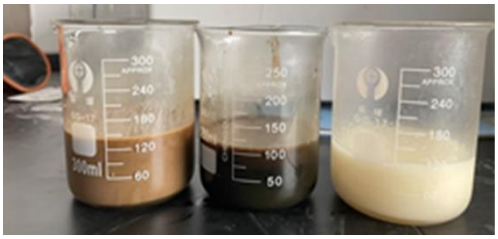

(a) Three different ratio of epoxy resin

(b) Curing condition

Fig. 2 Curing condition of three different ratio of the 6002-type epoxy resin

For the highly transparent epoxy resin, it has the advantages of good transparency, less bubbles, high hardness and low curing conditions. According to the previous multiple blending tests, the curing volume ratio of epoxy resin：curing agent = 2.5：1 was finally determined. Under this ratio, the curing time of epoxy resin was the shortest and the strength was the highest.

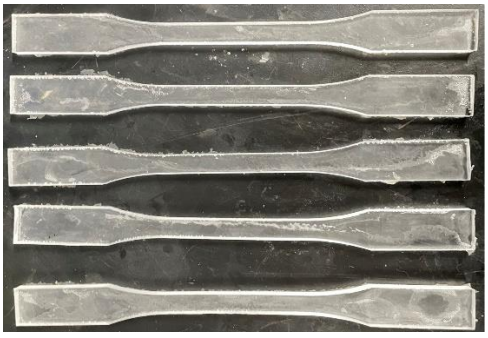

Fig. 3 Cured epoxy resin tensile specimen

As shown in Fig. 3, the cured epoxy resin had a smooth surface and good light transmittance. It was found in tests that the highly transparent epoxy resin can be completely cured at 85 °C for 2h, and can also be completely cured at room temperature for 24 h. So the epoxy resin is superior to the 6002-type epoxy resin in terms of curing performance and practicality. The high-transparent epoxy resin was finally selected as the carrier matrix of the GQDs for subsequent experiments.

2.3. Selection of the solvent

Due to the need to uniformly disperse the GQDs into the epoxy resin in the later stage, it is necessary to select a solvent that can fully dissolve the GQDs, and can be mutually soluble with the epoxy resin, while being volatile. The following three solvents were selected: N-methylpyrrolidone (NMP), anhydrous ethanol and water. The GQDs were dissolved in different solvents at a concentration of 30mg/ml, and the dissolution was observed after full stirring and dispersion. As shown in Fig. 4, the solubility of the GQDs in three solvents was good, and the GQDs can be fully dissolved.

The three solvents dissolved with GQDs were mixed into the epoxy resin in proportion, and the corresponding proportion of curing agent was added to fully stir and then put into the ultrasonic dispersion instrument for ultrasonic dispersion for 5min. The three composite solutions were poured into petri dishes to observe the situations before and after curing for 24 hours. As shown in Fig. 5, the fusion of NMP, anhydrous ethanol and epoxy resin before curing was good, whereas it was difficult for water to fuse with the epoxy resin. Besides, a large number of bubbles were generated after stirring and dispersing. After curing for 24 hours, the epoxy resin in the culture dish added with NMP and anhydrous ethanol had been cured well. However, only a part of the epoxy resin with water as solvent had been cured, resulting in the stratification of water and epoxy resin. Considering that anhydrous ethanol can be completely volatilized during the curing process of epoxy resin, it had little effect on the strength of epoxy resin after curing, so anhydrous ethanol was finally selected as the solvent.

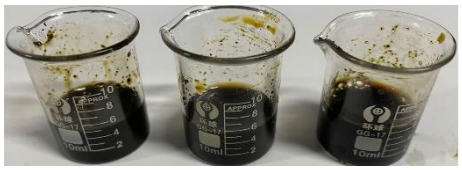

(a) Dissolution of GQDs in solvents

(b) Before curing

(c) After curing

Fig. 4 Three different solvents (from left to right: NMP, anhydrous ethanol and water)

2.4. Optimal concentration of the GQDs solution

The fluorescence intensity of GQDs solutions with different concentrations is different, and the GQDs have fluorescence quenching characteristics [16,17] (the fluorescence intensity of graphene quantum dots decreases, the luminescence time is shortened, and even fluorescence quenching occurs). So it is not the higher the concentration of GQDs, the greater the fluorescence intensity.

Table 1
Different CQDs solution concentration

Concentration (mg/ml)	10	20	30	40	50	60
Anhydrous ethanol (ml)	40	40	40	40	40	40
GQDs (g)	0.4	0.8	1.2	1.6	2.0	2.4

To achieve the best fluorescence performance of the composites, it is necessary to determine the optimal concentration of the GQDs solution. The GQDs were dissolved in anhydrous ethanol. The following six concentration gradients were designed, as shown in Table 1.

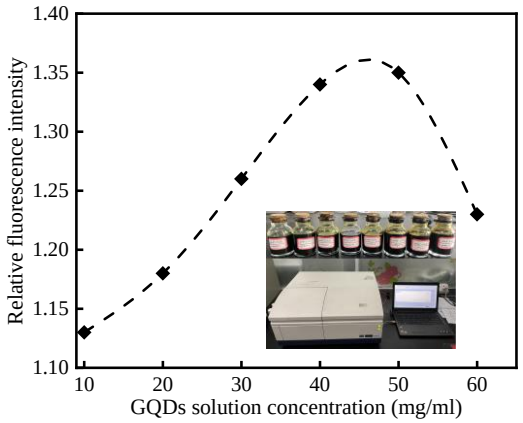

Fig. 5 Optimal concentration curve of GQDs solution

After uniform dispersion, the fluorescence intensity of the six groups of solutions was measured by a fluorescence spectrophotometer (F-7000). The measurement results are shown in Fig. 5. The relative fluorescence intensity was used to compare the fluorescence intensity of each concentration of GQDs solution. It can be seen that the relative fluorescence intensity of the GQDs solution increased with the increase of concentration before 45 mg/ml, and reached the maximum when the concentration of the solution reached 45 mg/ml. After that, the number of the GQDs per unit area increased, whereas the fluorescence intensity decreased due to the fluorescence quenching phenomenon of quantum dots. Considering the amount of the GQDs and the convenience of the later ratio, 40 mg/ml was used as the optimal fluorescence concentration of the GQDs solution.

2.5. Preparation process of the GQDs fluorescence sensor

The preparation of the composite material was carried out in the following three steps. (i) The GQDs were dissolved in the anhydrous ethanol and mechanically stirred for 3 minutes. And then the GQDs solution was placed in an ultrasonic disperser for 5 minutes to disperse the agglomerated GQDs in the solution. (ii) The GQDs solution, epoxy resin and curing agent were mixed at a volume ratio of 0.9 : 2.5 : 1, and the mixed solution was stirred with a glass rod for 3 minutes to fully integrate the three. The stirred solution was placed in an ultrasonic dispersion instrument for another 5 minutes of ultrasonic dispersion, so that the GQDs can be uniformly dispersed into the epoxy resin. (iii) The prepared composite solution was cured in two ways. One is to put the composite solution into a drying oven and cure at 85 °C for 2h. The other is cured at room temperature for 24 h. The preparation process is shown in the Fig. 6.

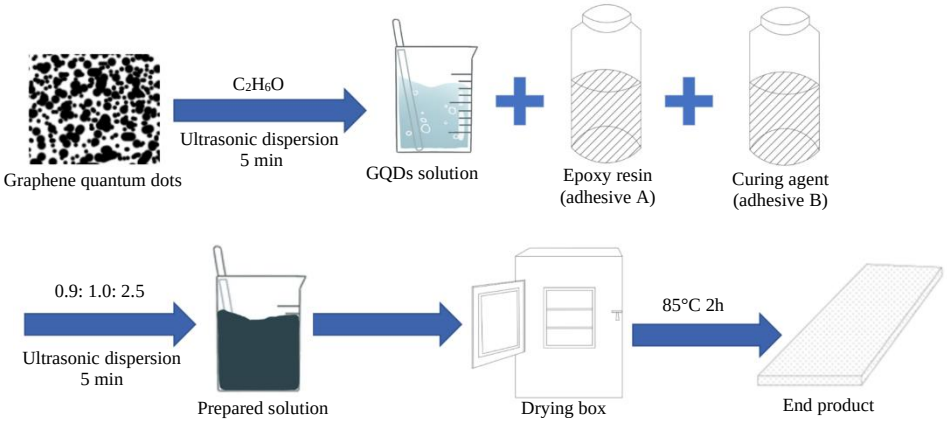

Fig. 6 GQDs fluorescence sensor preparation flow chart

3. Tensile strain monitoring of the GQDs fluorescence sensor

3.1. Tensile fluorescence response of the GQDs fluorescence sensor

3.1.1. Sample design

According to the Chinese standard GB/T 2567-2021 [18], the tensile sample of the epoxy resin was designed, as shown in Fig. 7(a). Considering the late demoulding, the silica gel mold was customized in the size of Fig. 7(a). Two batches of epoxy resin tensile samples were poured, one batch was blank epoxy resin tensile samples, and the other batch was the GQDs-epoxy resin composites tensile samples.

According to the preparation process in Section 2.5, two batches of samples were prepared. The prepared composite solutions were poured into silica gel molds for curing, and the curing method was selected to cure at room temperature for 24 hours. This curing method can greatly reduce the bubbles inside the composite after curing, and the surface after curing is smooth and flat, without uneven stress. The cured blank epoxy resin tensile samples are shown in Fig. 7(b), and Fig. 7(c) shows the GQDs-epoxy resin composites tensile samples. It can be seen that under the irradiation of ultraviolet light with a wavelength of 365 nm, the tensile samples exhibited photoluminescence.

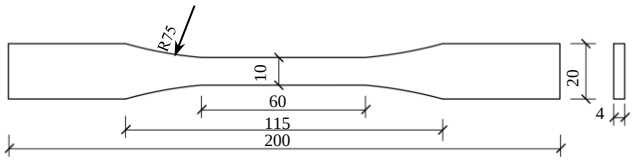

(a) Tensile sample size of epoxy resin

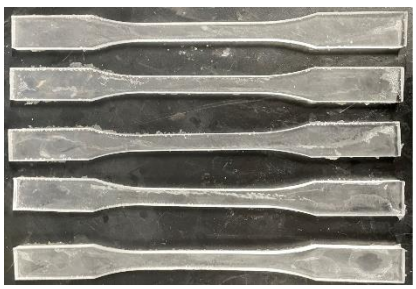

(b) Blank epoxy resin tensile sample

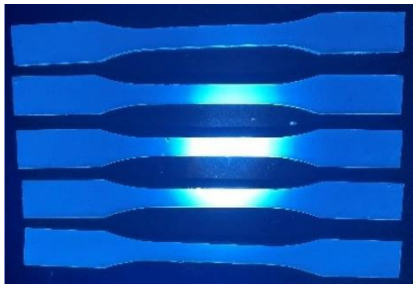

(c) Tensile samples of the GQDs-epoxy resin composites

Fig. 7 Epoxy resin tensile sample

3.1.2. Test device and loading scheme

Fig. 8 shows the test device composed by the universal material testing machine and fluorescence response monitoring system. The fluorescence response monitoring system was built by fluorescence fiber spectrometer, LED 365 nm ultraviolet light source and Y-type fiber. The fluorescence response changes of tensile test were recorded by fluorescence fiber spectrometer. In the experiment, the GQDs fluorescence sensor can achieve photoluminescence under local irradiation of ultraviolet light at 365 nm wavelength.

The loading device was universal material testing machine (SANS), and the loading rate of epoxy resin tensile specimen was set to 1 mm/min.

When measuring the sample each time, it was necessary to keep a certain distance between the optical fiber probe and the measured sample, so that the measured fluorescence spectrum data was more accurate. Through the previous experiments, it was found that the distance between the optical fiber probe and the sample was most suitable in the range of 0.5 cm to 1 cm. This distance range can ensure the accuracy of the measured fluorescence spectrum, and can effectively collect the real-time change of fluorescence intensity. The change of the fluorescence intensity was collected every 1 s.

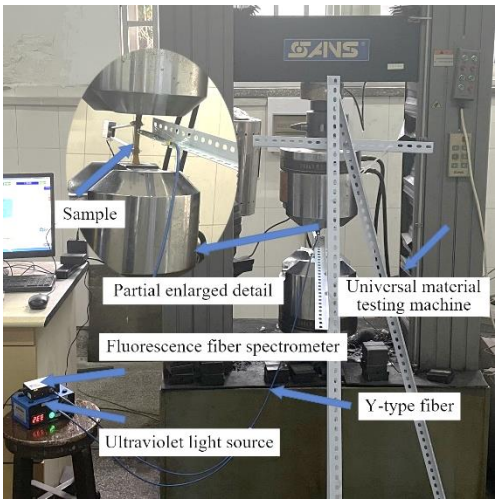

Fig. 8 Test device

3.1.3. Test results and analysis

As shown in Fig. 9, the maximum stress of the blank epoxy resin tensile samples was basically maintained at about 40 MPa, and the maximum strain was maintained at about 6 %. The stress-strain curves of the two blank epoxy resin tensile samples were similar, and the stability during stretching was good, which can serve as a matrix for carrying GQDs.

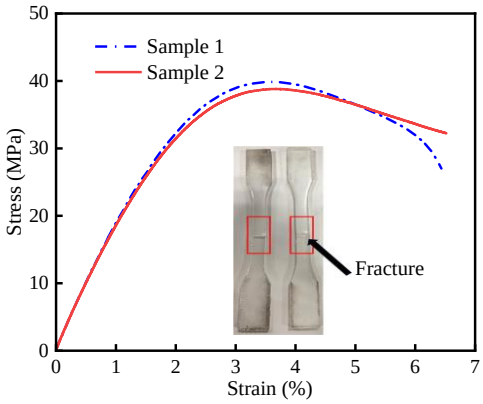

Fig. 9 Tensile stress-strain curves of blank epoxy resin tensile samples

As shown in Fig. 10(a)-(b), the fluorescence intensity of the GQDs-epoxy resin composites tensile samples changed in real time with the tensile strain during the tensile test, and the fluorescence intensity decreased with the increase of the tensile strain. The two curves showed an approximate linear relationship. It was also observed in the tensile experiment that the fluorescence intensity of some tensile samples increased with the increase of strain in the early stage (Fig. 10(c)). Compared with the blank epoxy resin tensile sample in Fig. 9, the maximum strain has been greatly improved, but the maximum stress has been reduced by about 10 %. This showed that the incorporation of GQDs increased the toughness of epoxy resin to a certain extend. Fig. 11 shows the photo of the GQDs-epoxy resin composites tensile samples after fracture, it can be seen that the samples produced a large strain.

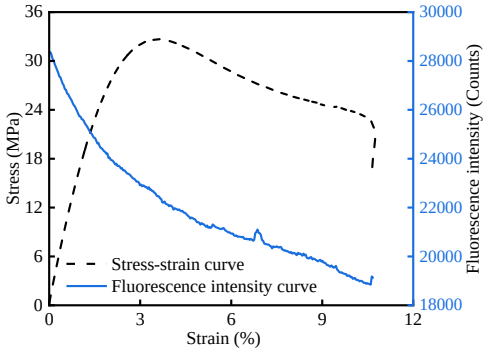

(a) Composites smple 1

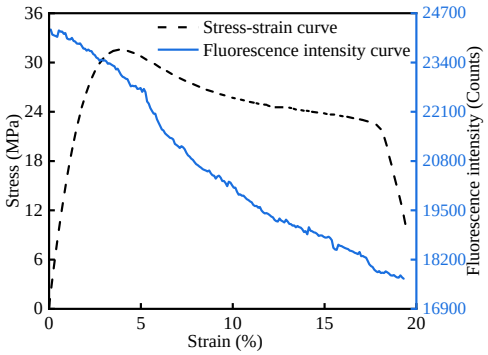

(b) Composites smple 2

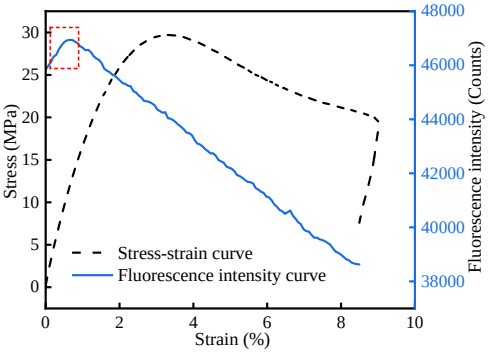

(c) Composites smple 3

Fig. 10 Stress and fluorescence intensity of GQDs-epoxy resin composites samples

Fig. 11 Tensile samples after fracture

As shown in Fig. 12, as the tensile strain increased during the experiment, the number of the GQDs per unit area decreased, which led to a decrease in fluorescence intensity. At the same time, when the GQDs were dispersed into epoxy resin, some quantum dots may agglomerate. During the stretching process, the agglomerated GQDs were pulled apart to expose more GQDs to ultraviolet light, which led to an increase in fluorescence intensity as the tensile strain increased. In the tensile experiment, the change of the number of GQDs per unit area may be one of the reasons for the change of fluorescence intensity.

However, the strain-induced separation of the GQDs aggregates did

increase the number of GQDs exposed to ultraviolet light, resulting in an increase in photoluminescence intensity (fluorescence intensity), which was also observed in the tensile experiment.

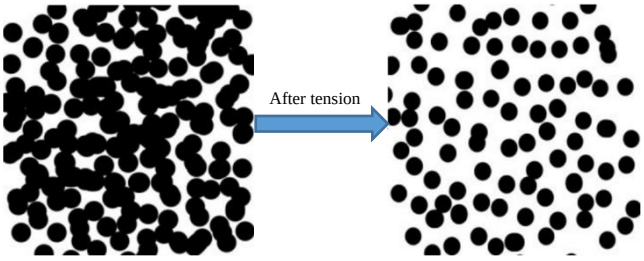

Fig. 12 Comparison of the number of GQDs unit area after tensile experiment

In general, the photoluminescence intensity of the rated number of graphene quantum dots may be related to its quantum yield, that is, the lower the quantum yield, the lower the photoluminescence intensity of graphene quantum dots. Carrión et al. [19] believed that the photoactivation process depends on many factors, including atmospheric conditions (oxygen, humidity), light intensity, the presence of water, and the polarity of the solvent. It can be considered that the tensile strain causes the change of related factors in the photoactivation process of graphene quantum dots, which leads to the decrease of photoluminescence intensity.

3.1.4. Contrast experiment

To prove that the fluorescence response to tensile strain is a unique phenomenon and characteristic of GQDs material, two groups of contrast experiments were set up to investigate whether the common fluorescent material will have a fluorescence response to tensile strain after it is mixed with epoxy resin to make tensile samples. Two representative fluorescent materials [20] were selected. One was a red ultra-bright phosphor with a red fluorescence color, and the other was a yellow phosphor with a green fluorescence color, as shown in Fig. 13.

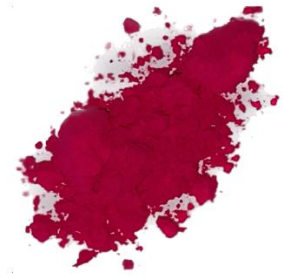

(a) Red phosphors

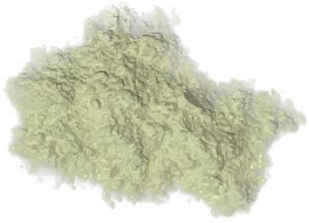

(b) Yellow phosphors

Fig. 13 Two groups of phosphors in contrast experiments

The two phosphors were also mixed into anhydrous ethanol at a concentration of 40 mg/ml, and the fluorescence spectrum was measured by fluorescence fiber spectrometer after fully stirring and dispersing, as shown in Fig. 14. The peak wavelength of the fluorescence spectrum of the red phosphor was 606 nm with a fluorescence intensity of 52639 Counts, and the fluorescence color was red (Fig. 14(a)). Fig. 14(b) shows the fluorescence spectrum of the yellow phosphor. The peak wavelength was 530 nm with a fluorescence intensity of 36779 Counts, and the fluorescence color was green. It can be seen that the fluorescence effects of these two phosphors were excellent and representative.

The dispersed two groups of phosphor solutions were prepared into tensile samples of the epoxy resin doped with phosphor according to the Section 2.5 preparation process, as shown in Fig. 15. The tensile test was carried out after 24 hours of curing to explore whether the samples in the contrast test would have a fluorescence response during the tensile process.

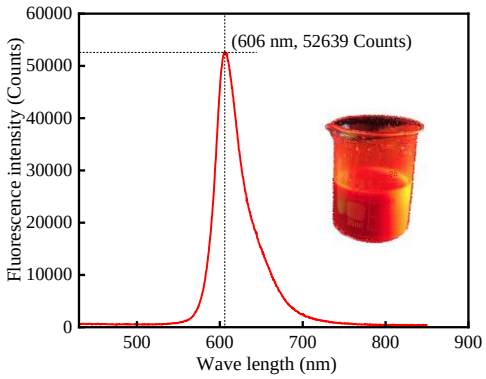

(a) Red phosphors

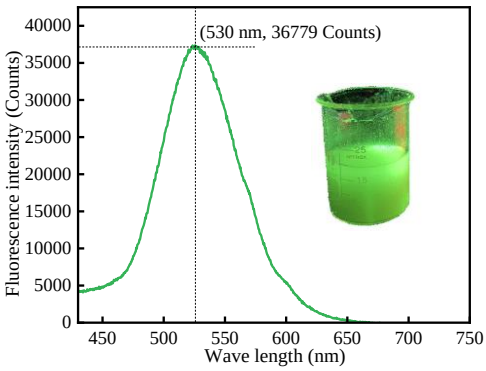

(b) Yellow phosphors

Fig. 14 Spectrogram of two groups of phosphors

(a) Tensile samples with phosphors

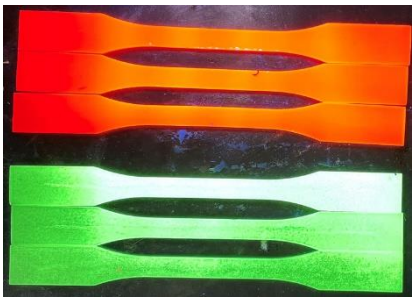

(b) Fluorescence effect after 365 nm UV excitation

Fig. 15 Tensile samples of the epoxy resin doped with phosphor

The test device in Fig. 8 also was employed in the contrast test, and the tensile rate was consistent with the tensile samples of GDQs-epoxy resin composites (1mm/min). The experimental phenomena of the two phosphors were consistent. Taking the red phosphor as an example, as shown in Fig. 16. No regular increase or decrease of the fluorescence intensity with the change of tensile strain was observed during the tensile process. The fluorescence intensity-loading time curve was basically a constantly changing broken line

without any regularity, and the fluorescence stability was very poor. After comparison, it was found that the tensile strain fluorescence response of the GQDs was a unique characteristic of such materials, while other traditional fluorescent materials did not have this characteristic.

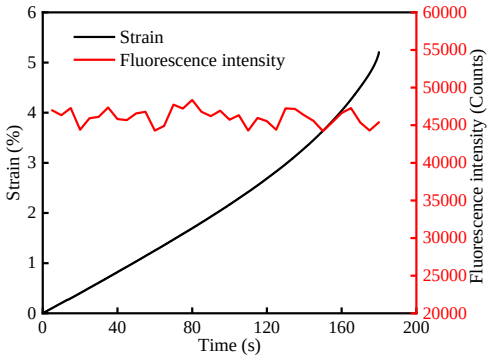

Fig. 16 Strain-fluorescence intensity response curves of tensile samples with phosphors

3.2. Fluorescence response of the GQDs fluorescence sensor to cyclic loading

In reality, the strain of steel structure always changes in real time, and large building structures are basically under cyclic loading during the long run [21]. In this section, the GQDs-epoxy resin composites was coated on the surface of the steel sample to investigate their ability to maintain a consistent fluorescence response under cyclic loading.

3.2.1. Sample design

According to the Chinese standard GB/T 6398-2017 [22], the tensile steel sample was designed, as shown in Fig. 17(a). To make the test more representative, the most widely used Q235 steel in the building structure was selected to make the steel sample.

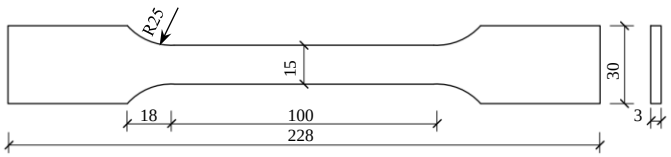

(a) Tensile steel sample size

(b) Steel samples coated with the GQDs-epoxy resin composites

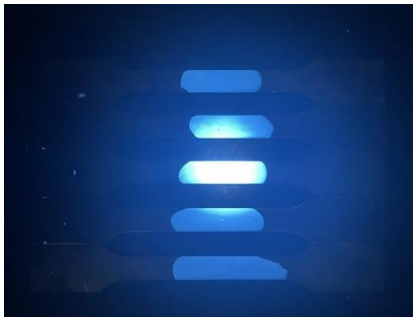

(c) Fluorescence effect after 365 nm UV excitation

Fig. 17 Tensile steel sample

The surface of the tensile steel sample was scrubbed with alcohol to remove surface dusts and make the surface clean and smooth. Through the preparation process in Section 2.5, the prepared composite material mixed solution was dropped onto the gauge section of the Q235 steel sample, and a uniform and smooth film was formed by the gravity of the liquid itself. After being placed at room temperature for 24 hours, the film can be cured on the Q235 tensile specimen, as shown in Fig. 17(b). When the Q235 steel sample was irradiated with 365 nm ultraviolet light, it can be seen that a strong blue fluorescence was generated at the coating, as shown in Fig. 17(c).

3.2.2. Loading scheme

The tensile steel sample coated with GQDs-epoxy resin composites were placed in the universal material testing machine in Fig. 8 for cyclic loading and unloading. The steel sample was installed in the fixture on both sides, and the two ends of the sample were clamped by the rotating handle. The loading and unloading can be realized by moving the fixture on the upper side. During the loading process, the steel sample was kept within the elastic range.

The loading system adopted force-controlled loading, the loading rate was 50 N/s, and the fluorescence intensity was collected every 400 N. Until the load reached 6 kN, the loading was stopped and held for 10 seconds (maintained the stability of the load, facilitated the collection of fluorescence intensity data). Then unloaded from 6 kN, and the unloading process was consistent with the loading process. When unloaded to 100 N, stopped unloading and held for 10 seconds. The fluorescence response of the GQDs-epoxy resin composites to cyclic loading was investigated by repeated cycles.

Fig. 18 shows the response of the GQDs-epoxy resin sensor fluorescence intensity to stress and strain. the Q235 steel specimen had been in the elastic range under cyclic loading. The photoluminescence intensity (fluorescence intensity) of the GQDs-epoxy resin sensor had a good synchronization with the stress and strain of the steel sample. The fluorescence intensity increased with the increase of stress and decreased with the decrease of stress (Fig. 18(a)). The fluorescence intensity increased with the increase of strain and decreased with the decrease of strain (Fig. 18(b)). The curves of fluorescence response were basically linear, indicating that the GQDs-epoxy resin sensor had a high sensitivity to the change of stress and strain.

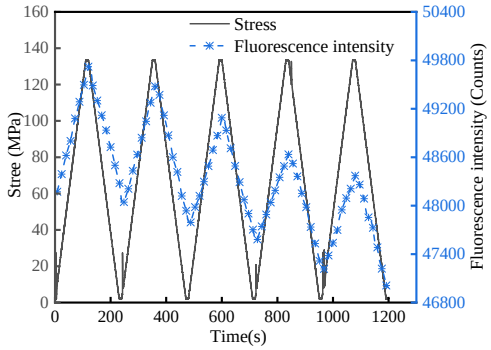

(a) Response of the sensor fluorescence intensity to stress

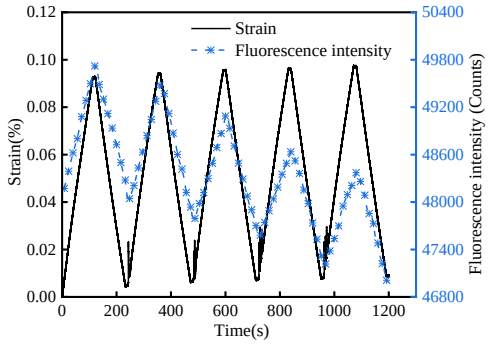

(b) Response of the sensor fluorescence intensity to strain

Fig. 18 Response of the sensor fluorescence intensity to stress and strain

It can also be seen from Fig. 18 that the fluorescence response accuracy and stability of the GQDs-epoxy resin sensor were better in the first three cycles. At the fourth and fifth cycles, the fluorescence response effect began to be less stable, and the overall attenuation of the fluorescence intensity began to increase, but the trend of increase and decrease with stress and strain still existed. There may be two reasons for this instability. The first is that the epoxy resin is not a linear elastic material, and residual stress occurred inside the epoxy resin during

multiple loading and unloading. The second reason is that the adhesion between the GQDs-epoxy resin sensor and the steel sample was weakened, and the phenomenon of asynchrony occurred, which led to the instability of the fluorescence response.

The change trend of the fluorescence intensity of the GQDs-epoxy resin sensor indicates that there is an interaction between the GQDs and the epoxy resin, which may be related to internal stress, strain, time dependence of epoxy resin, creep, residual stress and so on [23]. At present, the potential mechanism of this interaction is not clear, and further research and discussion are needed. This may be related to the separation of GQDs aggregates during the tensile process in small strain cyclic loading, resulting in a change in the number of GQDs per unit area.

4. Numerical simulation

4.1. Modeling method

To more clearly investigate the stress of the GQDs-epoxy resin composites when it is coated on the tensile steel member, the numerical simulation of the tensile steel sample coated with the GQDs-epoxy resin composites was carried out. Abaqus/Implicit was adopted for modeling, and the modeling parameters are as follows in Table 2. Since the loading of the steel sample is in the elastic the numerical simulation.

The tensile pressure of 200 MPa was set at both ends of the model as the load. Considering that it is difficult to realize the thin film thickness in practical application, the thinnest thickness of the simulation analysis is controlled at 0.5mm. The coating thickness of the GQDs-epoxy resin composites was set to three groups: 0.5mm, 1mm and 2mm. The FE model is shown in Fig. 19.

Table 2
Abaqus modeling parameters

Component	Density (t/mm^3)	Young's modulus (MPa)	Poisson ratio	Mesh size (mm)
Steel sample	7.9×10^{-9}	206000.0	0.3	1.0
Composites	9.5×10^{-10}	1500.0	0.4	0.1

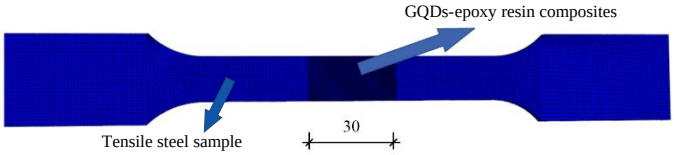

Fig. 19 FE model of steel sample coated with the GQDs-epoxy resin composites

(a) 0.5mm-thickness of the GQDs-epoxy resin composites

(b) 1 mm-thickness of the GQDs-epoxy resin composites

(c) 2 mm-thickness of the GQDs-epoxy resin composites

Fig. 20 Mises diagrams of composites with different thicknesses

4.2. Numerical simulation results and analysis

During the tensile process of the steel sample, the GQDs-epoxy resin composites will also be subjected to different stresses. To make the stress of the composites uniform, it is necessary to study the stress and strain of the composites on the steel sample under different thickness. Fig. 20 shows the Mises diagrams of composites with a thickness of 0.5 - 2 mm. The stress distribution of the composites with a thickness of 0.5 mm is relatively uniform. However, when the thickness becomes 1 mm, the stress along the thickness direction begins to appear non-uniform phenomenon. When the thickness reaches 2 mm, the non-uniform distribution of stress along the thickness direction is aggravated. It shows that the increase of thickness will lead to the aggravation of stress non-uniform, and the deterioration of stress-strain synchronization will affect the fluorescence response accuracy of the GQDs fluorescence sensor. To select the appropriate coating thickness, it is necessary to further investigate the effect of composite thickness on stress and strain.

As shown in Fig. 21(a), the stress and strain values of six points are extracted at the same spacing along the thickness direction. As shown in Fig. 21(b), the stress and strain of the 0.5 mm-thick composites along the thickness direction show an increasing trend, and the stress and strain at the end far from the surface of the steel sample reach the maximum. For the composites with a thickness of 1 mm (Fig. 21(c)), the strain shows a decreasing trend along the thickness direction, while the stress increases first and then decreases. As shown in Fig. 21(d), when the thickness changes to 2 mm, the attenuation of stress and strain along the thickness direction increases, and the stress and strain at the end far from the surface of steel sample are the smallest. Fig. 22 compares the stress and strain of each thickness at the ends near and far from the steel surface, it is found that as the thickness increases, both of the stress and strain at the ends

near and far from the steel surface decrease.

The reason for the phenomenon of Figs. 21-22 is that only one side of the composites is bonded to the surface of the steel sample, and the stress and strain of the composites are transmitted through the bonding force. Due to the stress and strain development inside the epoxy resin and the characteristics of the viscoelastic material, the excessive thickness of the composites will affect the synchronization of stress and strain, resulting in stress and strain reduction and uneven distribution. Therefore, through the comparative analysis, it is found that the stress and strain synchronization and distribution of the composites with a thickness of 0.5 mm are the best when subjected to tensile load. With the increase of thickness, especially when the thickness changes to 2 mm, the stress and strain of the whole composite layer will be unevenly distributed and the synchronization will become worse.

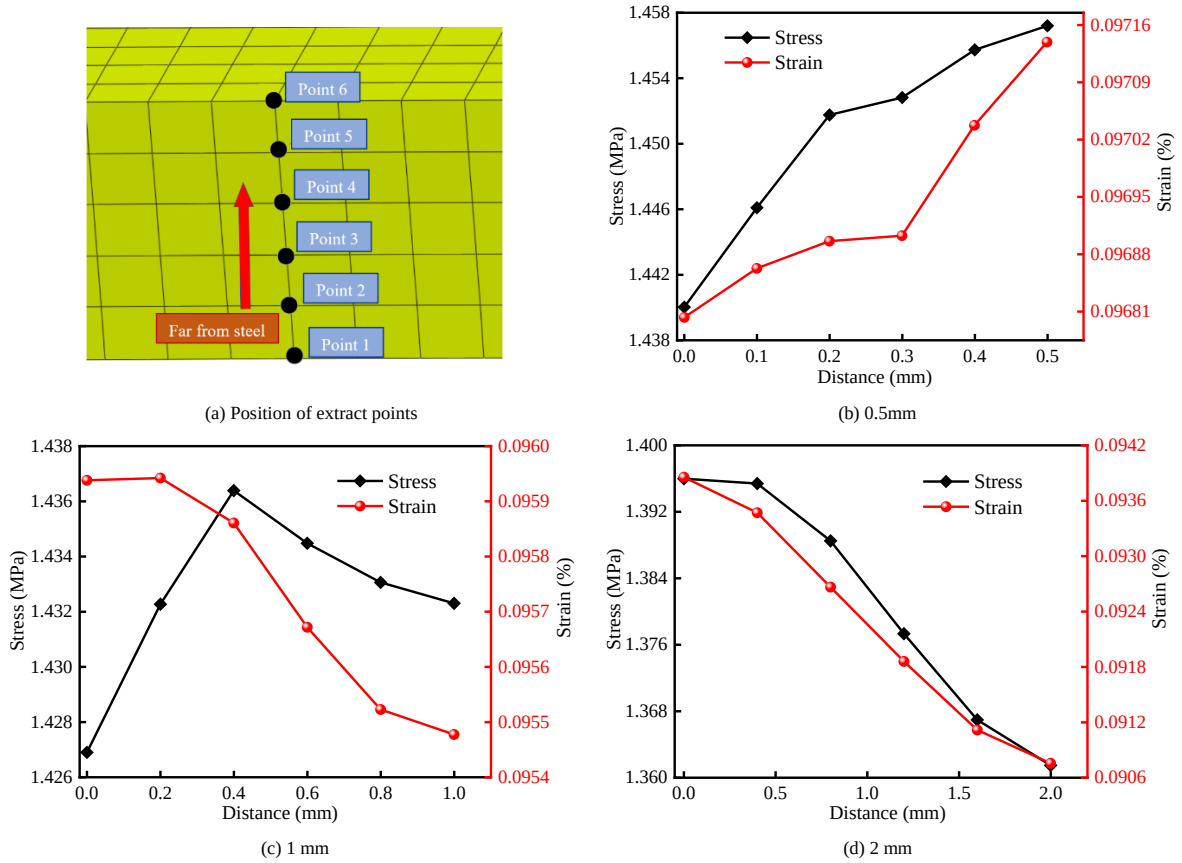

(a) Position of extract points

(b) 0.5mm

(c) 1 mm

(d) 2 mm

Fig. 21 Position of extract points and stress-strain comparison of composites from the near end to the far end

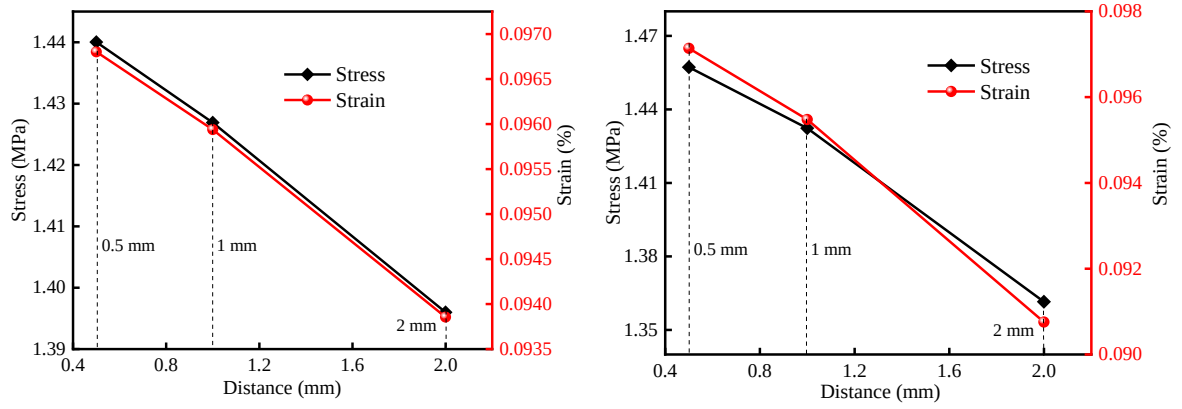

(a) Near the steel sample surface

(b) Far from the steel sample surface

Fig. 22 Stress-strain comparison of composites near and far from the steel sample end

5. Conclusions

In this study, through a series of preliminary deployment experiments, a GDQs fluorescence sensor was successfully synthesized. It was poured into a standard tensile sample, and the uniaxial tensile experiment was carried out by the pouring method. After that, the GDQs fluorescence sensor was uniformly applied to the Q235 standard tensile steel sample by drop coating method, and the cyclic loading experiment was carried out. Furthermore, the stress and strain of the GQDS-epoxy resin composites coated on tensile steel samples with different thicknesses were studied by numerical simulation. The following conclusions can be drawn:

(1) Through the compounding test, it was determined that the highly transparent epoxy resin and anhydrous ethanol were emplyed as the carrier matrix and the solvent of the GQDs. Considering the fluorescence quenching phenomenon of GQDs, the optimal concentration of GQDs solution was 40 mg/ml. The preparation process of the GQDs-epoxy resin composites was standardized. And two curing methods of composites were selected, which were curing at 85 °C for 2h and curing at room temperature for 24h.

(2) The GQDs fluorescence sensor has a good fluorescence response to the tensile strain. After the tensile sample was made, the fluorescence intensity

decreased with the increase of the tensile strain, showing an approximate inverse relationship. The incorporation of the GQDs in the will tensile sample improve the toughness of epoxy resin to a certain extent.

(3) Cyclic test was carried out on the tensile steel samples coated with the GQDs fluorescent sensors. The fluorescence intensity of the the GQDs fluorescent sensors increased with the increase of steel stress and strain, and decreased with the decrease of steel stress and strain. The fluorescence response accuracy and stability were better in the first three cycles, whereas at the fourth and fifth cycles, the fluorescence response effect began to be less stable, and the overall attenuation of the fluorescence intensity began to increase, but the trend of increase and decrease with stress and strain still existed.

(4) Numerical simulation shows that the increase of thickness will lead to the aggravation of stress non-uniform, and the deterioration of stress-strain synchronization will affect the fluorescence response accuracy of the GQDs fluorescence sensor. Through the comparative analysis, the stress and strain synchronization and distribution of the composites with a thickness of 0.5 mm are the best when subjected to tensile load.

References

[1] Zheng X. T., Ananthanarayanan A., Luo K. Q. and Chen P., "Glowing Graphene Quantum Dots and Carbon" Dots: Properties, Syntheses, and Biological Applications", Small, 11(14), 1620-1636, 2015.

[2] Zheng P. and Wu N. Q., "Fluorescence and Sensing Applications of Graphene Oxide and Graphene Quantum Dots: A Review", Chemistry-an Asian Journal, 12(18), 2343-2353, 2017.

[3] Shi J. Y., Chan C. Y., Pang Y. T., Ye W. W., Tian F., Lyu J., Zhang Y. and Yang M., "A fluorescence resonance energy transfer (FRET) biosensor based on graphene quantum dots (GQDs) and gold nanoparticles (AuNPs) for the detection of mecA gene sequence of Staphylococcus aureus", Biosensors & Bioelectronics, 67, 595-600, 2015.

[4] Kortel M., Mansuriya B. D., Santana N. V. and Altintas Z., "Graphene quantum dots as flourishing nanomaterials for bio-imaging, therapy development, and micro-supercapacitors", Micromachines, 11(9), 2020.

[5] Li M. X., Chen T., Gooding J. J. and Liu J. Q., "Review of Carbon and Graphene Quantum Dots for Sensing", ACS Sensors, 4(7), 1732-1748, 2019.

[6] Kalkal A., Kadian S., Pradhan R., Manik G. and Packirisamy G., "Recent advances in graphene quantum dot-based optical and electrochemical (bio) analytical sensors", Materials Advances, 2(17), 5513-5541, 2021.

[7] Kalpana H. M. and Prasad V. S., "Development of the invar36 thin film strain gauge sensor for strain measurement", Measurement Science and Technology, 25(6), 2014.

[8] Murray M. J., Murray J. B., Ogden H. M. and Redding B., "Dynamic temperature-strain discrimination using a hybrid distributed fiber sensor based on Brillouin and Rayleigh scattering", Optics Express, 31(1), 287-300, 2023.

[9] Khoo S. W., Karuppanan S. and Tan C. S., "A review of surface deformation and strain measurement using two-dimensional digital image correlation", Metrology and Measurement Systems, 23(3), 461-480, 2016.

[10] Liu H., Zhao X. H., Yang X. Y., Wang Y. X., Wu M., Jiang J. T., Wu G. R., Yuan K. J., Sui L. Z. and Zou B., "Piezochromic luminescence in all-inorganic core-shell InP/ZnS nanocrystals via pressure-modulated strain engineering", Nanoscale Horizons, 5(8), 1233-1239, 2020.

[11] Wang J. D., Ning H. R., Wang J., Kershaw S. V., Jing L. H. and Xiao P., "Effects of repetitive pressure on the photoluminescence of bare and ZnS-Capped CuInS2 quantum dots: implications for nanoscale stress sensors", ACS Applied Nano Materials, 5(4), 5617-5624, 2022.

[12] Yin S. F., Zhao Z. M., Luan W. L., and Yang F. Q., "Optical response of a quantum dot–epoxy resin composite: effect of tensile strain", RSC Advances, 6(22), 18126-18133, 2016.

[13] Zhao Z. M., Luan W. L., Yin S. F. and Tu S. D., "Real-time monitoring of crack propagationin metals based on quantum dots", China Mechanical Engineering, 26(17), 2374-2377, 2015.

[14] Zhang Y., Nie J. H. and Li L. J., "Piezotronic effect on the luminescence of quantum dots for micro/nano-newton force measurement", Nano Research, 11(4), 1977-1986, 2018.

[15] Ghaffarkhah A., Hosseini E., Kamkar M., Sehat A. A., Dordanihaghighi S., Allahbakhsh A., Kuur C. and Arjmand M, "Synthesis, Applications, and Prospects of Graphene Quantum Dots: A Comprehensive Review", Small, 18, 2102683, 2022.

[16] Achadu O. J. and Nyokong T., "Interaction of Graphene Quantum Dots with 4-Acetamido-2,2,6,6-Tetramethylpiperidine-Oxyl Free Radicals: A Spectroscopic and Fluorimetric Study", Journal of Fluorescence, 26(1), 283-295, 2016.

[17] Das R., Rajender G. and Giri P. K., "Anomalous fluorescence enhancement and fluorescence quenching of graphene quantum dots by single walled carbon nanotubes", Physical Chemistry Chemical Physics, 20(6): 4527-4537, 2018.

[18] Chinese Standard GB/T 2567-2021: Test methods for properties of resin casting body, Standards Press of China, Beijing, China, 2021.

[19] Carrión C., Cárdenas S., Simonet B. M. and Valcárcel M., "Quantum dots luminescence enhancement due to illumination with UV/Vis light", Chemical Communications, 35, 5214-5226, 2009.

[20] Hong G. Y., "Research progress of rare earth luminescent materials", Journal of Synthetic Crystals, 44(10), 2641-2651, 2015.

[21] Ge H. B. and Kang L., "Ductile crack initiation and propagation in steel bridge piers subjected to random cyclic loading", Engineering Structures, 59, 809-820, 2014.

[22] Chinese Standard GB/T 6398-2017: Metallic materials - Fatigue testing - Fatigue crack growth method, Standardization Administration of China, Beijing, China, 2017.

[23] Karimi B. and Ramezanzadeh B., "A comparative study on the effects of ultrathin luminescent graphene oxide quantum dot (GOQD) and graphene oxide (GO) nanosheets on the interfacial interactions and mechanical properties of an epoxy composite", Journal of Colloid and Interface Science, 493, 62-76, 2017

Advanced Steel Construction – Vol. 20 No. 2 (2024) 144–148
DOI:10.18057/IJASC.2024.20.2.6
(Special Issue: *11st International Conference on Advances in Steel Structures, ICASS'2023, Kuching, Sarawak, Malaysia*)

DIRECT ANALYSIS METHOD IN SELF-CLIMBING FORMING AND WORKING PLATFORM

Gao-Hong Ye [1], Zhi-Xiang Yu [1,*], Dong Liu [2], Huan He [1], Lin-Xu Liao [1] and Lei Zhao [1]

[1] *Southwest Jiaotong University, Chengdu, China*
[2] *HUASHI Engineering Technology (Shenzhen) Co, Ltd., Shenzhen, China*
** (Corresponding author: E-mail: yzxzrq@home.swjtu.edu.cn)*

ABSTRACT

Due to the complex connection of components and significant initial defects in the formwork structure, the utilization of a direct analysis method to design the formwork structure can effectively address the shortcomings of traditional first-order linear design methods in formwork design standards. Taking a practical engineering project as an example, a direct analysis method for the construction of a SCP structure was proposed. Based on its design results, a comparative analysis with the traditional first-order linear design method was conducted to clarify the influence of considering initial defects and second-order effects on support reaction force, deformation, and stress ratio. This provided a reference basis for the design of SCP structures. Based on the results, cross-sectional optimization was carried out on the key components of the SCP structure. Following optimization, the stress ratio distribution of the structure was found to be more reasonable, and a 25.63% reduction in steel consumption was achieved, thus demonstrating the feasibility of the direct analysis method in the design and optimization of the SCP structure.

ARTICLE HISTORY

Received: 8 April 2024
Revised: 24 May 2024
Accepted: 5 June 2024

KEYWORDS

Self-climbing forming and working platform;
Direct analysis method;
Initial defect;
Optimization

1. Introduction

Because of their high efficiency, standardization, lightweight, and other attributes, various automated formwork systems are becoming more and more in demand in the construction of high-rise buildings, which is in line with the rapid development of these structures. Self-climbing forming and working platform (SCP) is a kind of integrated hydraulic jacking formwork for core-tube structure construction. It has the advantages of high load-bearing capacity, high space utilization rate, and high personnel comfort, which can significantly accelerate the construction speed of high-rise buildings [1-2]. Due to the low number of supports and high loads, the pursuit of a superior load-to-weight ratio while ensuring safety is one of the most important design goals of SCP.

In the Chinese standards [3-5] for formwork and scaffolding, their design is mainly based on the traditional first-order linear design method. SCP is a product of the development of construction technology, which has many forms of member connection, and it is complicated to determine the calculation length coefficient of members. Moreover, the number of members is large, and it is difficult to avoid overall defects and member defects in the process of production, transportation and repeated assembly of members. Therefore, it is difficult to guarantee the calculation accuracy of the traditional design method.

The Standard for design of steel structures GB50017-2017 implemented in China in 2018 [6] introduced the direct analysis method. Compared with the first-order linear design method based on the calculation length coefficient method, the direct analysis method introduces the initial defects of the overall structure and components, considering " P-Δ-δ" Nonlinear analysis and load-bearing capacity verification of second-order structural effects do not require the use of the calculated length coefficient method for component stability analysis. However, as a non-linear analysis, this method cannot directly stack different load combinations after they are calculated separately. It is necessary to combine the loads and apply them to the structure before analysis.

Regarding the application and research of direct analysis method in various structures, Chan Siulai. et al. used NIDA software to analyze steel frame structures and found that direct analysis method is more accurate and effective than first-order design method based on computational length coefficient method [7]. Shu Ganping et al. compared the calculation results with experiments, verifying the effectiveness and reliability of the direct analysis method for structural analysis of semi-rigid connected steel frames [8]. Wang Fawu et al. further developed a direct analysis and optimization method for semi-rigid frames[9]. In addition, Ding Zhixia et al. studied the continuous collapse of structures based on direct analysis method and compared it with traditional design methods [10]. Zhao Lei et al investigated the effect of initial geometric defects on the stabilizing capacity of spanning plane trusses [11]. Yu Zheng et al analyzed the design and optimization of cable structures [12]. In past studies, the direct analysis method has been successfully applied in a variety of structures.

As a typical steel frame structure, various types of construction formwork are often designed and analyzed based on their construction in existing research [2,13-14], but no direct analysis method has been applied in their structural design.

2. Overview of the SCP structure

The SCP used for the construction of the core tube of a high-rise building is shown in Fig. 1, including machine platforms, suspension platforms, the grid beam, the lattice column frame and support frames. The structure consists of 6 levels of operation platforms along the longitudinal direction, the height of the positive platform part is 9.8m, the height of the negative platform part is 9.5m, the total height of the structure is 19.3m, and the horizontal dimension is 8m×8m. The negative platform is mainly used as the maintenance platform, the 0-level platform is the operation platform for formwork, and the +1 and +2 platforms are used for concreting, reinforcement binding, and stacking of loads.

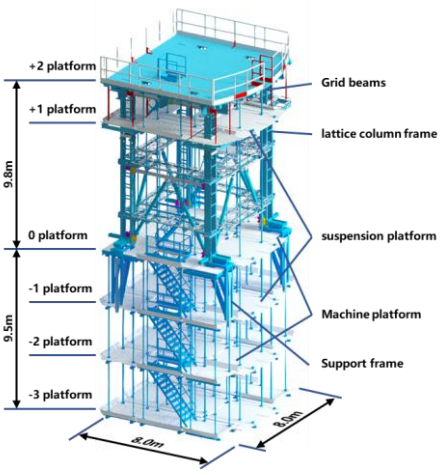

Fig. 1 SCP structure

The force transfer of the SCP structure is clear. As shown in Fig. 2, its force transmission path includes two parts. One is that each suspension platform transmits its load to the secondary beam of the +2 platform through the suspension rods, and then transmits the load to the support frame through the grid beam and the lattice column; another is each negative machine platform directly transmits the load to the 0-level machine platform through the suspension rod, and the zero-up machine platform is directly connected with the

lattice column to transmit the load to the support frame in a downward direction. Ultimately, the support frame is anchored to the core-tube by pre-embedded anchors to transfer the loads to the core-tube.

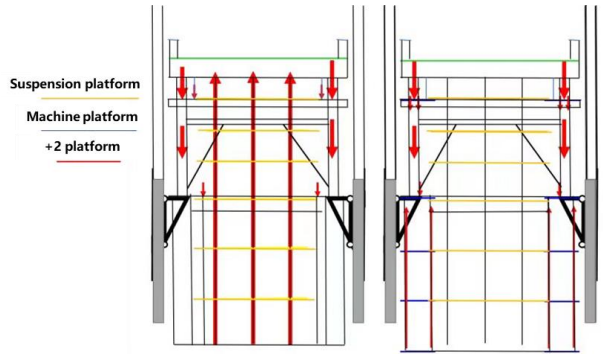

Fig. 2 Force transmission path

According to the force transmission characteristics of the structure, the lattice column frame, the grid beam and support frames are called the main frame (as shown in Fig. 3). Each platform is connected to the main frame, whose structural characteristics are shown in Fig. 4, including the main beam and secondary beam. The pivot point of the main beam is directly connected to the suspension rod or lattice column, and the secondary beam is supported on the main beam. In addition, the secondary beam of the +2 platform is responsible for transferring the load of the suspension rod and the +2 platform stacking load, and is supported on the grid beam.

Fig. 3 main frame

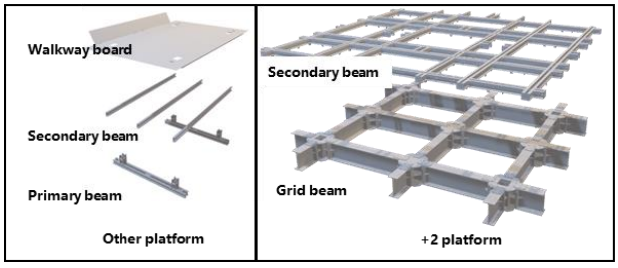

Fig. 4 Platform structure

3. Direct analysis method of SCP

3.1. Initial defects

The structural characteristics of the SCP cause its suspension platform stiffness to be very small, and its buckling mode is reflected as the lateral deformation of each suspension platform, and the consideration of the overall initial defect of the structure in accordance with the first order buckling mode is not in line with the purpose of the structural initial defects imposed. As a structure with regular shape and significant story separation, the overall initial defects can be added to the initial geometric defects representative value Δ_{ni} at the corresponding story height according to the Standard for design of steel structures (e.g., Eq. 1).

$$\Delta_{ni} = \frac{h_i}{250}\sqrt{0.2 + \frac{1}{n_s}} \tag{1}$$

In the Eq. 1, h_i is the height of the calculated floor; Δ_{ni} is the total gravity load design value for the i-th floor; n_s is the total number of layers in the structure.

The initial defect of the member is shown in Fig. 4. Considering the influence of the initial deformation and residual stress of the member, it is determined by calculating the half-cycle sine curve as shown in Equation 2. e_0 is the initial deformation at the midpoint of the member, x is the distance from the end of the member, and l is the total length of the member.

$$\delta_0 = e_0 \sin\frac{\pi x}{l} \tag{2}$$

Since the elastic-plastic development of the material is not considered, the initial deformation e_0 of the member is selected in accordance with the representative value of the integrated defects of the member in the Standard for design of steel structures.

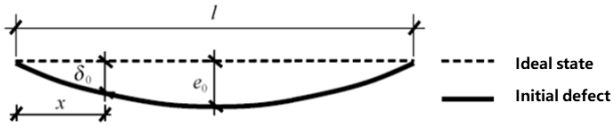

Fig. 5 Initial defect of member

3.2. Nonlinear analysis and verification

The nonlinear analysis is carried out after applying different combinations of loads to the structure. The internal forces in the members obtained from the analysis are substituted into Eq. (3) for verification.

$$\frac{N}{Af} + \frac{M_x^{ii}}{M_{cx}} + \frac{M_y^{ii}}{M_{cy}} \le 1.0 \tag{3}$$

N is the design value of axial force; A is the gross section area; f is the design value of strength of steel; M_x^{ii}, M_y^{ii} are the design value of second-order bending moment around the x-axis and y-axis, respectively; M_{cx} and M_{cy} are the design value of bending capacity around the x-axis and y-axis, respectively.

3.3. Design process

The design process of the direct analysis method is clear and concise, and there is no need to determine the calculation length coefficient one by one for the complicated members. The direct analysis method can be used for the design of the top mold structure by referring to the steps of "simplification, modeling → applying load → load combination → applying initial defects → nonlinear analysis → member strength checking".

4. Computational model

A wireframe model is established using 3D drawing software in accordance with the centerline of the members, and the primary and secondary beams are simplified from stacked to intersecting, but the loads are only applied to the secondary beams. The nodes are simplified as rigid or hinged with reference to the actual connections. The boundary conditions of the structure are shown in Fig. 5, all of which are hinged supports. The steel used in the model is Q235B.

In addition to the structure's self weight, the dead loads include those loads that can be considered permanent, such as sidewalks, handrails, stairs, formwork, and ancillary structures. The live loads refer to its working condition, which is determined by the working condition load planning of the SCP, and the live load cases are shown in Table 1. For the load combinations, the basic combination of "1.3×DL+1.5×LL" is used for the bearing capacity and bearing reaction, and the standard combination of "1.0×DL+1.0×LL" is used for the displacement calculation. These combinations are determined according to the standards.

Table 1
Working state load

Platform	Load/kN·m^{-2}
+2	5.00
+1	2.00
0	1.50
-1	0.75
-2	0.75
-3	0.75

5. Comparison between Direct Analysis and First Order Linear Analysis

NIDA has been used for direct analysis and first-order linear analysis.

5.1. Support reactions

The SCP in the example has four supports (Fig. 6), which are fixed to the core-tube, and their design is a key factor to ensure the construction safety and structural reliability, according to the basic combination of loads, the vertical support reaction force of each support is extracted as shown in Table 2.

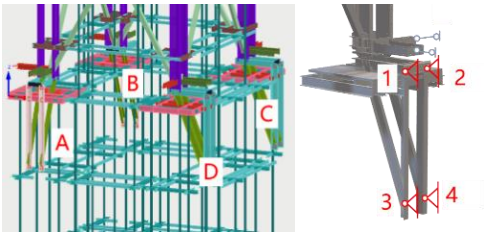

Fig. 6 Supports and its ID

Table 2
Support reaction force

ID	First-order linear analysis/kN	Direct analysis/kN	δ/%
A1	15.65	19.63	25.43
A2	25.44	25.51	0.28
A3	173.02	170.87	-1.24
A4	179.78	177.52	-1.26
B1	22.84	23.00	0.70
B2	16.89	20.69	22.50
B3	179.56	177.30	-1.26
B4	174.24	172.05	-1.26
C1	30.35	29.78	-1.88
C2	12.20	13.98	14.59
C3	184.41	183.57	-0.46
C4	176.44	176.56	0.07
D1	13.21	15.25	15.44
D2	28.25	27.73	-1.84
D3	178.76	178.66	-0.06
D4	184.70	183.63	-0.58
Total	1595.74	1595.74	0.00

Comparing the results of the first-order linear analysis and the direct analysis, the maximum support reaction force of both appeared in the D4 support, which was 184.7kN and 183.6kN, respectively, and the relative error of the two was only 0.58%; and the total support reaction forces were basically the same due to the same applied loads.

The maximum relative error was found in support A1, which reached 25%, but the absolute error was only 3.98kN, which is still small on the scale of the total support reaction force. This is the performance of the direct analysis method after considering the initial defects of the support frame members and the structure as a whole, which is the performance of the feedback to the support reaction force, and it can be seen that the use of the direct analysis method can give the design parameters of the reasonable support to the design of the support in this project.

5.2. Deformation

Comparing the displacement calculation results of the two design methods, the maximum vertical displacements obtained by the first-order linear analysis and the direct analysis are 9.80 mm and 9.82 mm, respectively, and the maximum vertical displacements are located in the cantilevered position of a suspension platform, and the displacement calculation results of the two methods are verified by each other.

5.3 Stress ratio

Fig. 7 shows the comparison of the stress ratio results between the first order linear analysis and the direct analysis method in NIDA.

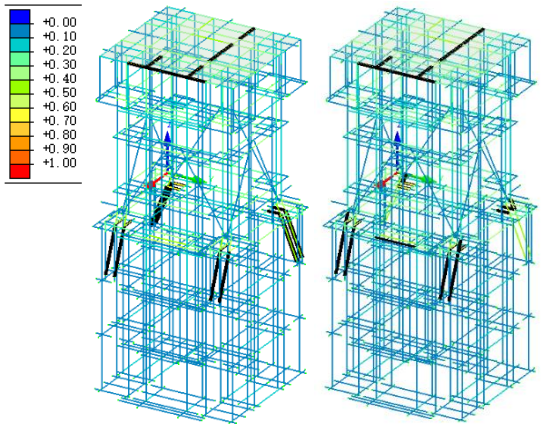

Fig. 7 Stress ratio

The maximum stress ratio for first-order linear analysis was 0.801, and the maximum stress ratio for direct analysis method was 0.799. In Fig. 7, the elements with a stress ratio greater than 0.5 were shown in black, and the elements with a greater stress ratio in both methods were the secondary beams of +2 beams, the secondary beams of 0 platform and the diagonal supports of the support frames.

The design results of direct analysis method and first-order linear analysis in NIDA were compared. After the difference between the two, the average difference in stress ratio was 0.0014. Overall, the results of the two were relatively close, with 91.1% of the unit stress ratios differing between -0.01 and 0.01. Statistics were conducted on elements with stress ratios exceeding 0.01, and a total of 119 elements with higher stress ratios were designed using the direct analysis method.

Statistics were conducted on units with stress ratios exceeding 0.01, and a total of 119 elements were found to have higher stress ratios using the direct analysis method. Among them, 64.7% were horizontal members, mainly bending members. There were a total of 52 elements with relatively low stress ratio using the direct analysis method, of which 73.1% were non-horizontal members, mainly axial and compression bending members. This is because the SCP structure is a typical vertical structural system, and the horizontal bending members increase in the increase of the initial defect design bending moment, resulting in an increase in the stress ratio. The vertically distributed members are mainly compression members, and the first-order linear analysis is more unfavorable than the actual situation due to the direct consideration according to the calculated length factor.

There were 16 elements with the difference of stress ratio greater than 0.1, as shown in Fig. 8, all of which were diagonal braces of the support frame. The diagonal bracing was divided into two elements, in which the lower, longer segments had smaller stress ratios under direct analysis, and the upper, shorter segments had larger stress ratios under direct analysis. This was due to the design value of bending moment in the compression bending member in the application of the initial defects increased significantly, the shorter element due to the compression bearing capacity verification coefficient was not significantly different, so the overall stress ratio increased, while the longer element although the design value of the bending moment increased, but due to the calculation of length coefficients were not taken into account, compression bearing capacity verification coefficient was significantly reduced, and the

overall stress ratio was reduced.

In the actual situation as the same member, the stress ratio of the upper and lower elements in the results of the direct analysis method was closer and more in line with the actual situation.

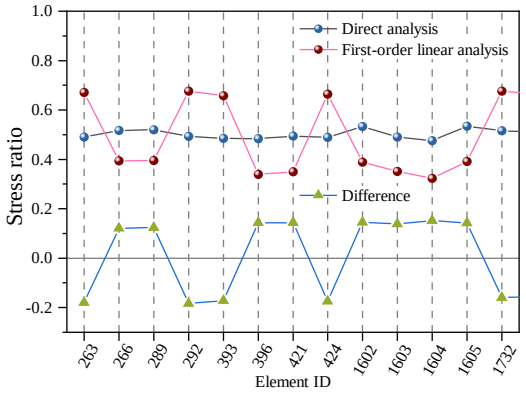

Fig. 8 Elements with stress ratio differences exceeding 0.1

6. Structural optimization

6.1. Optimization Schemes

In this example, the SCP structure has a large self-weight and most of the members have relatively low stress, so there is a large optimization space. This optimization was mainly based on cross-section optimization, and kept the cross-section type as much as possible to meet the original node connection mode, and for the convenience of assembly, the number of excessive cross-section was not increased, so as to realize the comprehensive optimization with the goal of high efficiency and light weight. By reducing the self-weight of the structure, the support reaction force can also be further reduced and the safety margin of the support anchorage point can be improved.

The cross sections of some members were optimized, and the comparison of the cross sections before and after optimization is shown in Table 3. The total weight was reduced from 35.02 tons to 26.05 tons after optimization, which was about 25.63%.

Table 3
Cross-section optimization scheme

Component	Size/Model [a]		weight loss
	Before	After	
Machine platform beams	C 20B	C 20B	-
0.5 story platform beams	C 16B	C 16B	-
Platform secondary beam	C 10	HT 100×50×3.2/4.5	40.19
Platform primary beam	2C 10	2C 100×50×4	51.59
Suspension rods	F 50×5	F 50×4	37.33
Grid beams	HM 594×302×14/23	HN 600×200×10/15	45.76
+2 story secondary beam	2C 10	2C 14B	-67.85
lattice column	C 40B	C 40A	9.60
Support frame beam	C 14B	C 14B	-
Support frame column	L 200×125×16	L 200×125×16	-
Support frame diagonal supports	C 22B	C 22B	-
Main frame diagonal supports	J 160×130×8.5/9.6	J 160×130×6/6	31.77

[a:] C: U-steel; 2C: doble U-steel; F: square tube; H: H-steel; L: L-steel; J: rectangular tube.

6.2. Optimization results

The stress ratio cloud diagram after optimization is shown in Fig. 7. The overall distribution pattern was similar to that before optimization, and the elements with stress ratios greater than 0.5 were changed to 0-story and +1-story platform beams, which were not included in main frame elements. Compared to the pre-optimization, the stress ratios of the elements of the +2 platform, the machine platform, and the main frame diagonal supports have been reduced.

The stress ratio-number of elements distribution before and after optimization is shown in Fig. 9. After reducing the amount of steel used by 25.63%, there was no significant increase in the number of high stress ratio elements, and the percentage of elements with stress ratios greater than 0.4 increased by only 4% from 2.3%, retaining a large safety margin. Due to the high number of horizontal elements, the number of elements with stress ratios less than 0.1 was reduced after optimization.

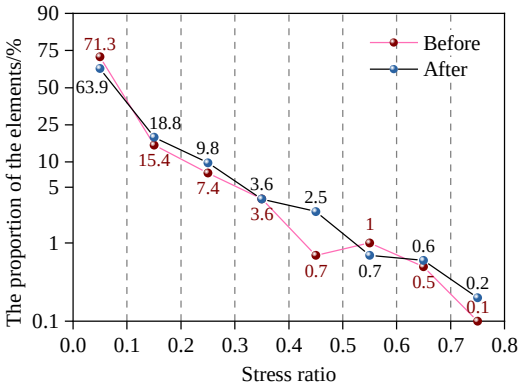

Fig. 9 Distribution of the number of elements with different stress ratios

The comparison of the main parameters before and after optimization is shown in Table 4. The stiffness decreased with the reduction of the cross section of some members, the maximum vertical displacement increased from 9.82mm to 11.74mm, and the maximum vertical displacement of the main frame increased from 3.55mm to 5.94mm, which still met the usage requirements. The vertical reaction force decreased from 1595.74kN to 1475.45kN due to the decrease in the self-weight of the structure, with a decrease of 7.54%. The maximum vertical reaction of the support still occurred at the D4 support and decreased from 183.63kN to 169.35kN, with a decrease of 7.78%. After optimization, the design value of the support load was reduced to a certain extent.

Table 4
Optimization result parameters

Parameters	Before	After
Maximum vertical displacement/mm	9.82	11.74
Maximum vertical displacement of the main frame/mm	3.55	5.94
Total vertical support reaction force/kN	1595.74	1475.45
Maximum support reaction force/kN	183.63	169.35
Maximum stress ratio	0.75	0.75

7. Conclusions

This paper introduces the direct analysis method of the top mold structure, compares it with the traditional first-order linear design method, and optimizes the structure based on this method. The following conclusions can be drawn from the data presented.

(1) The design and optimization of SCP using direct analysis method is simpler and more efficient than the first-order linear design method based on the calculation of length coefficients.

(2) The outcomes of the direct analysis are largely congruent with those of first-order linear analysis. The discrepancy is primarily attributable to the divergence in calculation methodologies between the two.

(3) In the example, by using the direct analysis method, 25.63% of the steel consumption was saved through cross-sectional optimization, while maintaining a high safety margin.

The direct analysis method is unable to fully consider the detailed construction of structural connection nodes. Consequently, it is planned to conduct node performance analysis in the future in order to obtain the semi-rigid parameters of each node. This will facilitate multi-scale optimization design.

References

[1] Sai Gaddam Mohan and Achuthan Aravindan, "A comparative study on newly emerging type of formwork systems with conventional type of form work systems", Materials Today: Proceedings 33, 736-740, 2020.

[2] Liu Dong, Fan Zhaofu, Zhang Yanzhi, Dong Jianju and Yuan Sheng, "Application of SCP Platform System in the Construction of Tower Core Tube in Xi' an International Trade Center", Construction Technology, 48(02), 67-73, 2019.
[3] Sowndharya Ar. and Vidhya Ar., "Analysing advanced formwork system for high rise building construction", International Research Journal of Modernization in Engineering Technology and Science, 4(6), 2131-2139, 2022.
[3] GB 51210-2016, Unified standard for safety of scaffold in construction, China Architecture & Building Press, Beijing, 2016.
[4] JGJ 459-2019, Technical standard for self-climbing integrated scaffolding and formwork equipment with steel platform, China Architecture & Building Press, Beijing, 2018.
[5] JGJ 195-2018, Technical standard for the hydraulic climbing formwork engineering, China Architecture & Building Press, Beijing, 2018.
[6] GB50017-2017, Standard for design of steel structures, China Architecture & Building Press, Beijing, 2017.
[7] Chan Suilai and Liu Yaopeng, "Second-order Direct Analysis for Steel Frame Structure by NIDA", Construction Technology, 41(20), 61-64+98, 2012.
[8] Ganping Shu, Liu Wei, and Chan Siulai, "Theoretical research on direct analysis method for semi-rigid steel frames", Journal of Building structure 35(08), 142-150, 2014.
[9] Wang Fawu, Liu Yaopeng, Zhou zhihua and Chan Suilai. "Optimization of semi-rigid steel frames with second-order direct analysis", Proceedings of the 9th International Conference on Advances in Steel Structures, ICASS. 10, 2018.
[10] Ding Zhixia, Liu Yaopeng, Du Zhaolei and Chan Siulai. "The application of direct analysis method in progressive collapse", Steel Construction (Chinese & English), 35(2), 13-28, 2020.
[11] Zhao Lei, Qi Xin, Zheng Tenghu, Yu Zhixiang and Xu Hu, "Influence of Initial Geometric Imperfection on the Stability Bearing Capacity of a Cross-Story Plane Truss", Progress in Steel Building Structures, 24(04), 66-73, 2022.
[12] Yu Zheng, Xue Suduo and Wang Lijun, "Application of direct analysis design method in cable structure design", Construction Technology, 48(20), 1-4, 2019.
[13] El Sayed Ahmed Yehia, Darwish Mohamed and Nassar Khaled, "Design and Constructability of Novel Extendable Arched Steel Truss Falsework", Journal of Construction Engineering and Management, 147(3), 04020187, 2021.
[14] Hong Geon-Ho and Jung Seong-Won, "Development of auto-climbing formwork system for composite core walls", Journal of Asian Architecture and Building Engineering, 21(2), 511–520, 2022.

Advanced Steel Construction – Vol. 20 No. 2 (2024) 149–159
DOI:10.18057/IJASC.2024.20.2.7
(Special Issue: *11st International Conference on Advances in Steel Structures, ICASS'2023, Kuching, Sarawak, Malaysia*)

BIFURCATION BUCKLING LOAD OF STEEL ANGLE WITH RANDOM CORROSION DAMAGE

Liang Chen [1], Jing-Zhou Zhang [2, *], Si-Wei Liu [1] and Zhi-Wei Yu [2]

[1] *Department of Civil and Environmental Engineering, The Hong Kong Polytechnic University, Hung Hom, Kowloon, Hong Kong, China*
[2] *School of Civil Engineering, Guangzhou University, Guangzhou, China*
[*] *(Corresponding author: E-mail: 205352@gzhu.edu.cn)*

ABSTRACT

This paper numerically studies the bifurcation buckling load of steel angle members affected by random corrosion pits. Six million Monte Carlo simulations are conducted, in which the effects of member length, section type, area loss ratio, and corrosion depth on the bifurcation buckling load of steel angles are considered. The key statistical characteristics of the reduction factors of buckling load for steel angles are analyzed. A probability-based relationship between the reduction factor of buckling load and the area loss ratio of steel angles is also proposed for the practical design. It is found that corrosion can potentially change the buckling mode of steel angle members from flexural buckling to torsional buckling. When the member length is small, the bifurcation buckling load of the steel angle is significantly affected by the corrosion depth. However, with the increase in member length, the effect of corrosion depth tends to decrease. The reduction factors of the buckling load of steel angles follow a normal distribution. A larger area loss ratio will result in a larger standard deviation of the reduction factors. For steel angles with the same area loss ratio, the mean values of the reduction factors of different section types are very close.

ARTICLE HISTORY

Received: 8 April 2024
Revised: 16 May 2024
Accepted: 5 June 2024

KEYWORDS

Buckling load;
Steel angle;
Random corrosion;
Monte Carlo simulation;
Area loss ratio;
Corrosion depth

1. Introduction

Steel structures will inevitably be corroded due to exposure to an aggressive environment. Corrosion weakens the strength and ductility of steel material and, meanwhile, reduces the sectional area of steel components, which results in the deterioration of steel structures. The deterioration process of steel structures is highly random and unpredictable, which reduces the safety and reliability of the structure by a great extent [1].

Currently, a considerable amount of literature can be found on the corrosion effects of steel structures. The research objects of these studies mainly include: steel material [2-5], plate [6-9], rebar [10-14], beam [15-17], column [18-24], joint [25-28], pipeline [29-32], and structure [33-37]. Zhao *et al.* [2] numerically studied the mechanical properties of Q345 steel with random corrosion pits. The reduction of the nominal ultimate strength of corroded Q345 steel was affected by both the mass loss ratio and corrosion depth. Wang *et al*. [9] studied the compression behavior of corroded steel plates, considering different pit shapes, distributions, and depths. It was found that corrosion pits will not only reduce the ultimate strength of steel plate but also change its failure mode. Zhang *et al*. [11] studied the corrosion evolution process in rebar and found that the corrosion depth followed the Poisson distribution, and the longitudinal nonuniformity factor (the ratio of average section area to the minimum one) followed the Gumbel distribution. Chen *et al*. [16] proposed an efficient algorithm to compute the elastic buckling load/moment of steel members with random corrosion pits. The results show that corrosion reduces the axial-torsional buckling load of the member with greater extent than the lateral-torsional buckling moment and flexural buckling load. Hisazumi and Kanno [24] investigated the compression behavior of corroded angle-section and channel-section steel members. The ultimate capacity of the member can be better described by the minimum section area of the member. Wang *et al*. [27] studied the cyclic performance of welded beam-to-column joints in a salt spray environment with 5% mass fraction of *NaCl* solution. When the corrosion time reached 18 months, the yield moment, ultimate moment, ultimate rotation, and total energy dissipation were decreased by 28.2%, 32.1%, 49.4%, and 70.8%, respectively. In the study by Huang *et al*. [37], the fatigue reliability of a ship welded structure with random corrosion was evaluated. Altogether 151,527,600 random corrosion pits were generated in the numerical model. The relationship between the fatigue damage of the structure and corrosion deterioration was further quantified.

From the above studies, a considerable number of conclusions have been reached with great practical value. However, there are still some shortcomings existing in current studies. First, the section types of these members are mainly I-shaped [15-18] and circular-shaped [19, 20, 30, 32]. Relevant studies on angle members are scarce. Considering that the angle section is not symmetric, the mechanism of corrosion effect on the buckling load, as well as the failure mode of the corroded member, should be more complicated compared with the members with symmetric sections [24]. Therefore, a systematic understanding of the buckling load of corroded steel angle members is necessary. Second, to sufficiently capture the random nature of corrosion pits, using commercial finite element analysis software is cumbersome and time-consuming to ensure a sufficient number of Monte Carlo simulations. Therefore, an efficient algorithm is required to study the effect of random corrosion pits on steel members.

This paper numerically studies the bifurcation buckling load of steel angle members with random corrosion pits. Six million Monte Carlo simulations are conducted, in which the effects of member length, section type, area loss ratio, and corrosion depth on the bifurcation buckling load of steel angles are studied. The key statistical characteristics of the reduction factors of buckling load for steel angles are analyzed. A probability-based relationship between the reduction factor of buckling load and the area loss ratio of steel angles is also proposed. This paper is divided into seven sections. After this Introduction, analytical calculations of the buckling loads for steel angle members are introduced in Section 2. The simulation of random corrosion pits is illustrated in Section 3. A flowchart to compute the buckling load of steel angles with random corrosion pits is given in Section 4. Verification of the proposed algorithm is conducted in Section 5. Parametric studies of the buckling loads of corroded steel angle members are conducted in Section 6. The main findings and conclusions from this paper are summarized in Section 7.

2. Bifurcation buckling load

For steel angle members in compression, typical buckling modes are shown in Fig. 1 [38, 39]. Note that the local plate buckling mode is not considered in this study. The section has the smallest and largest bending rigidity about *V*- and *W*-axis, respectively.

The bifurcation buckling load of the compressed steel members with simply supported boundary conditions can be obtained by solving the following equation [40, 41]:

$$P_{cr}^3(r^2 - v_s^2 - w_s^2) - P_{cr}^2[(P_v + P_w + P_r)r^2 - P_w v_s^2 - P_v w_s^2] + P_{cr} r^2 (P_v P_w + P_w P_r + P_r P_v) - (P_v P_w P_r r^2) = 0 \quad (1)$$

wherein P_{cr} is the bifurcation buckling load of the steel member in compression. P_v and P_w are the flexural buckling load of the member about the *V*- and *W*-axis, respectively. P_r is the torsional buckling load of the member. P_v, P_w and P_r are given by [41]:

$$P_v = \frac{\pi^2 E I_v}{L^2} \quad (2)$$

$$P_w = \frac{\pi^2 EI_w}{L^2} \tag{3}$$

$$P_r = \frac{GJ + \pi^2 EI_\omega / L^2}{w_s^2 + v_s^2 + (I_w + I_v)/A_0} \tag{4}$$

wherein E and G are the Young's modulus and shear modulus of steel, respectively. A_0 is the section area. L is the member length. J is the section torsional rigidity. I_v and I_w are the section moment of inertia about V- and W-axis, respectively. I_ω is the section warping constant. w_s and v_s are the w- and v-coordinate of section shear center, respectively. Detailed calculations of these parameters can be found in Ref. [41].

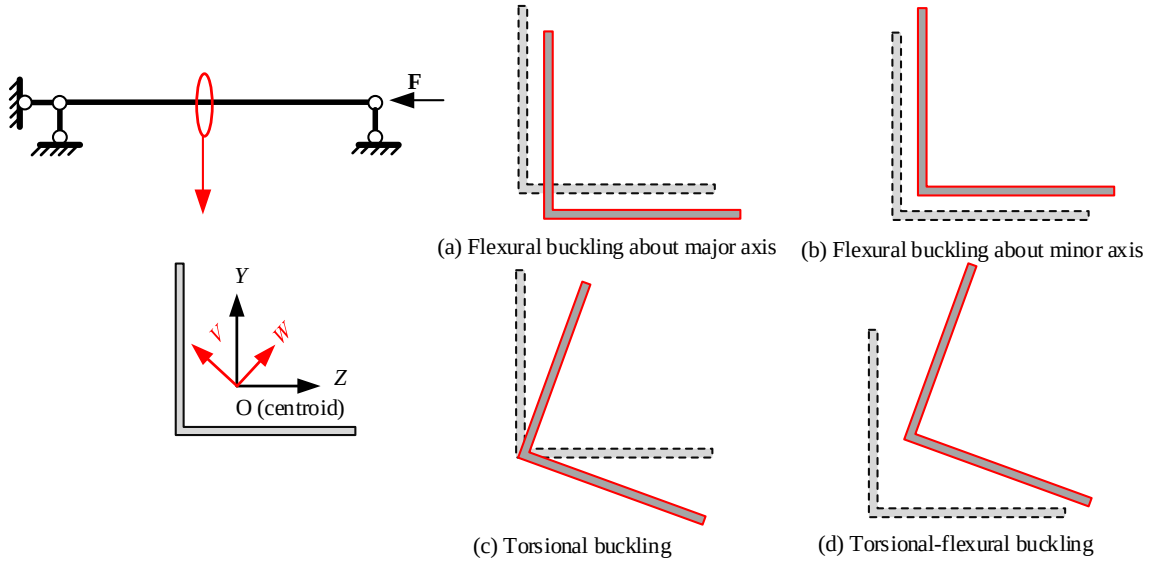

Fig. 1 Typical buckling modes of steel angle member in compression

3. Simulation of corrosion pits

Fig. 2 shows the simulation of random corrosion pits on the section. H and W represent the length of the two legs and t is the thickness of the intact section. The section is initially meshed into several line segments, with mesh size of l_s=1 mm. t_d is the corrosion depth, and the corrosion damage is considered by reducing the segment thickness by the value of t_d. For simplicity, the thickness of each damaged segment is assumed to be identical.

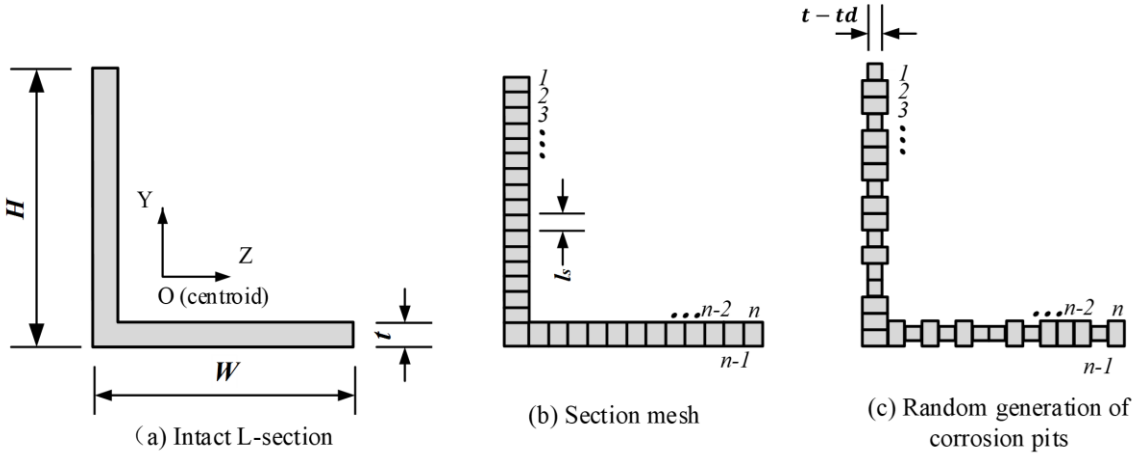

Fig. 2 Modeling of random corrosion pits

The total number of damaged segments n_d can be computed by:

$$n_d = \frac{A_0 \eta_A}{l_s t_d} = \frac{t N_0 \eta_A}{t_d} \tag{5}$$

wherein A_0 and η_A are the section area and section area loss ratio, respectively. N_0 is the total segment number (including both the intact and damaged segments).

In Equation (5), once the corrosion depth and section area loss ratio is known, the total number of damaged segments at the section can be determined. In this study, the considered values for the corrosion depth and section area loss ratio are 0.2-0.9 times the section thickness and 10%-50%, respectively. The details are summarized in Table 1. After the total number of damaged segments is determined, the corrosion pits are randomly generated at different locations on the section by Monte Carlo simulation. Then the section parameters in Equations. (2)-(4) can be computed and the bifurcation buckling load of the member P_{cr} in Equation (1) can be solved.

Table 1
Considered values of corrosion depth and section area loss ratio

Area loss ratio η_A	Corrosion depth t_d
10%	0.2t, 0.3t, 0.4t, 0.5t, 0.6t, 0.7t, 0.8t, 0.9t
20%	0.3t, 0.4t, 0.5t, 0.6t, 0.7t, 0.8t, 0.9t
30%	0.4t, 0.5t, 0.6t, 0.7t, 0.8t, 0.9t
40%	0.5t, 0.6t, 0.7t, 0.8t, 0.9t
50%	0.6t, 0.7t, 0.8t, 0.9t

4. Flowchart

The flowchart for calculating the bifurcation buckling load of a corroded steel angle member is illustrated in Fig. 3. The section area loss ratio and corrosion depth are firstly assigned. Then the total number of corrosion pits is calculated, and the corrosion pits are generated randomly at the section. Subsequently, section key parameters J, I_v, I_w, w_s, v_s, and I_o in Equations (2)-(4) are calculated, and the bifurcation buckling load of the member can be determined. The sample size of the Monte Carlo simulation is set to be 5000 for a given total number of corrosion pits. The reasonability of this value will be verified in Section 6. All the values of the section area loss ratio and corrosion depth are traversed by the algorithm. The bifurcation buckling loads of the members in each Monte Carlo simulation are exported.

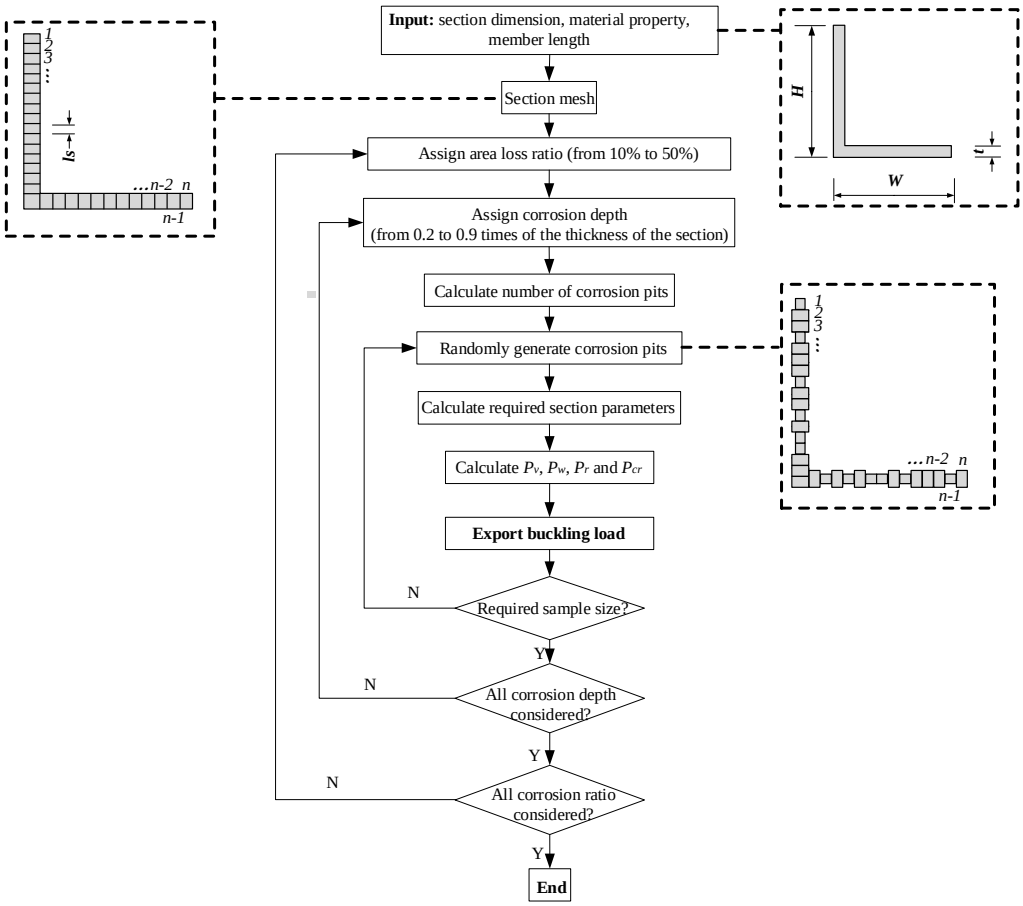

Fig. 3 Flowchart for determining the buckling loads of steel angle member with random corrosion pits

5. Verification

The software MASTAN2 [42] is used to verify the reliability and accuracy of the proposed algorithm. MASTAN2 is an educational structural analysis software. The bifurcation buckling loads from MASTAN2 and proposed algorithm for simply supported angle member are compared. Ten values of member length are considered, from 0.5 m to 5 m, with an interval of 0.5 m. Four section types are studied, as shown in Fig. 4. Section A is an intact section. Sections B, C and D are corroded sections, with area loss ratio of 10%. The comparisons of the buckling load from MASTAN2 and proposed algorithm are shown in Fig. 5. The error is calculated by:

$$\text{Error (\%)} = \frac{P_{cr-proposed} - P_{cr-MASTAN2}}{P_{cr-MASTAN2}} \tag{6}$$

wherein $P_{cr\text{-}proposed}$ and $P_{cr\text{-}MASTAN2}$ are the bifurcation buckling load from proposed algorithm and MASTAN2, respectively.

It can be seen that satisfactory agreements have been achieved between the results from the proposed algorithm and MASTAN2. The errors of the proposed algorithm are generally within 2%. The largest error of 4% occurs for section D when the member length is 1 m. By comparing Fig. 5(b), (c), and (d), it is also found that the buckling loads of the member with sections B, C, and D are very close. For example, for the member length of 2.5 m, 3m, and 3.5 m, the buckling loads of the member with sections B, C, and D are about 200 kN, 150 kN, and 100 kN, respectively.

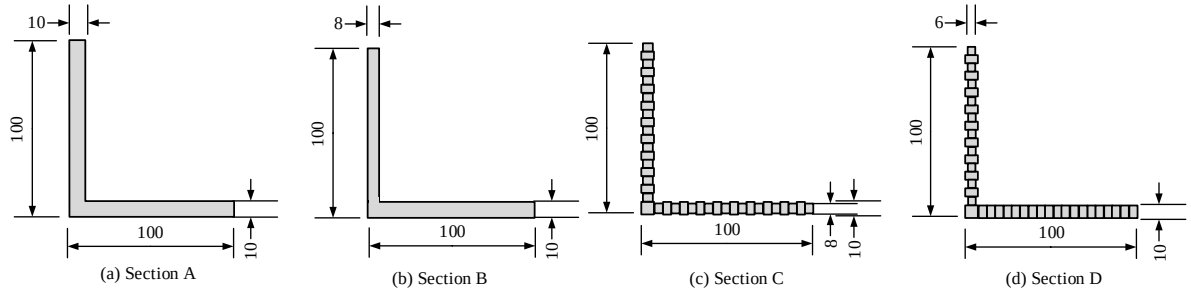

Fig. 4 Sections selected for verification of the algorithm

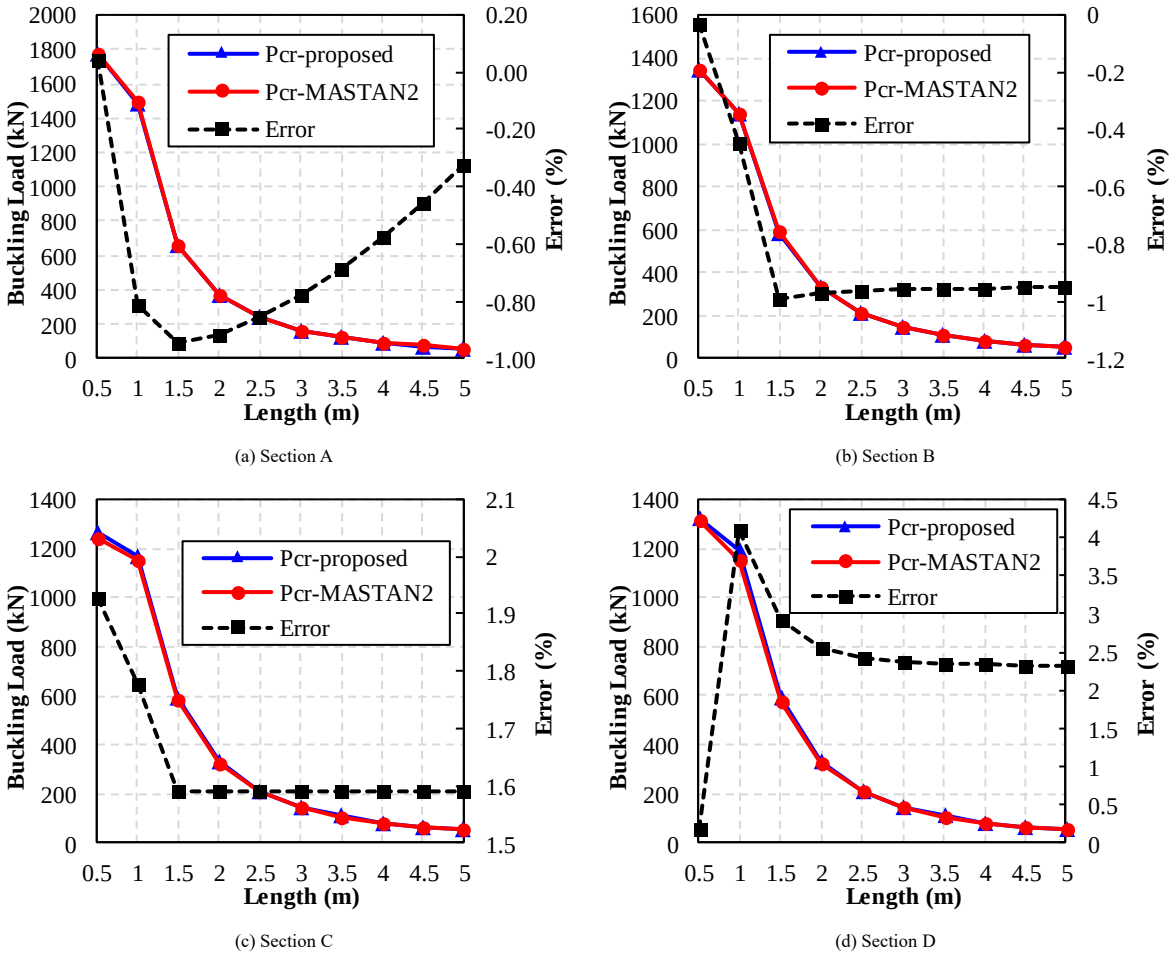

(a) Section A (b) Section B

(c) Section C (d) Section D

Fig. 5 Validation of the proposed algorithm

6. Bifurcation buckling load assessment

A total of six million Monte Carlo simulations are conducted to study the bifurcation buckling load of corroded steel angles. The considered variables include the member length, section dimension, area loss ratio, and corrosion depth. The values of section area loss ratio and corrosion depth are presented in Table 1. Five sections are selected from the code of Structural Steel Equal and Unequal Leg Angles [43], three of which are equal leg angles, and two are unequal leg angles. For each section, eight values of member length are considered. The details are given in Table 2. A convergence study is firstly conducted to determine a reasonable sample size of Monte Carlo simulation in each corrosion scenario, considering both the efficiency and accuracy of the algorithm. After computation, the buckling curves of corroded steel angle members are exhibited. The effects of the area loss ratio and corrosion depth on the buckling load of steel angle are analyzed. Moreover, the relationship between the reduction factor and the area loss ratio of the corroded steel angle is studied.

Table 2
Details of section dimension and member length

Section (mm)	I_y (cm^4)	I_z (cm^4)	i_y (cm)	i_z (cm)	Member length (m)
L100×100×12	207	207	3.02	3.02	0.5, 1, 1.5, 2, 2.5, 3, 3.5, 4
L150×150×18	1050	1050	4.54	4.54	0.75, 1.5, 2.25, 3, 3.75, 4.5, 5.25, 6
L200×200×24	3330	3330	6.06	6.06	1, 2, 3, 4, 5, 6, 7, 8
L150×100×12	233	651	2.85	4.76	0.5, 1, 1.5, 2, 2.5, 3, 3.5, 4
L200×100×12	247	1440	2.67	6.43	0.5, 1, 1.5, 2, 2.5, 3, 3.5, 4

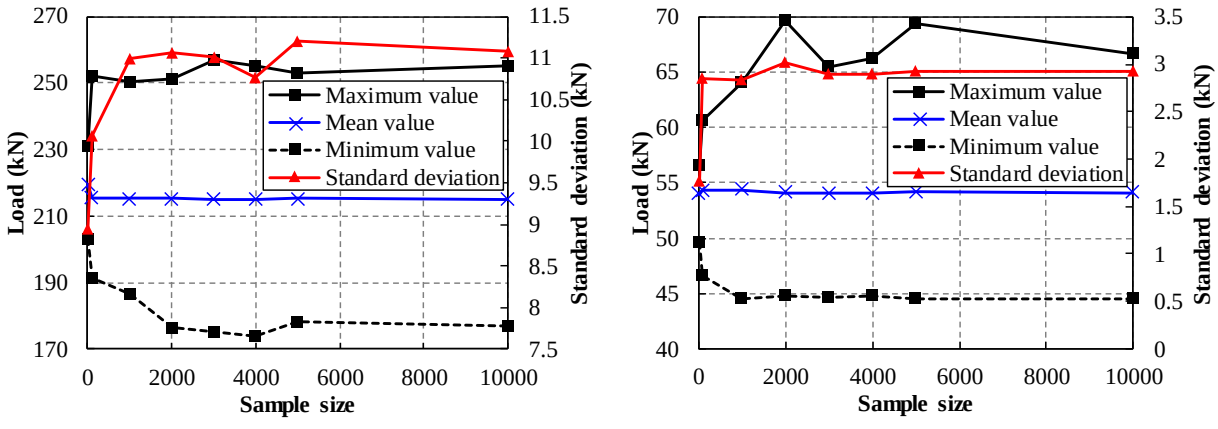

(a) P_w (b) P_v

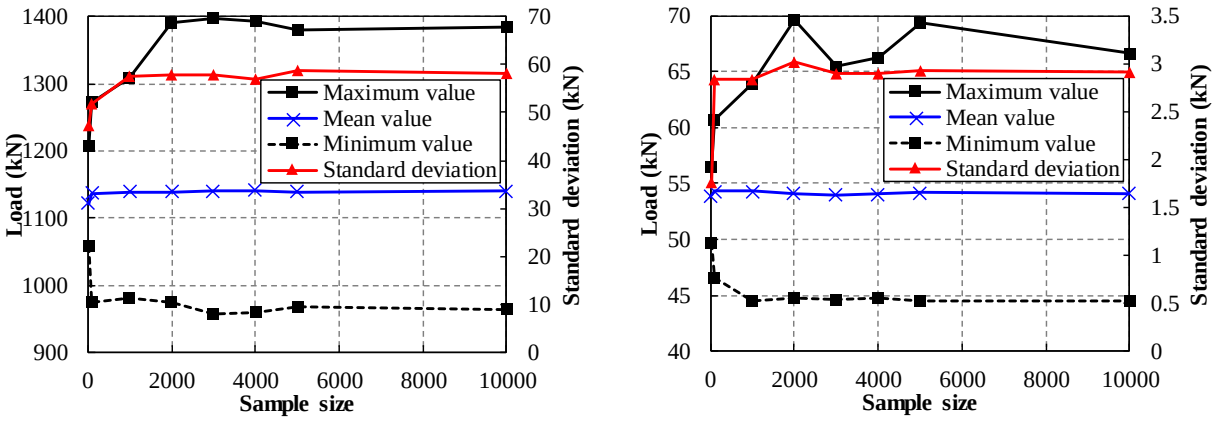

(c) P_r (d) P_{cr}

Fig. 6 Convergence study of Monte Carlo simulation

6.1. Sample size of Monte Carlo simulation

The steel angle member with the section of L100×100×12 and length of 4 m is selected to analyze the convergence of the Monte Carlo simulation. The section area loss ratio and corrosion depth are 50% and 9.6 mm (80% of the section thickness), respectively. The total number of corrosion pits in the section can be calculated by Equation (5), which is 125. Eight values of sample size are studied in the convergence analysis: 10, 100, 1000, 2000, 3000, 4000, 5000, and 10000. The results of buckling loads P_w, P_v, P_r, and P_{cr} in the convergence study are shown in Fig. 6. In these figures, the values of maximum, minimum, mean, and standard deviation of the buckling load for each sample size are presented. It can be seen that the sample size has a limited effect on the mean value of the buckling load of the member, while it has a relatively significant effect on the minimum, maximum, and standard deviation value of the buckling load. With the increase in the sample size, the minimum value of the buckling load decreases. The maximum and standard deviation values of the buckling load increase with the increase in the sample size. However, all the values tend to be stable when the sample size of the Monte Carlo simulation reaches 5000. Therefore, considering both the computational accuracy and cost, in the following study, the sample size of Monte Carlo simulation for a given area loss ratio and corrosion depth is designated to be 5000.

6.2. Buckling curve

Fig. 7 shows the lower bound of buckling curves of steel angle L200×100×12, in which Fig. 7(a) is for intact steel angle and Fig. 7(b)-(d) are for corroded steel angles with an area loss ratio of 50%. The legend name "$P_{crLowerB}$" refers to the lower bound of bifurcation buckling load P_{cr} of corroded steel angles. The corrosion depth for Fig. 7(b), Fig. 7(c) and Fig. 7(d) are 60%, 70%, and 80% of the section thickness, respectively. It can be seen from Fig. 7 that the bifurcation buckling load of the steel angle is always upper-bounded by the torsional buckling load P_r and flexural buckling load P_v. In Fig. 7(a), for the member length of 2 m, the flexural buckling load P_v is smaller than the torsional buckling load P_r, indicating that the buckling mode of the member is governed by the flexural buckling. In Fig. 7(b), however, for the member length of 2 m, the flexural buckling load P_v is greater than the torsional buckling load P_r, which suggests that the buckling mode of steel angle member will possibly be changed from flexural buckling to torsional buckling due to corrosion. Moreover, by comparing Fig. 7(b)-(d), it can be concluded that when the member length is small, even for a same area loss ratio, the bifurcation buckling load P_{cr} of steel angle can be significantly different due to the difference of corrosion depth. For example, in Fig. 7(b), for the member length of 0.5 m, the buckling load P_{cr} of steel angle with a corrosion depth of 60% is 320 kN, while it increases to 400 kN and 470 kN when the corrosion depth increases to 70% and 80%, respectively. However, with the increase in member length, the effect of corrosion depth on P_{cr} tends to decrease. For the member length of 2 m, the values of P_{cr} are all about 200 kN in Fig. 7(b)-(d). This is because when the member length increases, the bifurcation buckling load P_{cr} of the steel angle will be governed by the flexural buckling load, which is not significantly affected by the corrosion depth [16].

The lower bound of buckling curves of steel angle L150×100×12 is shown in Fig. 8. It can be observed from Fig. 7(b) and Fig. 8(b) that when the member length is relatively small, the bifurcation buckling load of steel angle L150×100×12 is greater than that of L200×100×12. This is because the section L200×100×12 is more asymmetric compared with section L150×100×12 and a more asymmetric section will result in a lower torsional buckling load of the steel angle. However, when the member length increases to more than 3 m, the bifurcation buckling load of the steel angle L150×100×12 becomes smaller than that of L200×100×12. Similar to Fig. 7, a change of the buckling mode of steel angle due to corrosion can also be observed in Fig. 8, *e.g.,* from Fig. 8(b) and Fig. 8(d), when the member length is 1.5 m, the buckling mode of the steel angle is governed by torsional buckling mode and flexural buckling mode, respectively.

To further quantify the effects of corrosion on the buckling loads of the steel angles, a reduction factor is defined, which is calculated by the ratio of the buckling load of the corroded steel angles to that of the intact steel angles. The reduction factors of the buckling loads of steel angle L200×100×12 and L150×100×12 with a length of 4 m are shown in Fig. 9(a) and Fig. 9(b), respectively. It is found that corrosion has the most detrimental effect on the torsional buckling load P_r of steel angles. When the area loss ratio reaches 50%, the buckling load P_{cr} and P_r of the steel angles decrease by more than 60% and 80%, respectively.

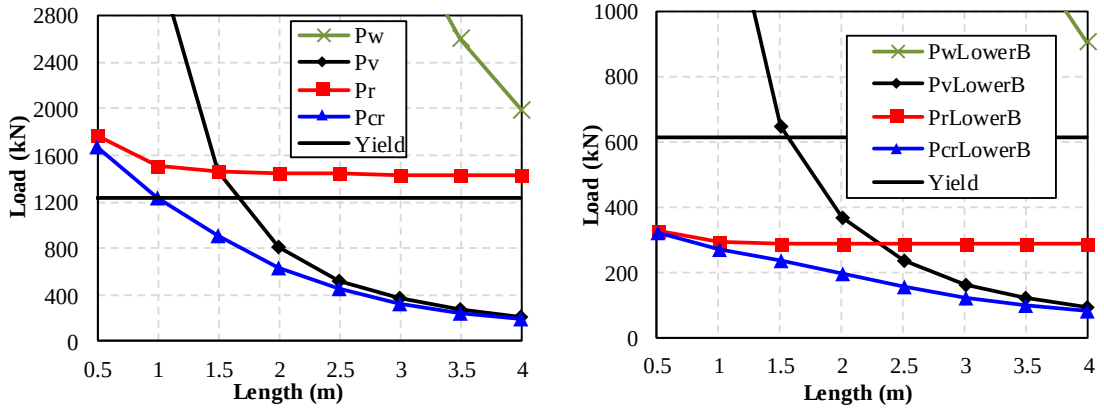

(a) Area loss ratio =0% and corrosion depth =0% (b) Area loss ratio =50% and corrosion depth =60%

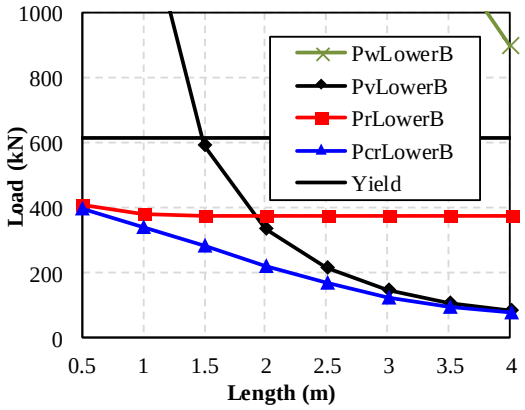

(c) Area loss ratio =50% and corrosion depth =70%

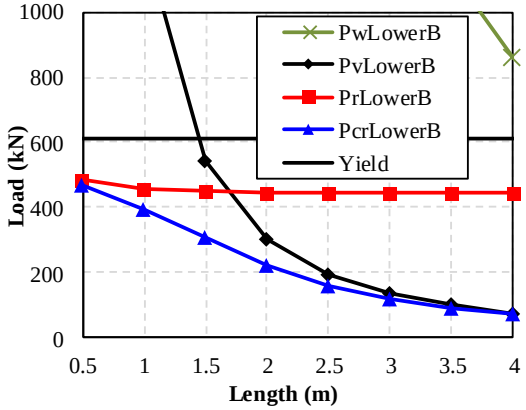

(d) Area loss ratio =50% and corrosion depth =80%

Fig. 7 Lower bound of buckling curve of steel angle L200×100×12

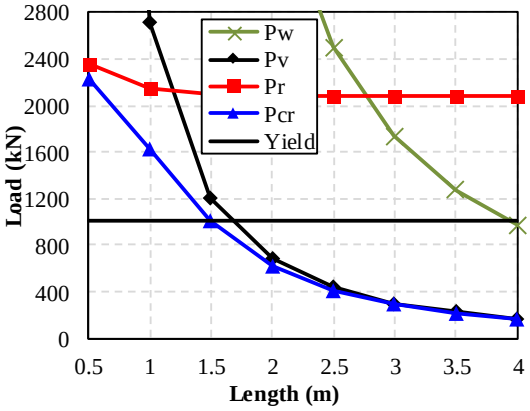

(a) Area loss ratio =0% and corrosion depth =0%

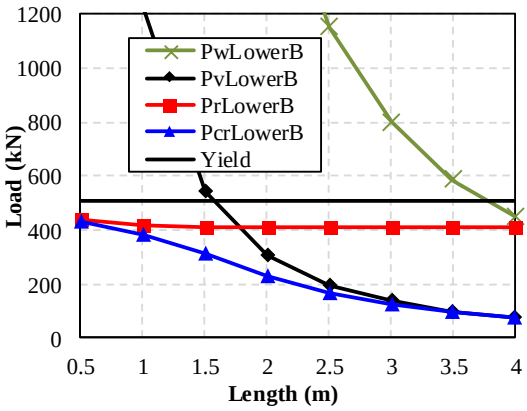

(b) Area loss ratio =50% and corrosion depth =60%

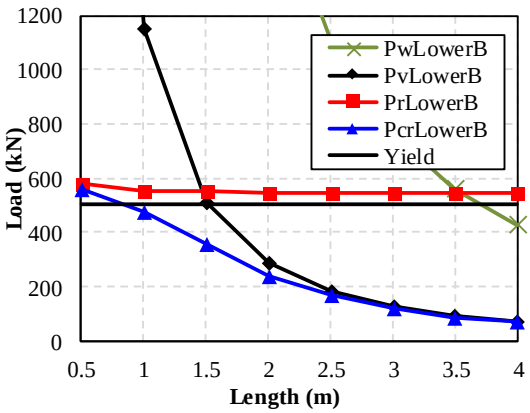

(c) Area loss ratio =50% and corrosion depth =70%

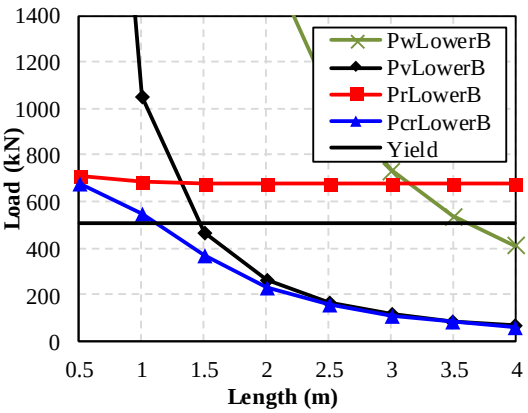

(d) Area loss ratio =50% and corrosion depth =80%

Fig. 8 Lower bound of buckling curve of steel angle L150×100×12

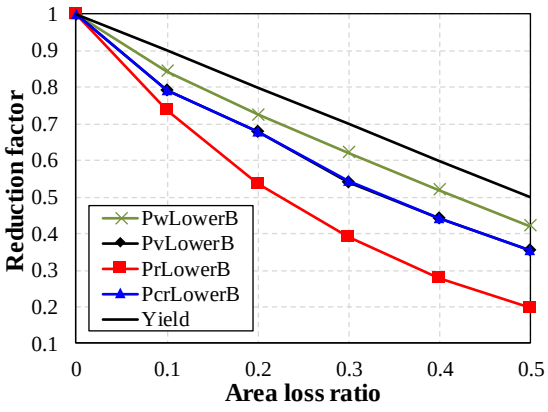

(a) L200×100×12

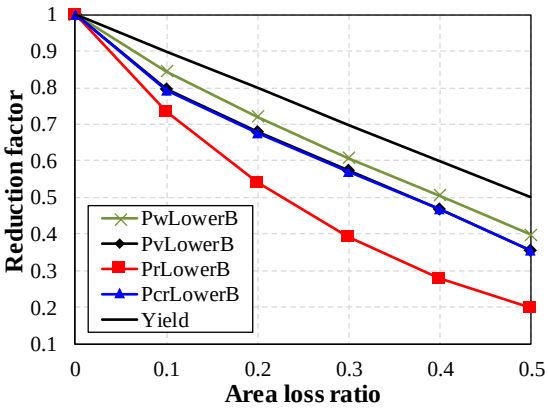

(b) L150×100×12

Fig. 9 Reduction factors of different buckling loads for member with length of 4 m

6.3. Effect of area loss ratio and corrosion depth

The effects of the area loss ratio on the bifurcation buckling load P_{cr} of steel angle L100×100×12 and L200×200×24 are shown in Fig. 10(a) and (b), respectively. The legend names "ALR" and "CD" refer to the section area loss ratio and corrosion depth, respectively. It has been found that a larger area loss ratio will result in a greater variation of the reduction factor. For instance, the reduction factor of the steel angle L100×100×12 ranges from 0.2-0.45 for the area loss ratio of 50%. However, the reduction factor ranges from 0.63 to 0.72 for the area loss ratio of 20%. When the member length increases, the reduction factor of buckling load P_{cr} tends to be a constant value. For the steel angle L100×100×12, when the member length is 4 m and corrosion depth is 60%, the reduction factor of the buckling load P_{cr} is about 0.72, 0.63, 0.52, and 0.46, corresponding to the area loss ratio of 20%, 30%, 40%, and 50%, respectively. The values of reduction factors for steel angle L200×200×24 in Fig. 10(b) are very close to those in Fig. 10(a).

The effects of corrosion depth on the buckling load P_{cr} of steel angle L100×100×12 and L200×200×24 are shown in Fig. 11(a) and (b), respectively. It is found that a smaller corrosion depth ratio will result in a greater variation of the reduction factor. For instance, the reduction factor of steel angle L100×100×12 ranges from 0.2-0.45 for the corrosion depth of 50%. However, the reduction factor ranges from 0.35-0.4 for the corrosion depth of 90%. It is interesting to note that a smaller corrosion depth will result in a smaller reduction factor for the member length of 0.5 m, but a larger reduction factor for the member length of 4 m. This phenomenon can also be discovered in Fig. 7 and Fig. 8. For the steel angle L100×100×12, when the member length is 4 m, and the area loss ratio is 50%, the reduction factor of the buckling load P_{cr} is about 0.45, 0.43, 0.42, and 0.4, corresponding to the corrosion depth of 60%, 70%, 80%, and 90%, respectively. The values of reduction factors for steel angle L200×200×24 in Fig. 11 (b) are very close to those in Fig. 11 (a)

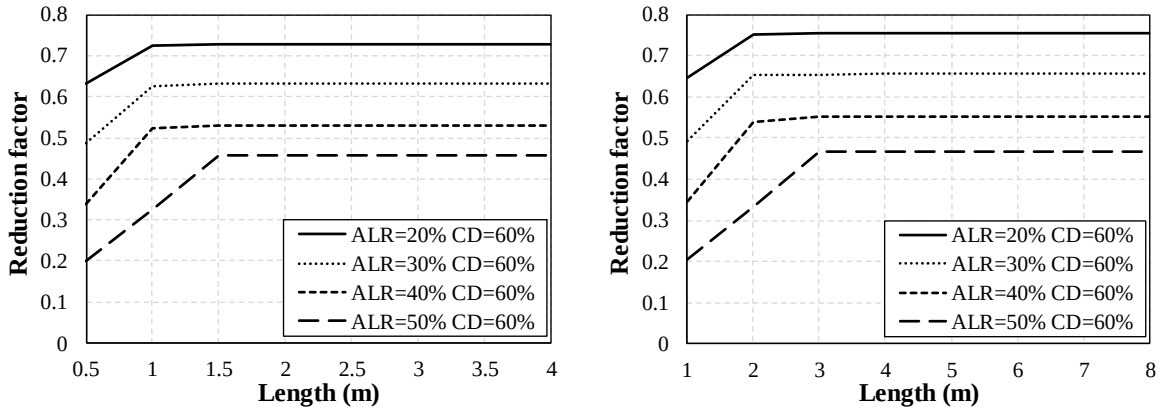

(a) L100×100×12 (b) L200×200×24

Fig. 10 Effect of area loss ratio on lower bound of buckling load P_{cr}

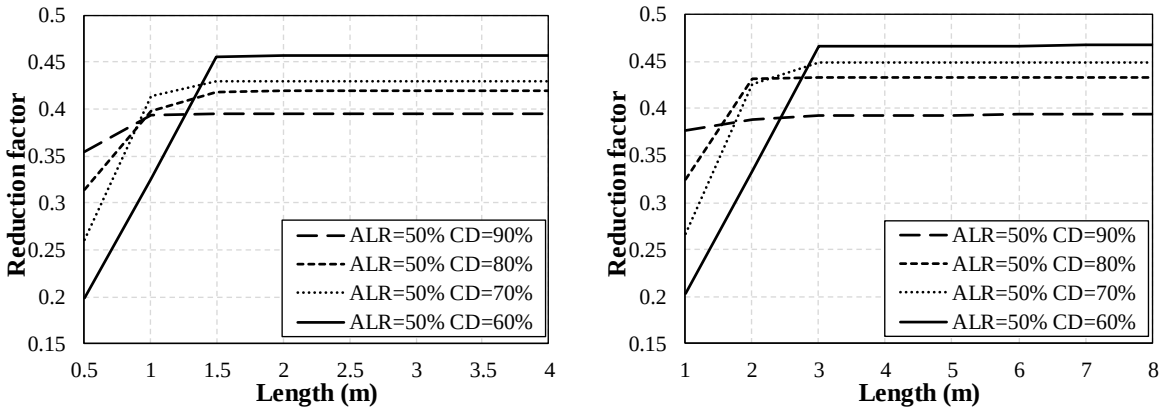

(a) L100×100×12 (b) L200×200×24

Fig. 11 Effect of corrosion depth on lower bound of buckling load P_{cr}

6.4. Discussion on the reduction factor

In Sections 6.2 and 6.3, only the lower bounds of the reduction factor of buckling load for steel angles are analyzed. To further study the corrosion effects on the buckling loads of steel angles, some key statistical characteristics, such as the mean value, standard deviation, and distribution of the reduction factors of buckling load P_{cr} from each Monte Carlo simulation are calculated. A probabilistic relationship between the reduction factor and area loss ratio is also established. The mean value and standard deviation of the reduction factor are shown in Table 3. Note that the total number of Monte Carlo simulations for a certain area loss ratio has considered the variations of corrosion depth. For example, for the area loss ratio of 10%, the possible corrosion depth can be 0.2t, 0.3t, 0.4t, 0.5t, 0.6t, 0.7t, 0.8t, and 0.9t (shown in Table 1). For each corrosion depth, the sample size of the Monte Carlo simulation is 5,000. Therefore, the total number of the Monte Carlo simulations for the area loss ratio of 10% is 40,000.

It can be seen that the mean values of the reduction factors of steel angles are about 0.9, 0.8, 0.7, 0.6, and 0.5 for the area loss ratio of 0.1, 0.2, 0.3, 0.4, and 0.5, respectively. The section type has a limited effect on the mean values of the reduction factors. However, the standard deviations of the reduction factors are affected by the section type. The section with larger asymmetry has a greater standard deviation of reduction factors. For example, for the area loss ratio of 50%, the standard deviation of reduction factors of steel angle L200×100×12 is 0.031, while the standard deviation of reduction factors of steel angle L200×200×24 is 0.0171. Moreover, a larger area loss ratio will also result in a larger standard deviation of reduction factors.

The probability density functions (PDFs) of the reduction factor for different steel angles are shown in Fig. 12. Take Fig. 12(a) as an example, the PDF is obtained as follows. For the area loss ratio of 10%, there are 40,000 values of reduction factors of the buckling load P_{cr}. The minimum value, maximum value, and range of these reduction factors are firstly determined. Then the range of reduction factors are divided into 25 intervals. For each interval, the number of reduction factors within this interval is determined, and the PDF can be calculated. For other area loss ratios, the PDF can be obtained in a similar way.

From the shape of the PDF for the reduction factors of buckling load P_{cr}, it can be found that the reduction factors generally obey a normal distribution. With the increase in area loss ratio, the shape of the PDF becomes wider and

shorter, indicating a greater standard deviation of the reduction factor. Fig. 13 compares the actual PDF and the PDF of normal distribution for the reduction factors of steel angle L100×100×12. Note that the PDF of reduction factors following the normal distribution can be determined once the actual mean value and standard deviation are known. The mean value and standard deviation of the reduction factors of buckling load P_{cr} for each steel angle are summarized in Table 3. It can be concluded from Fig. 13 that the normal distribution can reliably capture the characteristic of the distribution of the reduction factors.

Table 3
Mean value and standard deviation of the reduction factor of buckling load P_{cr}

Section	Area loss ratio	Total number of Monte Carlo simulation	Mean value μ	Standard deviation σ
L100×100×12	0.1	40,000	0.9019	0.0139
	0.2	35,000	0.8016	0.0189
	0.3	30,000	0.7029	0.0221
	0.4	25,000	0.6018	0.0239
	0.5	20,000	0.5029	0.0251
L150×150×18	0.1	40,000	0.9005	0.0114
	0.2	35,000	0.8005	0.0153
	0.3	30,000	0.7019	0.0178
	0.4	25,000	0.6009	0.0194
	0.5	20,000	0.502	0.0199
L200×200×24	0.1	40,000	0.9006	0.0098
	0.2	35,000	0.8007	0.0132
	0.3	30,000	0.7015	0.0152
	0.4	25,000	0.6011	0.0164
	0.5	20,000	0.5014	0.0171
L150×100×12	0.1	40,000	0.8992	0.0161
	0.2	35,000	0.7973	0.0218
	0.3	30,000	0.6964	0.0248
	0.4	25,000	0.5941	0.0264
	0.5	20,000	0.4939	0.0271
L200×100×12	0.1	40,000	0.895	0.0179
	0.2	35,000	0.7903	0.0242
	0.3	30,000	0.6875	0.0283
	0.4	25,000	0.583	0.0307
	0.5	20,000	0.4814	0.031

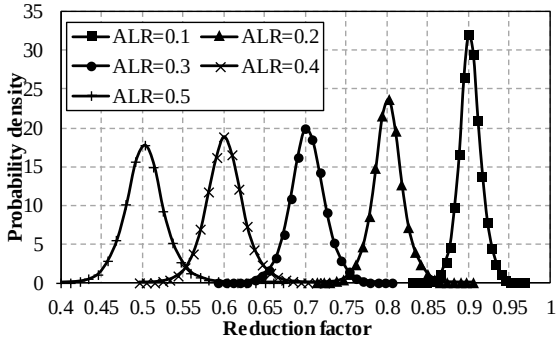

(a) L100×100×12

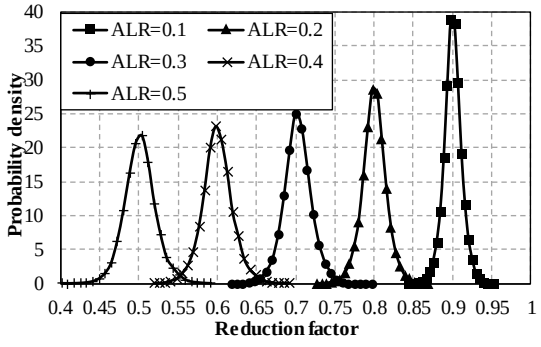

(b) L150×150×18

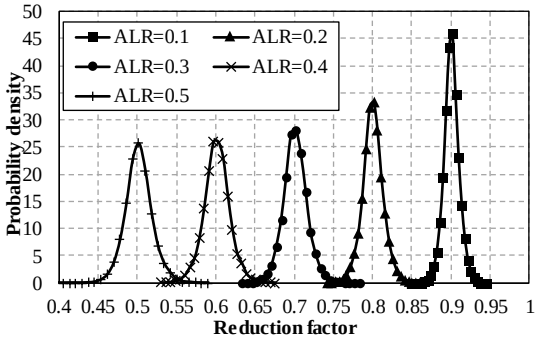

(c) L200×200×24

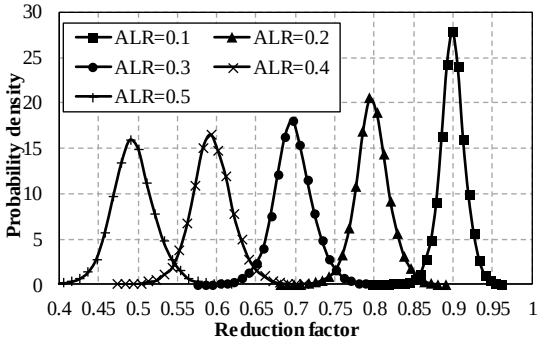

(d) L150×100×12

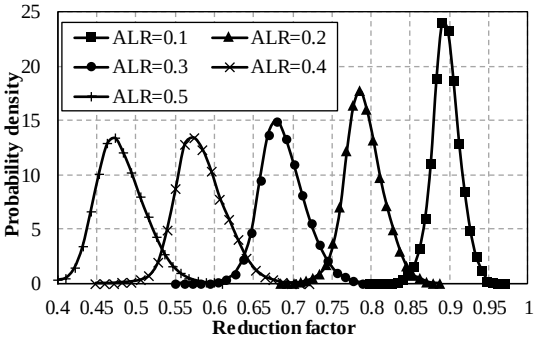

(e) L200×100×12

Fig. 12 Distribution of the reduction factor of buckling load P_{cr}

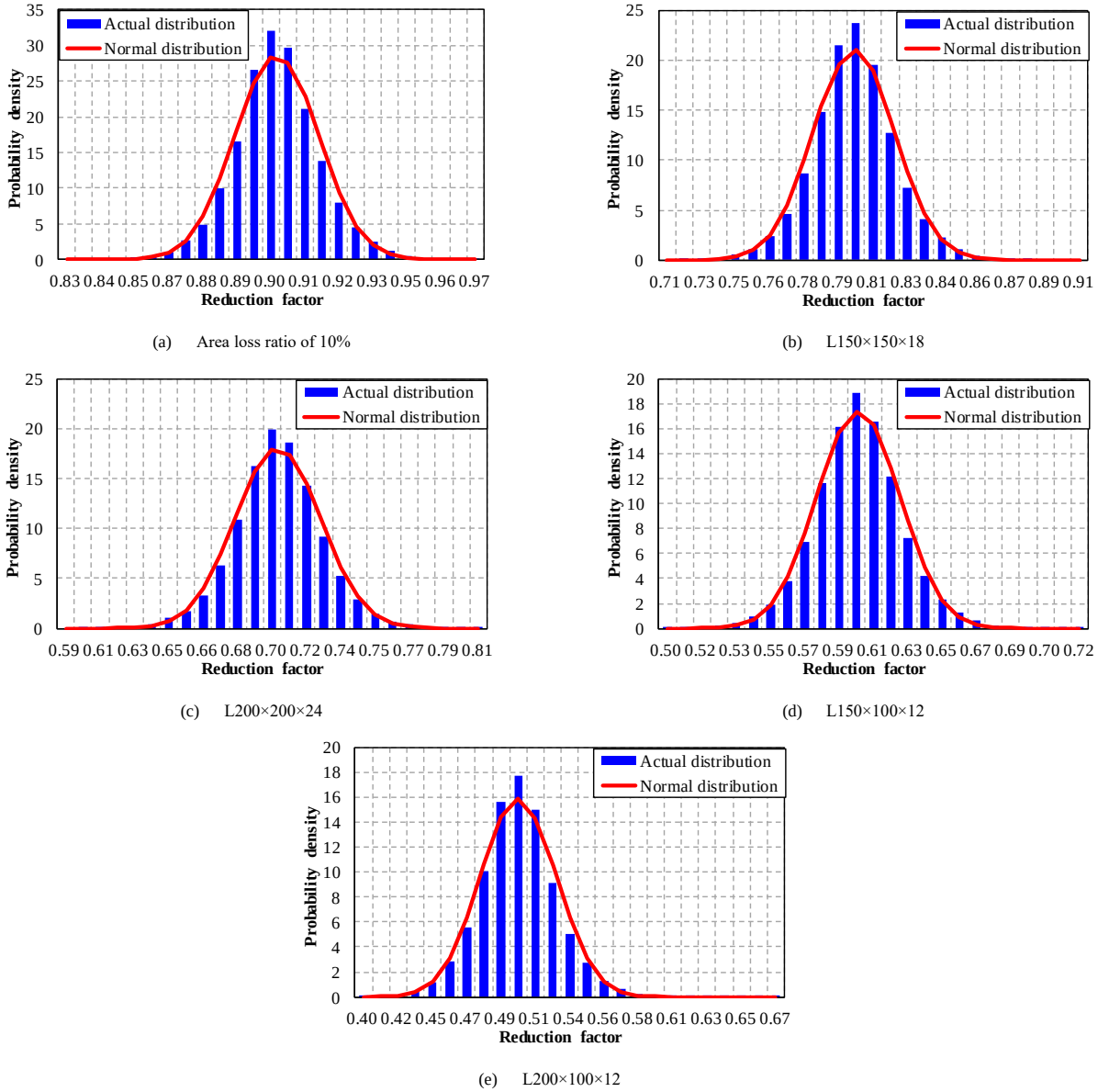

(a) Area loss ratio of 10%

(b) L150×150×18

(c) L200×200×24

(d) L150×100×12

(e) L200×100×12

Fig. 13 Goodness of fit test of the reduction factor for steel angle L100×100×12

6.5. Practical design method

Based on the results of parametric studies, a probabilistic relationship between the reduction factor of buckling load and area loss ratio for steel angle is established, as shown in Fig. 14. Note that the reduction factors for all steel angles are included in Fig. 14. Therefore, for area loss ratios of 0.1, 0.2, 0.3, 0.4, and 0.5, there are 200000, 175000, 150000, 125000, and 100000 dots shown in Fig. 14, respectively. The solid blue line indicates the mean value of the reduction factor. The dashed red line and solid red line are the lower bound and upper bound for the values within one standard deviation of the mean value, respectively. The dashed black line and solid black line are the lower bound and upper bound for the values within three times the standard deviation of the mean value, respectively.

Fig. 14 also gives the probability for the reduction factor within one, two, and three times the standard deviation of the mean value. For the area loss ratio of 0.1, the probabilities for the reduction factor within one, two, and three times the standard deviation of mean value are 0.725, 0.945, and 0.991, respectively, which are very close to the analytical values of 0.683, 0.955, and 0.997 for

normal distribution. It again indicates that the reduction factors of the buckling load of steel angles follow a normal distribution. It should be noted that the probability is calculated by the ratio of dot number satisfying requirements to the total dot number, rather than the ratio of segment length. For example, for the area loss ratio of 0.2, the probability for the reduction factor within three times the standard deviation of the mean value is 0.9913. However, the ratio of segment length within three times the standard deviation of mean value to total segment length is obviously less than 0.9913. This is because the distribution density of data fails to be shown in Fig. 14 due to the excessive amount of data.

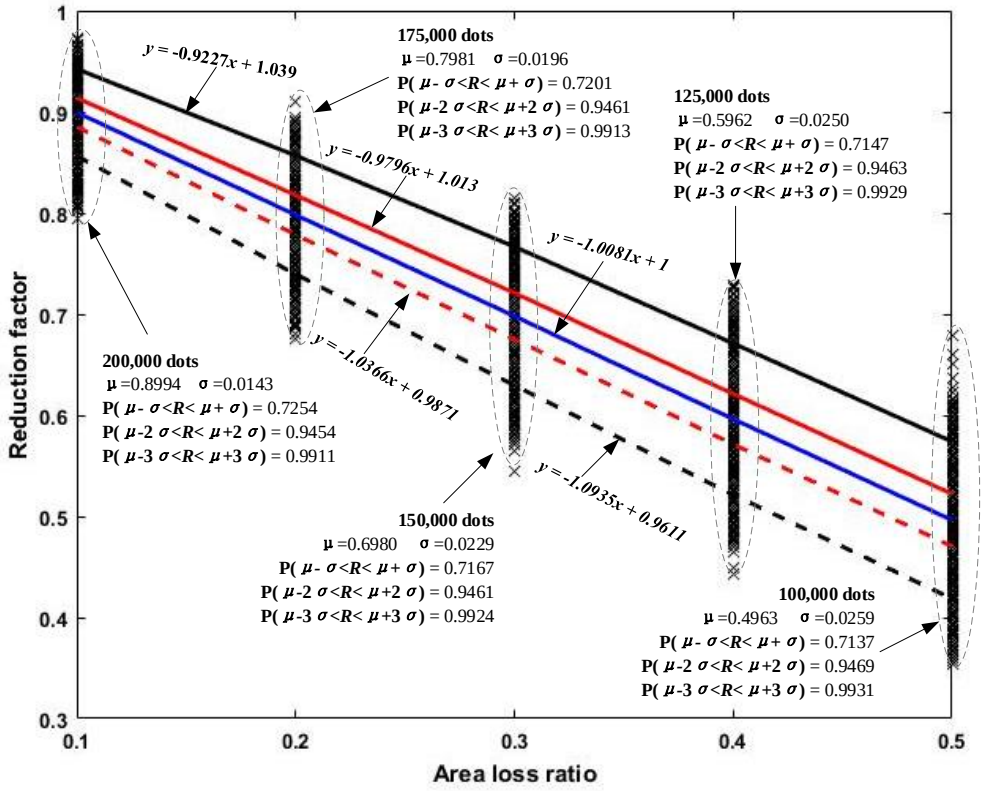

Fig. 14 Regression of the reduction factor of buckling load P_{cr} for all steel angle members

7. Conclusion

This paper presents a numerical study on the bifurcation buckling load of steel angle members with random corrosion pits. The effects of member length, section type, area loss ratio, and corrosion depth on the bifurcation buckling load of steel angles are studied. A probability-based relationship between the reduction factor of buckling load and the area loss ratio of steel angles is proposed. The following conclusions can be drawn from this study:

- The reduction factors of the buckling load of steel angles obey a normal distribution. A larger area loss ratio will result in a larger standard deviation of the reduction factors.
- For steel angles with the same area loss ratio, the mean values of the reduction factors of different section types are very close. For area loss ratios of 10%, 20%, 30%, 40%, and 50%, the mean values of the reduction factors of buckling load for steel angles are about 0.9, 0.8, 0.7, 0.6, and 0.5, respectively.
- The detrimental effects of corrosion on the torsional buckling load and flexural buckling load are different. Therefore, the buckling mode of steel angle members may changed from flexural buckling to torsional buckling due to corrosion.
- When the member length is small, the bifurcation buckling load of the steel angle is significantly affected by the corrosion depth. However, as the member length increases, the effect of corrosion depth tends to decrease.

References

[1] Kumar R, Cline DBH, Gardoni P. A stochastic framework to model deterioration in engineering systems. STRUCT SAF 2015;53:36-43.
[2] Zhao Z, Zhang H, Xian L, Liu H. Tensile strength of Q345 steel with random pitting corrosion based on numerical analysis. THIN WALL STRUCT 2020;148:106579.
[3] Xiao L, Peng J, Zhang J, Cai C. Mechanical Properties of Corroded High Performance Steel Specimens Based on 3D Scanning. ADV STEEL CONSTR 2019;15(2):129-36.
[4] Sheng J, Xia J. Effect of simulated pitting corrosion on the tensile properties of steel. CONSTR BUILD MATER 2017;131:90-100.
[5] Dang H, Liang A, Feng R, Zhang J, Yu X, Shao Y. Experimental study on mechanical properties and low-cycle fatigue behaviour of stainless steels subjected to salt spray and dry/wet cycle. INT J FATIGUE 2022;165:107187.
[6] Zhao Z, Zhang N, Wu J, Gao Y, Sun Q. Shear capacity of steel plates with random local corrosion. CONSTR BUILD MATER 2020;239:117816.
[7] Xu S, Qiu B. Experimental study on fatigue behavior of corroded steel. Materials Science and Engineering: A 2013;584:163-9.
[8] Silva JE, Garbatov Y, Guedes Soares C. Ultimate strength assessment of rectangular steel plates subjected to a random localised corrosion degradation. ENG STRUCT 2013;52:295-305.
[9] Wang R, Ajit Shenoi R, Sobey A. Ultimate strength assessment of plated steel structures with random pitting corrosion damage. J CONSTR STEEL RES 2018;143:331-42.
[10] Hua J, Wang F, Wang N, Huang L, Hai L, Li Y, et al. Experimental and numerical investigations on corroded stainless-clad bimetallic steel bar with artificial damage. J BUILD ENG 2021;44:102779.
[11] Zhang W, Chen J, Yu Q, Gu X. Corrosion evolution of steel bars in RC structures based on Markov chain modeling. STRUCT SAF 2021;88:102037.
[12] Ma Y, Guo Z, Wang L, Zhang J. Experimental investigation of corrosion effect on bond behavior between reinforcing bar and concrete. CONSTR BUILD MATER 2017;152:240-9.
[13] Srivaranun S, Akiyama M, Bocchini P, Christou V, Frangopol DM, Fukushima H, et al. Effect of the interaction of corrosion pits among multiple tensile rebars on the reliability of RC structures: Experimental and numerical investigation. STRUCT SAF 2021;93:102115.
[14] Liu J, Huang H, Ma ZJ, Chen J. Effect of shear reinforcement corrosion on interface shear transfer between concretes cast at different times. ENG STRUCT 2021;232:111872.
[15] Zhang Z, Xu S, Wang H, Nie B, Su C. Flexural buckling behavior of corroded hot-rolled H-section steel beams. ENG STRUCT 2021;229:111614.
[16] Chen L, Liu S, Zhang J, Yam MCH. Efficient algorithm for elastic buckling of corroded I-section steel members with Monte Carlo simulation. THIN WALL STRUCT 2022;175:109216.
[17] Zhao Z, Mo S, Xiong Q, Liu H, Liang B. Moment capacity of H-section steel beam with randomly located pitting corrosion. PROBABILIST ENG MECH 2021;66:103161.
[18] Zhang Z, Xu S, Wang Y, Nie B, Wei T. Local and post-buckling behavior of corroded axially-compressed steel columns. THIN WALL STRUCT 2020;157:107108.
[19] Wang R, Guo H, Shenoi RA. Experimental and numerical study of localized pitting effect on compressive behavior of tubular members. MAR STRUCT 2020;72:102784.
[20] Wang H, Zhang Z, Qian H, Fan F. Effect of local corrosion on the axial compression behavior of circular steel tubes. ENG STRUCT 2020;224.
[21] Wang R, Guo H, Shenoi RA. Compressive strength of tubular members with localized pitting damage considering variation of corrosion features. MAR STRUCT 2020;73:102805.
[22] Xu S, Zhang Z, Qin G. Study on the seismic performance of corroded H-shaped steel columns. ENG STRUCT 2019;191:39-61.
[23] Zhang J, Chen L, Liu S, Yam MCH. Efficient elastic buckling assessment algorithm for steel members with random non-uniform corrosion. ENG STRUCT 2022;266:114550.
[24] Hisazumi K, Kanno R. Column Buckling of Corroded Steel Angles and Channels: Experiments and Failure Mode Analyses. J STRUCT ENG 2021;147(8).
[25] Zhao Z, Zhou S, Zheng C, Tang L. Predictions of compression capacity of randomly corroded

WHSJs based on artificial neural network. MECH ADV MATER STRUC 2020:1-9.
[26] Yang Y, Li W, Xu T, He Z, Zhao D. Experimental study of hysteretic behavior of corroded steel with multi-angle welding joints. J CONSTR STEEL RES 2021;187:106990.
[27] Wang H, Wang Y, Zhang Z, Liu X, Xu S. Cyclic behavior and hysteresis model of beam-column joint under salt spray corrosion environment. J CONSTR STEEL RES 2021;183:106737.
[28] Chen H, Liu H, Chen Z. Residual behaviour of corroded welded hollow spherical joints subjected to eccentric loads. J CONSTR STEEL RES 2021;182:106661.
[29] Bao J, Zhou W. A random field model of external metal-loss corrosion on buried pipelines. STRUCT SAF 2021;91:102095.
[30] Chakraborty S, Tesfamariam S. Subset simulation based approach for space-time-dependent system reliability analysis of corroding pipelines. STRUCT SAF 2021;90:102073.
[31] Mazumder RK, Salman AM, Li Y. Failure risk analysis of pipelines using data-driven machine learning algorithms. STRUCT SAF 2021;89:102047.
[32] Bu Y, Yang L, Zhu Z, Wang F. Testing, simulation and design of offshore lined pipes under axial compression. MAR STRUCT 2022;82:103147.
[33] Zhang X, Zheng S, Zhao X. Experimental and numerical study on seismic performance of corroded steel frames in chloride environment. J CONSTR STEEL RES 2020;171:106164.
[34] Yang Y, Wu Q, He Z, Jia Z, Zhang X. Seismic Collapse Performance of Jacket Offshore Platforms with Time-Variant Zonal Corrosion Model. APPL OCEAN RES 2019;84:268-78.
[35] Ji CY, Xue HZ, Shi XH, Gaidai O. Experimental and numerical study on collapse of aged jacket platforms caused by corrosion or fatigue cracking. ENG STRUCT 2016;112:14-22.
[36] Zhang H, Ha L, Li Q, Beer M. Imprecise probability analysis of steel structures subject to atmospheric corrosion. STRUCT SAF 2017;67:62-9.
[37] Huang W, Garbatov Y, Guedes Soares C. Fatigue reliability of a web frame subjected to random non-uniform corrosion wastage. STRUCT SAF 2014;48:51-62.
[38] OSZVALD K. Buckling of Corroded Steel Angle Members under Compression.; 2014.
[39] Zhang L, Liang Y, Zhao O. Laboratory testing and numerical modelling of pin-ended hot-rolled stainless steel angle section columns failing by flexural-torsional buckling. THIN WALL STRUCT 2021;161:107395.
[40] Ziemian RD. Guide to Stability Design Criteria for Metal Structures: John Wiley & Sons, 2010.
[41] Liu S, Gao W, Ziemian RD. Improved line-element formulations for the stability analysis of arbitrarily-shaped open-section beam-columns. THIN WALL STRUCT 2019;144:106290.
[42] R. Ziemian, W. McGuire, S.W. Liu. MASTAN2 v4.0.; 2019.
[43] The British Standards Institution. Structural Steel Equal and Unequal Leg Angles (BS EN 10056-1:2017).; 2018.

Advanced Steel Construction – Vol. 20 No. 2 (2024) 160–168
DOI:10.18057/IJASC.2024.20.2.8
(Special Issue: *11st International Conference on Advances in Steel Structures, ICASS'2023, Kuching, Sarawak, Malaysia*)

EXPERIMENTAL STUDY OF SCISSOR FRAME STRUCTURES WITH FEM VALIDATION OF LOAD IMPACT ON MANUAL LOCKING MECHANISM

Jian Jun Moy and Cher Siang Tan *

Faculty of Civil Engineering, Universiti Teknologi Malaysia, Johor, Malaysia
** (Corresponding author: E-mail: tcsiang@utm.my)*

ABSTRACT

Scissor frame structures (SFS) have attracted significant attention due to their flexibility of deployment and stiffens once fully deployed. These features benefit prefabrication and transportation over traditional frame structures, with potential for modular structure implementation. However, current research often neglects structural analysis, focusing on geometrical and kinematic designs. This oversight, combined with critical load conditions at the locking mechanism linkage, risk underdesigning the SFS and leading to potential structural failure. This study conducted load testing on four SFS specimens with varying cross-sections and heights. Results were discussed based on the measured strain, displacement, and validation with FEM modelling. Analysis shows that despite the flexibility inherent in their pivotal points and multi-plane connections, the SFS exhibits linear behavior under external loads within the elastic range, with symmetrical results akin to single-plane action. Furthermore, three SFS FEM models, developed using SCIA Engineer software, were validated and revealed that loading on the locking mechanism linkage severely impacts structural efficiency. The capacities of the SFS specimens, calculated based on measured critical stress and stiffness, highlight the diverse effects of scissor depth and cross-section on SFS structural behaviour. This paper provides essential experimental data for SFS, assisting engineers in precise structural analysis and assessment.

ARTICLE HISTORY

Received: 8 April 2024
Revised: 5 June 2024
Accepted: 11 June 2024

KEYWORDS

Scissor frame structures;
Locking mechanism and linkage;
Experimental test;
Stress and stiffness;
Fabrication imperfections;
FEM modelling

1. Introduction

Deployable structures are designed to be deployed and retracted along a predetermined deployment path, offering the flexibility to meet specific application requirements while allowing for convenient storage. Extensive research has been conducted on deployable structures, including various types [1]. Scissor structures, also known as scissor frame structures (SFS), are among the most widely used deployable structures in the industry in different fields, which are widely used in aerospace [2], mechanical [3] and civil engineering [4, 5]. The advantage of the SFS over other deployable structures is that it is easier to build and assemble because it only requires a single 1-D member, comparable to a frame structure. Furthermore, unlike other structures, SFS can be constructed to fold into a very compact form, as examined by T.H. Kim [6]. In order to construct an SFS, a pivotal point is introduced on the intermediate length of the members. The behaviour of the SFS can be significantly influenced by the geometry of the scissor members and the location of the pivotal point. The three most commonly used scissors units were translational [7], polar [8], and angulated [9] units. These mechanisms were ingeniously merged to construct numerous SFS that can carry out wide range of functions when implemented in practical applications. According to the literature [10, 11], the integration of deployable structures and modular systems constitutes a significant development in construction technology. These innovative designs are not only easier to fabricate and transport but also possess the ability to expand and withstand substantial loads, ensuring they perform their intended functions effectively. Understanding the load behavior of SFS under real-world conditions remains crucial for maintaining their structural integrity and performance. By addressing these considerations, the construction industry can maximize the utility and efficiency of these advanced systems, enhancing adaptability, cost-effectiveness, and sustainability in modern building practices.

The application of deployable structures includes large-span roof structures [12-14], bridge structures [4, 5], temporary structures [15] and scaffoldings [16]. Previously, Emilio Perez Pinero constructed a deployable structure with a movable theatre utilising the translational unit [17]. Felix Escrig's proposal to use an SFS as a roof cover for a swimming pool in Seville [18] has proven successful, with the structure still standing today. These large-scaled applications have demonstrated the use of SFS and their benefits in construction. However, despite the success of these constructions, current research trend on SFS often revolves around trial-an-error geometrical form-finding method [19] and analytical methods [7, 8] to design the form without considering the structural integrity under various load conditions. In an article published by K. K. Vu et al. [20], the authors acknowledge the issue of neglecting structural stability during the kinematic and geometrical form-finding design of the SFS. Their study proposes to perform an exhaustive approach to generate alternative forms of Deployable Tension-Struct Structures (DTSS) incorporating kinematic and stability checks during the iterations. However, despite these advancements, the structural performance of SFS remains underexplored compared to their kinematic and geometrical design. This highlights the need for further research focusing on the load-bearing capabilities and real-world performance of SFS.

Without boundary conditions, an SFS is essentially a mechanism due to its inherent mobility and cannot carry any external load. However, by introducing additional bars or supports to limit its deployed height or length, the mechanism becomes static and capable of resisting external loads [21]. To analyse the structural behaviour of SFS under external loads, various methodologies have been introduced. C. J. Gantes uses the equilibrium continuum to approximate the displacement of a 2D scissor plane structure (SPS) and a 3D scissor frame structure (SFS). Furthermore, A. Kaveh et al. [22] and W. Shan et al. [23] developed stiffness matrices for duplet (a scissor unit) and uniplet (scissor members), which can be integrated with conventional stiffness matrix to determine the structural integrity. T. Kokawa [24] proposed another approach to simplify structural analysis by reducing the degrees of freedom from 10 to 2, utilising an equivalent spring model to represent the scissor loop. Although extensive research on structural analysis has been conducted on SFS under various load conditions, some critical aspects remain underexplored. One such aspect is the structural performance of the linkages in additional locking mechanisms. These connections often exhibit inherent weaknesses, making them structurally unfavorable when subjected to external loads. However, when performing structural analysis, many designers tend to over-constrain the nodes, making them overly rigid. This approach often leads to overestimating the structural integrity of the overall structure, resulting in designs that may not be sufficiently robust. Additionally, imperfections caused by fabrication and installation can further exaggerate these issues, reducing structural stiffness and leading to lower failure load factors [14]. While much research has focused on modeling and structural analysis for typical load conditions, the effects of loads acting on the locking mechanisms of SFS remain unproven and not validated against FEM models in the literature. This highlights the need for further experimental studies to validate theoretical models and understand the actual performance of SFS.

The focus of this study is to conduct experimental and numerical investigation on a proposed SFS enhanced with additional manual locking members. The experimental results of displacement and stress measurements at critical points on the scissor members are compared to three proposed SFS FEM models: standard rigid modelling, considering imperfections, and completely removing the locking mechanism. This comprehensive discussion identifies and showcases the structural behaviour of the SFS and highlights the crtitical condition when the loading is applied directly to the locking mechanism linkage, emphasising the importance of accurate modelling techniques.

2. Methodologies

This section comprehensively explains the assembly of the experimental specimens, the experimental design and procedure, and the data analysis plan. The details of the SFS FEM model and the three proposed SFS FEM models for validation were also included in this section.

2.1. Experimental specimens specifications

The experimental specimens from Table 1 was assembled utilising steel sections with steel grade of S 275. The Young's modulus, E, Poisson's ratio, ν, and density, ρ, of the designated steel are 210000 N/mm^2, 0.3, and 7850 kg/m^3, respectively. To improve the scalability of the results given a total applicable loading of 1500 N, smaller steel sections were utilised. Rectangular and square hollow steel sections (RHS and SHS) were selected for the scissor members due to their even stress distribution. Using SHS simplifies stress validation by recalculating the bending moment on the section surface based on the strain gauge measurements. Table 1 provides the lists of scissor frame structures with their specimen IDs, cross-section names, structural frame depths.

Table 1
List of specimens and their structural member cross-section

Specimen ID	Cross-Section Name	Frame Depth, h (mm)	Area, A (mm^2)	Moment of Inertia, I (mm^4)
SS-SHS25251.8-0.50	SHS 25 × 25 × 1.8 mm thk.	500	167	15074.81
SS-SHS25251.8-0.25	SHS 25 × 25 × 1.8 mm thk.	250	167	15074.81
SS-RHS50251.8-0.50	RHS 50 × 25 × 1.8 mm thk.	500	257	82266.39
SS-SHS25252.5-0.50	SHS 25 × 25 × 2.5 mm thk.	500	225	19218.75

The configuration of the SFS was built with two sets of SPS, each consisting of a chain of three translational units connected by a series of linkages as illustrated in Fig. 1(a). This configuration was chosen for its standardised scissor member fabrication, facilitating repetitive production. In the SFS, the additional locking mechanism was added by assembling four bars bolted to a multipurpose linkage shown in Fig. 1(a) enhancing the stiffness and rigidity of the SFS. To adjust the frame depth, the length of the bars for the locking mechanism can be calculated and predetermined before fabrication. When the SFS is in the undeployed state, the locking mechanism are free to rotate, accommodating the movement of the group of scissor members. Upon deployed to the predetermined frame depth, the movement of the scissor members is structed by the locking mechanism. Pre-drilled bolt holes on the locking mechanism linkage and the bars allow for additional manual bolt insertion, fixing the connection and the entire structure in place. The process of deployment of the locking mechanism is illustrated in Fig. 1(b). To improve the the effectiveness of the proposed SFS, snap-fit fasteners can be design and applied to the structure [25]. The strength and capacity of these snap-fit fasteners can be further studied for use in high load-bearing applications. However, in this experimental study, simplified steel bolts were used for manual locking purposes. Based on the schematic drawing shown in Fig. 2, a series of connection linkages were fabricated to join all translational units from various axis directions and the locking mechanism together to form a manual locking SFS.

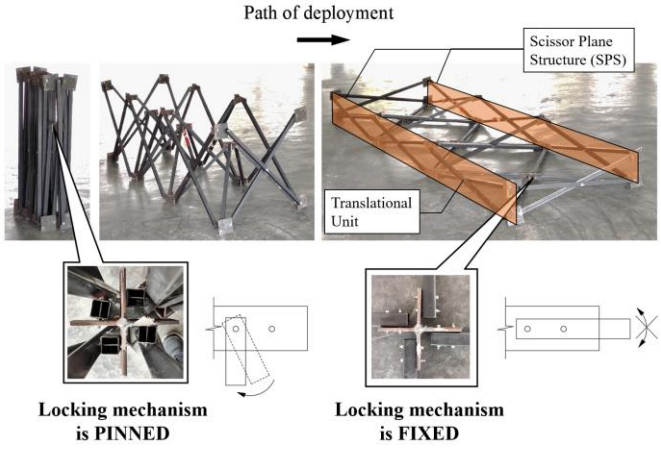

(a)

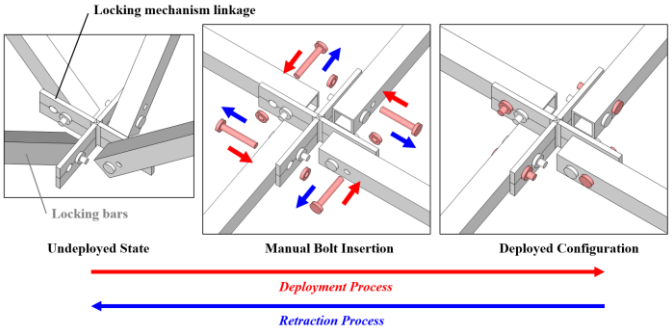

(b)

Fig. 1 Illustration of (a) an actual SFS model and its deployment process, and the (b) simultaneous deployment process of a locking mechanism

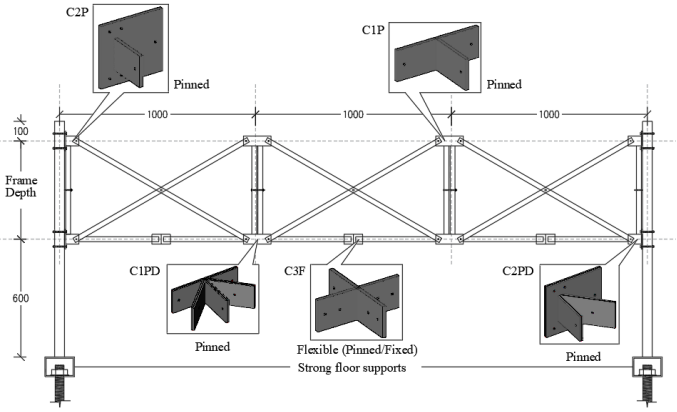

(a)

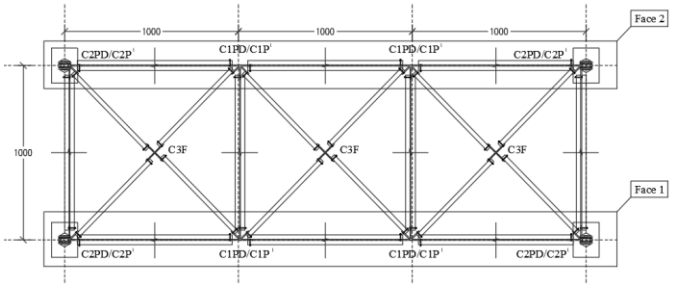

*Note:
1BOT/TOP connection linkage label

(b)

Fig. 2 Dimension and details of the SFS and connection labels shown in (a) elevation view and (b) plan view

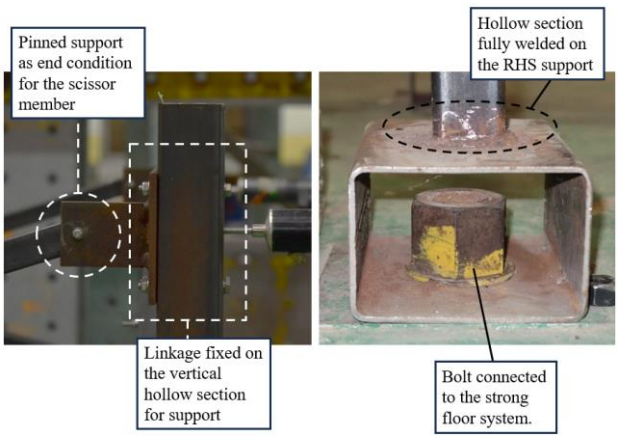

Fig. 3 Illustration of vertical hollow section support and the floor support system for SFS

The support for the SFS was fabricated to simulate the steel columns that hold the SFS in place. The SFS was connected to these column at four corners as shown in Fig. 2. The steel members used for the support columns were SHS

50 × 50 × 4.0 mm thk. Additionally, the support was designed to connect to the strong floor system in the laboratory, ensuring that the support members were fixed in the positions shown in Fig. 3.

For the purpose of this study, the SFS was subjected to manual continuous loading with several 5 kg (approximately 50 N) plate at each point of interest. The loading points were set at the center of each C3F mentioned in Fig. 2, which are at the center of the locking mechanism linkage. Each loading point was subjected to a m,aximum load of 500 N, resulting in an overall maximum total load of 1500 N on the SFS. The application of load at the locking mechanism linkage allows the investigation to verify the effectiveness of the locking mechanism after loading. When the SFS is loaded, it experiences a vertical displacement, hence a clearance of 600 mm between the SFS and the floor was provided as planned in Fig. 2. An illustration of the experiment under loading is shown in Fig. 4. When the load was applied to the SFS, the stress is distributed throughout the scissor members.

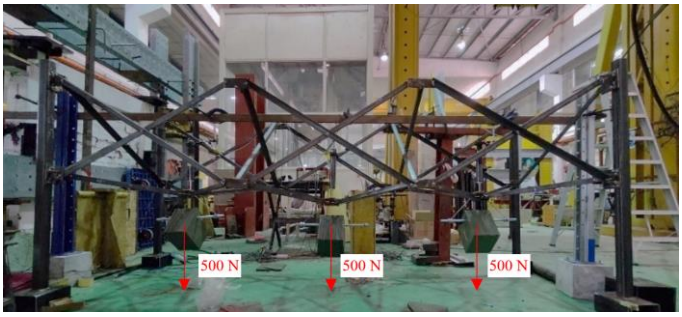

(a)

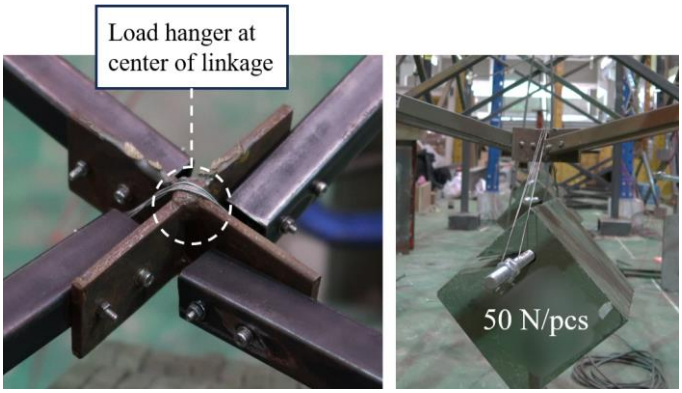

(b)

Fig. 4 Illustration of loading scenario during the experiment for (a) overall view and (b) close-up view

Linear Variable Differential Transformers (LVDTs) and strain gauges were employed to measure displacement and strain in the scissor members. An LVDT with a 100 mm measurement range was used to measure displacement from the SPS under loading condition. The positions of the LVDTs and its actual setup are shown in Fig. 5. To account for uncertainties in the experimental testing, the LVDTs were vertically aligned during the setup. Furthermore, the LVDTs were positioned so that only half of their range (50 mm) was used to obtain measurements in the positive or negative directions.

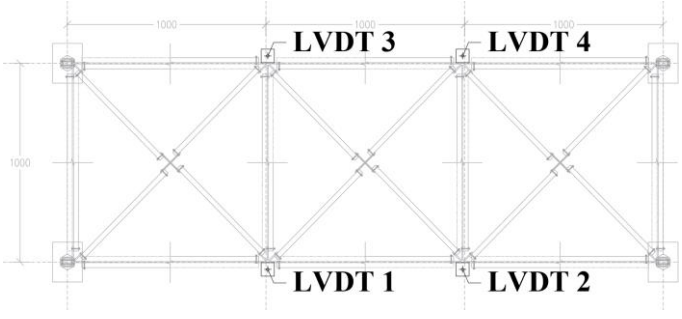

(a)

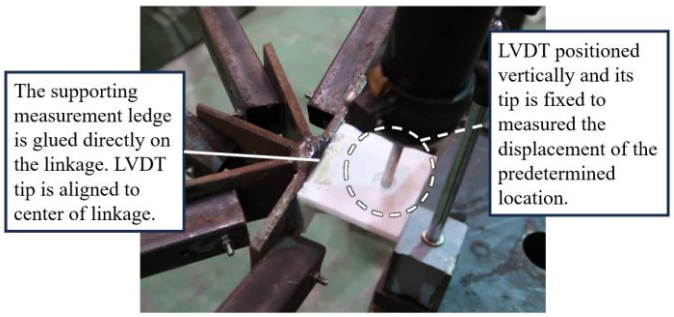

(b)

Fig. 5 Illustration of (a) predetermined location of LVDTs and its (b) actual setup

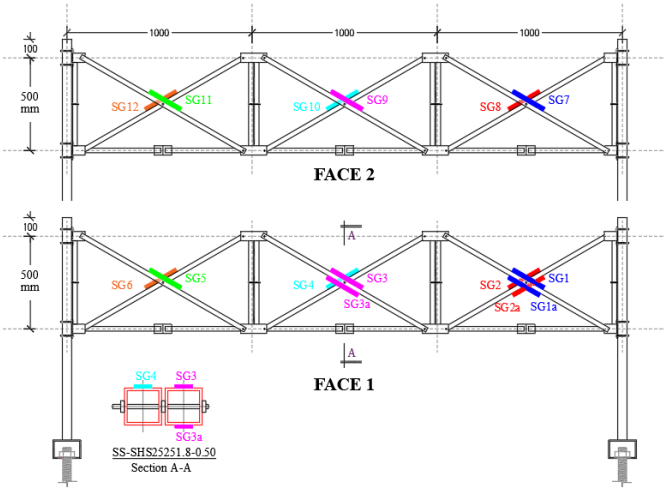

(a)

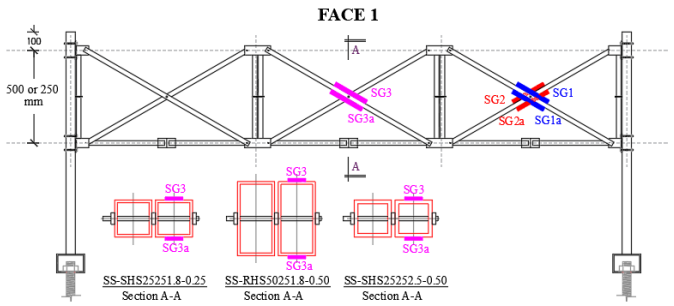

(b)

Fig. 6 Location of strain gauges of (a) SS-SHS25251.8-0.50 and (b) others

2.2. Experimental design and procedure

The experiment was conducted in a structural lab equipped with a strong floor system to provide robust support for the specimen. Before the test, the SFS was carefully set-up, ensuring the proper placement of the load hanger, LVDT, and strain gauge as mentioned in Section 2. The data logger readings from the LVDT and strain gauge were zeroed before the start of the test to establish a baseline reference.

The test began by continuously placing the load plates (50 N) at the designated load points. The deflection of the structure was observed, and a waiting time of 30 seconds was employed before data collection, as recommended by J. P. Valcarcel et al. [26] in a similar load tests. The data collected included the displacement of the SFS (measured by LVDT) and the strain at critical points in the scissor members (measured by strain gauge). The loading process was repeated until a load of 500 N was reached at each load point. Once this load was achieved and the corresponding data was recorded, the load plates were gradually retracted to measure the displacement and strain during the unloading phase. The entire experiment was repeated at least twice on the same specimen to account for permanent displacement of the SFS due to initial structural set.

The same testing procedure was performed on the following three specimens. For SS-SHS25251.8-0.50, the overall stress behaviour throughout the SFS were being analysed to validate the symmetrical of the structure. Furthermore, comparison between the stress and displacement results of all specimen mentioned in Table 1 will be compared and discussed.

2.3. Experimental results analysis

The stress verification was conducted to study the stress behaviour at critical location on the scissor members as shown in Fig. 6. The SFS was fabricated symmetrically, allowing cross-checking of the stress around the structure. The symmetrical equivalent stress locations are noted to be SG 1, SG 6, SG 7, SG 12; SG 2, SG 5, SG 8, SG 11; SG 3, SG 4, SG 9, SG 10.

It was assumed that the stress distribution within the hollow steel section remained uniform under the applied loading as shown in Fig. 7. The experiment results indicated that the scissor members remained in the elastic zone under the total applied loading of 1500 N. Additionally, the neutral axis shift was not considered since the members were still behave elastically due to the small load [27]. Utilising the fundamental bending stress formula in Fig. 7, the bending moment experienced by the scissor members under the applied loading was calculated by multiplying the assumed elastic modulus and section modulus with the strain obtained from the strain gauges in the experiment. With the data extracted from the experiment, the bending moment diagram of the SFS can be obtained.

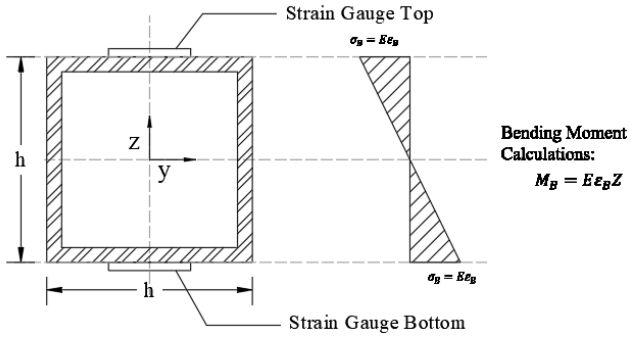

*Note:
σ_B is bending stress, E is young modulus, M_B is bending moment, σ_B is bending strain, Z is section modulus.

Fig. 7 Elastic stress profile in the cross-sections

In overall, total of four specimens were being compared of their stresses and displacment measured. The comparison involved assessing the overall maximum deflection observed at the SPS and determining the structure's stiffness using the best-fit line (trendline) function in Microsoft Excel. For the stress result comparison, the analysis aimed to identify the most influenced point when the cross-sectional properties of the scissor member were modified. This approach provides a comprehensive understanding of how variations in cross-sectional propertiues impact the stress distribution and overall structural performance of the SFS.

2.4. FEM Modelling

In this study, SCIA engineer software was employed to model the experimental specimens of the SFS with their material and mechanical properties were as mentioned in Section 2.1. The purpose of the FEM modelling analysis was to compare the results of three different FEM models to the experimental results where the load acts on the center of the locking mechanism linkage. The three FEM models consists of FEM 1, FEM 2 and FEM 3. Where, FEM 1 is the standard FEM model, which includes the locking mechanism and has no imperfections introduced in the SFS; FEM 2 introduces imperfections in the SFS; while FEM 3 excludes the locking mechanism from the SFS. Consequently, FEM 1 serves as the control model for all comparisons in this analysis.

2.4.1. FEM 1 model: Standard modelling

The base model of FEM 1 includes several key properties: a pinned connection as the beam end condition for the scissor member, a pivotal joint, a locking mechanism linkage, and a pin supported point on the strong floor. The standard modelling diagram of the SFS for FEM 1 is presented in Fig. 8, with additional modelling details is explained consecutively in Table 2.

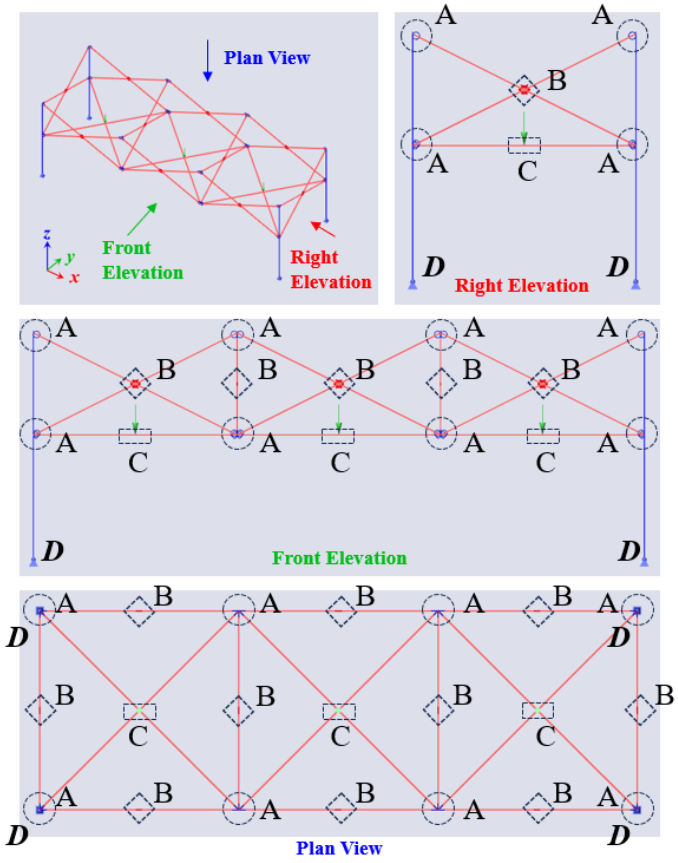

Fig. 8 Wireframe diagram of FEM 1 base model with labels

Table 2
Modelling boundary conditions of the SFS with labels from Fig. 8

Notation	Modelling	Remark
A	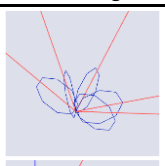	End conditions of scissor members are pinned joints, allowing rotation about the major axis of the scissor member.
B	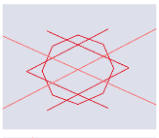	Unique cross-link plugin that allows separation of rotation ry of each adjacent scissor member while constraining other degrees of freedom. Functions similarly to a pivotal defined master/slave node constraint.
C		Load acting on the intersecting node of the locking mechanism. The node of the locking mechanism connects the locking bars rigidly at the intersection. Refer to Fig. 1, for the locking mechanism concept.
D	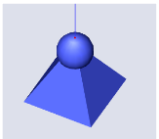	Pinned connection below the vertical supporting members to simulate the support condition on the strong floor.

One of the most challenging aspects of the SFS is modelling the pivotal point. The pivotal joint is crucial in an SFS because its location can significantly alter the deployment behaviour, whether translational or polar. However, modelling the pivotal joint is modelling the pivotal joint is not as straightforward as defining a typical pinned node on the intersecting point. The boundary conditions of the pivotal joint are illustrated in Fig. 9.

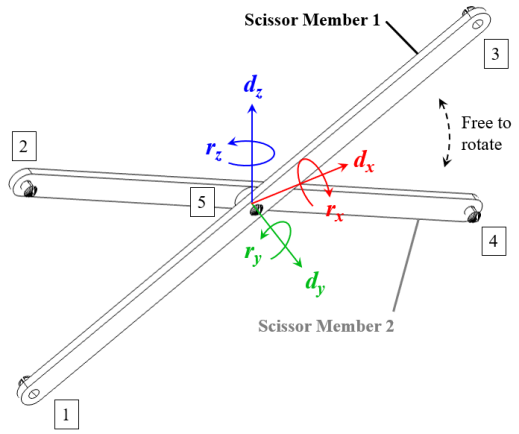

Fig. 9 3-D Local axis of pivotal joint of a scissor unit

In Fig. 9, the variables d_x, d_y, and d_z represents the displacement of the node of each scissor member at the pivotal joint along the x, y and z axes, respectively. Similarly, r_x, r_y, and r_z denote the rotation of the node of each scissor member about the x, y and z axes, respectively. At the pivotal point, it is important to note that the displacement d_x, d_y, and d_z of both scissor members will always move in the same direction, as they are constrained by each other with a pin. A unique property of the pivotal point in the SFS is that r_y is free to rorate for each connected scissor member 1 and 2, whereas r_x and r_z remain constant. Furthermore, the scissor member remains continuously connected from node 1 to node 5 to node 3 for scissor member 1 and from node 2 to node 5 to node 4 for scissor member 2. Thus, the modelling of the pivotal joint constraint should include these features to accurately capture the behaviour of the scissor members in the model. Fig. 10 illustrates the load cases affecting the SFS, with their response to the applied load indicated by the blue dashed line.

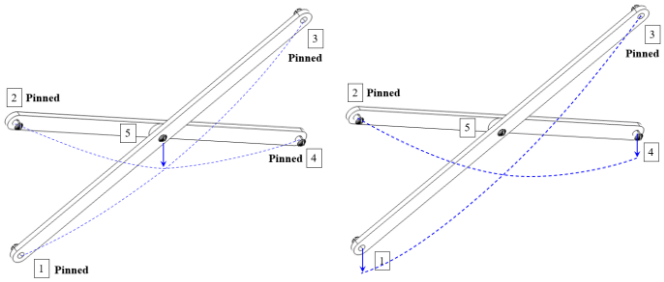

(a) (b)

Fig. 10 A scissor unit under various load at (a) center of the pivotal point and at (b) Point 1 and Point 4.

At Fig. 10(a), the load is applied directly on the pivotal point of the scissor member with the pinned supports are defined at point 1, 2, 3 and 4. At Fig. 10(b), the load is applied on point 1 and 4 where the pinned support is defined at point 2 and point 3. In both load cases, the adjacent scissor members will transfer shear force along the xz plane when the load is applied, causing them to bend about the pivotal point. To capture this behaviour in the modelling, a master-slave node approach [28] can be used to define the constraint between both scissor member at the pivotal point. The boundary condition of this mid-beam connection is to constrain the degree of freedom of d_x, d_y, d_z, r_x and r_z of both scissor members. Meanwhile ry of both scissor members remains freely rotatable.

2.4.2. FEM 2 model: Standard modelling incorporating imperfection due to Fabrication and Installation offsets.

During the fabrication of the SFS, achieving high accuracy is crucial to obtain the desired deployed and retracted states. Therefore, the dimensions of the SFS should be fabricated as precise as possible. However, due to workmanship and human error, especially in large structures, fabrication errors are inevitable.

In this study, imperfections due to workmanship were calculated under the assumption that the locking bar has a fabrication error of 0.5% at both ends of the structure. The error includes the bolt hole were not aligned at the desired location, which lengthen the open span of the locking bar. As illustrated in Fig. 11, even slight errors in the structural dimension can accumulate, resulting in imperfections up to 81 mm. To account for these imperfections, the modelling in this study rounded the imperfection up to a whole number of 100 mm. This conservative approach ensures that the model covers a wider range of potential deviations, providing a safety margin that enhances the robustness and reliability of the analysis.

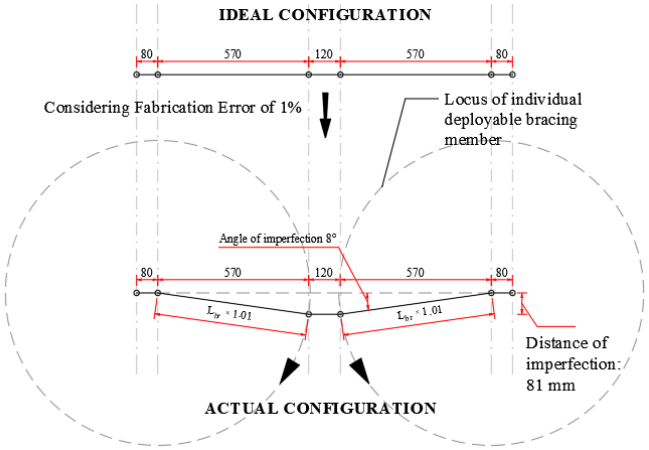

Fig. 11 A scissor unit under various load at (a) center of the pivotal point and at (b) Point 1 and Point 4

2.4.3. FEM 3 model: Standard modelling without consideration of locking mechanism.

For this configuration, the locking mechanism was removed from the SFS. Despite this removal, the SFS was still able to carry the load since it is still pinned connected to the vertical hollow sections for support. The load in this case was assumed to be equally distributed among all the nodes where the locking mechanism would normally connect. The purpose of this configuration is to identify the behaviour of the SFS when subjected to external loads without the presence of the locking mechanism. While the locking mechanism is removed from the modelling, it is assumed that the load is transferred equally to each point on the modelling of the SFS. The structural model elevation and 3D view is shown in Fig. 12.

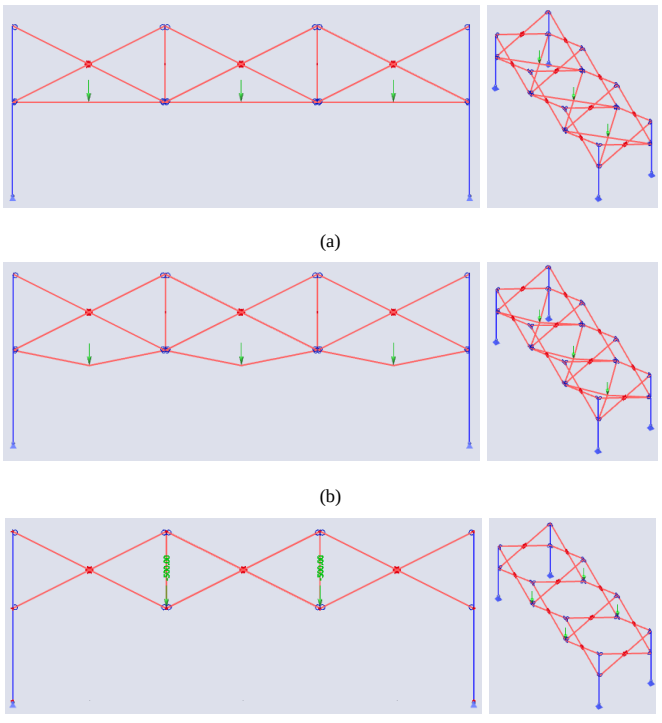

(a)

(b)

(c)

Fig. 12 Illustration of three modelling of SFS (a) FEM 1, (b) FEM 2, and (c) FEM 3

3. Results and discussions

This section summarises and discusses the load test results on the SFS.

Several key findings and observations were obtained from conducting the experimental tests and analysing the collected data sets. These findings offer valuable insights into the structural behaviour of the SFS. Additionally, a numerical comparison with the experimental results will be conducted for validation, ensuring the accuracy and reliability of the model.

3.1. Stress distribution measured in SFS.

Based on the strain gauge results, measurements were obtained that reflect the surface strain at the attachment points. For this analysis, the strain values were converted to stress, assuming an elastic modulus of 210000 N/mm² for the steel. As shown in Fig. 13, the behavior of all calculated stresses for SS-SHS25251.8-0.50 was consistent. The figure shows that the stress for the first set is negative, the second set is positive, and the third set is negative. Positive stress values indicate tensile stress, while negative values represent compressive stress. Based on Fig. 13, the highest calculated stress for SS-SHS25251.8-0.50 is -78.96 MPa, measured at Face 2.

When adjacent scissor members are connected to each other with a pivotal joint, they connect at different planes, as depicted in Fig. 9. However, despite the offsets of each scissor member at the pivotal connection, the results of the strain gauges placed at the top and bottom of the scissor member at the pivotal point show symmetrical behavior, as shown in Fig. 13, with the stress calculated for the top and bottom sections having opposite signs, represented by the solid and dashed lines, respectively. This symmetrical behavior is demonstrated by the ratio difference tabulated in Table 3, where values closer to 1.0 indicate symmetry in the scissor member. At the pivotal point of the scissor member, when tensile stress is on the top and compressive stress is on the bottom, the scissor member experiences a hogging moment at that location, and vice versa. Hence, the SFS can be modelled as a 2D member in the software with a clear definition of the boundary conditions discussed in Section 2.4.1.

According to Fig. 13 and Fig. 14, it is evident that all results align in terms of the sign of the stress found at the top of the scissor member. At SG1/SG1a and SG3/SG3a, the SFS experiences a sagging moment, while at SG2/SG2a, the scissor member experiences a hogging moment when subjected to loading. Therefore, when an SFS is subjected to loading, the scissor member connected to the top of the supporting part will experience a hogging moment induced by the shear force from the adjacent scissor member. Differences in the strain gauge readings may also be caused by the sensitivity of the gauges. Given the small magnitude of the loading, the strain gauge values may vary significantly; however, the consistency of the readings indicates that the SFS is symmetrical and performs as expected.

Another notable observation is that the gradient of the curve is relatively straight, indicating that the scissor member is still behaving within the elastic zone. Additionally, the scissor members exhibit no nonlinear attributes, resulting in the linear graph plotted in Fig. 14. Therefore, the analysis shows that the SFS behaves linearly during the static deployed state when subjected to loading, despite its unique flexible properties.

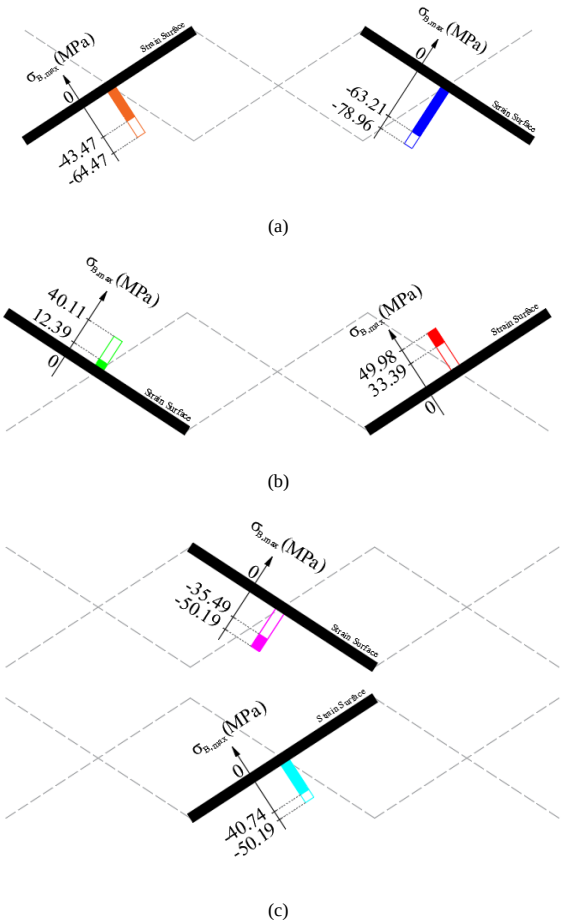

*Note:
[1]Solid fill represents strain gauge reading at Face 1
[2]No fill represents strain gauge reading at Face 2
[3]Strain surface directly the surface of the strain gauge measuring the data.

Fig. 13 Illustration of the calculated stresses depicted on the SFS schematic diagram for (a) Set 1: SG1, 6, 7, 12; (b) Set 2: SG 2, 5, 8, 11; and (c) Set 3: SG 3, 4, 9, 10 symmetrical members

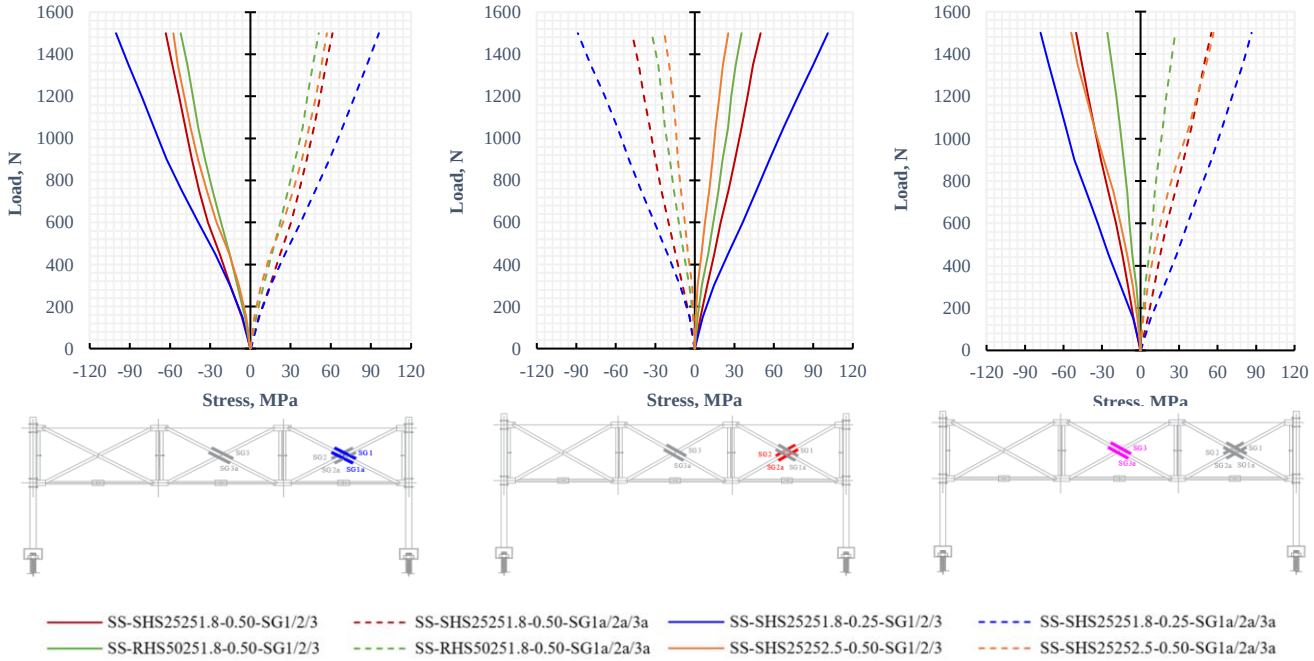

Fig. 14 Load vs stress curve of the SFS measured at (a) SG1/SG1a, (b) SG2/SG2a and (c) SG3/SG3a

Table 3
Critical stress of scissor member under 1500 N

Specimen ID	Critical Stress at 1500 N, MPa						Ratio Difference			Calculated Bending Moment, Nm			Load/ Weight Ratio, N/kg
	SG1	SG1a	SG2	SG2a	SG3	SG3a	SG1/ SG1a	SG2/ SG2a	SG3/ SG3a	M_1	M_2	M_3	
SS-SHS25251.8-0.50	-63.21	61.32	49.98	-47.67	-50.19	55.23	1.03	1.05	0.91	74.91	-58.74	63.42	44.49
SS-SHS25251.8-0.25	-100.38	95.97	101.01	-88.83	-77.91	86.52	1.05	1.14	0.90	118.12	-114.20	98.92	48.12
SS-RHS50251.8-0.50	-52.08	51.03	35.49	-32.76	-25.83	27.09	1.02	1.08	0.95	169.15	-111.96	86.82	28.68
SS-SHS25252.5-0.50	-57.54	57.12	25.41	-23.1	-53.97	56.91	1.01	1.10	0.95	87.80	-37.15	84.91	33.63

The critical stress of the scissor member at 1500 N was recorded in Table 3. The table shows that the specimen SS-SHS25251.8-0.25 has the highest stress among all the participating specimens that are at SG1 which is -100.38 MPa, followed by SS-SHS25251.8-0.50, SS-SHS25252.5-0.50, and finally SS-RHS50251.8-0.50, with stress value of -63.21 MPa, -57.54 MPa, and -52.08 MPa respectively. Based on observations, it was noted that a reduced depth increases the bending stress that each member must resist during the static stage. However, while calculating the bending moment based on the fundamental bending stress equations, it was found that SS-RHS50251.8-0.50 yields higher bending moment results. This is due to the fact that the cross-sectional area of SS-RHS50251.8-0.50 provides a higher moment of inertia compared to the other scissor members, increasing the section modulus and the stiffness of the scissor member, which in turn increases the calculated bending moment. Additionally, the calculated bending moments shown in the table indicate that M_1 always has the highest bending compared to other critical locations. This critical bending moment is attributed to several factors, including the pin-connected end support and the direct loading by adjacent scissor members, which introduce high shear forces at the pivotal point of the SFS, resulting in significant bending at that location. Therefore, in the structural analysis and design of the SFS, special care must be taken with the scissor member at the end support, as it will have to resist higher internal forces compared to the scissor units at the center of the structure. Finally, utilizing the experimental data, the bending moment diagram can be drawn as shown in Fig. 15.

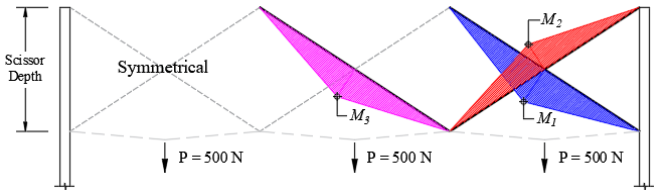

*Note:
M_1, M_2, M_3 value represents the calculated bending moment in Nm based on their signs, with values taken from Table 3. Negative values are accounted for in the figure to depict hogging moment at M_2 in the SFS.

Fig. 15 Typical bending moment diagram for all SFS

3.2. Displacement analysis of SFS.

Shown in Fig. 16 are the displacements of the SFS specimens recorded by the LVDT in the experiment. It was observed that despite the high flexibility of the SFS, the displacement response under load remains linear. Comparison between all the specimens shows that the SFS with the cross-section having the highest properties of area and moment of inertia, SS-RHS50251.8-0.50, has the highest stiffness among all the specimens, with k equal to 430.12 N/mm. This is followed by SS-SHS25252.5-0.50, SS-SHS25251.8-0.25, and finally SS-SHS25251.8-0.50, with stiffness measured at 253.96 N/mm, 168.55 N/mm, and 165.29 N/mm, respectively. The best-fit line shows a very high r^2 value, indicating that the data points closely agree with the best-fit line and confirming the linear displacement behavior of the SFS.

Further analysis of the displacement, as shown in Fig. 16, includes another line connecting the data points in addition to the best-fit line. It was found that the line connecting the data points at the initial stage shows the SFS exhibiting slightly stiffer behavior at the start of the loading stage. The initial stiffness of the SFS is largely due to the joints of the SFS. When lightly loaded, the joints retain some degree of fixity, providing very small moment resistance and slightly increasing the stiffness of the SFS at the initial stage, approximately from 0 N to 800 N. In an ideal scenario, pin connections are assumed to have no moment resistance, meaning they allow rotation without resisting it. However, in practical situations, real-world pin joints may not be perfectly frictionless or free of any resistance. The slight resistance can provide a small amount of moment resistance at the initial stages of loading at the joint, increasing the stiffness of the whole structure slightly. This phenomenon occurs due to factors like friction within the pin joint, the imperfect fit of the pin, or slight deformation of the joint components under load, which can create a temporary semi-rigid behavior. As the loading increases, these minor resistances are overcome, and the joints transition to their expected behavior as fully pinned connections. At this point, the joints no longer provide significant moment resistance, and the SFS's stiffness returns to what is expected for a pinned system. This transition from semi-rigid to fully pinned behavior results in the observed reduction in stiffness as the load increases beyond the initial stage.

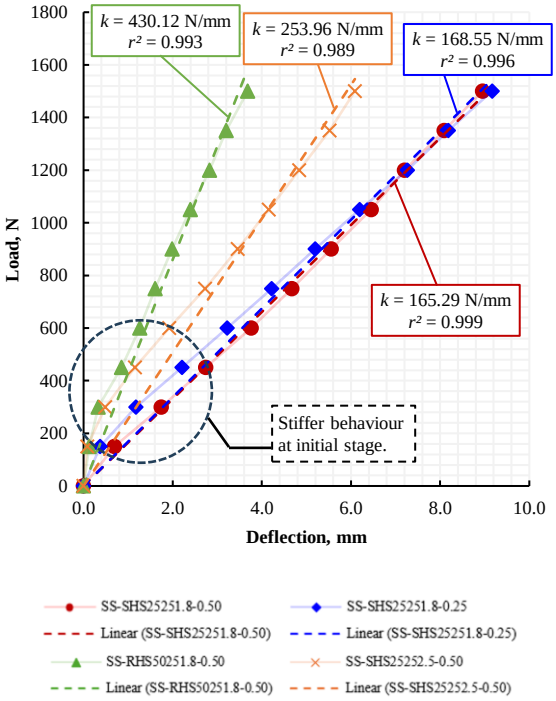

*Note:
Dashed line indicate the best-fit line based on the displacement data from 0 N load to 1500 N load.
Where,
k is the stiffness of the SFS calculated by the gradient of the best-fit curve
r^2 is the degree of best fit of the data points to the line, with 1.0 being very compatible and 0.95 to be the acceptance limit of the compatibility.

Fig. 16 Graph of displacement vs applied load for all SFS

Furthermore, when comparing the critical stress from Table 3 with stiffness from Fig. 16, it was shown that changing the cross-section of the scissor member did not result in significant differences in stress distribution. Instead, when the depth of the SFS is reduced, the stress experienced by each scissor member increases significantly, as noticeable when comparing SS-SHS25251.8-0.50 to SS-SHS25251.8-0.25. The greatest difference between them is at SG2, where the ratio difference of the 250 mm to the 500 mm scissor depth is 2.02. When the depth of the SFS reduces, the load-to-steel weight ratio of the SFS increases. The load-to-steel weight ratio of SS-25251.8-0.25 is 48.12 N/kg, the highest among the specimens. As load/weight ratio increases, fewer steel members are present to resist the same load, causing stresses on scissor members to increase.

However, on the other hand, when the section properties of the cross-section increase, the stiffness of the SFS also increases. For instance, the specimen SS-RHS50251.8-0.50, which has greater section properties such as area (A) and moment of inertia (I), achieved a stiffness of 430.12 N/mm. The load-to-steel weight ratio of this specimen is the lowest, at 28.68 N/kg. As the section properties of a section increase, its structural stiffness also increases, allowing for greater capacity and displacement. Hence, further study should be proposed to account for the stress and stiffness behavior of the SFS to determine the optimum configuration for the SFS.

By compiling the displacement data from Fig. 16 and the stress data from Table 3, the load capacity of the SFS before the scissor member starts to experience yielding can be approximated, assuming the yield stress, f_y of the steel section is 275 N/mm² and the structure behaves linearly. The calculation of the predicted maximum load is shown in Table 4. The predicted maximum load up to 275 N/mm² stress is calculated based on the critical stress from the experiment using the ratio method. Whereas, the predicted maximum load up to the displacement limit of National Annex of MS EN 1993-1-1 [29] was calculated based on the stiffness measured from the experiment. According to MS EN 1993-1-1, the allowable displacement for the SFS for a 3.0 m span is 15 mm. In Table 4, the displacement of the SFS specimen is calculated accordingly and it was found that, based on the displacement limit by MS EN 1993-1-1, the predicted maximum load $P_{d,max}$ shows lower load compared to $P_{\sigma,max}$. Hence, from this result, it can be noted that the stiffness of the SFS greatly governs the design of the SFS.

Table 4
Summary of specimen's stiffness and critical stresses and their predicted capacity

Specimen ID	Stiffness, k (N/mm)	Critical Stress at 1500 N	Predicted Maximum load up to 275 MPa stress, $P_{\sigma,max}$ (kN)	Predicted maximum load up to MS EN 1993-1-1 displacement limit [29], $P_{d,max}$ (kN)
SS-SHS25251.8-0.50	165.29	62.27	6.62	2.48
SS-SHS25251.8-0.25	168.55	98.18	4.20	2.53
SS-RHS50251.8-0.50	430.12	51.56	8.00	6.45
SS-SHS25252.5-0.50	253.96	57.33	7.20	3.81

3.3. Experimental results comparison with FEM modelling

Three FEM models were developed to compare their results with the experimental results. The data from these comparisons are tabulated in Table 5. Furthermore, based on the data in Table 5, Fig. 17 was plotted to illustrate the closeness of the experimental data to the numerical modeling results.

Table 5
Tabulation of compilation and comparison of experimental and FEM results

Parameters	Specimen ID	Results			
		EXP	FEM 1	FEM 2	FEM 3
d, mm	SS-SHS25251.8-0.50	8.95	2.47	6.19	10.54
	SS-SHS25251.8-0.25	9.17	2.12	6.36	7.41
	SS-RHS50251.8-0.25	3.68	0.97	1.45	2.1
	SS-SHS25252.5-0.25	6.09	2.11	4.94	8.3
	Best-fit gradient (mm/mm)	-	**3.63**	**1.42**	**0.92**
M_1, Nm	SS-SHS25251.8-0.50	74.91	21.34	41.65	100.05
	SS-SHS25251.8-0.25	118.12	16.2	52.65	74.43
	SS-RHS50251.8-0.25	169.15	37.64	53.55	105.87
	SS-SHS25252.5-0.25	87.8	22.58	42.5	100.21
	Best-fit gradient (Nm/Nm)	-	**4.49**	**2.41**	**1.17**
M_2, Nm	SS-SHS25251.8-0.50	-58.74	-10.22	-44.9	-71.17
	SS-SHS25251.8-0.25	-114.2	-11.47	-70.42	-81.58
	SS-RHS50251.8-0.25	-111.96	-8.83	-39.06	-64.53
	SS-SHS25252.5-0.25	-37.15	-10.07	-44.38	-70.56
	Best-fit gradient (Nm/Nm)	-	**7.88**	**1.60**	**1.12**
M_3, Nm	SS-SHS25251.8-0.50	63.42	19.94	62.22	76.94
	SS-SHS25251.8-0.25	98.91	21.05	61.59	58.92
	SS-RHS50251.8-0.25	86.82	48.53	76.54	83.17
	SS-SHS25252.5-0.25	84.91	22.26	63.09	77.32
	Best-fit gradient (Nm/Nm)	-	**2.56**	**1.26**	**1.10**

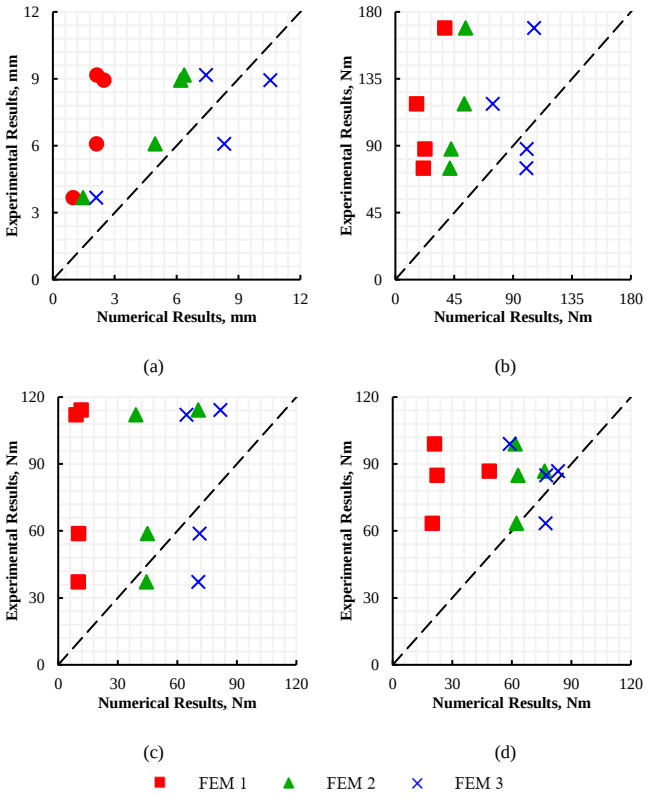

Fig. 17 Comparison graph of experimental data and numerical data for the (a) displacement, (b) M_1, (c) M_2, and (d) M_3

In Fig. 17, the numerical and experimental results were plotted on a graph where the black dashed line represents the 1:1 ratio between the experimental and numerical model results. If the data points are above the black dashed line, the experimental results are higher than the numerical results. Conversely, if the data points fall below the black dashed line, the numerical results are higher than the experimental results. Additionally, the best-fit gradient is calculated from the best-fit line with an additional point at (0,0) was added to each data set, representing zero values for both the experimental and numerical results. The best-fit line was not drawn in the figure to avoid confusion; instead, the gradient values were listed in Table 5 for more comprehensive discussion and comparison.

According to Table 5, FEM 1 shows the highest gradient difference among the modeling configurations for all the parameters which are 3.63, 4.49, 7.88, and 2.56 for d, M_1, M_2, and M_3 respectively. FEM 1 is the standard FEM model for the SFS with loading acting at the center point of the locking mechanism linkage. Although the locking mechanism linkage was fixed with pinned joint connections as shown in Fig. 1(b), this does not ensure that the joint is rigid and continuous. Compared to the experimental results, the FEM 1 model yields smaller results, indicating that it overpredicts the stiffness of the SFS.

In FEM 2, initial imperfections due to fabrication and assembly of the SFS are considered. The results from FEM 2 are closer to the experimental results, which are 1.40, 2.41, 1.60, and 1.26 for d, M_1, M_2, and M_3 respectively, nearly twice more accurate than the results from FEM 1. However, the experimental results are still higher than the numerical results. FEM 3 shows the closest results to the experimental data, as indicated by a best-fit gradient very close to 1.0. For FEM 3, the best-fit gradients achieved

for the parameters are 0.92, 1.17, 1.12, and 1.10 for d, M_1, M_2, and M_3 respectively. This outcome demonstrates that when the load acts on the locking mechanism, even if it is fixed at the center, the efficiency of the locking mechanism is reduced, rendering it structurally ineffective in the SFS. Therefore, it is crucial to avoid applying load directly to the linkage of the locking mechanism. If necessary, the SFS should be designed to resist the load without relying on the locking mechanism as a structural component. These findings underscore the importance of considering the effects of load application and structural imperfections in the design and analysis of the SFS to ensure accurate modeling and reliable performance.

4. Conclusions

The structural behavior of the scissor frame structures (SFS) under the influence of load at the locking mechanism was investigated through experimental investigation and numerical analysis. Based on the outcomes, several significant findings can be summarised as follows:

1. Stress analysis from the experimental study showed that, although scissor members were connected side by side in two planes, the stress remained symmetrical, allowing for simplified numerical modeling assuming single-plane action.
2. Critical stress was measured at the calculated bending moment M_1, closest to the support, indicating the need for careful design consideration near the support.
3. Altering the cross-section does not significantly affect stress distribution but greatly impacts stiffness. Conversely, changing the depth greatly affects stress distribution. Further study is needed to optimise these features.
4. The resistance of each SFS specimen was calculated based on experimental stiffness and stress, as linear behavior is observed during loading. The deflection limit, according to the National Annex of MS EN 1993-1-1, governs the design, since the predicted maximum load was lower than the predicted maximum load based on the yield strength of steel.
5. Validation of FEM with the experimental model showed that when the load acts directly on the locking mechanism linkage, standard FEM, FEM 1 modeling overpredicts rigidity due to overconstraint.
6. Including linkage imperfections in FEM 2 and FEM 3 significantly improved numerical accuracy, aligning results more closely with the physical model.

Acknowledgement

This work was supported by the Ministry of Higher Education under Fundamental Research Grant Scheme (FRGS/1/2023/TK06/UTM/02/6) and Universiti Teknologi Malaysia (04M87).

References

[1] J. J. Moy, C. S. Tan, S. Mohammad, and A. R. Z. Abidin, "State-of-Art review on deployable scissor structure in construction", Structures, 42, 160-180, 2022.
[2] A. S. K. Kwan, "A Parabolic Pantographic Deployable Antenna (PDA)", International Journal of Space Structures, 10(4), 195-203, 1995.
[3] B. Suthar and S. Jung, "Design and Bending Analysis of a Metamorphic Parallel Twisted-Scissor Mechanism", Journal of Mechanisms and Robotics, 13(4), 040905, 2021.
[4] X. Yu, Y. Yang, Y. Ji, and L. Li, "Experimental Study on Static Performance of Deployable Bridge Based on Cable-Strengthened Scissor Structures", Advances in Civil Engineering, 2021, 4373486, 2021.
[5] C. H. Yan and T. A. Aik, "Design and Analysis of Emergency Deployable Bridge", International Journal of Mechanical Engineering and Robotics Research, 9(10), 1393-1399, 2020.
[6] T.-H. Kim, J.-E. Suh, and J.-H. Han, "Deployable truss structure with flat-form storability using scissor-like elements", Mechanism and Machine Theory, 159, 104252, 2021.
[7] K. Roovers and N. De Temmerman, "Deployable scissor grids consisting of translational units", International Journal of Solids and Structures, 121, 45-61, 2017.
[8] K. Roovers and N. De Temmerman, "Geometric design of deployable scissor grids consisting of generalized polar units", Journal of the International Association for shell and spatial structures, 58(3), 227-238, 2017.
[9] S. Krishnan and Y. Liao, "Geometric Design of Deployable Spatial Structures Made of Three-Dimensional Angulated Members", Journal of Architectural Engineering, 26(3), 04020029, 2020.
[10] V. Beatini *et al.*, "Integration of origami and deployable concept in volumetric modular units", Scientific Reports, 12(1), 19180, 2022.
[11] L. Zhu *et al.*, "Conceptual design and fabrication of modular deployable origami structures for architectural-scale applications", Proceedings of IASS Annual Symposia, 2022(9), 1-8, 2022.
[12] K. K. Vu, J. Y. Richard Liew, and K. Anandasivam, "Deployable tension-strut structures: from concept to implementation", Journal of Constructional Steel Research, 62(3), 195-209, 2006.
[13] Y. Akgün, C. J. Gantes, W. Sobek, K. Korkmaz, and K. Kalochairetis, "A novel adaptive spatial scissor-hinge structural mechanism for convertible roofs", Engineering Structures, 33(4), 1365-1376, 2011.
[14] J. G. Cai, Z. Ye, X. Y. Wang, Y. X. Xu , and J. Feng, "Static and kinematic behaviour of a foldable truss roof structure", Advanced Steel Construction, 14(4), 14, 2017.
[15] V. S. Rajashekhar, K. Thiruppathi, and R. Senthil, "Modelling, Simulation and Control of a Foldable Stair Mechanism with a Linear Actuation Technique", Procedia Engineering, 97, 1312-1321, 2014.
[16] C. J. Gantes, *Deployable structures: analysis and design*. Boston: WIT Press, 2001.
[17] P. Fernández-Serrano, "Martino.:“The ‘movable Theatre’from Emilio Pérez Piñero. A Space-time Journey.”", Proceeding of the II National Congress of Pioneros de la arquitectura moderna Española: aprender de una Obra. Foundation Alejandro de la Sota, 2, 469-479, 2015.
[18] F. Escrig, J. Perez Valcarcel, and J. Sanchez, "Deployable cover on a swimming pool in Seville", Journal of the International Association for Shell and Spatial Structures, 37(1), 39-70, 1996.
[19] N. F. Dinevari, Y. Shahbazi, and F. Maden, "Geometric and analytical design of angulated scissor structures", Mechanism and Machine Theory, 164, 104402, 2021.
[20] K. K. Vu, J. Y. R. Liew, and K. Anandasivam, "Deployable Tension-Strut Structures: Structural Morphology Study and Alternative Form Creations", International Journal of Space Structures, 21(3), 149-164, 2006.
[21] F. Escrig, "Expandable space structures", International Journal of Space Structures, 1(2), 79-91, 1985.
[22] A. Kaveh and A. Davaran, "Analysis of pantographic foldable structures", Computers & Structures, 59(1), 131-141, 1996.
[23] W. Shan, "Computer analysis of foldable structures", Computers & Structures, 42(6), 903-912, 1992.
[24] T. Kokawa, "A trial of expandable arch," in *Proc. of IASS Symposium in Milano*, 1995, vol. 1, pp. 501-510.
[25] B. Willems, W. Dewulf, and J. R. Duflou, "Active snap-fit development using topology optimization", International Journal of Production Research, 45(18-19), 4163-4187, 2007.
[26] J. Pérez-Valcárcel, M. Muñoz-Vidal, F. Suárez-Riestra, I. R. López-César, and M. J. Freire-Tellado, "Deployable cylindrical vaults with reciprocal linkages for emergency buildings", Structures, 33, 4461-4474, 2021.
[27] J. Ma and T. Welo, "Analytical springback assessment in flexible stretch bending of complex shapes", International Journal of Machine Tools and Manufacture, 160, 103653, 2021.
[28] J. Muñoz, G. Jelenić, and M. A. Crisfield, "Master–slave approach for the modelling of joints with dependent degrees of freedom in flexible mechanisms", Communications in Numerical Methods in Engineering, 19(9), 689-702, 2003.
[29] DOSM, "Malaysia National Annex To Eurocode 3: Design of Steel Structures - Part 1-1: General Rules and Rules For Buildings", 2010.

Advanced Steel Construction – Vol. 20 No. 2 (2024) 169–178
DOI: 10.18057/IJASC.2024.20.2.9
(Special Issue: *11st International Conference on Advances in Steel Structures, ICASS'2023, Kuching, Sarawak, Malaysia*)

SUPER-RESOLUTION RECONSTRUCTION AND HIGH-PRECISION TEMPERATURE MEASUREMENT OF THERMAL IMAGES UNDER HIGH-TEMPERATURE SCENES BASED ON NEURAL NETWORK

Yi-Chuan Dong, Jian Jiang *, Qing-Lin Wang, Wei Chen and Ji-Hong Ye

Jiangsu Key Laboratory of Environmental Impact and Structural Safety in Engineering, Xuzhou, China
** (Corresponding author: E-mail: jian.jiang@cumt.edu.cn)*

ABSTRACT

Accurate temperature readings are vital in fire resistance tests, but conventional thermal imagers often lack sufficient resolution, and applying super-resolution algorithms can disrupt the temperature and color correspondence, leading to limited efficiency. To address these issues, a convolutional network tailored for high-temperature scenes is designed for image super-resolution with the internal joint attention sub-residual blocks (JASRB) efficiently integrating channel, spatial attention mechanisms, and convolutional modules. Furthermore, a segmented method is developed for predicting thermal image temperature using color temperature measurements and an interpretable artificial neural network. This approach predicts temperatures in super-resolution thermal images ranging from 400 to 1200°C. Through comparative validation, it is found that the three-neuron neural network approach demonstrates superior prediction accuracy compared to other machine learning methods. The seamlessly combined proposed super-resolution architecture with the temperature measurement method has a predicted RMSE of 20°C for the whole temperature range with over 85% of samples falling within errors of 30°C.

ARTICLE HISTORY

Received: 4 June 2024
Revised: 4 June 2024
Accepted: 11 June 2024

KEYWORDS

High-temperature scene;
Infrared thermal imaging;
Neural networks;
Image super-resolution;
Color temperature prediction

1. Introduction

Steel structures, despite their widespread use, suffer from poor fire resistance, leading to significant performance degradation, as exemplified by the loss of mechanical properties in portal frames at 600°C [1]. To tackle this problem, fire resistance testing is crucial for assessing component performance under high temperatures. During the test, obtaining comprehensive and precise temperature data is paramount. While thermocouples offer reliable measurements, they are limited to single points and prone to failure, compromising efficiency. Infrared thermal imaging cameras offer a solution by capturing the entire two-dimensional temperature field. However, their high cost and low-resolution present challenges, particularly in medium to large-scale fire tests, where detailed temperature data are essential.

The limited resolution of thermal imagers hinders the acquisition of optimal temperature data in experiments, and the small temperature matrix fails to precisely represent spatial temperatures, thus sparking interest in enhancing the resolution of instruments for production and cost challenges [2]. As a result, algorithmic image processing emerges as a cost-effective and efficient alternative. The existing interpolation methods [3] are swift, but their effectiveness is limited, especially when dealing with large scaling factors. Reconstruction-based super-resolution techniques [4,5], which leverage prior knowledge and predefined data dictionaries, offer superior image reconstruction but increase workload and reduce processing speed.

With the advancement of artificial intelligence, the convolutional neural network (CNN) based method has emerged as the preferred approach due to its strong learning ability and flexible adjustability [6,7,8]. Utilizing the CNN architecture, this method seamlessly transforms low-resolution images (LR) into super-resolution versions (SR), ensuring close resemblance to the original high-resolution images (HR).

Multiple studies have focused on refining the CNN super-resolution architecture, incorporating advancements such as residual learning, image sampling, and attention mechanisms [9]. Residual learning, embodied in models such as Very Deep Super-resolution Network (VDSR) [10], Deeply-recursive Convolutional Network (DRCN) [11], Deep Recursive Residual Network (DRRN) [12], and Enhanced Deep Residual Super-resolution Network (EDSR) [13], boosts the learning capacity through modular expansion and skip connections. Image sampling, enhanced by Shi et al. [14] with subpixel convolution, efficiently converts channel data to spatial features. Zhang et al. [15] combined channel attention [16,17] with residual blocks in their model, creating a high-efficiency module (RCAB). This integration maximized the benefits of the attention mechanism but still had an issue by introducing residual scaling.

In comparison to the aforementioned visible light image SR model, research on thermal image processing is more constrained. Initial super-resolution models for thermal images were primarily derived from visible light models: including Thermal enhancement network (TEN) [18], Brightness-Based Network [19], and GAN architecture [20]. A significant hurdle in thermal image processing research is the challenge of acquiring high-quality and highly pertinent datasets. Public thermal image datasets [21,22] predominantly feature infrared grayscale images from everyday settings. These single-channel images offer limited assistance in training three-channel color thermal models, thus yielding subpar outcomes. Additionally, existing models often lack tightly integrated attention and residual learning mechanisms, leading to bulky networks. He et al. [23] employed a two-stage cascade architecture for ×8 super-resolution, progressively restoring the image size from ×2 to the desired target. While effective for learning multi-scale features, its focus on large scaling factors results in a sizable model with reduced operational efficiency. These studies mainly focused on image resolution, ignoring its suitability for temperature measurement. Even with super-resolution techniques, the altered color, temperature logic, and image format make the enlarged images incompatible with thermal analysis software.

Infrared thermal imagers in the domain of image temperature measurement utilize the blackbody radiation correlation formula to determine the color-temperature correspondence for each pixel [24]. However, existing color temperature measurement algorithms designed for high temperatures, such as two-color method [25], laser speckle photography [26], and image fusion techniques [27], often demand sophisticated and costly optical devices along with stable, vibration-free systems. Their intricate setup and restrictive measurement requirements pose significant challenges for direct application in high-temperature environments.

Prediction models based on machine learning only need to be given input characteristics to predict the target, and this method has effectively proven its worth in a range of detection tasks related to fire [28,29,30] and structural engineering [31,32,33]. Sun et al. [34] introduced an enhanced BP network for adaptive spatial data sensing to measure tunnel ceiling temperatures. Its efficacy was validated through tunnel fire tests, with a prediction error of just 0.12 under dimensionless scaling. Chen et al. [35] proposed a machine learning method for structural analysis, incorporating a Physics-Informed Neural Network (PINN) to steer the training process. When dealing with small datasets, the prediction of the neural network closely resembles the results obtained from finite element software. The applicability and accuracy of this method were verified through four sets of examples. Wang et al. [36]

introduced an inverse model utilizing a Graph Neural Network (GNN) to address structural parameter identification from structural responses. This model transforms the truss structure into a GNN graph, delivering precise inversion outcomes even with limited data. Its strong interpretability and high potential in structural analysis make it a valuable tool. Sharifi et al. [37] employed artificial neural networks to assess the load-bearing capacity of various corroded steel beams under localized loads, accurately predicting the failure of these deteriorated beams.

In this paper, a specialized CNN architecture designed for high-temperature environments was proposed to address the challenges of low-resolution thermal images and the incompatibility of super-resolution techniques for temperature readings in fire tests, as is shown in Fig. 1. This architecture was enhanced with the Joint Attention Sub-Residual Block (JASRB), generated precise, high-definition color and temperature mappings. A temperature measurement approach utilizing artificial neural networks was developed for super-resolution images. Fire tests were conducted to validate the accuracy of the separated approach and their combination.

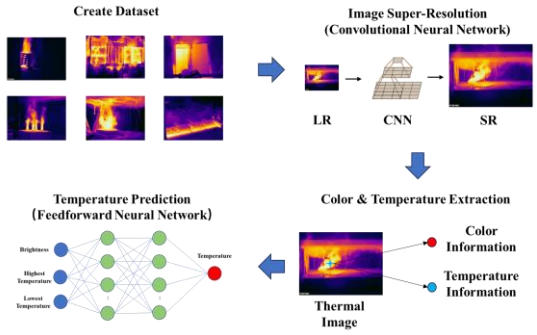

Fig. 1 Overall architecture of super-resolution network

2. Super-resolution of thermal images

The proposed architecture is an innovative thermal image super-resolution (SR) network that features a multi-path structure with JASRBs. It has four main parts: the LR image processing part (Part 1), the preliminary clarification part (Part 2), the fine recovery part (Part 3), and the image reconstruction part (Part 4). The core of the architecture lies in the preliminary clarification and fine recovery parts, which use different JASRB configurations.

2.1. Inputs and Outputs

The proposed architecture is designed to enhance thermal imaging resolution by utilizing pairs of low and high-resolution images for network training. To faithfully replicate LR images captured by budget thermal cameras, HR images are down-sampled by a scale factor of four. The degradation function for this process can be stated as follows.

$$I_{LR}=D(I_{HR};\delta) \tag{1}$$

Where I_{LR} denotes the original low-resolution image; while D signifies the Bicubic image interpolation function employed for image degradation mapping; I_{HR} represents the high-resolution image, and δ, represents the scaling factor, is set to 4 in this context.

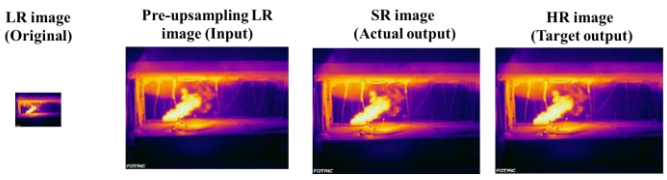

Fig. 2 Input and Output of the CNN architecture

The input to the CNN is a low-resolution image that has undergone Bicubic interpolation for pre-upsampling (Fig. 2). This interpolation ensures that the image size matches the target high-resolution (HR) image, despite the internal clarity remaining insufficient. The objective of CNN is to produce a high-resolution image, with the actual output being a super-resolution (SR) image. In practical scenarios, the HR image remains unknown. Hence, the primary goal of this undertaking is to align the SR image closely with the HR image, thereby elevating the thermal image quality in unfamiliar settings. Nonetheless, discrepancies often arise between the actual and target outputs, necessitating optimization to narrow this divergence.

2.2. Network architecture

As shown in Fig. 3, the LR image processing part preprocesses input imagery, adjusting dimensions with bicubic interpolation to match the specifications of the RGB input layer. It then segments RGB images into 48×48×3 patches for network training. The details of hyperparameter settings for the first convolutional layers in each part are listed in Table 1.

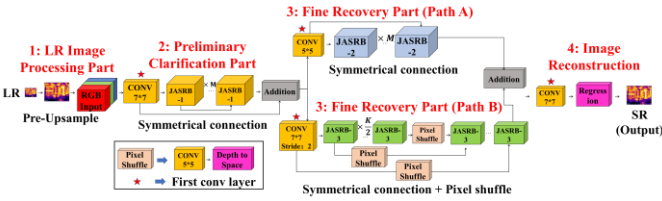

Fig. 3 Overall architecture of super-resolution network

Table 1
Parameters of the first convolutional layer of each part of the network

Position	Num Filters	Kernel Size	Stride
Part 2	48	7*7	1
Part 3 Path A	64	5*5	1
Part 3 Path B	64	7*7	2
Part 4	3	7*7	1

The preliminary clarification part aims to extract prominent features from thermal images using convolutional layers with few filters for efficiency. The large-scale features, often comprising shallow details like scene structure, can be adeptly extracted via convolutional layers with few filters. It employed a 7×7 receptive field, zero-padding, and stacked M JASRBs with symmetric connections to minimize shallow feature loss. The output is a 48×48×48 feature map.

The third segment restores intricate details using multi-path learning, converging diverse features from varying receptive fields. Learning image details is more challenging than shallow features due to their intricate link with large structures, leading to easy loss or misinterpretation [23]. Therefore, more extensive parameter learning is required. Similar to the preliminary clarification part, Path A amplified the filter and stacked M JASRBs used for deeper abstraction, while Path B halved the image size and introduced K JASRBs (where K is an even number) with pixel shuffling [14] to obtain different details from Path A. Finally, the segment used the element-wise addition layer to fuse the features from both paths, resulting in a 48×48×64 output patch.

The final part, the image reconstruction part, used a 3-channel convolutional layer to resize the output to RGB dimensions. A 7×7 convolution kernel aggregated features and a regression prediction layer produced the SR image.

This architecture used half-mean-square error loss as the loss function of the neural network, which can be expressed as:

$$Loss=\frac{1}{2}\sum_{p=1}^{HWC}(t_p-y_p)^2 \tag{2}$$

where H, W, and C denotes the height, width, and number of channels of the input image, respectively; t and y denote the target image and the image predicted by the network, respectively; p is linearly indexed into each element of t and y.

2.3. Joint attention sub-residual block (JASRB)

The performance of the network is primarily defined by the architecture, which consists mainly of JASRBs. Traditional modules such as RCAB, which integrate channel attention and residual modules, often yield limited benefits since channel attention alone may not significantly aid training. This holds

especially true in the case of thermal images, where color consistency restricts the amount of information obtainable from color channels, thereby highlighting the significance of spatial attention. Therefore, relying solely on channel attention mechanisms can lead to deficient learning ability, impeding deep network training. To address this, a custom spatial attention module was innovatively combined with the existing channel attention module within the RCAB framework.

The overall structure of the JASRB is shown in Fig. 4, which consists of three parts: the Convolution Module (CM), the Channel Attention Module (CAM, Fig. 4b) [15], and the proposed Spatial Attention Module (SAM, Fig. 4c). The channel attention module compacts the feature graph and generates the channel weight matrix of 1×1×*C*. It demonstrates the significance of every channel in the feature map subsequent to the output of CM. The details of hyperparameter settings for the convolutional layers in each JASRB are listed in Table 2. All kernels in Table 2 are 3×3 in size with a stride of 1, ensuring network consistency and efficiency.

Table 2
Number of filters of each JASRB in different parts

Location	Num Filters	Kernel Size	Stride
CM Conv1	192	256	128
CM Conv2	48	64	64
SAM Conv1	64	64	64
SAM Conv2	1	1	1
CAM Conv1	10	10	10
CAM Conv2	48	64	64

A spatial attention extraction block consists of two convolutional layers activated by the ReLU function [38]. The first convolution layer maps the features directly to the higher-dimensional space and learns them, while the second convolution layer integrates them into the one-dimensional space. This combination is straightforward and can generate a weight matrix of size *H*×*W*×1, representing the more important spatial position in the image. The expression for this part is as follows:

$$F_s=\omega_I*max(0,\omega_E*\mathrm{F}_o+b_E)+b_I \tag{3}$$

$$g=\frac{1}{1+e^x} \tag{4}$$

$$s_{CA}=g(F_s) \tag{5}$$

where F_s denotes the features learned through spatial attention; ω_E, b_E and ω_I, b_I respectively denotes the weights and biases of the first and second convolutional layers of the proposed spatial attention extraction block, that is, the internal weights and other information of the feature learning layer and the feature integration layer; F_o represents the original features; g denotes the Sigmoid function and s_{CA} denotes the final spatial attention matrix.

The output of the entire block can then be expressed as:

$$X_i=\omega_{i|2}*max(0,\omega_{i|1}*F_o+b_{i|1})+b_{i|2} \tag{6}$$

$$F_i=F_{i\text{-}1}+(s_{CA}*s_{SA}*X_{i\text{-}1}) \tag{7}$$

where $\omega_{i|1}$, $b_{i|1}$ and $\omega_{i|2}$, $b_{i|2}$ denotes the weights and biases of the first convolutional layer and the second convolutional layer in the residual block respectively; X_i and $X_{i\text{-}1}$ are the residual information between the current layer and the previous layer after learning; $F_{i\text{-}1}$ and F_i denotes the output features of the current layer and s_{CA}, s_{SA} is the channel and spatial attention feature matrix in current layer, respectively.

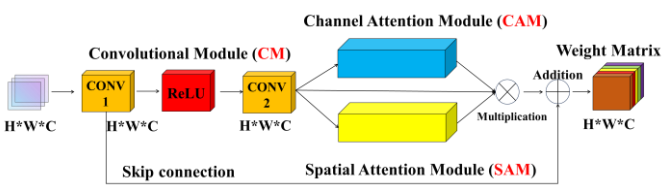

(a) Joint attention sub-residual block (JASRB)

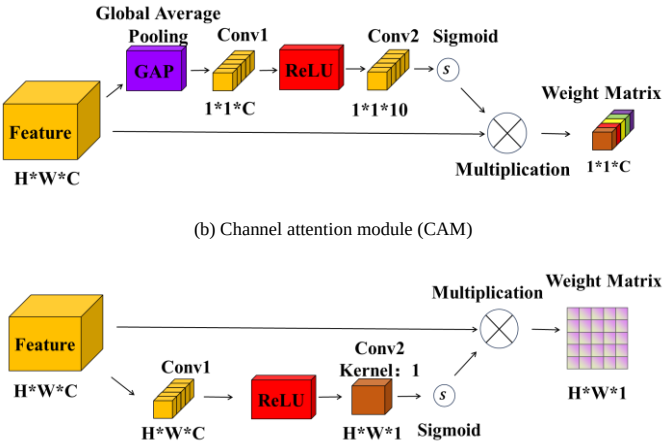

(b) Channel attention module (CAM)

(c) Spatial attention module (SAM)

Fig. 4 Architecture of CAM, SAM and JASRB

By integrating both channel and spatial attention mechanisms within the skip connection, improved residual scaling efficiency and enhanced learning of spatial image features can be achieved, as evident in sections 2.4.2.2 and 2.4.3.3.

2.4. Training of the convolutional neural network

2.4.1. Training details

The GPU used for training was NVIDIA GeForce RTX3060Ti, and the CPU was Intel Core i7-10700CPU. During the training process, the minibatch size was set to 32, and the optimizer was Adam optimization [39]. For a total of 100 epochs of training (a total of 120000 iterations), the learning rate was set to 0.001 and decreased to half of the original value every ten rounds during the training process. Each training image was randomly cropped into 64 patches, with random shuffling performed in each iteration, and L2 regularization was applied to prevent the gradient from being excessively large. The network training platform was MATLAB R2022b. The initial weight and bias learning rate of the convolution layer were set as 1.

2.4.2. Dataset

In this study, 750 thermal images were employed, which were partitioned into a training set comprising 600 images, a validation set of 50 images, and two test sets, each containing 50 images. The first test set served for the ablation study aimed at refining the architectural hyperparameters, whereas the second test set was utilized for the ultimate model comparison. This approach mitigated the risk of hyperparameter optimization outcomes being exclusively tailored to a subset of the dataset. Fig. 5 displays a schematic overview of the thermal images dataset captured in various fire scenes, along with the shooting equipment. Utilizing thermal images from diverse scenes enhances the generalization of CNN and elevates the quality of training.

The Fotric348 series handheld thermal imager was employed, boasting a 640×480 thermal image resolution. The specially formatted images of the instrument can export the temperature matrix using the software of the manufacturer, AnalyzIR. Its uncooled infrared focal plane detector has a response band of 7-14μm and can detect temperatures between -20°C and 1200°C. Thermal image emissivity is set to 0.95, in this part, emissivity does not affect the quality of the image. The reasons for using this setting are explained in detail in section 3.4.1.

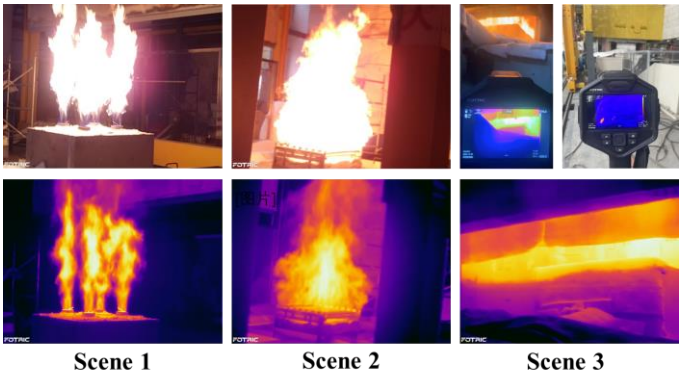

Fig. 5 Shooting equipment and some scenes

The thermal imager was positioned 4~15m from the fire source to obtain the pictures, and such shooting distance is typical for civil engineering applications. To ensure stability and prevent focusing issues due to external factors, a tripod was used throughout the image capture process.

2.5. Experimental simulation

2.5.1. Evaluation index

The evaluation metrics for the proposed super-resolution network include Peak Signal-to-noise Ratio (PSNR), Structural Similarity (SSIM), and Natural Image Quality Evaluator (NIQE) [10]. PSNR measures the difference between HR and SR images based on the maximum pixel value and root mean square error. The calculation formula of PSNR is:

$$PSNR=10log_{10}\frac{peakval^2}{MSE(A,Ref)} \tag{8}$$

where *peakval* specifies the range of the image data type. For 8-bit images, the *peakval* value is 255; *MSE (A, Ref)* represents the mean square error between the specified image *A* and the reference image *Ref*. A higher PSNR indicates smaller differences, with values between 30 and 40 considered acceptable distortion loss and above 40 indicating near-original quality.

SSIM assesses the similarity of two images by evaluating brightness, contrast, and structure independently, ranging from 0 (no similarity) to 1 (identical images). The calculation formula of SSIM is:

$$SSIM(x,y)=[l(x,y)]^{\alpha}\cdot[c(x,y)]^{\beta}\cdot[s(x,y)]^{\gamma} \tag{9}$$

$$l(x,y)=\frac{2\mu_x\mu_y+C_1}{\mu_x^2\mu_y^2+C_1} \tag{10}$$

$$c(x,y)=\frac{2\sigma_x\sigma_y+C_2}{\sigma_x^2\sigma_y^2+C_2} \tag{11}$$

$$s(x,y)=\frac{\sigma_{xy}+C_3}{\sigma_x\sigma_y+C_3} \tag{12}$$

where $l(x,y)$, $c(x,y)$ and $s(x,y)$ represent brightness term, contrast term and structure term respectively; μ_x, μ_y, σ_x, σ_x and σ_{xy} represent the local mean, standard deviation and cross-covariance of the image *x*, *y*. C_1, C_2 *and* C_3 represent three constants respectively, where $C_1=(K_1L)^2$, $C_2=(K_2L)^2$, $C_3=0.5^* C_2$. K_1 and K_2 are 0.01 and 0.03 respectively, and *L* represents the pixel value range, which is 255 for 8-bit images.

NIQE, which does not require a reference image, assesses naturalness by measuring distribution differences against multivariate natural scenes, with lower values indicating better visual quality in line with human perception [40].

2.5.2. Ablation study

To validate the hyperparameter settings, the impact of spatial attention mechanisms, and the use of double residual scaling factors, three ablation tests were conducted to assess the optimal number of network modules, evaluate the significance of JASRB components, and verify the residual scaling approach within JASRB.

2.5.2.1. JASRB module quantity analysis

The number of JASRBs in the two paths in the network determines the prediction accuracy and other critical indicators of the neural network. The output of this super-resolution task will be used in image temperature recognition. Any inaccurate prediction may significantly affect the temperature output, and therefore the SR image should be as clear as possible.

The number *M* of two modules was set from 3 to 5, and the module number *K* of path B was set as 2 or 4. Table 3 shows the prediction results of different module numbers. Since the learnable parameters of the comparison module did not increase significantly, and the images were relatively clear, the changes of indicators were relatively small. The clearer the image, the more difficult it is to restore. The reason for the fact is that only the delicate parts of the image were left, and it was also challenging to discover them. The improvement of index represents the degree of the repair of details, every increase of 0.1 in PSNR is more helpful for detail recovery. These details hardly have a significant impact on the indicators, but they do have a great impact on the image temperature measurement in the third section of the paper.

Table 3
Number of JASRBs

Number of *M* and *K*	PSNR(dB)	SSIM	Time(s)
3, 4（baseline）	39.9947	0.9986	1.55
3, 2	39.9626	0.9986	1.32
4, 2	40.0961	0.9986	1.56
4, 4	40.2143	0.9987	1.57
5, 2	39.7860	0.9986	1.72
5, 4	0	0	0

As the number of modules increased, the network training effectiveness improved until *M* reached 5, whereupon performance started to deteriorate, signifying the peak capacity of network. Adding more depth beyond this point failed to facilitate meaningful learning. Furthermore, as the module count *K* rose, gradient explosion ensued, leading to unbounded training losses. When considering single-image reconstruction time, using the minimum number of modules yielded the fastest computation. Nevertheless, prioritizing image quality, the model with both *M* and *K* set to 4 emerged as the optimal choice.

2.5.2.2. Internal importance analysis of JASRB

To validate the significant impact of incorporating spatial attention on the network, and to precisely assess the importance of each submodule for guiding parameter adjustment, a submodule with minimal parameters was employed as the baseline model. Subsequently, a comparison was made by elevating the parameters of the three respective submodules to a certain level.

The comparison results, summarized in Table 4, revealed that the SAM was nearly as crucial as the CM, while the CAM had a more negligible contribution. Specifically, the PSNR of the CM and SAM increased by 0.5167 and 0.4973, respectively. The superior performance of the residual block can be attributed to its direct connection with the original information, preventing information loss during interlayer transfers. The improvement of proposed SAM closely approached the optimal value, despite not being directly linked to the original features.

Table 4
Comparison of the importance of each part of the sub-module

Models	PSNR(dB)	SSIM	Parameters
Baseline model	38.0406	0.9976	212.3k
Add parameters in CM	38.5573	0.9980	378.3k
Add parameters in CAM	38.2125	0.9977	379.1k
Add parameters in SAM	38.5379	0.9979	380.1k

Therefore, the CM and SAM should be considered more when assigning learnable parameters. This principle was followed when deciding the parameters within the module in this paper.

2.5.2.3. Residual scaling

Residual scaling, the practice of multiplying residuals by a coefficient ranging from 0 to 1, aims to enhance network stability and accuracy. Typically, based on prior research, this scaling factor was set between 0.1 and 0.3 [13,41]. Nevertheless, this approach lacks adaptability as it uniformly applies the same factors across both shallow and deep network layers, potentially leading to over- or under-scaling that can hinder network performance.

In contrast, JASRB introduce two attention modules that learn the residual scaling value dynamically. These modules serve dual purposes: as weight matrices of attention mechanisms and as residual scaling factors.

To validate the superiority of the proposed method over empirical coefficient settings, several comparative experiments were conducted: A. Using learnable residuals scaling of SAM and CAM (the proposed method); B. Replacing the spatial attention with a scaling layer with a fixed parameter of 0.2, which corresponds to a small scaling coefficient; C. Replacing the SAM with a scaling layer with a fixed parameter of 0.8, which corresponds to a large scaling coefficient; D. Without any attention, connect the residuals directly to a scaling layer with a fixed parameter of 0.2. E. Use CAM only (RCAB method). All tests only employed one module to ensure identical amounts of learnable parameters across methods, resulting in minimal variations in RSNR and SSIM, while still illustrating the impact of incorporating various methods.

The results in Table 5 show that method A achieved the best results, indicating that the proposed method was the best. Meanwhile, the comparison of methods B and D revealed that the effect of using attention was consistently better than that of setting residual scaling by experience. The comparison of methods B and C shows that a lower scaling factor was generally better, which was the similar trend in the reference [40]. Method E revealed that single-channel attention struggled to learn image features effectively, and its residual scaling was also inadequate.

Table 5
Comparison of different residual scaling methods

Methods	PSNR(dB)	SSIM
A	38.7357	0.9981
B	38.0389	0.9977
C	37.9230	0.9976
D	36.7100	0.9975
E	34.5550	0.9954

In addition, if only a single type of attention mechanism was used (Method E), the residual scaling coefficient was directly the attention weight matrix. Only one attention matrix may still lead to a high scaling coefficient, and these points may still not be fully scaled. In the proposed approach, two attention matrices were multiplied and the resulting joint attention matrix consisted of very small values. This ensured that the pixels not been fully scaled were further scaled. Essentially, the joint matrix imposed a stronger scaling effect on those features, and this scaling effect was adaptively learned.

Fig. 6 and Fig. 7 depict the training progress of the refined model following ablation test optimization. During the initial training phase, both the loss function and root mean square error undergo fluctuations before steadily declining to zero. Additionally, the high validation frequency of the validation set (every 50 iterations) appears to cause slight oscillations, but these remain within an acceptable range of 0~1. Hence, it can be inferred that the network has been effectively trained.

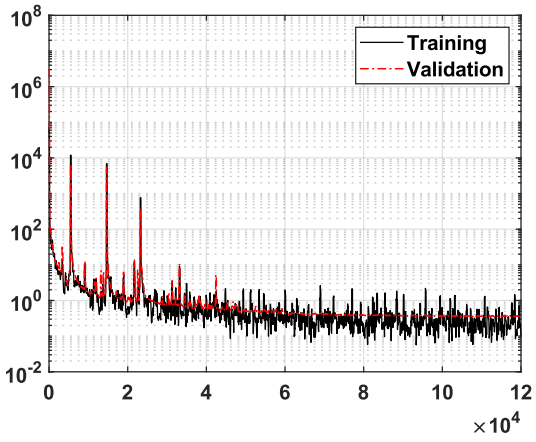

Fig. 6 Training process: loss function

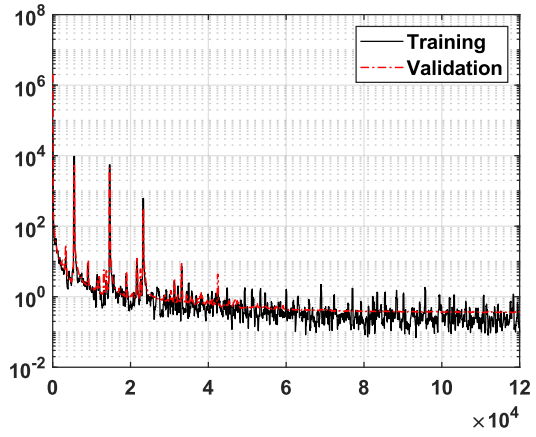

Fig. 7 Training process: Root mean square error

2.6. Training results

The proposed method was compared with four super-resolution techniques: bicubic [3], EDSR [13], PAN [42], and GSRTI [43] which are renowned for their performance in image enhancement. These methods incorporate various modules such as residual blocks and attention mechanisms.

EDSR, PAN and GSRTI were replicated using Matlab deep network designer, adhering to the architecture of the original paper. The main difference between the original model and our replication is the use of MSE loss, as we prioritized architectural performance and considering that the PSNR and SSIM by MSE loss is comparable to other loss functions [44]. All models used the training and test sets outlined in section 2.4.2, undergoing 100 training rounds totaling 240,000 iterations.

Table 6 and Fig. 8 present reconstruction results alongside others. The proposed method excelled in all evaluation metrics. Bicubic and GSRTI showed limited improvement. While EDSR and PAN offered some clarity, their PSNR and SSIM scores were notably lower due to color correspondence issues. Specifically, in the RGB color model, the same color can be represented by multiple different RGB values. The evaluation metrics revealed that the EDSR and PAN models learned incorrect dolor correspondence relationships. Conversely, the proposed method excelled in indicator results and image clarity with no color correspondence errors and closely resembling the HR image, and exhibited competitive performance.

Table 6
Comparison between the SR method in this paper and other methods

Methods	PSNR(dB)	SSIM	NIQE
Bicubic	32.4	0.9938	5.6395
EDSR	24.457	0.9804	5.0797
PAN	21.951	0.9476	4.9926
GSRTI	32.635	0.9942	5.1761
Proposed	40.129	0.9987	4.8965

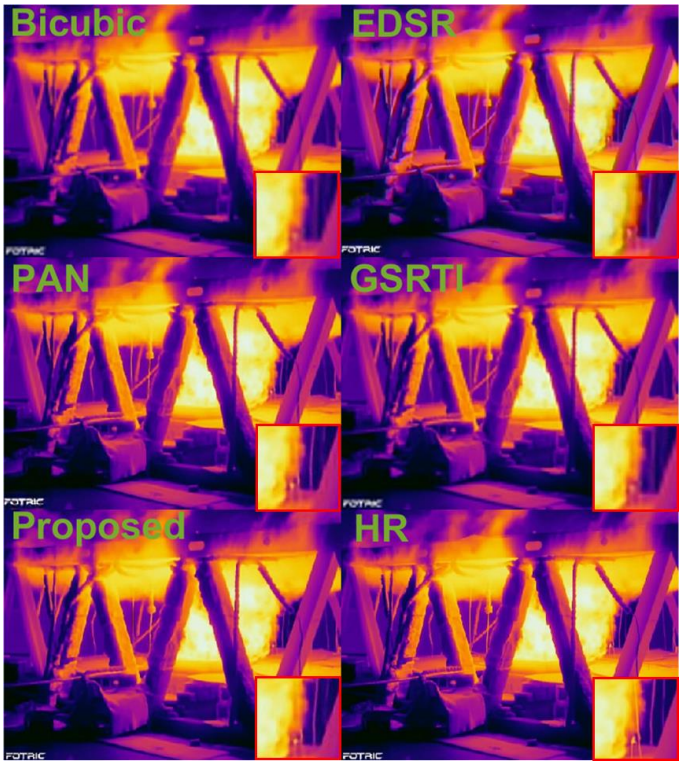

Fig. 8 Sample of the reconstructed image

3. Prediction of image temperatures

3.1. Prediction method

Enhancing image resolution alone is insufficient to justify the use of SR images for temperature measurement. Consequently, there is an urgent need to devise a temperature measurement method for SR images that spans a wide

range. In current unenclosed space fire tests, the peak temperature, influenced by fuel, seldom exceeds 1200°C [1,45]. Thus, a temperature measurement range of 400 to 1200 °C was selected.

In thermal imaging, a given color can signify varying temperatures. This is due to the fixed color scale but adjustable temperature range during imaging. This complexity makes it challenging for CNN to predict temperature distributions across various scenes. Additionally, the efficiency of CNN is constrained by its architecture, leading to slow training and application. Contrary to CNN, Artificial Neural Networks (ANNs) only need some pixels from the thermal image along with their corresponding temperatures to learn the color-temperature relationship. This simplified approach can then be directly applied to measure specific points in positional thermal images, enhancing deployment efficiency and streamlining the temperature prediction process compared to CNN.

An ANN-based method was proposed. Since the temperature range involved in high-temperature scenarios is extensive, using one neural network to predict all pixels to be measured within 1200°C directly is tough, and its training requires too many samples. As shown in Fig. 9, the temperature samples were divided into eight segments from 400°C to 1200°C with a temperature difference of 100°C. Correspondingly, eight simple ANN models were established, and each was tailored to correspond with a specific temperature segment.

Meanwhile, datasets were made for each ANN model. The dataset was then divided into many small sections every 100°C. For images falling within a specific temperature difference segment, pixels are consistently classified into corresponding small temperature sections based on their actual temperature, while also saving pixel color and the temperature information of the entire image. This information serves as the input and output for the ANN, as further detailed in section 3.2.

The case in Fig. 10 shows the overall progress of the section of 900°C. The first small square in the upper left corner represents the data with a small temperature segment of 900~1000°C, which is the highest temperature range in this situation. The lowest temperature in the lower right corner is from 0 to 100°C, which represents the lowest temperature range.

Datasets were made and trained separately for HR and SR images, and the corresponding model was trained using the corresponding sample sets to ensure the accuracy of the network.

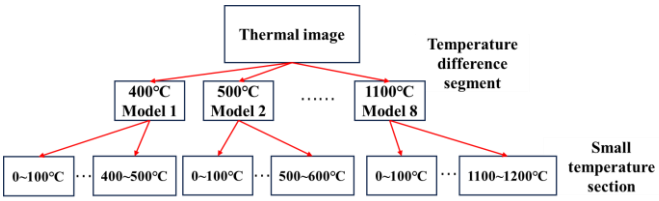

Fig. 9 Temperature division scheme

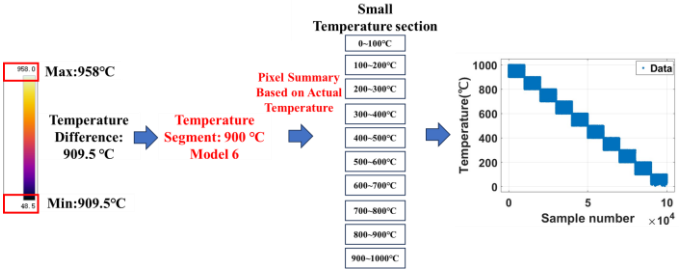

Fig. 10 Sample selection process of each small temperature range in the 900°C temperature difference section

3.2. Network architecture

In every ANN model, the input consists of the brightness value of a specified pixel in the thermal image, as well as the maximum and minimum temperature values from the corresponding thermal image, and the model outputs the estimated temperature of that specified point. Temperature recognition was performed using a single hidden layer feedforward neural network, the structure of which is shown in Fig. 11.

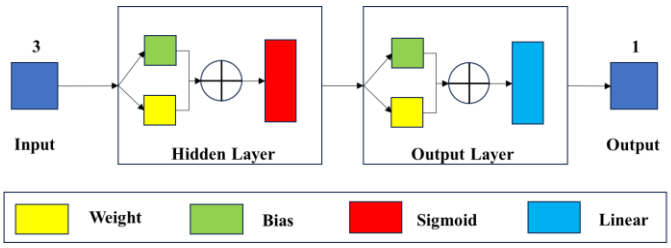

Fig. 11 Artificial neural network architecture

Given the wide temperature range and the need to train multiple neural networks with large sample sizes, efficiency becomes crucial. The Levenberg-Marquardt backpropagation algorithm [46] was utilized in this study, combining the best gradient descent and Gauss-Newton methods. This approach ensures both rapid convergence near the optimal solution and robustness even when far off, and it uses the MSE loss as the loss function. The algorithm is calculated as follows:

$$X_{k+1}=X_k-\left[J^TJ+\mu I\right]^{-1}J^Te \tag{13}$$

where X_k and X_{k+1} represent the current and next solution vectors respectively; J represents the Jacobian matrix; μ is the damping factor; I represents the Identity matrix; e represents the error vector.

The cornerstone of this approach lies in the utilization of a damping factor μ for adaptive adjustment during iterations. When μ is set to zero, the algorithm transforms into the Newton method, renowned for its rapid and precise convergence near the error minimum. Conversely, as μ increases, the algorithm shifts towards the gradient descent method. The ultimate objective is to transition to the Newton method as swiftly as possible, with μ undergoing adaptive reduction in each iteration, thereby ensuring efficiency and accuracy in neural network training.

3.3. Interpretation of neural network model

The black box characteristic of artificial neural networks limits their transparency, as they can only produce predictions without explaining how those predictions are generated. ANNs cannot reveal the specific influence and rationale behind each effect of the input on the prediction outcomes, thereby challenging the trustworthiness of the model [47]. The Shapley additive interpretation proposed by Lundberg et al. [48] can quantify the contribution of each feature in the ANN and consider the mutual influence between features. The Shapley value of the i-th feature of query point x is defined by the value function v:

$$\varphi_i(v_x)=\frac{1}{M}\sum_{S\subseteq\mu\{i\}}\frac{v_x(S\cup\{i\})-v_x(S)}{\frac{(M-1)!}{|S|!(M-|S|-1)!}} \tag{14}$$

where M is the number of features; μ is the set of all features; $|S|$ is the number of elements in set S; $v_x(S)$ is the value function of the feature of measurement point x in set S, and its value represents the expected contribution of the features in S to the prediction of measurement point x.

The Shapley value is primarily utilized for explaining local samples, which involves multiple neural networks with tens of thousands of samples each, incurs extremely high computational costs. To circumvent this, four extreme temperature scenarios was used to interpret the relationship of the input arguments and the output argument in the proposed neural network models: a. A neural network temperature segment operating within 400°C (spanning from 0~500°C), specifically measuring temperatures within the range of 400 to 500°C. b. The same neural network temperature segment as in scenario a, but now measuring temperatures only within the range of 0~100°C. c. A neural network temperature segment operating within 1100°C (spanning 0~1200°C), particularly attending to temperatures within the bracket of 1100~1200°C. d. The neural network temperature segment from scenario c, but with a focus on temperatures within the interval of 0~100°C.

Fig. 12 shows the Shapley values for the features of the SR neural network model in the four scenarios. These values revealed the significance of the three inputs of the neural network. The color, crucial in thermal imaging for temperature detection, was reflected by brightness, which had high Shapley values. The network also used max and min temperature values to control the temperature measurement range. While these two features cannot determine temperature directly, they played a key role in controlling the

temperature output results in different temperature ranges.

In scenarios a and c, where the temperature measurement ranges align with the highest temperatures reachable by their respective neural networks, the neural network inputs positively impact the output, driving the network to output high-temperature predictions. Conversely, in the extreme low-temperature cases of b and d, the Shapley values are uniformly negative, indicating that the input features decrease the output temperature.

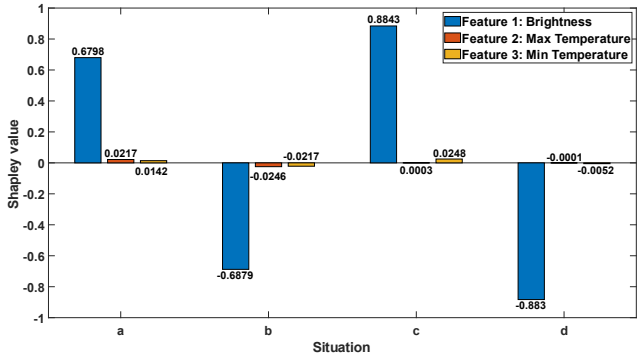

Fig. 12 Shapley values of SR model under four extreme temperature scenarios

3.4. Training of the artificial neural network

3.4.1. Training details

Unlike super-resolution architecture training, the image temperature measurement dataset demands thermal images spanning various temperature ranges. A total of 233 high-temperature flame scene images from the fire tests in section 2.4.2 were selected, ensuring 10,000 samples covering all small temperature segments within each range.

The emissivity of the thermal image remains set at 0.95. This is because, in this method, instead of focusing on a specific object measurement point, the entire spatial temperature field is measured, with the emissivity representing that of the air. Moreover, the primary aim of the methodology of this paper is to present a color temperature prediction approach, and a fixed emissivity effectively streamlines the temperature measurement process.

For each sub-segment, the data was split into training (70%), validation (15%), and testing (15%) sets. This section presents prediction results using these test sets. Both HR and SR image datasets were created using identical methodologies and images, with the HR dataset facilitating network optimization.

Before training, the normalization function was used in Matlab to normalize the data set within ±1. The feedforward neural network was carried out in the fitting toolbox in Matlab R2022b, and the network was trained for a maximum of 1000 rounds. Several early termination conditions were set, and these specific termination conditions can be found in the function “trainlm” in Matlab. All trainings were performed three times to minimize the deviation caused by different initial random parameters.

3.4.2. Evaluation indicators

Four indicators were used to comprehensively compare the overall error, prediction stability, and number of outliers in the dataset. RMSE serves as a widespread metric for assessing regression models, efficiently identifying substantial errors. A minimal RMSE is desirable for an optimal model. The percentage of sample errors within ±30°C provides a comprehensive overview of the prediction sample, emphasizing that a high-quality prediction requires a balance between low error rates and consistent predictability. The MAE indicator resembles RMSE in measuring network errors but offers a simpler calculation and reduced sensitivity to outliers. The point where the sampling error is beyond ±100°C is called the flawed point. These points cannot be accurately predicted by the network model, which can indicate the approximate error limit of the network.

3.4.3. Optimization of neuron number

The number of neurons is crucial to the network prediction results, and an appropriate number of neurons can improve the network prediction accuracy. In this section, the number of neurons was selected as 3, 5, and 10 to represent fewer, medium, and more neurons, respectively. Tests were performed on the HR image dataset, and the evaluation indicators are the main indexes. Figs. 13 and 14 compare the training results. The 3-neuron model showed the best accuracy and stability in all evaluation indicators. Using more neurons for simple tasks can easily cause a mismatch between network and task complexity, thereby reducing the training effect. In this task, using a low-complexity three-neuron model demonstrated the highest accuracy and stability.

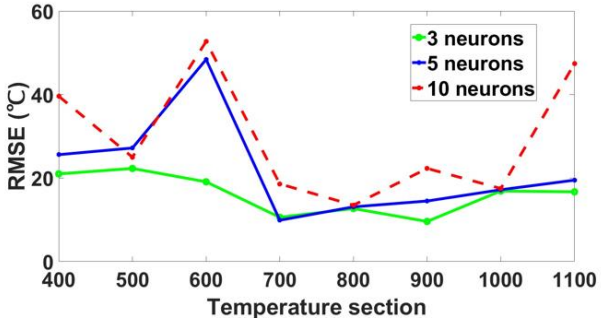

Fig. 13 RMSE of different neurons

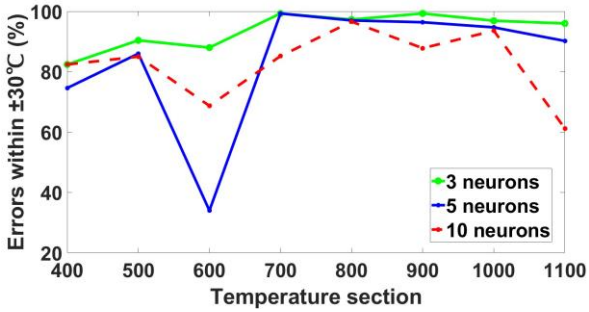

Fig. 14 Proportion of samples within ±30°C of prediction error in different neurons

Fig. 15 and Fig. 16 depict the synchronized convergence of the training, test, and validation sets after optimizing the neuron count in both the lowest (400°C) and highest (1100°C) temperature difference segments. No adverse effects, such as overfitting, were observed. The training process of the remaining temperature difference sections was roughly the same. Due to space limitations, only the training process of the lowest and highest temperature difference sections is shown here.

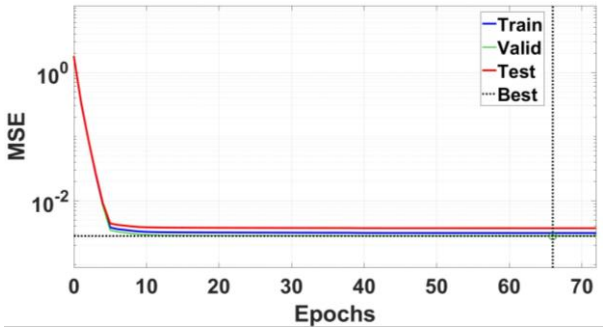

Fig. 15 Proportion of samples within ±30°C of prediction error in different neurons

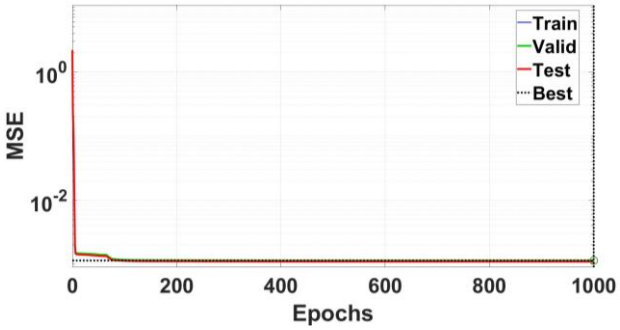

Fig. 16 Proportion of samples within ±30°C of prediction error in different neurons

3.5. Training results

The results in Table 7 show the prediction accuracy of both the HR and SR images using the proposed method. Please note that the accuracy of the neural network, trained using HR images, solely serves as a benchmark for comparison with the network trained using SR images. Simultaneously, the HR image training outcome represents the peak prediction accuracy attainable by the proposed color temperature prediction method for high-definition images. In reality, the HR image remains unknown, yet the SR image generated by this method demonstrates prediction accuracy similar to the HR image, which was revealed by the "Deviation" in Table 7. This suggests that the CNN super-resolution framework described in section 2 has successfully learned to achieve remarkable accuracy in representing color temperature relationships.

The average MAE was 14.2°C, with over 80% of samples falling within an error range of ±30°C. Please note that the temperature measurement range examined in this paper reaches up to 1200°C, and an error of this magnitude is clearly tolerable. This underscores the efficacy of our proposed method and the optimized ANN for high-temperature prediction tasks.

The error in color temperature prediction by the neural network may stem from the utilization of distinct prediction principles: formulas are typically employed for thermal cameras, whereas neural networks are used in the proposed method, potentially causing color-temperature inconsistencies. In addition, prediction accuracy was slightly lower above 900°C, likely due to environmental factors affecting the thermal camera.

Regression analysis on the neural network reveals that the predictions align accurately with target results, as is shown in Fig. 17. Most samples fell within the 95% confidence interval, indicating good responsiveness. In summary, models trained with SR images showed no significant degradation in prediction results.

Table 7
HR/SR image prediction accuracy

Segemnts (℃)	RMSE(°C)		MAE(°C)		Error in ±30(%)		Number of faults	
	HR	SR	HR	SR	HR	SR	HR	SR
1100	21	22.4	16.1	17.4	82.4	81.5	8	24
1000	22.3	26.5	19.5	16	90.4	81.6	134	129
900	19.1	23.7	15.5	18.6	88	80.6	1	4
800	10.6	15.1	8.3	11.8	99.3	95.4	0	1
700	12.7	19.1	9	13.8	97.3	90.3	6	24
600	9.6	16.3	7.5	11.5	99.3	93.4	0	9
500	16.9	15.4	12.3	10.3	96.9	94.1	0	5
400	16.7	16.9	14.6	13.9	96	94.8	0	3
Average	16.1	19.4	12.8	14.2	93.7	89	19	25
Deviation	3.3		1.4		4.7		6	

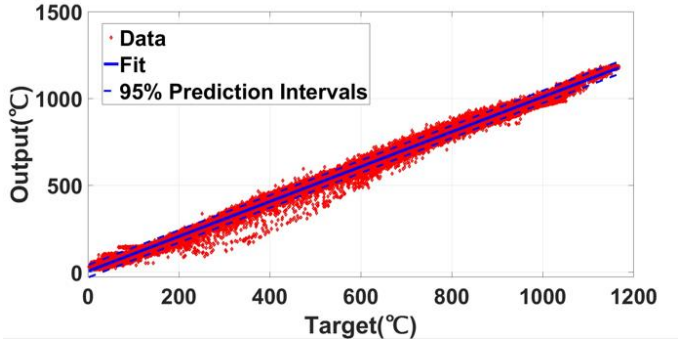

Fig. 17 Linear regression of SR image model

3.6. Model comparison

In section 3.5, the image temperature measurement technique exhibited good accuracy when being trained via neural networks. Nevertheless, distinct machine learning models often excel in specific scenarios. To underscore the robustness of the proposed temperature prediction approach, a comprehensive evaluation was conducted using various machine learning models, including SVM [49], kernel regression [50], regression tree [51], and linear regression [52]. For fairness, the same optimization algorithms, training, and test sets were employed as outlined in sections 3.4.

Figs. 18 and 19 revealed that the SVM and kernel regression exhibited higher errors and regression tree and linear regression demonstrated reasonable accuracy. However, considering prediction accuracy and stability across all temperature segments, a notable disparity remained between existing models and the proposed neural network. The poor performance of these four models stemmed from a mismatch between their complexity and the actual task complexity, resulting in either redundancy or waste.

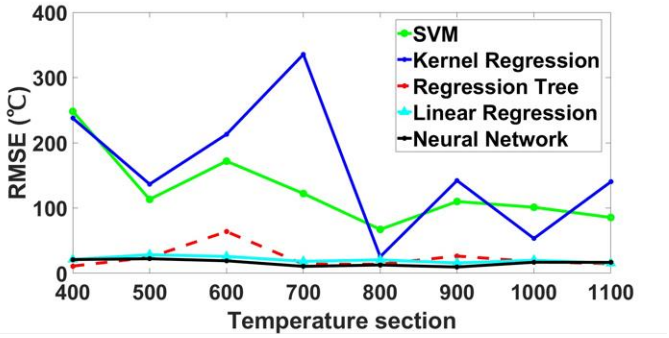

Fig. 18 RMSE of different machine learning models

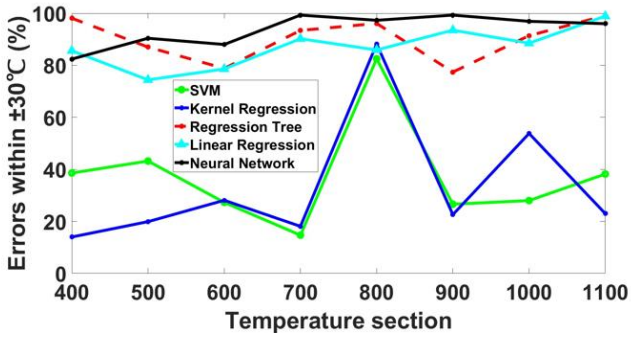

Fig. 19 Proportion of samples within the error of different models within ±30°C

4. Test validation

To validate the wide applicability of the proposed method in high-temperature environments, an extra fire test was conducted an extra fire test to assess the performance of both the super-resolution and prediction networks.

4.1. Test environment

Fig. 20 depicts the entire test scene for a set of cables coated with fire-resistant and flame-retardant sealant and with two ends on support. An oil basin filled with 30L of diesel oil was centrally positioned at the bottom and ignited. The thermal imager, situated 5 meters opposite the cable (Fig. 20d), was set to record the scene. The environmental temperature was set to 20°C with external optical temperature, and the relative humidity of 0.5, emissivity of 0.95, and picture noise reduction were used. Throughout the test, a thermal camera was applied to observe temperatures ranging from 0 to 1250°C.

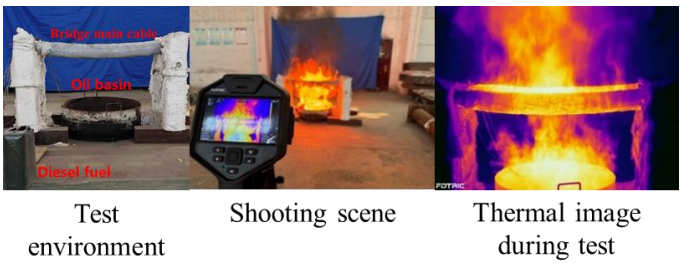

Fig. 20 Realistic fire test scenario of bridge cables

All SR images underwent processing based on the method outlined in section 2, while test sets for HR and SR images were generated using the color temperature measurement model as detailed in section 3.1. Given the brief shooting duration, each experiment produced a limited dataset. The 200 samples per temperature range were selected for testing. This resulted in a total of 800 test samples for a temperature difference segment of 400°C and 2400 samples for a segment of 1100°C.

4.2. Test results

By comparing the predicted outcomes with the actual thermal image outputs, the discrepancies are delineated in Table 8 and illustrated in Figs. 21 and 22. A slight decrease in predicted performance was found compared to previous scenarios. While RMSE, MAE, and the percentage of errors were within 30°C showing minor changes in degradation. Specifically, RMSE remained stable at approximately 20°C, and the proportion of samples with prediction errors within 30 °C only dropped slightly in certain sections, ranging between 70% and 80%. This performance degradation was expected in new scenarios as the network model may not have learned all relevant information. Nevertheless, the minimal decrease demonstrates the good generalization and accuracy of the proposed HR and SR temperature prediction model.

Table 8
HR/SR image prediction accuracy under the new scenario

Segemnts (°C)	RMSE(°C)		MAE(°C)		Error in ±30(%)		Number of faults	
	HR	SR	HR	SR	HR	SR	HR	SR
1100	25.5	21.5	19.8	18.1	71.2	85.7	0	0
1000	22.9	25.0	18.7	19.6	83	75.8	0	0
900	11	20.5	8.6	16.1	98.9	85	0	0
800	14.8	18.2	12.2	15.1	97.6	90.6	0	0
700	12.7	19.8	9.9	15.6	97.5	87.9	6	0
600	13	17.7	9.7	13.6	96.6	80	0	0
500	25.6	15.4	23.3	11.4	70.2	94.5	0	0
400	20.9	22	19.8	19.4	94.4	84.4	0	0
Average	18.3	20	15.2	16.1	88.7	85.5	0	0
Deviation	1.7		0.9		3.2		0	

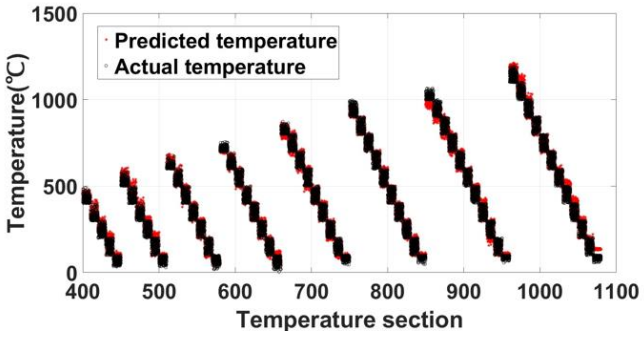

Fig. 21 HR model prediction results in new scenarios

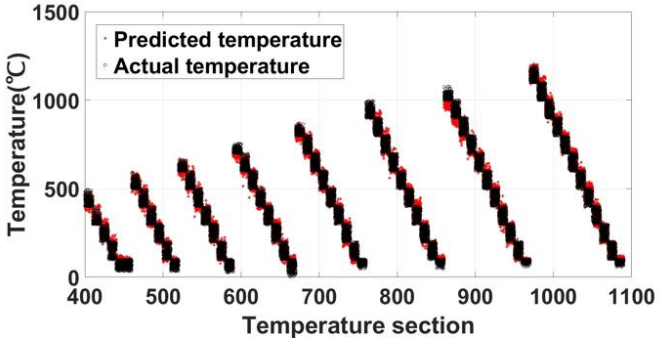

Fig. 22 SR model prediction results in new scenarios

4.3. Discussion

In section 3.6, it was observed that both the SVM regression model and the linear regression model can predict temperatures, albeit with slightly lower accuracy than the proposed model in the test set. To further evaluate the performance of the proposed method, the SR models were employed to specifically compare the errors of these ANN models.

The results can be found in Figs. 23 and 24. The proposed method consistently demonstrated the highest accuracy across most temperature ranges, with minimal and stable error fluctuations. Although the regression tree model showed good accuracy in certain temperature ranges, it exhibited large prediction errors in the 600°C and 1000°C ranges, indicating potential instability during flame ignition or sustained burning. Given reliable temperature data, the linear regression model was proved to be significantly less accurate than the regression tree model, rendering them unsuitable for practical applications.

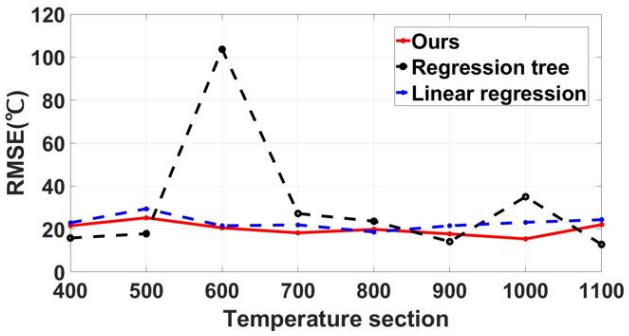

Fig. 23 RMSE of different machine learning models in new scenarios

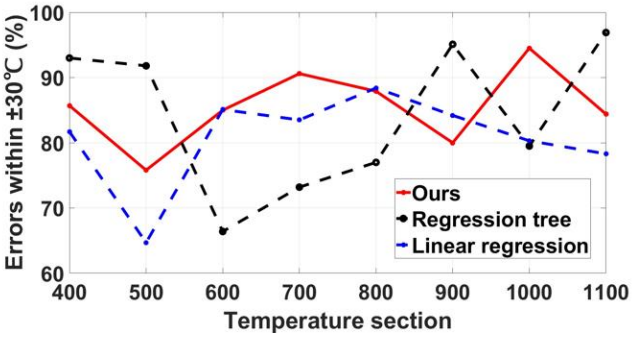

Fig. 24 Proportion of samples within the error of different machine learning models within ±30°C in new scenarios

5. Conclusions

This paper proposed a CNN super-resolution architecture tailored for thermal images in fire scenes, along with a color temperature prediction method for enhanced images. The superiority of the proposed method was validated against fire tests results. The following conclusions can be drawn:

(1) The JASRB module, integrating spatial and channel attention, was proposed for constructing the CNN architecture. This integration notably enhanced the super-resolution of images. With four modules in each core part, the architecture optimized super-resolution, achieving a PSNR of 40.214 dB and an SSIM of 0.9987. It not only refined image clarity but learned accurate color-temperature mappings.

(2) A color temperature measurement method was proposed for wide temperature ranges, utilizing an interpretable ANN. This network incorporated brightness and temperature data from designated points to enhance temperature predictions. Shapley analysis revealed that brightness significantly influenced the predictions of the network. Optimal performance was observed with three neurons in the ANN, yielding RMSE of 16.1°C and 19.4°C for HR and SR images, respectively. Notably, nearly 90% of test sample errors fell within ±30°C.

(3) By integrating super-resolution with the image temperature measurement model, the network effectively accomplished temperature prediction tasks. Additional fire test validated that the unknown thermal images maintained high prediction accuracy after super-resolution

processing. Furthermore, it is worth noting that the three-neuron neural network approach demonstrated superior prediction accuracy compared to other machine learning methods.

Acknowledgments

The work presented in this paper was mainly supported by the National Natural Science Foundation of China with grants 52127814 and 52078478, and the National Fire and Rescue Administration with grant 2023XFCX18.

References

[1] Lou, G. B., Hou, J., Qi, H. H., Jiang, Y., Zhong, B., Pang, Y., and Li, G. Q. Experimental, numerical and analytical analysis of a single-span steel portal frame exposed to fire. Engineering Structures, 302, 117417, 2024.

[2] Chudasama, V., Patel, H., Prajapati, K., Upla, K. P., Ramachandra, R., Raja, K., and Busch, C. Therisurnet - a computationally efficient thermal image super-resolution network. In Proceedings of the IEEE/CVF Conference on Computer Vision and Pattern Recognition Workshops (pp. 86-87), 2024.

[3] Keys, R. Cubic convolution interpolation for digital image processing. IEEE transactions on acoustics, speech, and signal processing, 29(6), 1153-1160, 1981.

[4] Kim, K. I., and Kwon, Y. Single-image super-resolution using sparse regression and natural image prior. IEEE transactions on pattern analysis and machine intelligence, 32(6), 1127-1133, 2010.

[5] Irani, M., and Peleg, S. Improving resolution by image registration. CVGIP: Graphical models and image processing, 53(3), 231-239, 1991.

[6] Li, J., Brown, C., Dzikowicz, D. J., Carey, M. G., Tam, W. C., and Huang, M. X. Towards real-time heart health monitoring in firefighting using convolutional neural networks. Fire Safety Journal, 140, 103852, 2023.

[7] Jiang, Y., Liu, Y., Zhan, W., and Zhu, D. Improved Thermal Infrared Image Super-Resolution Reconstruction Method Base on Multimodal Sensor Fusion. Entropy, 25(6), 914, 2023.

[8] Hodges, J. L., Lattimer, B. Y., and Luxbacher, K. D. Compartment fire predictions using transpose convolutional neural networks. Fire Safety Journal, 108, 102854, 2019.

[9] Wang, Z., Chen, J., and Hoi, S. C. Deep learning for image super-resolution: A survey. IEEE transactions on pattern analysis and machine intelligence, 43(10), 3365-3387, 2020.

[10] Kim, J., Lee, J. K., and Lee, K. M. Accurate image super-resolution using very deep convolutional networks. In Proceedings of the IEEE conference on computer vision and pattern recognition (pp. 1646-1654), 2016.

[11] Kim, J., Lee, J. K., and Lee, K. M. Deeply-recursive convolutional network for image super-resolution. In Proceedings of the IEEE conference on computer vision and pattern recognition (pp. 1637-1645), 2016.

[12] Tai, Y., Yang, J., and Liu, X. Image super-resolution via deep recursive residual network. In Proceedings of the IEEE conference on computer vision and pattern recognition (pp. 3147-3155), 2017.

[13] Lim, B., Son, S., Kim, H., Nah, S., and Mu Lee, K. Enhanced deep residual networks for single image super-resolution. In Proceedings of the IEEE conference on computer vision and pattern recognition workshops (pp. 136-144), 2017.

[14] Shi, W., Caballero, J., Huszár, F., Totz, J., Aitken, A. P., Bishop, R., ... and Wang, Z. Real-time single image and video super-resolution using an efficient sub-pixel convolutional neural network. In Proceedings of the IEEE conference on computer vision and pattern recognition (pp. 1874-1883), 2016.

[15] Zhang, Y., Li, K., Li, K., Wang, L., Zhong, B., and Fu, Y. Image super-resolution using very deep residual channel attention networks. In Proceedings of the European conference on computer vision (ECCV) (pp. 286-301), 2018.

[16] Woo, S., Park, J., Lee, J. Y., and Kweon, I. S. Cbam: Convolutional block attention module. In Proceedings of the European conference on computer vision (ECCV) (pp. 3-19), 2018.

[17] Hu, J., Shen, L., and Sun, G. Squeeze-and-excitation networks. In Proceedings of the IEEE conference on computer vision and pattern recognition (pp. 7132-7141), 2018.

[18] Choi, Y., Kim, N., Hwang, S., and Kweon, I. S. Thermal image enhancement using convolutional neural network. In 2016 IEEE/RSJ international conference on intelligent robots and systems (IROS) (pp. 223-230). IEEE, 2016.

[19] Lee, K., Lee, J., Lee, J., Hwang, S., and Lee, S. Brightness-based convolutional neural network for thermal image enhancement. IEEE Access, 5, 26867-26879, 2017.

[20] Liu, S., Yang, Y., Li, Q., Feng, H., Xu, Z., Chen, Y., and Liu, L. Infrared image super resolution using gan with infrared image prior. In 2019 IEEE 4th International Conference on Signal and Image Processing (ICSIP) (pp. 1004-1009). IEEE, 2019.

[21] Rivadeneira, R. E., Sappa, A. D., and Vintimilla, B. X. Thermal Image Super-resolution: A Novel Architecture and Dataset. In VISIGRAPP (4: VISAPP) (pp. 111-119), 2020.

[22] Hwang, S., Park, J., Kim, N., Choi, Y., and So Kweon, I. Multispectral pedestrian detection: Benchmark dataset and baseline. In Proceedings of the IEEE conference on computer vision and pattern recognition (pp. 1037-1045), 2015.

[23] He, Z., Tang, S., Yang, J., Cao, Y., Yang, M. Y., and Cao, Y. Cascaded deep networks with multiple receptive fields for infrared image super-resolution. IEEE transactions on circuits and systems for video technology, 29(8), 2310-2322, 2018.

[24] Miklavec, A., Pušnik, I., Batagelj, V., and Drnovšek, J. A large aperture blackbody bath for calibration of thermal imagers. Measurement Science and Technology, 24(2), 025001, 2012.

[25] Pelzmann, T., Dupont, F., Sauté, B., and Robert, É. Two-color pyrometry for backface temperature and emissivity measurement of burning materials. International Journal of Thermal Sciences, 184, 107894, 2023.

[26] Zamarripa-Ramírez, J. C. I., Moreno-Hernández, D., and Martinez-Gonzalez, A. Simultaneous measurement of temperature and color spectrum of axisymmetric premixed flames using digital laser speckle photography and an image processing approach. Measurement Science and Technology, 32(10), 105903, 2021.

[27] Shan, L., Huang, H., Hong, B., Zhao, J., Wang, D., and Kong, M. Temperature measurement method of flame image fusion with different exposures. Energies, 13(6), 1487, 2020.

[28] Zhong, Y., Li, X., Yang, Z., Liu, X., and Yao, E. A model for minimum ignition energy prediction of sugar dust clouds based on interactive orthogonal experiments and machine learning. Fire Safety Journal, 104111, 2024.

[29] Qu, N., Li, Z., Li, X., Zhang, S., and Zheng, T. Multi-parameter fire detection method based on feature depth extraction and stacking ensemble learning model. Fire Safety Journal, 128, 103541, 2022.

[30] Özyurt, O. The effect of time correlation function, Sauter mean diameter and asymmetry ratio on machine learning classifiers for particle discrimination by using light scattering. Fire Safety Journal, 141, 104002, 2023.

[31] Qu, X. S., Deng, Y. X., and Sun, G. J. INVESTIGATION ON BEHAVIOR OF STEEL CABLES SUBJECT TO LOCALIZED FIRE IN LARGE-SPACE BUILDINGS. ADVANCED STEEL CONSTRUCTION, 20(1), 1-11, 2024.

[32] Nan, Z., Orabi, M. A., Huang, X., Jiang, Y., and Usmani, A. Structural-fire responses forecasting via modular AI. Fire Safety Journal, 140, 103863, 2023.

[33] Couto, C., Tong, Q., and Gernay, T. Predicting the capacity of thin-walled beams at elevated temperature with machine learning. Fire Safety Journal, 130, 103596, 2022.

[34] Sun, B., Liu, X., Xu, Z. D., and Xu, D. BP neural network-based adaptive spatial-temporal data generation technology for predicting ceiling temperature in tunnel fire and full-scale experimental verification. Fire Safety Journal, 130, 103577, 2022.

[35] Chen, L., Zhang, H. Y., Liu, S. W., and Chan, S. L. SECOND-ORDER ANALYSIS OF BEAM-COLUMNS BY MACHINE LEARNING-BASED STRUCTURAL ANALYSIS THROUGH PHYSICS-INFORMED NEURAL NETWORKS. Advanced Steel Construction, 19(4), 411-420, 2023.

[36] Wang, Z. Q., Zheng, Z. Mengxiang, J. W., and Jiang, W. Q. INVERSION METHOD OF UNCERTAIN PARAMETERS FOR TRUSS STRUCTURES BASED ON GRAPH NEURAL NETWORKS. ADVANCED STEEL CONSTRUCTION, 19(4): p. 366-374, 2023.

[37] Sharifi, Y., and Tohidi, S. Ultimate capacity assessment of web plate beams with pitting corrosion subjected to patch loading by artificial neural networks. Advanced Steel Construction, 10(3), 325-350, 2014.

[38] Nair, V., and Hinton, G. E. Rectified linear units improve restricted boltzmann machines. In Proceedings of the 27th international conference on machine learning (ICML-10) (pp. 807-814), 2010.

[39] Kingma, D. P., and Ba, J. Adam: A method for stochastic optimization. arxiv preprint arxiv:1412.6980, 2014.

[40] Mittal, A., Soundararajan, R., and Bovik, A. C. Making a "completely blind" image quality analyzer. IEEE Signal processing letters, 20(3), 209-212, 2012.

[41] Szegedy, C., Ioffe, S., Vanhoucke, V., and Alemi, A. Inception-v4, inception-resnet and the impact of residual connections on learning. In Proceedings of the AAAI conference on artificial intelligence (Vol. 31, No. 1), 2017.

[42] Zhao, H., Kong, X., He, J., Qiao, Y., and Dong, C. Efficient image super-resolution using pixel attention. In Computer Vision–ECCV 2020 Workshops: Glasgow, UK, August 23–28, 2020, Proceedings, Part III 16 (pp. 56-72). Springer International Publishing, 2020.

[43] Ismail, I., Yefriadi, Y., Yuhefizar, Y., and Hendri, Z. The Generating Super Resolution of Thermal Image based on Deep Learning. Jurnal RESTI (Rekayasa Sistem dan Teknologi Informasi), 6(2), 289-294, 2022.

[44] Wang, Y., Zhao, L., Liu, L., Hu, H., and Tao, W. URNet: a U-shaped residual network for lightweight image super-resolution. Remote Sensing, 13(19), 3848, 2021.

[45] Jiang, J., Wang, C., Lou, G., and Li, G. Q. Quantitative evaluation of progressive collapse process of steel portal frames in fire. Journal of Constructional Steel Research, 150, 277-287, 2018.

[46] Marquardt, D. W. An algorithm for least-squares estimation of nonlinear parameters. Journal of the society for Industrial and Applied Mathematics, 11(2), 431-441, 1963.

[47] Liu, X., and Aldrich, C. Assessing the influence of operational variables on process performance in metallurgical plants by use of Shapley value regression. Metals, 12(11), 1777, 2022.

[48] Lundberg, S. M., and Lee, S. I. A unified approach to interpreting model predictions. Advances in neural information processing systems, 30, 2017.

[49] Andrew, A. M. An introduction to support vector machines and other kernel-based learning methods. Kybernetes, 30(1), 103-115, 2001.

[50] Huang, P. S., Avron, H., Sainath, T. N., Sindhwani, V., and Ramabhadran, B. Kernel methods match deep neural networks on timit. In 2014 IEEE International Conference on Acoustics, Speech and Signal Processing (ICASSP) (pp. 205-209). IEEE, 2014.

[51] Loh, W. Y. Regression tress with unbiased variable selection and interaction detection. Statistica sinica, 361-386, 2002.

[52] Street, J. O., Carroll, R. J., & Ruppert, D. (1988). A note on computing robust regression estimates via iteratively reweighted least squares. The American Statistician, 42(2), 152-154.

Advanced Steel Construction – Vol. 20 No. 2 (2024) 179–187
DOI:10.18057/IJASC.2024.20.2.10
(Special Issue: *11st International Conference on Advances in Steel Structures, ICASS'2023, Kuching, Sarawak, Malaysia*)

INFLUENCE OF SECTION SLENDERNESS ON THE AXIAL PERFORMANCE OF HIGH-STRENGTH COLD-FORMED STEEL BUILT-UP COLUMNS

Shin-Rui Kho [1], Adeline LingYing Ng [1,*], Hieng-Ho Lau [1], Emad Gad [2] and Krishanu Roy [3]

[1] *Faculty of Engineering, Computing and Science, Swinburne University of Technology (Sarawak Campus), Kuching 93350, Malaysia*
[2] *School of Engineering, Swinburne University of Technology, Hawthorn 3122, Australia*
[3] *School of Engineering Academic, University of Waikato, Hamilton 3216, New Zealand*
** (Corresponding author: E-mail: ang@swinburne.edu.my)*

ABSTRACT

Cold-formed steel (CFS) sections are widely utilised in roofing and framing systems due to their lightweight properties and ease of fabrication and construction. The application of CFS built-up sections was introduced to enhance the strength and stability of single channels. However, typical CFS channels possess slender profiles with a high section slenderness ratio $(w/t)_{max}$, making them susceptible to buckling and limiting their effectiveness. Consequently, this study examined the axial compression behaviour and cost-effectiveness of G550 high-strength CFS built-up sections with a reduced $(w/t)_{max}$ compared to conventional industry sizes. Experimental and numerical studies were conducted to assess the effect of member slenderness $(KL/r)_m$ and screw arrangement on the CFS built-up sections with different section slenderness. The results demonstrated that the proposed sections, with a lower $(w/t)_{max}$, significantly improved buckling resistance for members with $(KL/r)_m$ less than 90. This improvement is attributed to their more compact profile design, which restrained the occurrence of local buckling. Furthermore, these sections were found to be more cost-effective, offering greater strength at a reduced weight.

ARTICLE HISTORY

Received: 18 June 2024
Revised: 18 June 2024
Accepted: 18 June 2024

KEYWORDS

Axial compression;
High-strength cold-formed steel;
Slenderness ratios;
Screw arrangement;
Buckling resistance;
Cost-effectiveness

1. Introduction

The application of cold-formed steel (CFS) gained popularity due to its light gauge properties while achieving impressive performance [1-3]. However, the slender geometry layout makes it prone to buckling and leads to high instability of structural members [1,4-5]. Therefore, CFS built-up sections were introduced to enhance the load-carrying capacity and stability of single channels, and these sections are commonly applied in various types of structural members such as roof and wall systems, portal frames, columns, and beams [6-7]. Past research investigated the structural performance of various types of CFS built-up sections with different arrangements of CFS sections. The typical CFS built-up sections investigated in the past are shown in Fig. 1. Fig. 1(a) shows the typical CFS single channels applied in structural design and used to form the built-up sections. Moreover, Fig. 1(b) presented the different types of CFS built-up sections that have been investigated in previous research which include open built-up sections, closed built-up sections, built-up battened sections, built-up gapped sections, and other built-up sections (hybrid built-up section, multi-limbs built-up section, built-up hollow flange section, half-open built-up section, and cruciform built-up section). Notably, most of the studies mentioned above were conducted to investigate the axial capacity of built-up sections formed using existing CFS channels in the industry with a maximum width-to-thickness ratio, $(w/t)_{max}$ of 45 and above. A summary of the axial performance of CFS open built-up sections with different slenderness ratios is shown in Fig. 2 [8-15]. The axial capacity (P_u) in Fig. 2 was normalised by multiplying the ultimate tensile strength (f_u) and gross cross-sectional area (A_g) of the investigated sections for comparison to account for different material grades and section sizes.

It is more practical to form the built-up sections using the common sizes of CFS channels. However, the sections do not achieve full capacity as the normalised capacity was not close to the unity shown in Fig. 2, indicating that the section was not fully effective. As CFS channels have a slender profile that leads to high instability and is prone to buckle, a smaller $(w/t)_{max}$ is expected to enhance the buckling resistance and make the CFS sections more effective. Several research investigated the axial compression performance of CFS open built-up columns with different cross-section dimensions [10-15], but the effect of section slenderness was not discussed. Yet, Zhou et al. [12] claimed that the section slenderness was an important parameter that influences the capacity of the CFS built-up sections. Although many research was conducted, the axial behaviour of the CFS sections with the $(w/t)_{max}$ lesser than 45 is rarely explored, therefore the structural performance of the built-up sections fabricated using a small $(w/t)_{max}$ is worth examining. Apart from that, a reduced size of CFS sections is potentially more cost-effective if it can achieve a similar capacity to common CFS sections while utilising lesser materials. Furthermore, Vy and Mahendran [13] studied the effect of screw arrangement on the CFS open lipped built-up sections fabricated using common CFS sections. The axial compression capacity of the specimens with double rows fasteners was increased by an average of 4% compared to single row fasteners and the increase is relatively significant for slender columns. Meanwhile, the influence of the screw arrangement is unexplored for the built-up members with section slenderness lesser than 45. Therefore, this study aims to investigate the axial compression behaviour of CFS built-up columns fabricated with a $(w/t)_{max}$ ranging from 41 to 45. An experimental testing programme was carried out for 12 open lipped built-up columns with different member lengths (L) and screw spacing (a). Following this, finite element (FE) models were developed and validated using the experimental data. Finally, parametric studies were performed to examine further the effect of modified slenderness ratio $(KL/r)_m$ and screw arrangement on the proposed sections.

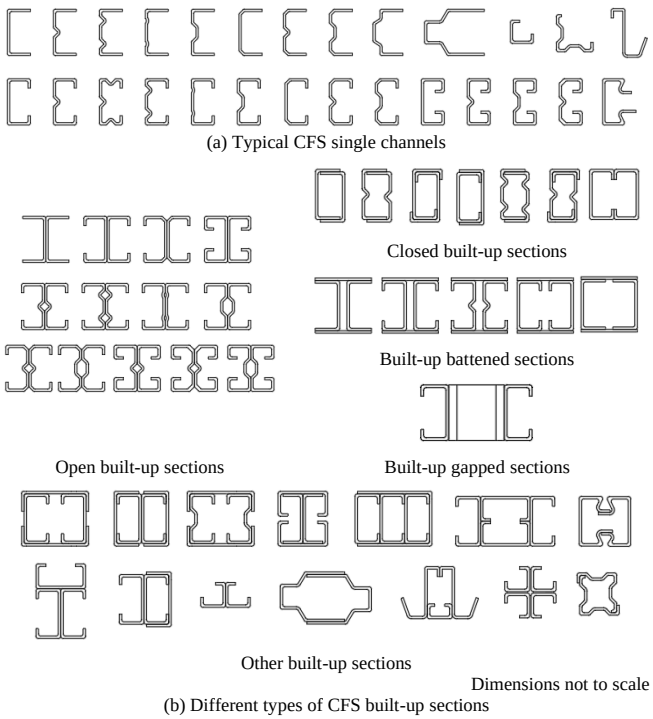

Fig. 1 Various types of CFS built-up sections investigated in past research

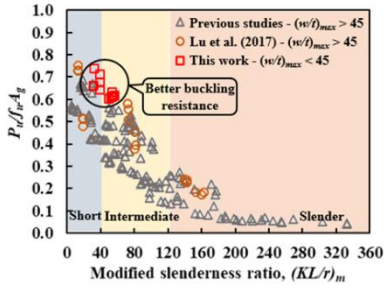

Fig. 2 Axial performance of CFS open built-up columns with different slenderness ratios

2. Experimental testing

2.1. Test specimens

The test programme consists of 12 sets of specimens fabricated with two scaled-down lipped channels connected back-to-back with self-drilling screws. The lipped channels were press braked from a 1 mm thick plain steel sheet with a nominal yield strength of 550 MPa with a nominal bend radius, *R* of 2.5 mm. The lipped channel was designed with a nominal width of 51 mm web *(h)*, 20 mm flange *(b)* and 10 mm lip *(d)* as shown in Fig. 3(a). The element widths of the proposed sections were scaled down with a $(w/t)_{max}$ ranging from 41 to 45. A single row of screws was designed to fasten the CFS channels to achieve good coupling conditions between the fastened sections. In addition, Gauge 12 self-drilling screws were used as the connector between the channels with a 50 mm end distance and two different intermediate screw spacings of 100 mm and 200 mm along the longitudinal direction. The dimensions of the self-drilling screw were presented in Fig. 3(b) with a diameter of 5.35 mm and a length of drill point 7 mm. Then, the measured dimensions for each specimen were indicated in Table 1. Prior to conducting the experimental testing, every specimen was labelled to indicate the sectional profile and the corresponding design parameters as shown in Fig. 3(c). The investigated built-up section was given a series name which is open lipped (OL) series and further differentiated into S100 and S200 series for different screw spacings.

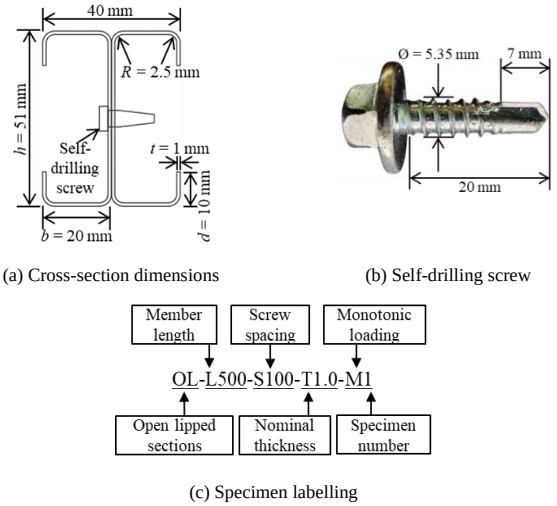

(a) Cross-section dimensions (b) Self-drilling screw

(c) Specimen labelling

Fig. 3 Detailed of proposed sections

Table 1
Measured specimen dimensions and parameters

Classification	Specimen		*h* (mm)	*b* (mm)	*d* (mm)	*t* (mm)	*L* (mm)	*a* (mm)	$(w/t)_{max}$	$(KL/r)_m$	A_g (mm^2)	δ
S100 series												
Short	OL-L300-S100-T1.0	M1	51.58	19.09	10.38	1.03	297	100	43.22	32.48	208.52	0.9
		M2	51.63	19.41	10.50	1.00	298	100	44.63	31.90	204.60	
		M3	51.59	19.79	10.00	1.06	299	100	41.95	31.76	215.66	
Intermediate	OL-L500-S100-T1.0	M1	51.79	18.59	11.08	1.04	501	100	42.99	52.30	211.71	0.7
		M2	52.17	19.75	11.02	1.04	504	100	43.36	49.54	217.08	
		M3	51.75	18.38	11.11	1.04	504	100	42.95	53.17	210.88	
S200 series												
Short	OL-L300-S200-T1.0	M1	51.20	19.52	9.94	1.00	298	198	44.20	39.26	201.94	0.7
		M2	52.03	19.54	10.71	1.06	299	199	42.37	38.99	218.55	
		M3	51.98	19.67	10.49	1.05	299	199	42.74	38.87	216.10	
Intermediate	OL-L500-S200-T1.0	M1	52.06	19.79	11.27	1.04	505	200	43.25	54.06	218.06	0.9
		M2	51.88	18.70	11.17	1.04	500	200	43.08	56.92	212.73	
		M3	52.47	19.63	11.07	1.04	503	200	43.64	54.65	217.41	

2.2. Material properties

The actual mechanical properties of the components, G550 steel sheets and self-drilling screws were determined by conducting the tensile coupon tests and screw shear tests in accordance with AS/NZS 4600:2018 [16]. Then, the test procedures of tensile coupon tests have been accounted for further considerations recommended in AS1391 [17] and Huang and Young [18]. A slow loading rate recommended for research purposes was adopted to obtain accurate mechanical properties of the steel materials. The measured stress-strain behaviour of steel and the shear behaviour of screw were summarised in Fig. 4 and used as constitutive models to apply the actual properties of the components to numerical models.

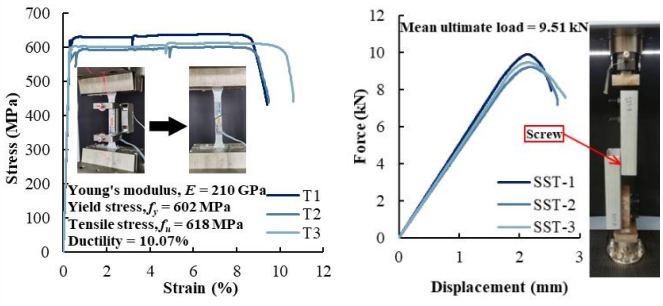

(a) Tensile coupon test results (b) Screw shear test results

Fig. 4 Material properties

2.3. Dimension and geometric imperfection measurements

All 12 specimens were measured before tests. The dimension measurement included the elements of web (h), flange (b), lip (d), thickness (t), member length (L), and intermediate screw spacing (a) and the measured data was listed in Table 1. The fabrication, installation, and transportation processes of the CFS specimen potentially caused geometric imperfections. Therefore, the initial global and local imperfections were also measured from the data point location indicated in Fig. 5. The global imperfection was measured at the mid-height of the specimen, while local imperfection was measured between the 200 mm central length with a 10 mm interval. Additionally, the datum points were controlled as zero for every measurement to ensure consistency. Then, the measured absolute maximum imperfection magnitudes (δ) were recorded in Table 1 which were the sum of absolute maximum global and local imperfections for each series.

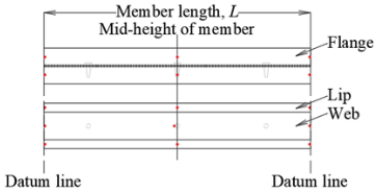

(a) Global imperfection

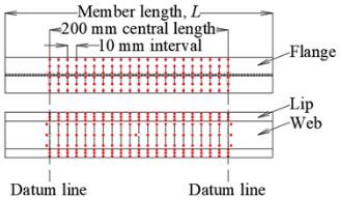

(b) Local imperfection

Fig. 5 Geometric imperfection measurement

2.4. Test setup and operation

The boundary conditions of the built-up columns were designed as pin-ended supports. Two supporting test rigs were specially fabricated to provide the pin-ended boundary condition of the specimens, which only allowed the rotation about the minor axis of the specimens. To ensure full contact between the specimen and the supports, both ends of each specimen are welded to 16 mm thick steel end plates before the test. The schematic diagram and fabricated fixtures of the test setup are shown in Fig. 6.

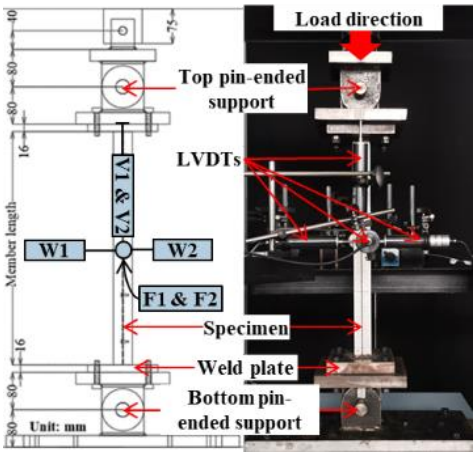

(a) Schematic diagram (b) Actual setup

Fig. 6 Test setup

Besides, the axial shortening and out-of-plane deformation were measured during the test using the linear variable displacement transducer (LVDT). Two LVDTs were set vertically at the middle of the top plate to determine the axial shortening of the specimen. Additionally, four LVDTs were used to measure the out-of-plane deformation for intermediate columns. Two LVDTs measured the displacement of the web elements while the other two LVDTs measured the displacement at the flanges. Nevertheless, only the out-of-plane deformation at the web elements was measured for short columns due to space limitations.

Since CFS is a strong material with relatively low ductility and the expected displacement before buckling is small, a displacement-controlled loading protocol was used to conduct the monotonic compression test. To determine the static response of the CFS built-up sections, a constant loading rate (0.2 mm/min) was selected to perform the test. A 1 kN preload was applied before executing the actual test to eliminate the gaps between test rigs and the specimen, ensuring uniform axial compression applied on the specimen. The test was terminated after a 20% drop in ultimate load was observed.

2.5. Experiment results

The test results are summarised in Table 2 and the observed axial behaviours are presented in Figs. 7 and 8. Based on the analysis, the axial behaviours of the investigated specimens were classified into three stages, which are yield point, ultimate point, and failure point. The yield point of each specimen was determined by using the equivalent elasto-plastic energy absorption method [19]. The ultimate point was identified when the peak load was achieved, while the failure point was measured at a 20% drop in the peak load.

2.5.1. Load-displacement behaviour and failure modes

All tested specimens behaved similarly throughout the test with no significant responses occurring at the elastic stage. Distortional buckling occurred once the applied load surpassed the yield point as indicated in Fig. 7 (refer to the axial shortening) while no local buckling was observed at this stage which may be restrained by their compact cross-section design. Other buckling modes were observed beyond the ultimate point (refer to the out-of-plane deformation). For short columns, local buckling and crushing were observed. The final failure mode was the interactive local-distortional buckling mode, including crushing at the specimen ends. Except for OL-L300-S200-T1.0-M2, no distortional buckling was observed due to the high initial imperfection in the specimen. Meanwhile, for intermediate columns, interactive local-distortional-global buckling was observed. Besides, there was a significant increase in out-of-plane deformation beyond the ultimate point due to the loss of stability of the member. The failure modes of investigated specimens at the failure point are shown in Fig. 8.

Table 2
Summary of experimental results

Specimen		P_y (kN)	Δ_y (mm)	P_u (kN)	Δ_u (mm)	P_u/f_uA_g	Buckling mode	
							Ultimate	Failure
S100 Series								
OL-L300-S100-T1.0	M1	90.38	0.88	95.05	1.04	0.74	D	LDC
	M2	77.96	0.74	83.63	0.96	0.87	D	LD
	M3	83.51	0.80	88.16	0.98	0.94	D	LDC
OL-L500-S100-T1.0	M1	77.67	1.15	79.96	1.25	0.61	D	DG
	M2	75.52	1.15	80.94	1.41	0.60	D	LDG
	M3	77.41	1.04	79.32	1.11	0.61	D	LDG
S200 series								
OL-L300-S200-T1.0	M1	84.43	0.83	88.74	1.01	0.71	D	LD
	M2	82.72	0.79	87.03	0.99	0.64	D	LDC
	M3	85.49	0.78	90.29	0.92	0.68	D	LDC
OL-L500-S200-T1.0	M1	81.72	1.20	85.12	1.30	0.63	D	LDG
	M2	78.29	1.15	81.01	1.29	0.62	D	LDG
	M3	78.31	1.21	82.48	1.50	0.61	D	LDG

Note: D = distortional buckling, LD = interactive local-distortional buckling, LDC = interactive local-distortional buckling with crushing, LDG = interactive local-distortional-global buckling.

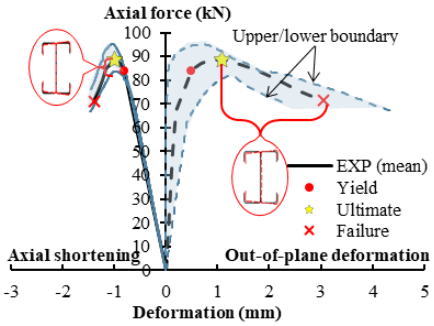

(a) OL-L300-S100-T1.0

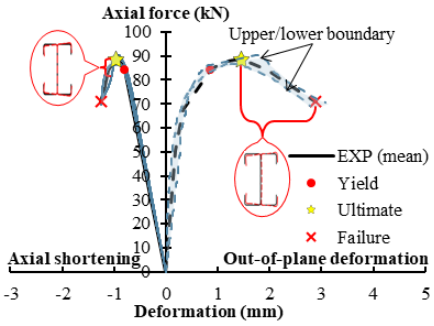

(b) OL-L300-S200-T1.0

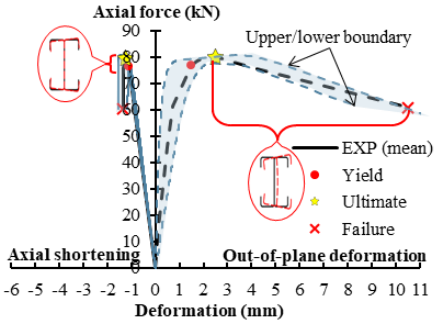

(c) OL-L500-S100-T1.0

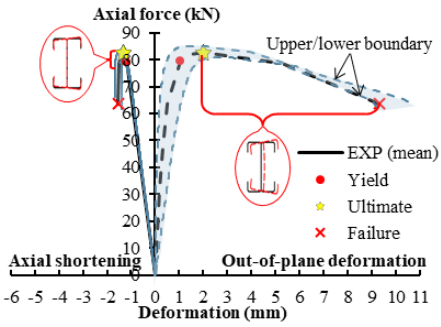

(d) OL-L500-S200-T1.0

Fig. 7 Experimental results of OL series

2.5.2. Composite action of built-up columns

Based on the failure modes in Fig. 8, the composite action of built-up columns was developed as the two channels deformed simultaneously. Besides, no separation of channels and failure at the screw connection was observed. The designed screw arrangement provided a good coupling effect although the intermediate columns with 200 mm screw spacing do not meet the recommended limit of screw spacing in AS/NZS 4600:2018 [20]. Only the short columns with 200 mm screw spacing buckled individually, as predicted in the design codes. It was also found that the investigated specimens achieved greater buckling resistance compared to specimens studied in previous research. As shown in Fig. 2, the normalised axial capacity is closer to unity, which means the proposed sections are more effective.

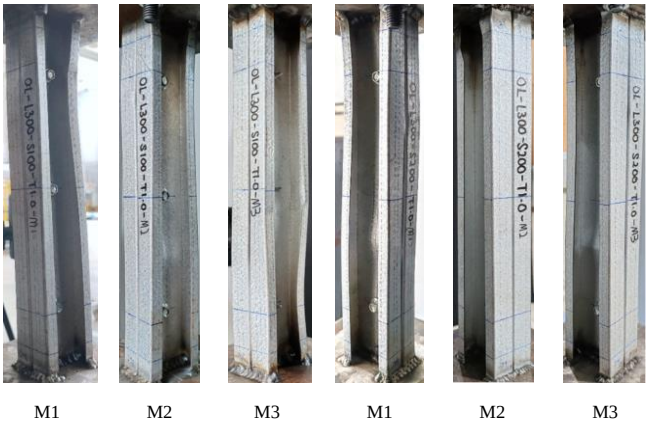

M1 M2 M3 M1 M2 M3

(a) OL-L300-S100-T1.0 (b) OL-L300-S200-T1.0

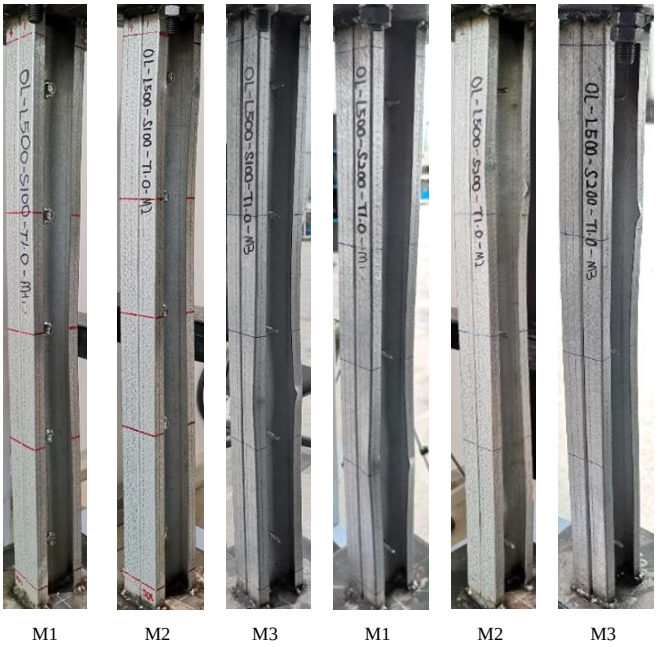

M1 M2 M3 M1 M2 M3

(c) OL-L500-S100-T1.0 (d) OL-L500-S200-T1.0

Fig. 8 Failure modes of OL series at failure point

3. Numerical simulation

3.1. Finite element model development

As the experimental testing was limited to short and intermediate columns, the axial behaviour of slender columns investigated was referred to Lu et al. [10]. The reported failure mode was pure global buckling for all slender built-up columns fabricated using lipped channels with $(w/t)_{max}$ ranging from 71.5 to 93. Therefore, the numerical model was verified and used to perform parametric studies in order to further examine the influence of section slenderness. The respective specimens were named LU series to ease the comparisons with the OL series (proposed section in this study).

3.1.1. Types of element and mesh

The CFS specimens were modelled according to their actual dimensions and assigned deformable shell elements type S4R5, in ABAQUS [21]. The mesh size adopted was 5 mm following mesh convergence studies to provide accurate and efficient FEA.

3.1.2. Material modelling

The material properties used to simulate the reference specimens were obtained from the experimental results of tensile coupon tests discussed in Section 2.2 and reported data in [10] for the OL series and LU series respectively. The engineering stress-strain curves were converted to true stress-strain curves. Then, the details of elasticity, plasticity, and ductile damage which were required to incorporate into FE models were determined based on the true stress-strain curves.

Furthermore, the screw position and arrangement assigned to FE models

were also according to the measured intermediate screw spacing and arrangement design such as single row screws for the OL series and double rows screws for the LU series. The screw properties were initially assumed as rigid and damage was considered upon reaching the mean ultimate shear capacity determined from the screw shear test. The damage initiation and evolution limits were set as the mean ultimate shear capacity and allowable deformation from the ultimate to the failure point.

3.1.3. Modelling of initial geometric imperfections

Furthermore, CFS sections commonly contain geometric imperfections caused during fabrication and transportation processes. These imperfections initiated out-of-straightness and small deflection, weakening the structural members' strength and stiffness [22,23]. Therefore, the measured initial geometric imperfection magnitudes were incorporated into the FE models.

3.1.4. Boundary conditions

The numerical models were assigned with the same pin-ended restraints as during experimental testing at both ends to achieve high-accuracy simulation. First, reference points (RPs) were generated at the centroid of the CFS built-up column at both ends. Then, all degrees of freedom (DOF) of the elements (web, flanges, and lips) of the CFS sections were constrained to the RPs using coupling type constraints. For the OL series, all the translational and rotational DOF were fully fixed at both RPs except the rotational DOF of the minor axis at both RPs and the axial translational DOF at the top RP, which was used to apply the displacement loading and to allow the vertical deformation of specimens. Meanwhile, the boundary conditions assigned to the LU series were similar to the OL series with an additional rotational release of the major axis at both RPs for the bidirectionally hinged supports. The assigned boundary conditions for each series are indicated in Fig. 9.

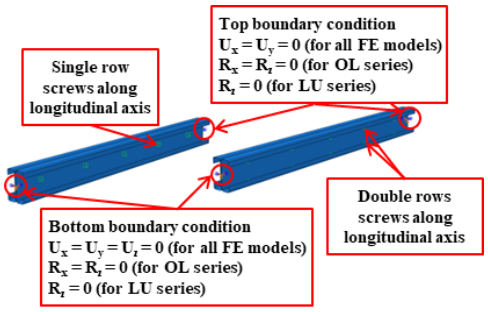

(a) Single row screw (b) Double rows screws

Fig. 9 Boundary conditions of FE models

3.1.5. Modelling techniques and loading procedure

The FEA involved two steps using different solution techniques. Firstly, an Eigenvalue buckling analysis was conducted using linear perturbation analysis to obtain the buckling shape and to incorporate the imperfection of the CFS specimens into the nonlinear models. A concentrated point load was applied at the top end of the specimen to simulate experimental testing conditions. Then, the measured maximum absolute initial imperfection was used as the magnitude and assigned to the lowest-order eigenmodes to model the initial state of the specimen of collapse analysis. Secondly, a nonlinear static analysis was utilised to load the specimen to failure. The nonlinear model was duplicated from the first model (eigenvalue buckling model) to ensure consistency of the utilised cross-sectional dimensions and other parameters throughout the entire FEA. To optimise the convergence issues, an automatic stabilization technique was adopted in this study, which can efficiently obtain a solution in the post-collapse stage with the help of artificial damping. The dissipated energy fraction and the ratio of stabilization to strain energy were set as 0.0002 and 0.05, respectively. Then, the loading protocol assigned in this step was displacement-controlled, which applies the final axial shortening obtained from experimental results at the top RP in the vertical direction to simulate the axial loading acting on the specimens.

3.2. Mesh convergence and independence study

Mesh convergence and independence studies were performed to examine the efficiency of the developed FE models. For the OL series, the study and analysis were completed by executing the FEA on the intermediate column with different mesh densities of 2 mm, 3 mm, 4 mm, 5 mm, 8 mm, 10 mm, and 20 mm. The comparisons of the outcomes are presented in Fig. 10. Only the failure mode of the FE model with a 5 mm mesh size was presented as it is the best-fit model. A 5 mm mesh size was selected for both short and intermediate models. A similar process was conducted for the LU series, both intermediate and slender columns were selected specimens to conduct this study. The intermediate column was validated again to ensure the 5 mm mesh size is still valid for the section size with greater section slenderness. It was found that a 5 mm mesh size is suitable for the intermediate column, while 8 mm is more efficient for slender columns presented in Fig. 11.

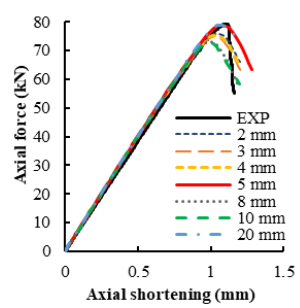

(a) Axial capacity with different mesh sizes

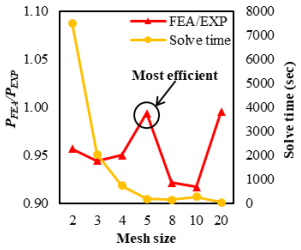

(b) Efficiency of FE models

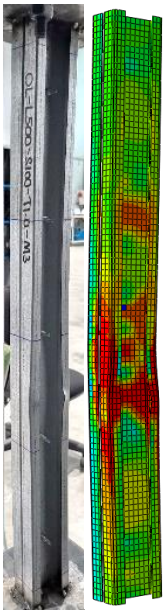

(c) Comparison of failure mode

Fig. 10 Mesh convergence and independence study of OL series

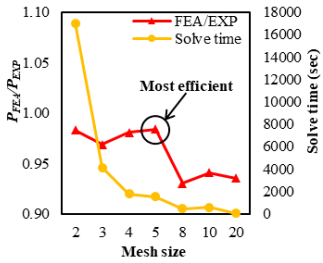

(a) MC3-140-A3

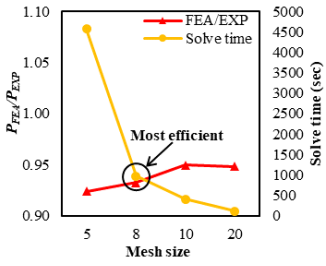

(b) LC3-140-A3

Fig. 11 Mesh convergence and independence study of LU series

3.3. Model validations

The FE models were validated by comparing the axial capacities, axial shortening, out-of-plane deformation, and failure modes obtained between the experimental and FEA results. All developed FE models show strong agreement in simulating the actual behaviour for each series. The FEA results fell within the upper and lower boundaries of experimental results which are shown in Figs. 12 and 13. For the LU series, a comparison between the out-of-plane deformation of experimental and numerical results was not performed as the relevant data was not reported. Nevertheless, the failure modes of the model matched the actual behaviours closely. A summary of the comparisons of the axial capacities, axial shortening, and out-of-plane deformation of experimental and numerical results at yield, ultimate, and failure points was presented in Table 3.

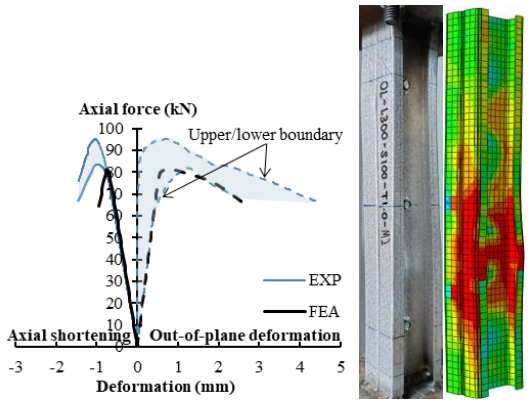

(a) OL-L300-S100-T1.0

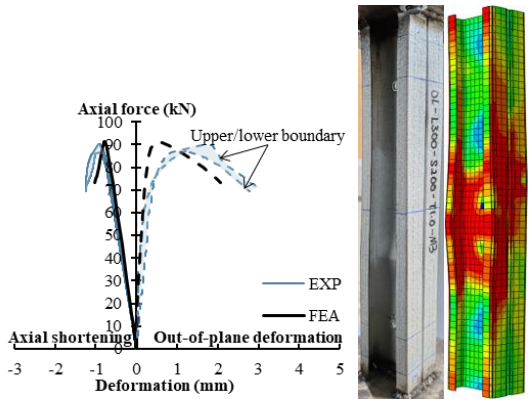

(b) OL-L300-S200-T1.0

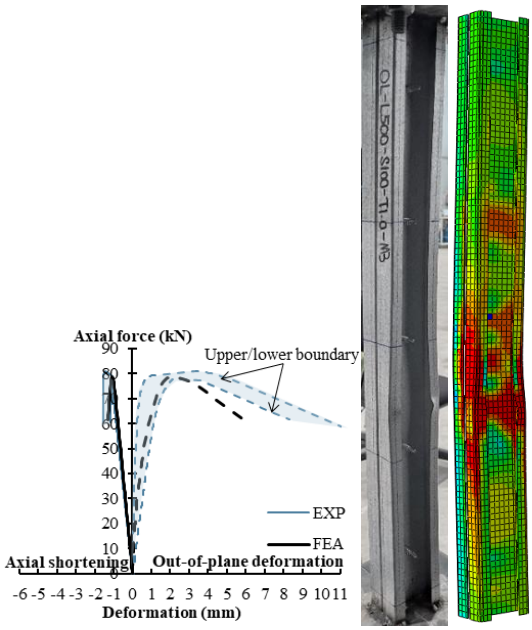

(c) OL-L500-S100-T1.0

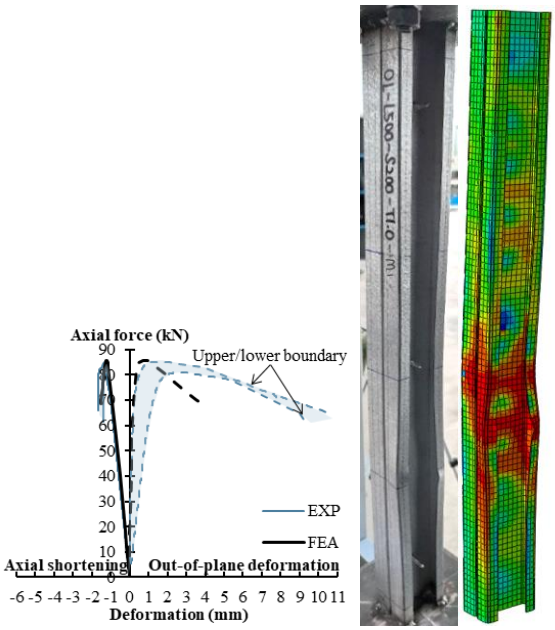

(d) OL-L500-S200-T1.0

Fig. 12 Model validation of OL series

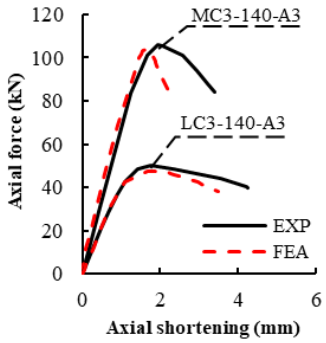

Fig. 13 Model validation of LU series

Table 3
Comparisons of experimental and numerical results

OL-L300-S100-T1.0-M2									
	Force (kN)			Axial shortening (mm)			Out-of-plane deformation (mm)		
	EXP	FEA	FEA/EXP	EXP	FEA	FEA/EXP	EXP	FEA	FEA/EXP
Yield	72.32	78.17	1.08	0.74	0.68	0.92	0.68	0.54	0.79
Ultimate	83.63	81.26	0.97	0.96	0.74	0.77	1.76	0.77	0.44
Failure	66.86	64.69	0.97	1.46	0.94	0.64	4.36	2.68	0.61
OL-L300-S200-T1.0-M3									
	Force (kN)			Axial shortening (mm)			Out-of-plane deformation (mm)		
	EXP	FEA	FEA/EXP	EXP	FEA	FEA/EXP	EXP	FEA	FEA/EXP

Yield	85.29	88.59	1.04	0.78	0.71	0.91	1.03	0.35	0.34
Ultimate	90.29	91.37	1.01	0.92	0.78	0.84	1.72	0.51	0.30
Failure	72.23	73.04	1.01	1.22	1.02	0.84	2.80	2.07	0.74
OL-L500-S100-T1.0-M3									
		Force (kN)		Axial shortening (mm)			Out-of-plane deformation (mm)		
	EXP	FEA	FEA/EXP	EXP	FEA	FEA/EXP	EXP	FEA	FEA/EXP
Yield	77.41	76.99	0.99	1.04	0.99	0.95	0.67	1.61	2.42
Ultimate	79.32	78.83	0.99	1.11	1.08	0.98	1.28	2.23	1.74
Failure	63.43	61.51	0.97	1.15	1.30	1.14	8.34	5.99	0.72
OL-L500-S200-T1.0-M1									
		Force (kN)		Axial shortening (mm)			Out-of-plane deformation (mm)		
	EXP	FEA	FEA/EXP	EXP	FEA	FEA/EXP	EXP	FEA	FEA/EXP
Yield	81.72	84.83	1.04	1.20	1.19	0.99	0.61	0.49	0.81
Ultimate	85.12	85.70	1.01	1.30	1.22	0.94	1.28	0.70	0.55
Failure	61.52	61.32	1.00	1.37	1.68	1.22	9.37	5.40	0.58
MC3-140-A3									
		Force (kN)		Axial shortening (mm)			Out-of-plane deformation (mm)		
	EXP	FEA	FEA/EXP	EXP	FEA	FEA/EXP	EXP	FEA	FEA/EXP
Yield	100.94	97.55	0.97	1.59	1.37	0.86	-	-	-
Ultimate	105.80	104.07	0.98	1.94	1.66	0.86	-	-	-
Failure	84.06	81.70	0.97	3.40	2.28	0.67	-	-	-
LC3-140-A3									
		Force (kN)		Axial shortening (mm)			Out-of-plane deformation (mm)		
	EXP	FEA	FEA/EXP	EXP	FEA	FEA/EXP	EXP	FEA	FEA/EXP
Yield	45.94	42.65	0.93	1.27	1.17	0.92	-	-	-
Ultimate	50.20	47.67	0.95	1.79	1.87	1.05	-	-	-
Failure	40.00	38.13	0.95	4.24	3.48	0.82	-	-	-

Table 4
Proposed parametric matrix for slenderness ratio

Classification		Specimen no.	*L*	*a*	$(KL/r)_m$
Short	OL series with 100 mm screw spacing	OL-L300-S100-1	300	100	33.55
Intermediate		OL-L500-S100-1	504	100	52.77
		OL-L700-S100-1	700	100	72.62
		OL-L900-S100-1	900	100	92.70
Slender		OL-L1100-S100-1	1100	100	112.88
		OL-L1300-S100-1	1300	100	133.11
		OL-L1500-S100-1	1500	100	153.39
Short	OL series with 200 mm screw spacing	OL-L300-S200-1	300	200	41.26
Intermediate		OL-L500-S200-1	504	200	57.98
		OL-L700-S200-1	700	200	76.49
		OL-L900-S200-1	900	200	95.76
Slender		OL-L1100-S200-1	1100	200	115.40
		OL-L1300-S200-1	1300	200	135.26
		OL-L1500-S200-1	1500	200	155.25
Short	LU series with 100 mm screw spacing	LU-L600-S100-2	600	100	31.60
Intermediate		LU-L1000-S100-2	1000	100	51.95
		LU-L1400-S100-2	1400	100	72.46
		LU-L1800-S100-2	1800	100	93.01
Slender		LU-L2200-S100-2	2200	100	113.59
		LU-L2500-S100-2	2500	100	133.42
		LU-L2900-S100-2	2900	100	154.72
Short	LU series with 200 mm screw spacing	LU-L600-S200-2	600	200	33.55
Intermediate		LU-L1000-S200-2	1000	200	53.16
		LU-L1400-S200-2	1400	200	73.33
		LU-L1800-S200-2	1800	200	93.69
Slender		LU-L2200-S200-2	2200	200	114.15
		LU-L2500-S200-2	2500	200	133.93
		LU-L2900-S200-2	2900	200	155.15

3.4. Parametric study

A parametric study was conducted to further study the axial behaviour of the CFS built-up sections with smaller $(w/t)_{max}$. To ensure the consistency of FE models and to make a fair comparison between parametric models, the verified models, OL-L500-S100, and LC3-140-A3 were selected for the parametric studies. In all parametric models, the $(w/t)_{max}$ of the OL and LU series was kept constant at 42.95 and 91.03 respectively to omit the influence of sectional slenderness on the axial capacity of CFS open built-up sections. The parameters studied were: (1) modified slenderness ratio, $(KL/r)_m$ and (2) screw arrangement for members with different section slenderness, $(w/t)_{max}$. The details of parametric models were summarised in Tables 4 and 5, each model was given a specimen number according to the series name, member length, screw spacing, and screw arrangement. Moreover, the parametric study on screw arrangement was only carried out for the FE models with an axial capacity closest to the mean capacity for each class (short, intermediate, and slender member).

Table 5
Proposed parametric matrix for screw arrangement

Specimen no.	*L* (mm)	*a* (mm)	$(KL/r)_m$	Screw arrangement
OL-L300-S100-2	300	100	33.55	Double rows
OL-L700-S100-2	700	100	72.62	Double rows
OL-L1500-S100-2	1500	100	153.39	Double rows
OL-L300-S200-2	300	200	41.26	Double rows
OL-L700-S200-2	700	200	76.49	Double rows
OL-L1500-S200-2	1500	200	155.25	Double rows
LU-L600-S100-1	600	100	31.60	Single row
LU-L1800-S100-1	1800	100	93.01	Single row
LU-L2900-S100-1	2900	100	154.72	Single row
LU-L600-S200-1	600	200	33.55	Single row
LU-L1800-S200-1	1800	200	93.69	Single row
LU-L2900-S200-1	2900	200	155.15	Single row

4. Result analysis and discussion

4.1. Effect of slenderness ratio

Results show that the OL series can achieve greater buckling resistance

when the member slenderness is less than 90 while the LU series can perform better when the slenderness increases as shown in Table 6 and Fig. 14. Besides, different buckling modes were observed for members with the same slenderness ratio but different section slenderness, especially for intermediate columns. The OL series was dominated by global buckling at the ultimate load followed by an interactive local-distortional-global buckling at the failure point. This was because the decrease in section slenderness restricted the occurrence of local and distortional buckling at the ultimate point. For the LU series, failure modes observed were interactive local-distortional buckling at the ultimate load and interactive local-distortional-global buckling at the failure point as reported in [10]. Apart from that, the OL series has greater structural integrity since they were more deformable and degraded gradually compared to the LU series when the member was slender.

Table 6
Summary of axial capacity with different slenderness ratios

Specimen	P_y (kN)	Δ_y (mm)	P_u (kN)	Δ_u (mm)	P_u/f_uA_g	Buckling mode	
						Ultimate	Failure
S100 Series							
OL-L300-S100-1	73.31	0.71	87.47	0.83	0.67	L	LD
OL-L500-S100-1	66.43	0.99	78.83	1.08	0.60	LD	LDG
OL-L700-S100-1	47.87	1.00	56.71	1.12	0.44	G	LDG
OL-L900-S100-1	28.94	0.76	40.72	1.18	0.31	G	LDG
OL-L1100-S100-1	22.78	0.76	26.51	0.95	0.20	G	LDG
OL-L1300-S100-1	17.10	0.68	20.37	0.81	0.16	G	LDG
OL-L1500-S100-1	12.14	0.60	16.05	0.71	0.12	G	G
LU-L600-S100-2	119.40	0.63	132.81	0.83	0.50	LD	LD
LU-L1000-S100-2	111.87	0.98	124.54	1.27	0.46	LD	LD
LU-L1400-S100-2	103.34	1.25	114.34	1.60	0.43	LD	LDG
LU-L1800-S100-2	92.93	1.46	98.86	1.76	0.37	LD	LDG
LU-L2200-S100-2	70.91	1.40	75.02	1.68	0.28	LD	LDG
LU-L2500-S100-2	66.11	1.50	68.09	1.73	0.25	G	G
LU-L2900-S100-2	52.14	1.66	52.24	1.82	0.20	G	G
S200 series							
OL-L300-S200-1	73.31	0.71	83.89	0.77	0.64	L	LD
OL-L500-S200-1	66.43	0.99	75.97	1.03	0.58	LD	LDG
OL-L700-S200-1	47.87	1.00	61.55	1.23	0.47	G	LDG
OL-L900-S200-1	28.94	0.76	37.87	1.18	0.29	G	LDG
OL-L1100-S200-1	22.78	0.76	26.33	1.03	0.20	G	LDG
OL-L1300-S200-1	17.10	0.68	20.06	0.87	0.15	G	LDG
OL-L1500-S200-1	12.14	0.60	15.97	0.71	0.12	G	G
LU-L600-S200-2	117.03	0.67	124.76	0.80	0.47	LD	LD
LU-L1000-S200-2	112.99	1.08	120.03	1.35	0.45	LD	LD
LU-L1400-S200-2	101.41	1.36	106.18	1.51	0.40	LD	LDG
LU-L1800-S200-2	85.90	1.49	92.42	1.71	0.34	LD	LDG
LU-L2200-S200-2	65.88	1.40	75.09	1.79	0.28	LD	LDG
LU-L2500-S200-2	66.41	1.66	66.84	1.76	0.25	G	G
LU-L2900-S200-2	51.80	1.66	51.86	1.82	0.19	G	G

Note: D = distortional buckling, LD = interactive local-distortional buckling, LDC = interactive local-distortional buckling with crushing, LDG = interactive local-distortional-global buckling.

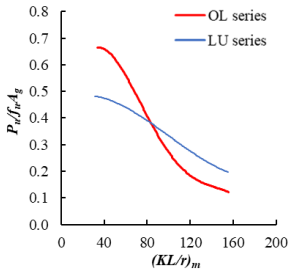

Fig. 14 Parametric study on slenderness ratio

4.2. Effect of screw arrangement

Based on the results in Section 4.1, OL-L300, OL-L700, OL-L1500, LU-L600, LU-L1800, and LU-L2900 were chosen to examine the effect of screw arrangement as summarised in Table 5. The effects of the screw arrangement were summarised in Table 7 and Fig. 15. Results show that the enhancement of the axial capacity is relatively more significant for short columns with greater section slenderness but minimal for intermediate and slender columns, especially for OL series as reported by [13]. This is because the proposed sections have a more compact design due to the reduced $(w/t)_{max}$ therefore, a single row screw is sufficient to form the built-up sections.

Table 7
Summary of axial capacity with different screw arrangement

Specimen no.	P_{FEA}		$P_{FEA\_double}/P_{FEA\_single}$
	Single row screws	Double rows screws	
OL-L300-S100	87.47	90.44	1.03
OL-L700-S100	56.71	56.94	1.00
OL-L1500-S100	16.05	16.09	1.00
OL-L300-S200	83.89	91.99	1.10
OL-L700-S200	61.55	56.02	0.91
OL-L1500-S200	15.97	16.09	1.01
LU-L600-S100	120.49	132.81	1.10
LU-L1800-S100	89.99	98.86	1.10
LU-L2900-S100	51.96	52.24	1.01
LU-L600-S200	121.25	124.76	1.03
LU-L1800-S200	89.19	92.42	1.04
LU-L2900-S200	51.50	51.86	1.01
		Mean	1.03
		SD	0.05
		COV	0.05

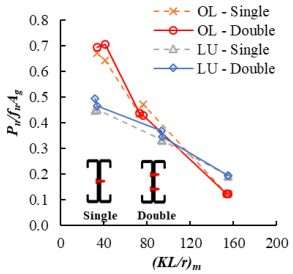

Fig. 15 Parametric study on screw arrangement

4.3. Cost efficiency

The reduction of $(w/t)_{max}$ was expected to enhance the buckling resistance of CFS sections yet provide a more cost-efficient design. To examine the cost efficiency of the proposed sections, the ultimate axial capacity was divided by the mass of steel materials for each investigated specimen for both the OL and LU series. The mass of steel was calculated by multiplying the density of steel

materials (7850 kg/m^3) with the cross-sectional area and length of the sections ($A_g \times L$). This is to identify the ability of the CFS sections to contribute to the axial capacity per unit weight. As shown in Fig. 16, the OL series is comparatively more cost-effective by achieving higher axial capacity while being relatively lighter in weight. However, the differences between the OL and LU series are getting closer for the slender members but still provide a better cost-performance ratio.

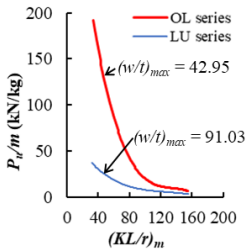

Fig. 16 Comparison of cost efficiency

5. Conclusion

Experimental testing and numerical simulation were performed to study the axial behaviour of the proposed CFS open lipped built-up columns (OL series) which were designed with a $(w/t)_{max}$ less than 45, beyond the common range investigated in previous studies. The axial performance of the proposed sections was compared with the LU series which is the common size of CFS built-up sections reported in [10]. This study found that:

- For columns with a $(KL/r)_m$ less than 90, the OL series demonstrated better performance in achieving higher normalised axial capacity compared to the LU series.
- A single row screw is sufficient to provide good coupling between the CFS built-up members for sections with $(w/t)_{max}$ less than 45.
- OL series are more cost-efficient compared to LU series, attributed to its compact cross-sectional design featuring a smaller gross area.

Acknowledgements

The authors would like to thank ASTEEL Sdn. Bhd. and the Ministry of Higher Education Malaysia under the Fundamental Research Grant Scheme (FRGS) with the grant number FRGS/1/2023/TK01/SWIN/02/1 for their support in this project.

References

[1] W. Yu., R.A. LaBoube, H. Chen, Cold-formed steel design, Wiley, Hoboken, 2020.
[2] L. Gardner, X. Yun, Description of stress-strain curves for cold-formed steels, Construction and Building Materials. 189 (2018) 527–538.
[3] FJ. Meza, J. Becque, I. Hajirasouliha, Experimental study of the cross-sectional capacity of cold-formed steel built-up columns, Thin-Walled Struct. 155 (2020) 106958.
[4] J.H. Zhang, B. Young, Numerical investigation and design of cold-formed steel built-up open section columns with longitudinal stiffeners, Thin-Walled Struct. 89 (2015) 178-191.
[5] S. Selvaraj, M. Madhavan, Design of cold-formed steel built-up columns subjected to local-global interactive buckling using direct strength method, Thin-Walled Struct. 159 (2021) 107305.
[6] C.C. Mei, A.L.Y. Ng, H.H. Lau, S.L. Toh, Applications of built-up sections in lightweight steel trusses, in: Proceedings of Sixth International Conference on Advances in Steel Structures (2009) 857-864.
[7] Y. Dai, K. Roy, Z. Fang, G.M. Raftery, K. Ghosh, J.B.P. Lim, A critical review of cold-formed built-up members: Developments, challenges, and future directions, Journal of Building Engineering. 76 (2023) 107255.
[8] H.H. Lau, T.C.H. Ting, An investigation of the compressive strength of cold-formed steel built-up I sections, in: Proceedings of Sixth International Conference on Advances in Steel Structures (2009) 441-449.
[9] H.D. Craveiro, L.P.C. Rodrigues, L. Laím, Buckling resistance of axially loaded cold-formed steel columns, Thin-Walled Struct. 106 (2016) 358-375.
[10] Y. Lu, T. Zhou, W. Li, H. Wu, Experimental investigation and a novel direct strength method for cold-formed built-up I-section columns, Thin-Walled Struct. 112 (2017) 125–139.
[11] T. C. H. Ting, K. Roy, H. H. Lau, J. B. P. Lim, Effect of screw spacing on behavior of axially loaded back-to-back cold-formed steel built-up channel sections, Advances in Structural Engineering. 21 (3) (2018) 474–487.
[12] T. Zhou, Y. Li, L. Ren, L. Sang, L. Zhang, Research on the elastic buckling of composite webs in cold-formed steel back-to-back built-up columns – Part I: Experimental and numerical investigation, Structures. 30 (2011) 115-133.
[13] S.T. Vy, M. Mahendran, DSM design of fixed-ended slender built-up back-to-back cold-formed steel compression members, J. Constr. Steel Res. 189 (2022) 107053.
[14] M. Abbasi, K.J.R. Rasmussen, M. Khezri, B.W. Schafer, Experimental investigation of the sectional buckling of built-up cold-formed steel columns, J. Constr. Steel Res. 203 (2023) 107803.
[15] Y. Cui, J. Zhang, C. Ma, M. Niu, K. Jiang, S. Li, A. Su, Testing, numerical modelling and design of G550 high strength cold-formed steel built-up section columns, Thin-Walled Struct. 196 (2024) 111529.
[16] AS/NZS. Cold-formed steel structures, AS/NZS 4600: 2018, Standards Australia and Standards New Zealand, Sydney, Australia, 2018.
[17] AS, Metallic Materials-Tensile Testing-Method of test at room temperature, AS 1391, Standards Australia, Sydney, Australia, 2020.
[18] Y. Huang, B. Young, The art of coupon tests, J. Constr. Steel Res. 96 (2014) 159–175.
[19] R. Park, Evaluation of ductility of structures and structural assemblages from laboratory testing, Bulletin of the New Zealand National Society for Earthquake Engineering. 22 (3) (1989) 155-166.
[20] AISI, North American Specification for the Design of Cold-Formed Steel Structural Members, AISI S100-16, American Iron and Steel Institute, Washington, DC, 2016.
[21] ABAQUS, (2017). Abaqus User Manual, Simulia, Dassault Systèmes, Providence, RI, 2017.
[22] K.H. Nip, L. Gardner, A.Y. Elghazouli, Cyclic testing and numerical modelling of carbon steel and stainless steel tubular bracing members, Eng Struct. 32 (2010) 424-441.
[23] D.A. Padilla-Llano, C.D. Moen, M.R. Eatherton, Cyclic axial response and energy dissipation of cold-formed steel framing members, Thin-Walled Struct. 78 (2014) 95-107.

Advanced Steel Construction – Vol. 20 No. 2 (2024) 188–198
DOI:10.18057/IJASC.2024.20.2.11
(Special Issue: *11st International Conference on Advances in Steel Structures, ICASS'2023, Kuching, Sarawak, Malaysia*)

TESTS, MODELLING AND DESIGN OF UNSYMMETRICAL BACK-TO-BACK COLD-FORMED STEEL ANGLES UNDER COMPRESSION

Beulah Gnana Ananthi. G [1, *], Kushal Ghosh [2], Krishanu Roy [2, *], Asraf Uzzaman [3] and James B.P. Lim [2]

[1] *Department of Civil Engineering, College of Engineering Guindy campus, Anna University, Chennai 600025, India*
[2] *School of Engineering, The University of Waikato, Hamilton 3216, New Zealand*
[3] *University of the West of Scotland, United Kingdom*
** (Corresponding author: E-mail: beulah28@annauniv.edu, kris.roy@waikato.ac.nz)*

ABSTRACT

Built-up cold-formed steel (CFS) unsymmetrical angles are increasingly used in structures such as portal frames, roof trusses, and transmission towers. However, there are limited studies on CFS unequal back-to-back angle columns (BBUAC) with stiffeners. This paper presents the results of six experimental tests on intermediate BBUAC with intermittent screw fasteners. The findings include the deformed shapes at failure and the load-axial shortening behavior. Additionally, a nonlinear finite element (FE) model that accounts for both material and geometric nonlinearity was developed. The experimental results were used to validate this FE model. The paper presents a total of 166 new data points, which include six concentric compressive tests and 160 finite element analysis (FEA) results on the compressive strength of BBUAC. The effectiveness of the current design rules, based on the Direct Strength Method (DSM), was also evaluated. The evaluation revealed that the current DSM is unconservative. As a result, a modified DSM approach is proposed.

ARTICLE HISTORY

Received: 22 May 2024
Revised: 15 June 2024
Accepted: 15 June 2024

KEYWORDS

Unsymmetrical back-to-back angles;
Cold-formed steel;
Axial capacity;
Local buckling;
Flexural buckling;
Finite element modelling

1. Introduction

Back-to-back unsymmetrical built-up cold-formed steel (CFS) angle columns (BBUAC) are commonly used in CFS construction [1–8]. To prevent independent buckling of angle sections in such composite designs, either welds or screws are applied intermittently at specified positions along their height. Both the North American Iron and Steel Institute (AISI) [9] and the Australian and New Zealand Standards (AS/NZS) [10] recommend adjusting the slenderness ratio to account for the placement of these fasteners. Recent work has explored the fusion of multiple angles (starred angles - Ananthi et al. [11]) to enhance the load-bearing capacity of these columns through composite action.

Apart from recent studies by Ananthi et al. [12-13] and Deepak et al. [14] on CFS back-to-back angle sections with intermittent stiffeners under concentric compression, little similar research exists in the literature. Notably, research on CFS compound angle sections without stiffeners under axial compression has been conducted by Vishnuvardhan et al. [15] and Qu et al. [16]. Ananthi [17] investigated the concentric compressive capacity of CFS compound box sections formed by joining two equal angles with intermittent screws. Ananthi et al. [12-13] also studied the behavior of CFS single and starred angles under concentric compression. However, besides the studies by Ananthi et al. ([2–3, 12-13]), no research has been reported on compound columns using intermittent stiffeners with both equal and unequal angles.

Back-to-back unequal angles offer a significant advantage where the longer leg can bear the load in case of local buckling failure once it reaches its yield stress limit (Ananthi et al. [12]). Additionally, Dar et al. [18], Aghoury et al. [19], and Anbarasu et al. [20] investigated the concentric compressive capacity of CFS columns with battens composed of four unlipped angles. Young and Chen [21] conducted column tests on CFS sections with uneven lipped angles, while Shi et al. [22] performed experimental and finite element evaluations on steel equal angle columns. Ellobody and Young [23] explored the fabrication of CFS single unequal angle sections as compression members.

This study experimentally investigates the concentric compressive capacity of intermediate-length BBUAC sections with and without intermittent stiffeners (see Fig. 1). Subsequently, a nonlinear finite element (FE) model incorporating geometric and material non-linearities, as well as intermittent fasteners, was developed and validated against the experimental results. Using this validated model, parametric studies were conducted on 160 FE models, varying from stub (300 mm) to slender (2000 mm) columns.

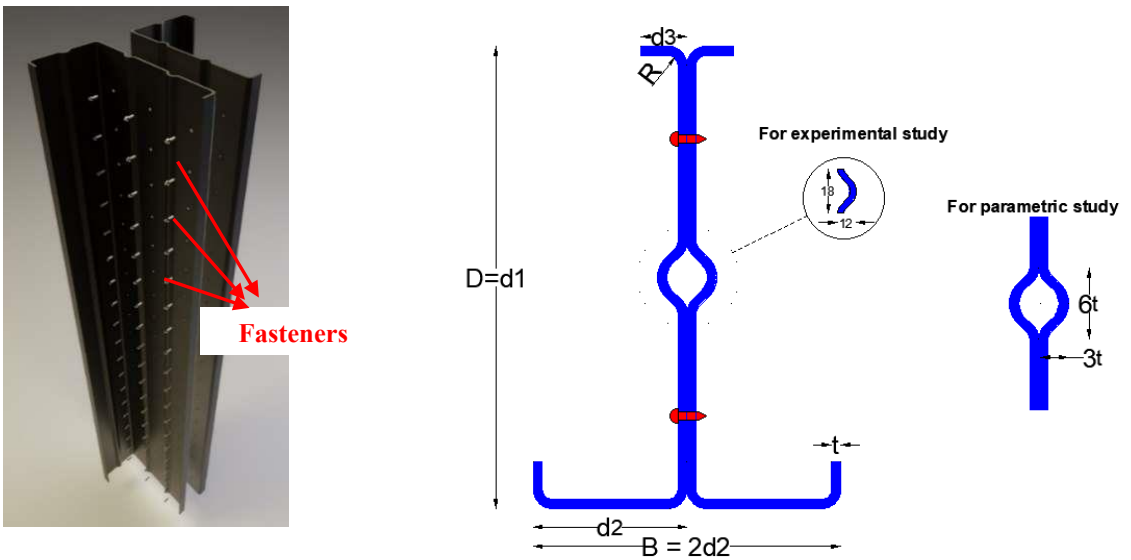

Fig. 1 Fasteners and stiffener details

To compare the experimental and FE-derived concentric compressive capacities with current design standards for stiffened BBUAC, this study presents detailed analyses and findings (see Figs. 1 and 2). The reports cover aspects such as failure modes, column length, and the effects of axial shortening under load on stiffened BBUAC. Notably, based on literature review, no existing study has analyzed the axial strength of BBUAC with various B/D ratios, which is addressed analytically in this study.

The experimental and parametric investigation results were further utilized to predict the concentric compressive strengths of BBUAC and assess their strengths in accordance with the Direct Strength Method (DSM) guidelines. An improved design equation for BBUAC is proposed based on experimental and FE findings, aiming to enhance the reliability of predicting the concentric compressive strengths of BBUAC sections with intermittent stiffeners.

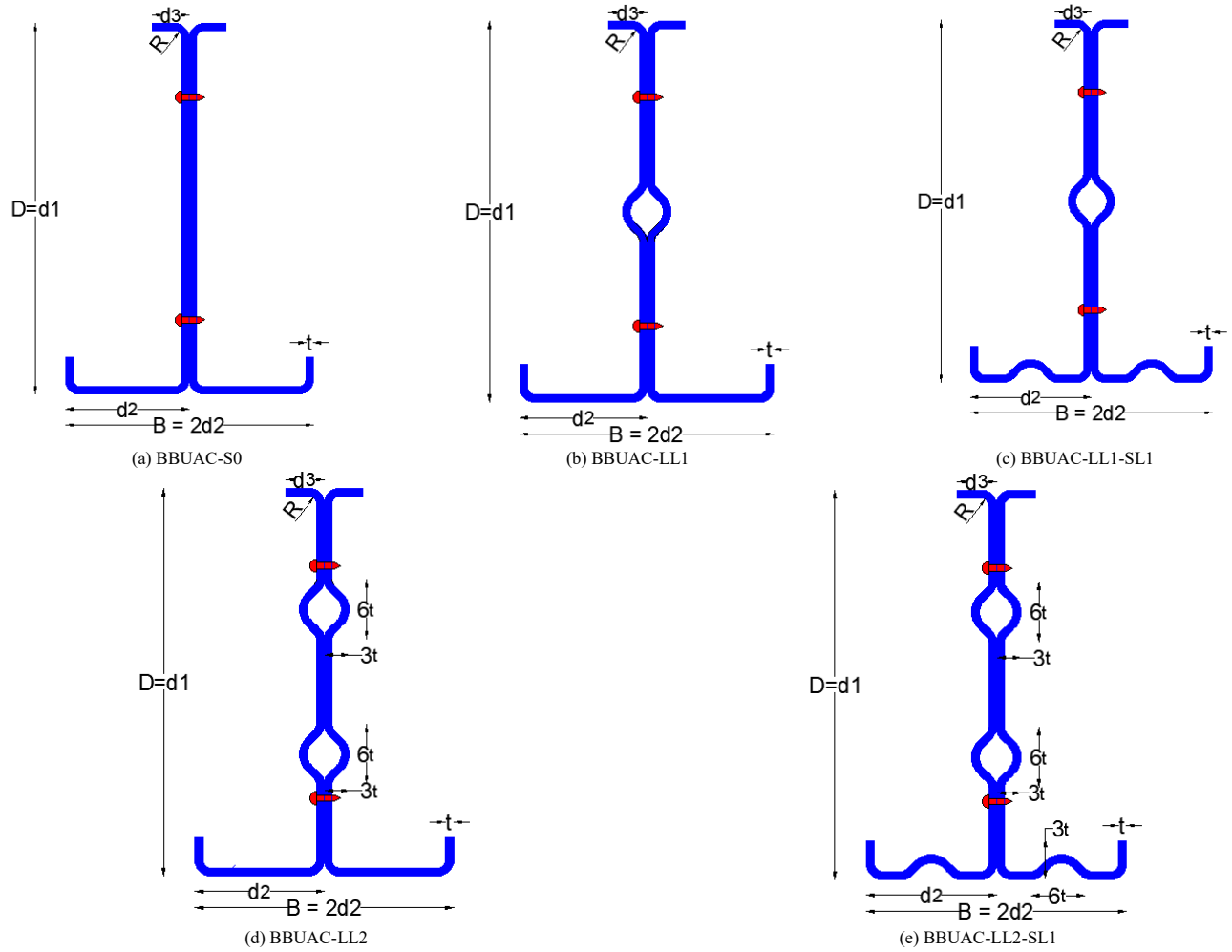

(a) BBUAC-S0 (b) BBUAC-LL1 (c) BBUAC-LL1-SL1

(d) BBUAC-LL2 (e) BBUAC-LL2-SL1

Fig. 2 Details of BBUAC examined in the experimental and parametric studies

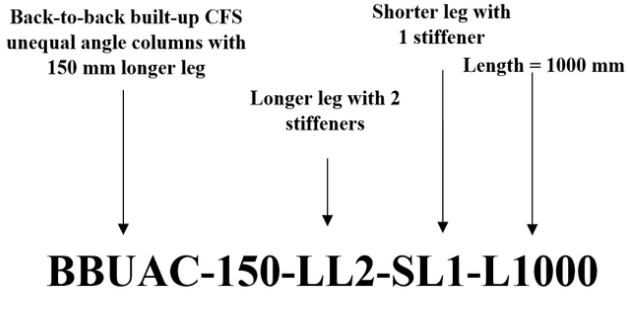

Fig. 3 BBUAC labelling

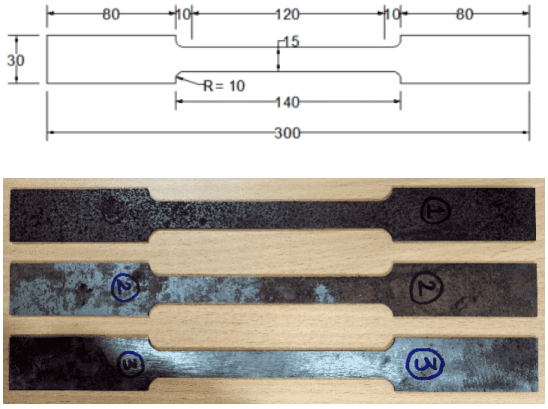

Fig. 4 Specification of coupons (cut from segments after forming)

2. Experimental investigation

2.1. Test specimen details

The experimental program focused on BBUAC configurations as depicted in Fig. 1. These consisted of two unequal angles joined to form unsymmetrical back-to-back angles using intermediate fasteners spaced 50 mm apart (refer to Fig. 1). The screw spacing was chosen in accordance with AISI [9] specifications for CFS built-up columns. Fig. 2 illustrates the B/D ratios considered: 0.75 and 1 for BBUAC120, and 0.67 and 1.00 for BBUAC150. Table 1 presents the new experimental results for six intermediate BBUAC sections.

2.2. Section labels

Labels assigned to the built-up sections denote angle section geometry, section type, and placement of intermittent stiffeners. Fig. 3 shows the labelling used in both the test program and parametric studies. For instance, BBUAC150-LL2-SL1-L300, explained as follows:

- **BBUAC150**: Unsymmetrical back-to-back angles formed using 2 unsymmetrical angles with a longer leg of 150 mm.
- **LL2**: Longer leg with 2 intermittent stiffeners.
- **SL1**: Shorter leg with 1 intermittent stiffener.
- **L300**: Column length of 300 mm.

2.3. Material testing

To characterize the material properties of the test specimens, tensile coupon tests were conducted following EN standards ISO 6892-1-2009 [24] (see Fig. 4). Testing was performed using the Zwick/Roell Z100 kN electromechanical testing equipment, as depicted in Fig. 5. The coupons underwent a loading applied at a constant crosshead speed of 0.01 mm/s. Fig. 6 presents stress-strain curves for the tested steel, including modulus of elasticity, yield stress, and ultimate stress values.

Fig. 5 Electromechanical testing machine (Zwick/Roell Z100 kN)

Table 1
FEA results against experimental results for BBUAC intermediate length sections

BBUAC: ID							Experimental results	FEA results		Design strengths (DSM)		
L=1000mm- S=50	d_1(mm)	d_2(mm)	d_3(mm)	T (mm)	L(mm)	S(mm)	P_{EXP} (kN)	P_{FEA} (kN)	P_{EXP} / P_{FEA}	P_{DSM} (kN)	P_{EXP}/ P_{DSM}	Buckling pattern
I: No stiffeners												
BBUAC120-S0-L1000	120.00	60.00	15.00	2.00	1000	50.00	102.03	108.55	0.94	89.99	1.13	Local+Flexural
BBUAC150-S0-L1000	150.00	75.00	15.00	2.00	1000	50.00	130.24	127.86	1.02	97.23	1.34	Local+Flexural
II: Longer leg with one stiffener												
BBUAC120-LL1-L1000	120.00	60.00	15.00	2.00	1000	50.00	141.38	138.60	1.02	95.73	1.48	Local+Flexural
BBUAC150-LL1-L1000	150.00	75.00	15.00	2.00	1000	50.00	138.35	142.07	0.97	105.59	1.31	Local+Flexural
III: Longer leg with two stiffener												
BBUAC150-LL2-L1000	150.00	75.00	15.00	2.00	1000	50.00	155.25	152.80	1.02	109.12	1.42	Local+Flexural
IV: Longer leg with two stiffener and one stiffener in the shorter leg												
BBUAC150-LL2-SL1-L1000	150.00	75.00	15.00	2.00	1000	50.00	158.83	161.34	0.98	123.06	1.29	Local+Flexural
Mean	-	-	-	-	-	-	-	-	**0.99**	-	**1.33**	-
COV	-	-	-	-	-	-	-	-	**0.03**	-	**0.09**	-

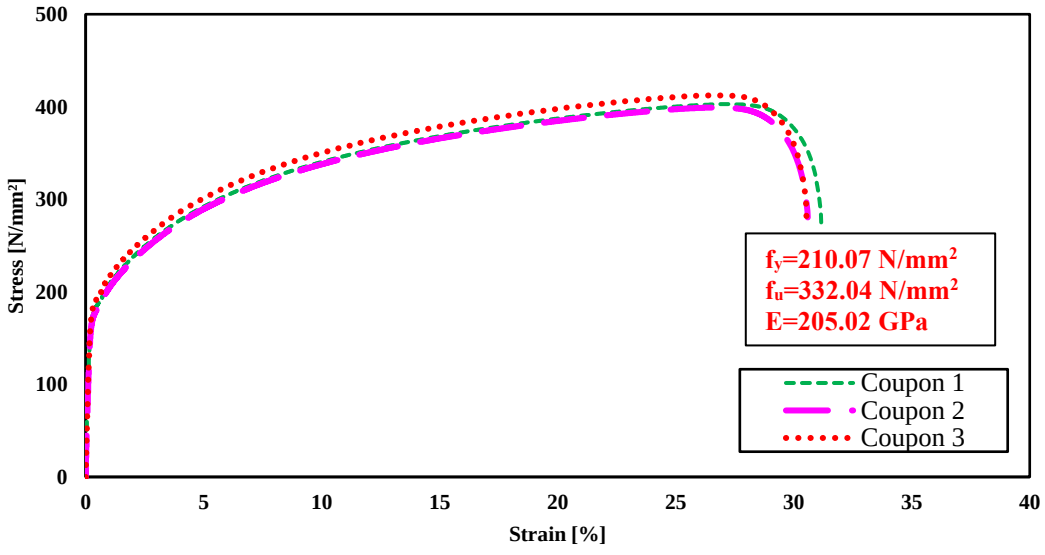

Fig. 6 Full stress-strain curve of BBUAC used in this research

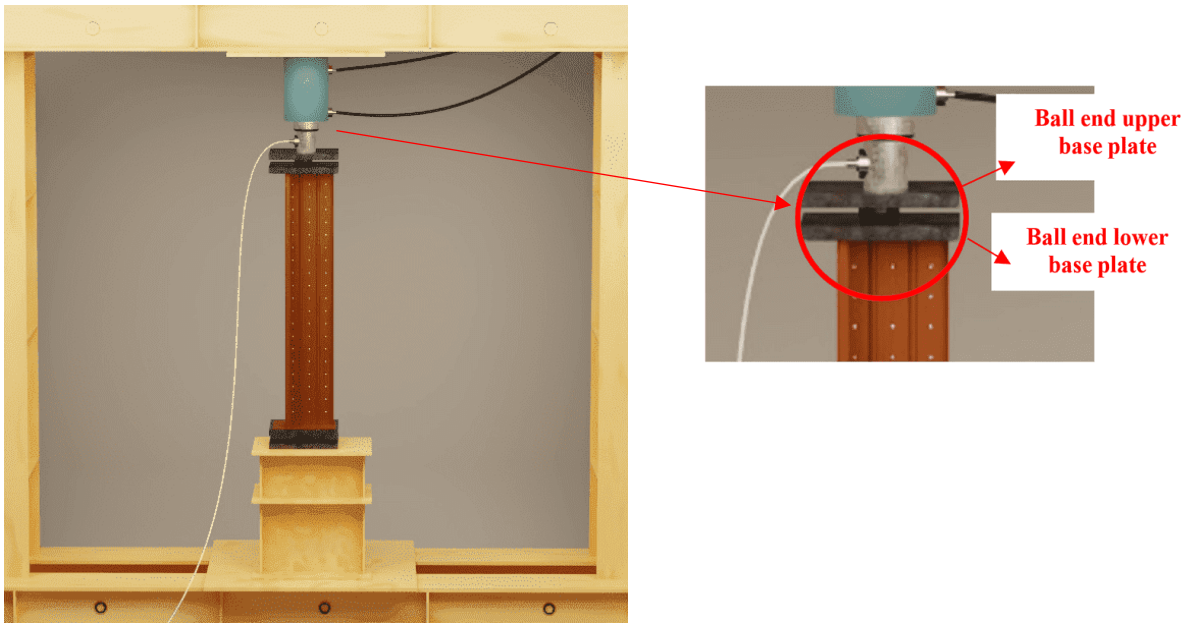

Fig. 7 Details of the experimental test

2.4. Experimental setup and loading techniques

The tests were conducted using a 100-tonne capacity loading frame, with a hydraulic ram and pump equipped with a 50-tonne capacity load cell for applying the load. The experimental specimens were supported under pinned boundary conditions at both ends, where two 200 mm x 200 mm x 10 mm thick end plates were welded to the specimen ends. To facilitate axial loading, a spherical groove measuring 150 mm x 150 mm and 25 mm thick was positioned between these plates. Additionally, a 40 mm spherical ball was placed within the groove to prevent the section from rotating or twisting around its longitudinal axis.

A machined base plate provided a level surface at the top and was welded to support the weight of the sections, ensuring the center of gravity aligned with the loading point. Fig. 7 illustrates the configuration of the test setup. Axial loading on the columns was applied using displacement control technique, with increments set to 1/10th of the maximum load and a loading rate of 0.35 mm/min. Beyond the maximum load, readings were taken to assess buckling strength until failure for each column specimen.

2.5. Test results

Table 1 presents six new experimental findings for the intermediate BBUAC specimens, complementing the concentric compressive strengths (P_{EXP}) reported by Ananthi et al. [12] for stub and short columns. Notably, BBUAC sections with two stiffeners in the longer leg and one stiffener in the shorter leg exhibit an average 16% higher concentric compressive strength compared to sections with only two stiffeners in the longer leg, as detailed in Table 1.

Fig. 8 illustrates the correlation between load and axial shortening for BBUAC150 intermediate-length columns. It shows a primarily linear relationship for BBUAC150-LL1-L1000, BBUAC150-LL2-L1000, and BBUAC150-LL2-SL1-L1000 up to 87%, 91%, and 96% of their respective ultimate failure loads (120 kN, 140 kN, and 152 kN). Non-linear behaviour is observed beyond the failure load.

Fig. 9 provides typical images depicting the failure modes of BBUAC150-S0-L1000, BBUAC150-LL1-L1000, BBUAC150-LL2-L1000, and BBUAC150-LL2-SL1-L1000 specimens from the experiments.

The concentric compressive strengths for sections with multiple stiffeners in the vertical leg with a greater B/D ratio were found to be much better than those for sections with only one longer leg stiffener. For intermediate columns, additional stiffener in the vertical leg improved the built-up sections' strength by an additional 10% on average. Only 15% of the additional strength was attributed to the shorter leg of the intermediate BBUAC's longitudinal stiffener, but it significantly contributed reducing the inside deflection along the major axis of the horizontal legs.

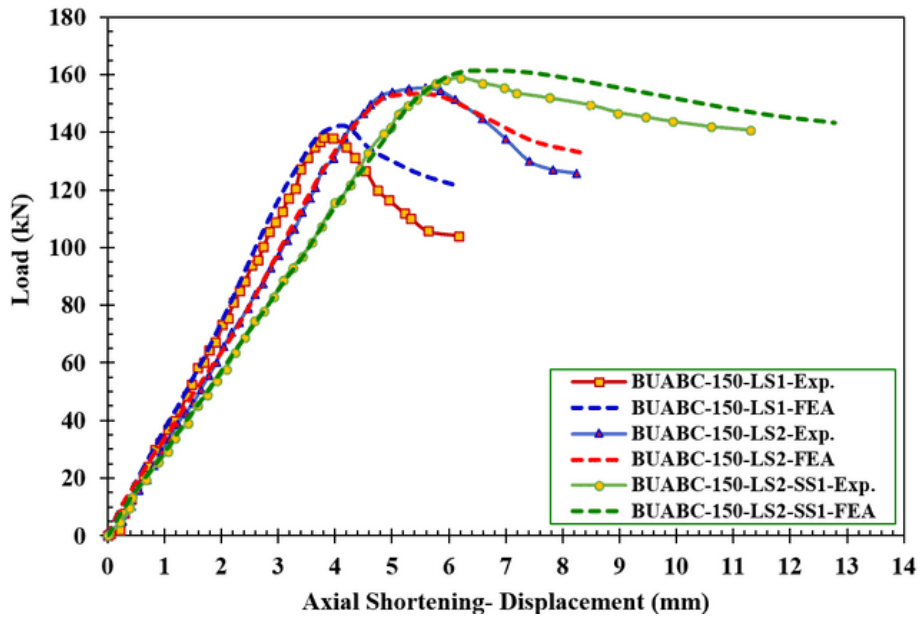

Fig. 8 Load versus axial shortening-displacement graphs for BBUAC

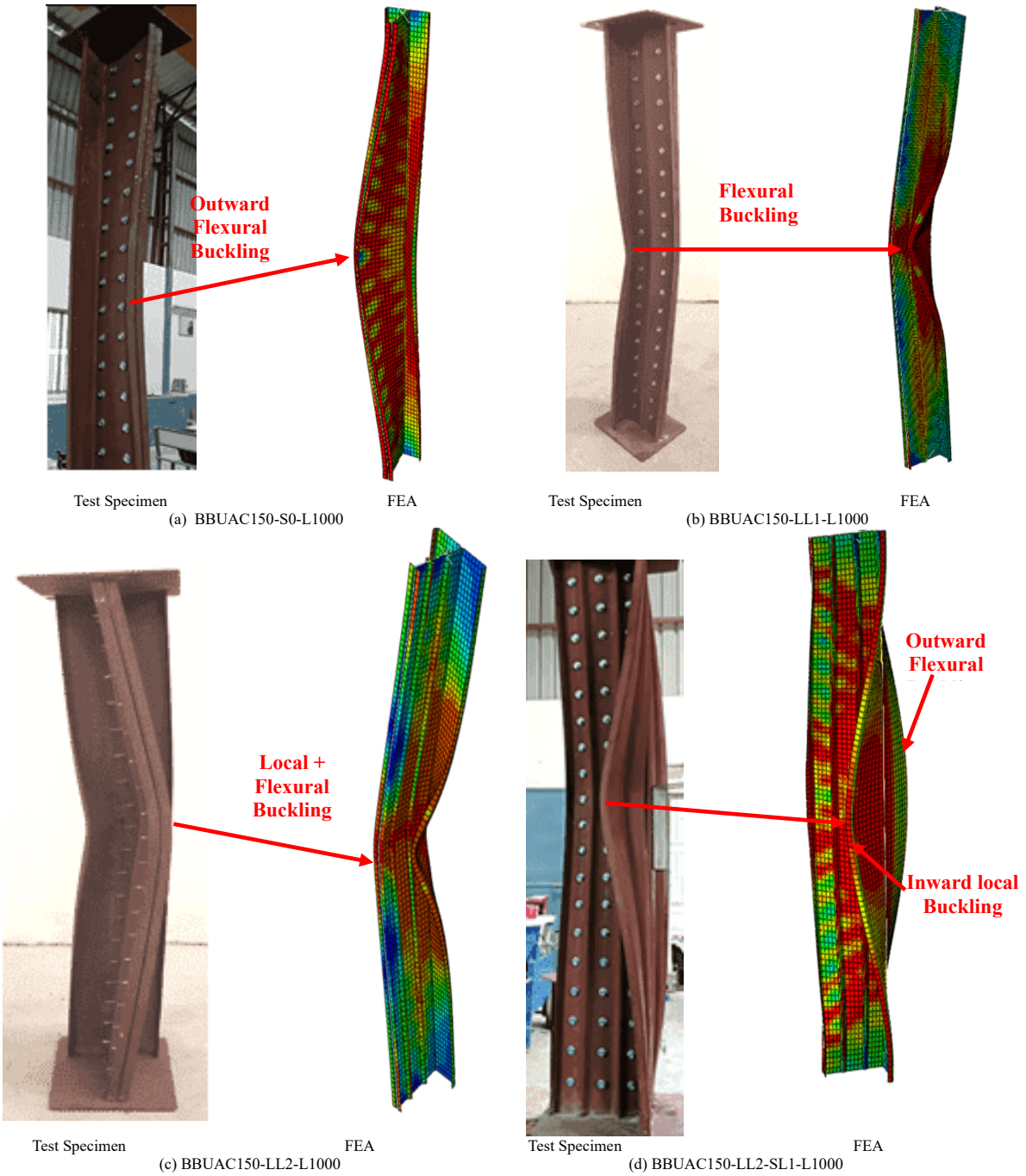

Fig. 9 Failure shapes for BBUAC for 1000 mm length

3. Finite element modelling

3.1. General

Finite Element (FE) models of the BBUAC sections subjected to axial compression were created using ABAQUS software version 6.18 [25]. Initially, linear buckling modes of the BBUAC were identified through eigenvalue analysis (BUCKLE), a feature available in the ABAQUS library. Subsequently, a non-linear analysis was performed using the Riks method. These FE models incorporated both local and global geometric imperfections, as well as material non-linearity. Detailed methods for these models are discussed in the following sections.

3.2. Geometrical and Material Properties

The study modelled the entire BBUAC geometry interconnected by fasteners. A metal plasticity model was applied for analysis and verification. In Section 5, which covers the parametric study, a simplified stress-strain curve adhering to the Von Mises yield criterion for elastic-perfect plastic behaviour was used. Stress and strain curves (engineering) obtained from coupon tests were converted into true stress and strain data for integration into the FE models (as per the equations below)

$$\sigma_{true} = \sigma(1+\varepsilon) \quad (1)$$

$$\varepsilon_{true} = \ln(1+\varepsilon) - {}^{\sigma_{true}}/_{E} \quad (2)$$

3.3. Contact surface and fastener modelling

The interaction between the longer legs of BBUAC sections was modelled using surface-to-surface contact (Fig. 10(a)). Normal contact was defined as "hard," assuming no penetration between the BBUAC sections. Since friction between parts was negligible, a frictionless interaction property was specified in the tangential direction, allowing surfaces to slide freely past each other [20].

There were no indications of fastener failures such as pulling, shearing, or tipping in Section 2.5, suggesting that the stiffness of the fasteners prevented sliding between overlapping sections of BBUAC. Self-tapping screws were used as fasteners to join the two unequal angles, with or without stiffeners, forming the BBUAC sections.

Fasteners were modelled using "beam elements" as point-based connections (Fig. 10(b) and (c)). Similar techniques can be found in the work of Ananthi et al. [20]. The fasteners were modelled with stiff surfaces and contact interactions, ensuring they did not experience shear failure (Fig. 10(d)).

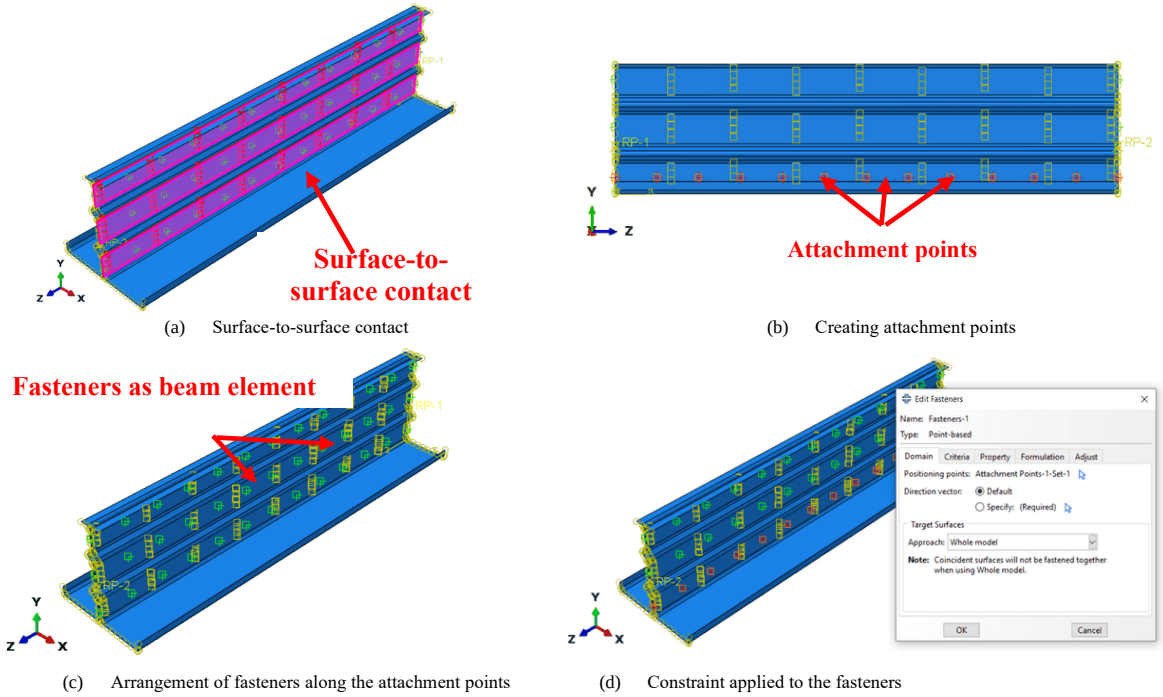

(a) Surface-to-surface contact (b) Creating attachment points

(c) Arrangement of fasteners along the attachment points (d) Constraint applied to the fasteners

Fig. 10 Contact surface and fasteners modelling for BBUAC150-LL2-L600

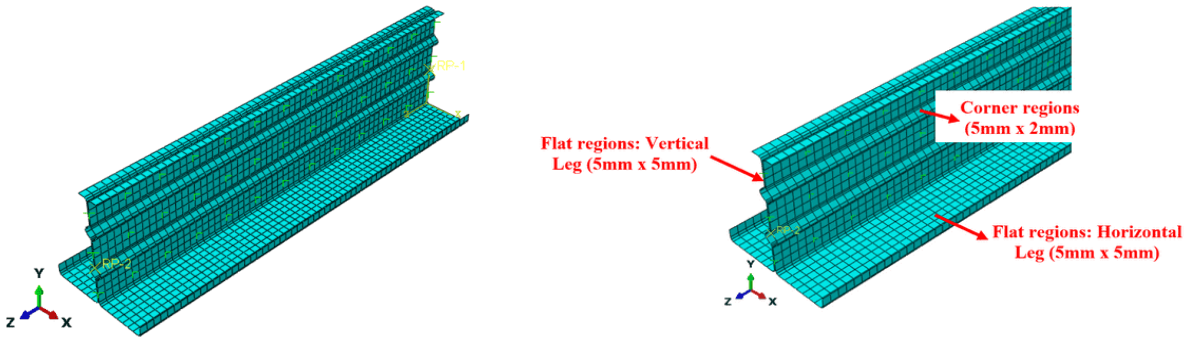

Fig. 11 FE meshing for BBUAC150-LL2-L600

A crucial factor in the structural performance of compound CFS sections is that of shear deformation. However, in this study, shearing, pulling, or tilting failure did not occur with the fasteners connecting the legs of BBUAC, as illustrated in Fig. 9. Additionally, there was no shear failure in the longer legs-connected fasteners, which kept the fasteners from moving. It should be noted that the end plates showed no signs of plate curling or cracking. It should be noted that the end plates showed no signs of plate curling or cracking.

3.4. Element type and FE meshing

The BBUAC sections (S0, LL1, LL2, LL1-SL1, and LL2-SL1) were modelled using 4-noded S4R5 quadrilateral thick shell elements, offering five degrees of freedom (DOFs) per node. This element type accommodates large rotations but assumes constant thickness throughout deformation and negligible strains.

Following a mesh sensitivity analysis, a mesh size of 5 mm × 5 mm was determined suitable for the dimensions of BBUAC sections. Aspect ratios close to 1 were maintained across BBUAC sections by adjusting the number of elements. Sample mesh patterns for the BBUAC150-LL2-L600 section are illustrated in Fig. 11. Similar modelling technique was used by Ananthi et al. [26], Fang et al. [27–28], Roy et al. [29-30], Dai et al. [31], Chen et al. [32], Masood et al. [33], and Liang et al. [34] for CFS columns.

3.5. Boundary and loading conditions

The FE model used simply supported end conditions with free edges. Translations were represented by U1, U2, and U3, and rotations in the x, y, and z directions by UR1, UR2, and UR3, respectively. Reference points RP1 and RP2, coinciding with the centres of gravity (CG) at both ends of BBUAC sections, were tied to all node sets using rigid body tie constraints (Fig. 12(a)).

An axial load was applied at the top end of RP2, with load distributed evenly along edges connected to RP (Fig. 12(b)). At RP2, major load was applied after releasing axial DOF and minor axis rotation (Fig. 12(c)), while all DOFs at RP1 were constrained except minor axis rotation (Fig. 12(d)). This setup simulated realistic experimental boundary conditions, ensuring no eccentricity in loading due to alignment of vertical centroidal axis and load line.

3.6. Modelling of initial geometric imperfections

Fabrication processes introduce initial imperfections in compression members affecting local and global buckling behaviour. Both local and global imperfections were considered, by performing eigenvalue analysis of BBUAC sections with varying thicknesses. Global and local imperfections were defined as 1/1000 times the column length and 0.006 times the thickness (wt) at mid-height, respectively, following Schafer and Pekoz [35]. First global and third local buckling modes are shown in Fig. 13 for BBUAC150-LL2-L600, derived from FEA. No distortional buckling occurred in any of the BBUAC specimens studied.

3.7. Validation of the FE model

Ultimate axial capacities from FEA (P_{FEA}) were compared with experimental capacities (P_{EXP}) for 1000 mm column lengths (Table 1). The average P_{EXP}/P_{FEA} ratio was 0.99 with a coefficient of variation (COV) of 0.03, indicating good agreement between tests and FEA results. Fig. 8 demonstrates the correlation between P_{EXP} and P_{FEA} load-axial shortening behaviour for BBUAC150 intermediate columns, showing consistent results across different configurations (Fig. 9).

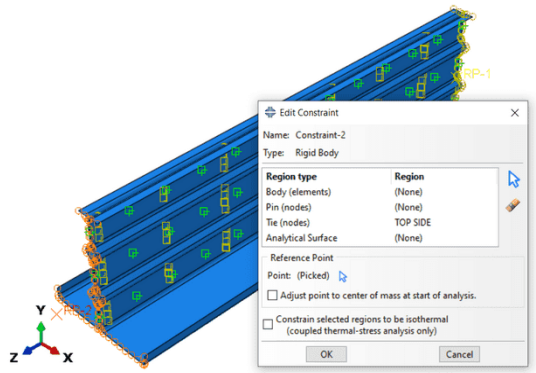

(a) Merging all nodes at the ends using rigid body constraint

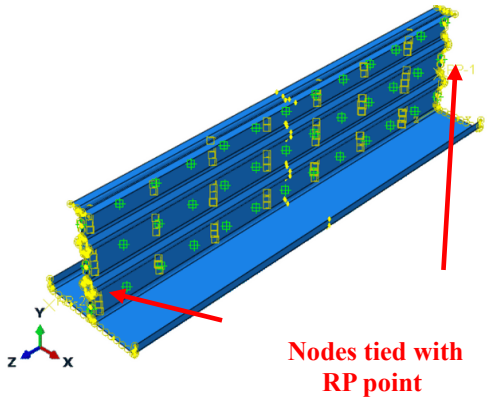

(b) Edges are tied to the reference points

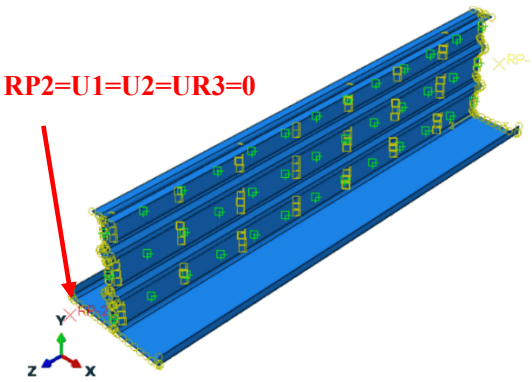

(c) Upper reference point with restraint conditions

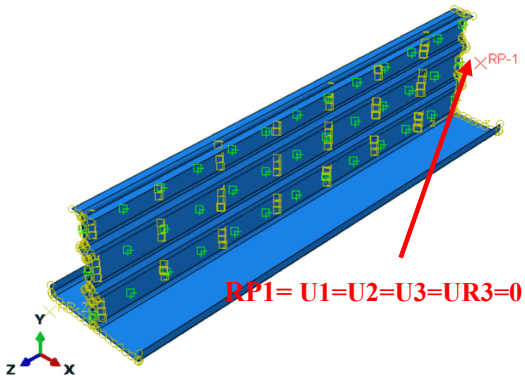

(d) Lower reference point with restraint conditions

Fig. 12 Applied boundary condition for BBUAC150-LL2-L600

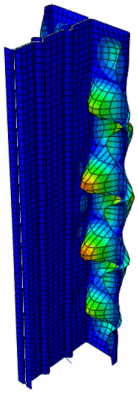

(a) Local buckling

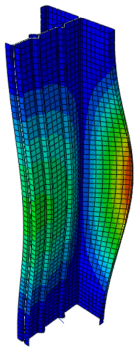

(b) Global buckling

Fig. 13 Initial imperfection contours for BBUAC150-LL2-L600, obtained from the FEA

4. Design guidelines as per AISI [9] and AS/NZ [10] standards

The unfactored axial capacity of BBUAC sections can be calculated using the guidelines provided by the AISI [9] and AS/NZS [10] design standards. The design capacity of these BBUAC sections can be determined in compliance with the given design requirements by utilising the effective width method (EWM) and DSM methodology.

$$P_{AISI\&AS/NZS} = A_e F_n \tag{3}$$

The critical buckling stress (F_n) can be calculated using Equations 4 and 5 as follows:

$$\text{For } \lambda_c \leq 1.5, F_n = \left(0.658^{\lambda^2}\right) F_y \tag{4}$$

$$\text{For } \lambda_c > 1.5, F_n = \left(\frac{0.877}{\lambda_c^2}\right) F_y \tag{5}$$

The non-dimensional critical slenderness (λ_c) can be calculated using Equation 6 as given below:

$$\lambda_c = \sqrt{\frac{F_y}{F_e}} \tag{6}$$

The minimal value of the local buckling capacity (P_{nl})), distortional buckling capacity (P_{nd}), and global buckling capacity (P_{ne}) is used to calculate the design capacity (P_{DSM}) for BBUAC sections [Equation 7].

$$P_{DSM} = \min\left(P_{ne}, P_{nl}, P_{nd}\right) \tag{7}$$

Eqs. (8–10) provide the design equations to determine the local buckling capacity (P_{nl}):

$$For\ \lambda_l \leq 0.776\ ; P_{nl} = P_{ne} \tag{8}$$

$$For\ \lambda_l > 0.776\ ; P_{nl} = \left[1 - 0.15\left(\frac{P_{crl}}{P_{ne}}\right)^{0.4}\right]\left(\frac{P_{crl}}{P_{ne}}\right)^{0.4} P_{ne} \tag{9}$$

$$\lambda_l = \sqrt{\frac{P_{ne}}{P_{crl}}} \tag{10}$$

Eqs. (11–13) provide the design equations to determine the distortional buckling capacity (P_{nd}):

$$For\ \lambda_d \leq 0.561\ ; P_{nd} = P_y \tag{11}$$

$$For\ \lambda_d > 0.561\ ; P_{nd} = \left[1 - 0.25\left(\frac{P_{crd}}{P_y}\right)^{0.6}\right]\left(\frac{P_{crd}}{P_y}\right)^{0.6} P_y \tag{12}$$

$$\lambda_d = \sqrt{\frac{P_y}{P_{crd}}} \tag{13}$$

Eqs. (14–16) provide the design equations to determine the global buckling capacity (P_{ne}):

$$For\ \lambda_c \leq 1.5\ ; P_{ne} = \left(0.658^{\lambda_c{}^2}\right) P_y \tag{14}$$

$$For\ \lambda_c > 1.5\ ; P_{ne} = \left(\frac{0.877}{\lambda_c{}^2}\right) P_y \tag{15}$$

$$\lambda_c = \sqrt{\frac{P_y}{P_{cre}}} \tag{16}$$

The nominal design concentric compressive strength of BBUAC sections was calculated using the aforementioned equations both with and without stiffeners. The joinery details between the two angle sections were replicated in this analytical model by imposing strict constraints at the locations of fasteners, such as in the x, y, and z directions, with degrees of freedom being controlled. The longitudinal degrees of freedom (in the y direction) were unrestricted along the length. In Tables 1 for the intermediate BBUAC with and without stiffeners, the design concentric compressive strengths estimated by the DSM equations are contrasted with the experimental and FE values.

5. Parametric study

A comprehensive parametric study was conducted using a validated FE model to evaluate the adequacy of current Direct Strength Method (DSM) guidelines. This study focused on the geometrical configurations of built-up unequal angles previously examined (BBUAC 120 and BBUAC 150) by Ananthi et al. [12]. Five distinct geometries (BBUAC-S0, BBUAC-LL1, BBUAC-LL1-SL1, BBUAC-LL2, and BBUAC-LL2-SL1) were investigated, varying between longer leg dimensions of 120 mm and 150 mm, and lengths ranging from 300 mm to 2000 mm.

Key findings from the parametric analysis include:

- BBUAC150-LL2 sections with two intermittent stiffeners in the longer leg and a B/D ratio greater than 0.67 exhibited superior concentric compressive strengths compared to sections with only a single intermittent longitudinal stiffener.
- Axial strength for BBUAC120-LL1 specimens with B/D ratios of 0.75 and 1.00 increased by approximately 5% compared to specimens from the BBUAC120-S0 series, irrespective of section thickness.
- While the addition of a shorter intermittent stiffener effectively controlled inward buckling along the major axis, it did not significantly enhance the axial strength. The multiple stiffeners reduced plate slenderness, contributing to increased axial strength.
- Failure mode analyses using the validated FE model indicated significant strength reduction beyond 1000 mm for all columns, regardless of thickness.
- Fig. 14 illustrates the failure modes of BBUAC150-LL1 (B/D: 1.00) series columns at different lengths (300 mm, 600 mm, 1000 mm, 1500 mm, and 2000 mm), showing evident signs of local and flexural buckling in columns longer than 1000 mm. Shorter columns (stub and short) with a thickness of 2 mm failed primarily due to local buckling.

Observations from the parametric study further revealed:

- Longitudinal intermittent stiffeners increase the nominal area of the plate and improve its buckling resistance. A single longitudinal stiffener can delay flexural buckling after local buckling but has limited impact on the load-carrying capacity.
- Fastener spacing used in this study was found adequate as no local buckling occurred between fastener spacings for both BBUAC120 and BBUAC150 configurations.
- Stiffeners effectively prevented out-of-plane local buckling in BBUAC150 sections, as evidenced by comparison of buckling modes.
- Failure in all intermediate and slender columns of both BBUAC120 and BBUAC150 was consistently attributed to combined local and flexural buckling, regardless of slenderness ratio or dimension ratio.
- Despite changes in B/D ratios from 0.67/0.75 to 1.00, the failure pattern remained consistent.

The study concluded that the number of fasteners specified in AISI S100-2016 [9] standard is sufficient to maintain the integrity of BBUAC sections, even for thinner columns, as no fasteners failed simultaneously during the analyses. These findings provide valuable insights into optimizing the design and performance of CFS compound unequal angle section columns under different loading conditions.

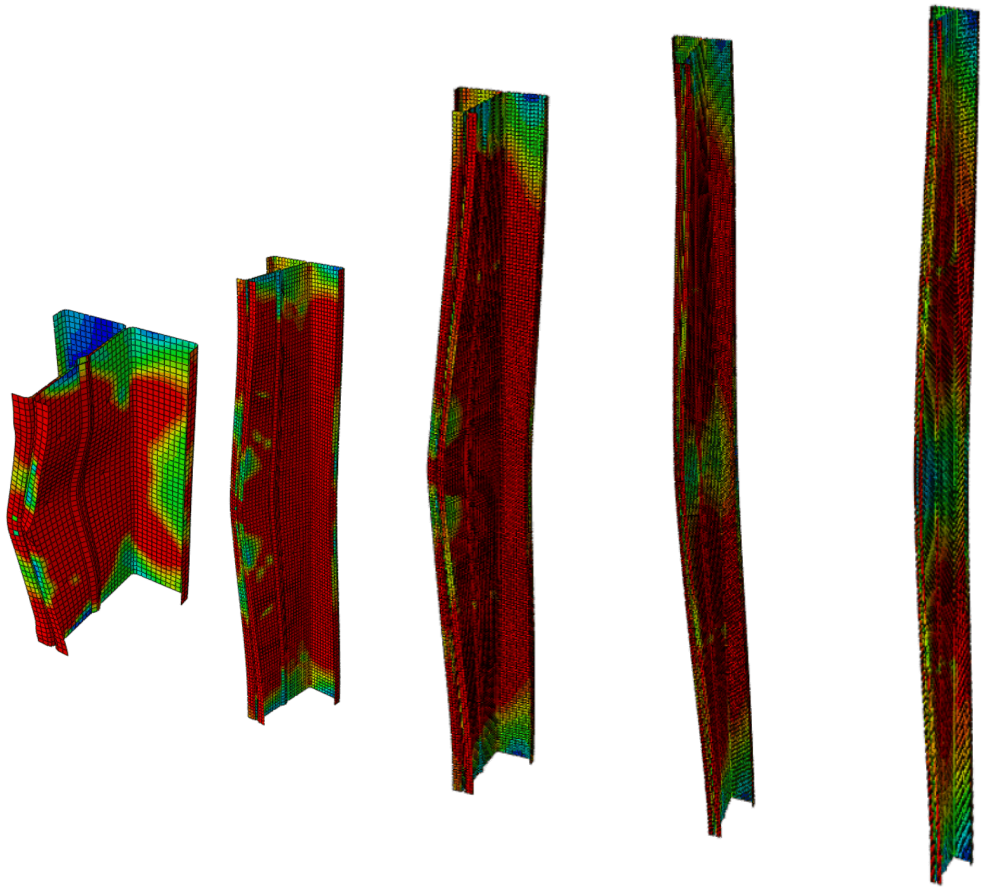

(i) L=300 mm (ii) L=600mm (iii) L=1000 mm (iv) L=1500mm (v) L=2000 mm

Fig. 14 Deformed shapes at failure for BBUAC150-LL1 (B/D:1.00) for 3 mm thickness from the FEA

6. Proposed design equations

The design curves outlined in AISI S100-2016 [9] and AS/NZS 4600:2018 [10] are typically categorized into two main regions. As detailed in Section 4 of this study, the first region applies when $\lambda_c \leq 1.5$ for flexural buckling, while the second region pertains to $\lambda_c > 1.5$. Similarly, for local buckling modes, the first region is defined when $\lambda_l \leq 0.776$, with the second region applicable when $\lambda_l > 0.776$.

Both AISI S100-2016 [9] and AS/NZS 4600:2018 [10] have been found to be overly conservative in estimating the axial strength of BBUAC, prompting this study to propose modifications to current design guidelines for determining BBUAC's concentric compressive strengths. Equations 12 and 13 introduce a modified column curve recommended by this study, aimed at providing safer, more accurate, and less scattered strength estimates. The new column curve is formulated as follows:

The concentric compressive flexural buckling strengths ($P_{Proposed\text{-}1}$) is given by Equation 17.

$$P_{Proposed-1}\begin{cases}\left(0.95^{\lambda^{1.35}_c}\right)P_y & \text{for } \lambda_c < 1.0\\ \left(\frac{1.45}{\lambda^{1.45}_c}\right)P_y & \text{for } \lambda_c \leq 1.7\\ \left(\frac{1.25}{\lambda^{1.15}_c}\right)P_y & \text{for } \lambda_c > 1.7\end{cases} \quad (17)$$

The concentric compressive local buckling strengths ($P_{Proposed-2}$) is given by Equation 18.

$$P_{Proposed-2}=\begin{cases}P_{ne} & \text{for } \lambda_l \leq 0.776\\ 1.25\left[1-0.15\left(\frac{P_{crl}}{P_{ne}}\right)^{0.4}\right]\left(\frac{P_{crl}}{P_{ne}}\right)^{0.4}P_{ne} & \text{for } \lambda_l > 0.776\end{cases} \quad (18)$$

Where

- P_{crl} is the elastic buckling load
- P_{crd} is the distortional buckling load
- P_{cre} is the global buckling load

These equations aim to better predict the concentric compressive strengths of BBUAC sections, taking into account both local and flexural buckling behaviours observed in the experimental and numerical studies conducted in this research. The proposed design strengths ($P_{Proposed\text{-}1}$ and $P_{Proposed\text{-}2}$) and the FEA coincide quite closely, as seen in Figs. 15 and 16.

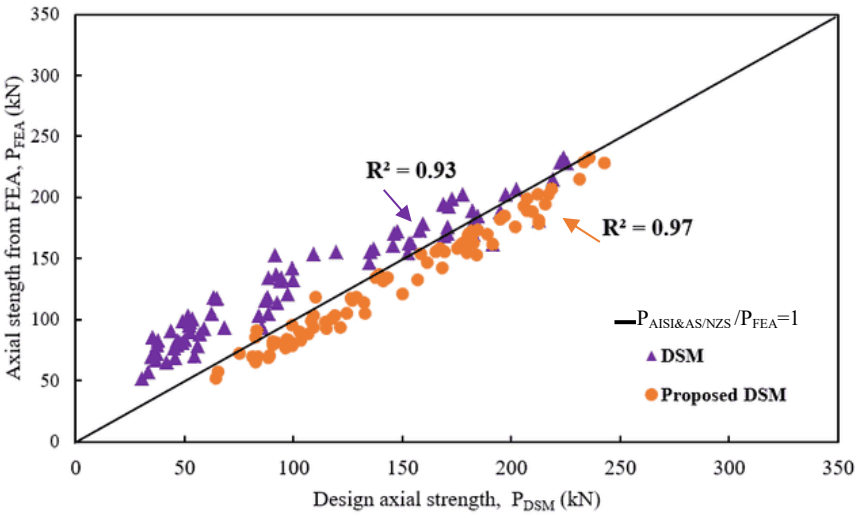

Fig. 15 Comparison of P_{FEA} versus P_{DSM} (2 mm)

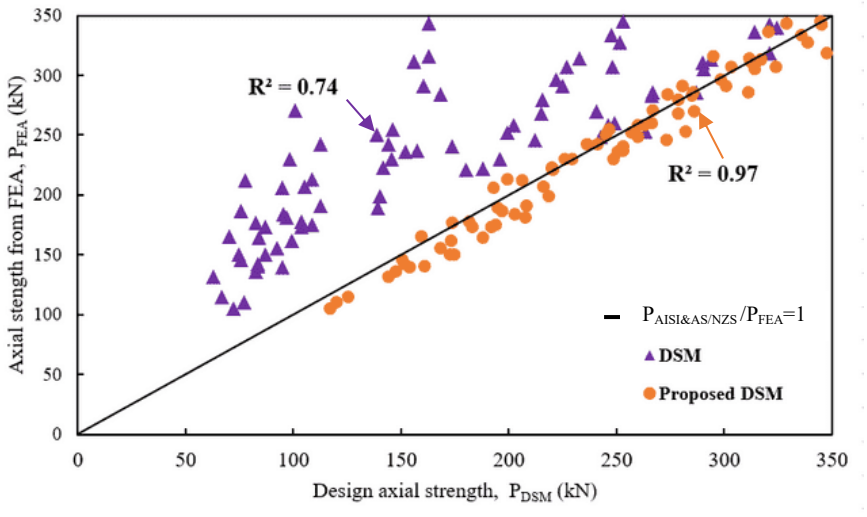

Fig. 16 Comparison of P_{FEA} versus P_{DSM} (3 mm)

7. Reliability analysis

The reliability of the proposed design equations was assessed using recommended design equations. According to the AISI S100-2016 [9] standard, a minimum reliability index (β) of 2.5 is advised for CFS members to ensure reliability. The reliability analysis conducted herein applied a load combination of 1.2 times Dead Load (DL) and 1.6 times Live Load (LL), following the American Society of Civil Engineers Standard (2005).

Statistical parameters such as the mean (P_m) and coefficient of variation (V_P) were determined for BBUAC120 and BBUAC150 sections with thicknesses of 2 mm and 3 mm, respectively. These parameters are critical for assessing the variability in material properties and loads.

Adjustment factors from the AISI S100-2016 [9] standard were used to calculate the reliability index. A resistance factor (φ=0.85) was consistently applied in the analysis. The results indicated that the proposed equations for predicting the axial capacity of both sections (BBUAC120 and BBUAC150) exceeded the minimum target reliability index (β) of 2.5. Therefore, the proposed design equations provide confidence in determining the concentric compressive strengths of BBUAC sections

8. Conclusion

This study investigated the concentric compressive strengths of CFS compound unequal angle section columns arranged back-to-back (BBUAC), both with and without stiffeners. The results of new experimental tests were presented, focusing on concentric compressive strengths, failure modes, and load versus axial displacement behavior. Nonlinear finite element analysis (FEA) models were developed and validated using these test results. A comprehensive parametric analysis involving 160 models was conducted to assess current design recommendations under the Direct Strength Method (DSM) against FE predictions.

Key conclusions drawn from this investigation include:

- Introducing a second intermittent stiffener in the longer leg of intermediate columns increased the strength of built-up sections by an average of 10%.
- Intermittent stiffeners in the shorter leg allowed for deflection along the major axis without significantly affecting concentric compressive strengths. These stiffeners enhanced the column's ability to resist major axis buckling by reducing plate slenderness.
- Stiffeners in the shorter leg effectively controlled major axis deflection but did not noticeably improve concentric compressive strengths.
- The strength of built-up columns decreased gradually with increasing length, primarily due to combined local and flexural buckling, leading to failure in columns longer than 600 mm.
- Current DSM methods tend to underestimate the concentric compressive strengths of BBUAC sections significantly. This study proposes refined design rules that consider both local and flexural buckling to better estimate these strengths.
- The proposed equations were validated through a comprehensive reliability analysis, ensuring accurate prediction of concentric compressive strengths for CFS angle sections with stiffeners.

These findings contribute to advancing the understanding and design methodologies for CFS compound unequal angle section columns, emphasizing the importance of intermittent stiffeners in enhancing structural performance against buckling while proposing improved design guidelines for practical applications.

Notations

A	Geometrical area;
A_e	Effective geometrical area;
CFS	Cold-formed steel;
AISI	American Iron and Steel Institute;
AS/NZS	Australian and New Zealand Standards;
DSM	Direct Strength Method;
EWM	Effective Width Method;
d_1	Longer leg dimension;
d_2	Shorter leg dimension;
d_3	Lip depth;
B	Total width = $2d_2$;
D	Total depth = d_1;
COV	Coefficient of variation;
FEM	Finite element modelling;
F_y	Yield strength;
F_n	Nominal compressive stress;
F_u	Ultimate tensile strength of steel;
f_y	Yield stress;
f_{ol}	Elastic local buckling stress;
f_{od}	Distortional buckling stress;
E	Modulus of elasticity;
L	Unbraced member length;
K	Effective length factor;
L_o	Gauge Length;
P_{DSM}	Design strength in accordance with AISI [5] & AS/NZS [6];
$P_{AISI/AS\&NZS}$	Compressive strength as per Direct Strength Method;
P_{EXP}	Axial capacity from the finite element analysis;
P_{FEA}	Axial capacity from experiments;
P_{cre}	Elastic flexural buckling load (critical);
T	Base metal thickness;
t	Thickness;
P_{nl}	Axial capacity for local buckling;
P_{nd}	Axial capacity for distortional buckling;
P_{ne}	Axial capacity for flexural buckling;
S	Spacing between the screws;
λ_l	Slenderness factor (local buckling);
λ_d	Slenderness factor (distortional buckling);
λ	Slenderness ratio;
DL	Dead load;
LL	Live load;

References

[1] Aruna G., Karthika V., Sukumar, S., "Finite element analysis and design of cold-formed steel built-up closed columns with flange and web intermediate stiffeners", *Canadian journal of civil engineering*, 47(10), 1175-1187, 2020. https://doi.org/10.1139/cjce-2019-0063.

[2] Ananthi G.B.G., Roy K., and Lim J.B.P, "Experimental and numerical investigations on axial strength of back-to-back built-up cold-formed steel angle columns", *Steel Compos. Struct., Int. J.*, 31(6), 601-615. 2019. https://doi.org/10.12989/scs.2019.31.6.601.

[3] Ananthi G.B.G., Roy K., Chen B., and Lim J.B.P., "Testing, simulation and design of back-to-back built-up cold-formed steel unequal angle sections under axial compression", *Steel Compos. Struct., Int. J.*, 33(4), 595-614. 2019. http://dx.doi.org/10.12989/scs.2019.33.4.595.

[4] Abdelrahman AH, Liu YP, Chan SL. Advanced joint slip model for single-angle bolted connections considering various effects. Advances in Structural Engineering. 2020 Jul;23(10):2121-2135.

[5] Abdelrahman AH, Du ZL, Liu YP, Chan SL. Stability design of single angle member using effective stress-strain method. Structures 2019 Aug 1 (Vol. 20, pp. 298-308).

[6] Hussain A, Liu YP, Chan SL. Finite element modeling and design of single angle member under bi-axial bending. Structures 2018 Nov 1 (Vol. 16, pp. 373-389). Elsevier.

[7] An LQ, Jiang WQ, Liu YP, Shi Q, Wang Y, Liu S. Experimental study of mechanical behavior of angles in transmission towers under freezing temperature. Advanced Steel Construction. 2018 Sep 1;14(3):461-78.

[8] Jiang WQ, Liu YP, Chan SL, Wang ZQ. Direct analysis of an ultrahigh-voltage lattice transmission tower considering joint effects. Journal of Structural Engineering. 2017 May 1;143(5):04017009.

[9] American Iron and Steel Institute, *North American specification for the design of cold-formed Steel Structural Members*; NAS S100. 2016.

[10] Standards Australia, "Cold-Formed Steel Structures", AS/NZS 4600:2018, *Standards Australia/ Standards New Zealand*. 2018.

[11] Ananthi G.B.G., Vishnuvardhan S and Knight G.M.S., "Experimental and numerical investigation on thin walled single and starred angle sections under compression", *Arabian Journal for Science and Engineering*, 40 (12), 3417-3427. https://doi.org/10.1007/s13369-015-1776-9. 2015.

[12] Ananthi G.B.G., Deepak M.S., Roy K., and Lim J.B.P., "Influence of intermediate stiffeners on the axial capacity of cold-formed steel back-to-back built-up unequal angle sections", *Structures.*, 32, 827-848. https://doi.org/10.1016/j.istruc.2021.03.059. 2021.

[13] Ananthi G.B.G., Roy K, Lim JB. Behaviour and strength of back-to-back built-up cold-formed steel unequal angle sections with intermediate stiffeners under axial compression. Steel and Composite Structures. 2022;42(1):1-22.

[14] Deepak MS, Ananthi G.B.G., Anupkumar GE, Harini BS, Kumar JM. Strength enhancements across various parts in intermediate and edge stiffened angle sections due to cold-forming. Materials Today: Proceedings. 2022 Jan 1; 65:1382-9.

[15] Vishnuvardhan S., "Behaviour of cold-formed steel single and compound angles in compression", Ph.D. Dissertation, Anna University, Chennai, India. 2006.

[16] Qu S., Zhang B., Guo Y., Sun Q., and Yi W., "Ultimate strength of pinned-end dual-angle cross combined section columns under axial compression", *Thin-Walled Structures*, 157, 107062. 2020. https://doi.org/10.1016/j.tws.2020.107062.

[17] Ananthi G.B.G., "A study on cold-formed steel compound angle section subjected to axial compression", *KSCE J. Civil Eng.*, 22(5), 1803-1815. https:// DOI 10.1007/s12205-017-1221-6. 2018.

[18] Dar M.A., Subramanian N., Rather A.I., Dar A.R., Lim J.B.P., Anbarasu M., and Roy K., "Effect of angle stiffeners on the flexural strength and stiffness of cold-formed steel beams", *Steel Compos. Struct., Int. J.*, 33(2), 225-243. 2019. https://doi.org/10.12989/scs.2019.33.2.225.

[19] El Aghoury M.A., El Salem A.H., Hanna M.T., and Amoush E.A, "Ultimate capacity of battened columns composed of four equal slender angles", *Thin-Walled Structures*, 63, 175-185. https://doi.org/10.1016/j.tws.2012.07.019. 2013.

[20] Anbarasu M., Adil, Dar M. "Improved design procedure for battened cold-formed steel built-up columns composed of lipped angles", *Journal of Constructional Steel Research*, 164, 105781. https://doi.org/10.1016/j.jcsr.2019.105781. 2020.

[21] Young B. and Chen J., "Column tests of cold-formed steel non-symmetric lipped angle sections", *J. Constr. Steel Res*., 64, 808-815. https://doi.org/10.1016/j.jcsr.2008.01.021. 2008.

[22] Shi G., Z. Liu, H.Y. Ban, Y. Zhang, Y.J. Shi, and Y.Q. Wang, "Tests and finite element analysis on the local buckling of 420 MPa steel equal angle columns under axial compression," *Steel Compos. Struct., Int. J*., 12(1), 31-51. https://doi.org/10.12989/scs.2011.12.1.031. 2011.

[23] Ellobody E. and Young B., "Design of cold-formed steel unequal angle compression members", *J. Constr. Steel Res.*, 45, 330-338. https://doi.org/10.1016/j.tws.2007.02.015. 2007.

[24] European Committee for Standardization (CEN), (2009), Metallic materials – Tensile testing. 1: method of test at room temperature', EN ISO 6892-1, Brussels, Belgium.

[25] ABAQUS (2018), Version 6.14-2, SIMULIA, Providence, RI, USA.

[26] Ananthi G.B.G., Roy K., Ghosh K, Pologanathan K, and Lim J.B.P, "An investigation on stiffened cold-formed steel unequal angle box section columns", *Journal of Building Engineering.*, 106989(76), 1-26. 2023. https://doi.org/10.1016/j.jobe.2023.106989.

[27] Fang Z., Roy K., Liang H., Pologanathan K., Ghosh K., Mohamed A.M., "Numerical simulation and design recommendations for web crippling strength of cold-formed steel channels with web holes under interior-one-flange loading at elevated temperatures", *Buildings,* 11 (12), 666. 2021.

[28] Fang Z., Roy K., Uzzaman A., Lim J.B.P., "Numerical simulation and proposed design rules of cold-formed stainless steel channels with web holes under interior-one-flange loading", *Engineering Structures,* 252, 113566. 2022.

[29] Roy K., Lau H.H., Ting T.C.H., Chen B., Lim J.B.P., "Flexural behaviour of back-to-back built-up cold-formed steel channel beams: Experiments and finite element modelling", *Structures,* 29, 235-253. 2021.

[30] Roy K, Lau HH, Lim JB. Finite element modelling of back-to-back built-up cold-formed stainless-steel lipped channels under axial compression. Steel Compos. Struct. 2019 Jan 1;33(1):37-66.

[31] Dai Y., Roy K., Fang Z., Chen B., Raftery G.M., Lim J.B.P., "A novel machine learning model to predict the moment capacity of cold-formed steel channel beams with edge-stiffened and un-stiffened web holes", *Journal of Building Engineering,* 53, 104592. 2022.

[32] Chen B, Roy K, Fang Z, Uzzaman A, Pham CH, Raftery GM, Lim JB. Shear capacity of cold-formed steel channels with edge-stiffened web holes, unstiffened web holes, and plain webs. Journal of Structural Engineering. 2022 Feb 1;148(2):04021268.

[33] Masood R., Lim J.B.P., VA González, K Roy, KIA Khan, "A systematic review on supply chain management in prefabricated house-building research", *Buildings* 12 (1), 40. 2022.

[34] Liang H, Roy K, Fang Z, Lim JB. A critical review on optimization of cold-formed steel members for better structural and thermal performances. Buildings. 2022, 12(1):34.

[35] Schafer, B.W. and Pekoz, T. (1998), "Computational modelling of cold-formed steel: characterizing Geometric imperfections and residual stress," J. Constr. Steel Res., 47, 193-210. https://doi.org/10.1016/S0143-974X (98)00007-8

Advanced Steel Construction – Vol. 20 No. 2 (2024) 199–207
DOI: 10.18057/IJASC.2024.20.2.12
(Special Issue: *11st International Conference on Advances in Steel Structures, ICASS'2023, Kuching, Sarawak, Malaysia*)

FLEXURAL BEHAVIOR OF REINFORCED HOLLOW HIGH STRENGTH CONCRETE FILLED SQUARE STEEL TUBE

Zhi-Jian Yang *, Shu Zhang, Wei-Zhe Cui and Guo-Chang Li

School of Civil Engineering, Shenyang Jianzhu University, Shenyang, PR China
** (Corresponding author: E-mail: faemail@163.com)*

ABSTRACT

Flexural behavior of reinforced hollow high strength concrete filled square steel tube was studied through test and finite element analysis. Six specimens were designed to consider effects of steel ratio and reinforcement ratio. The failure modes, bending moment-curvature curve, load-strain curve and distribution of the deflection curves were analyzed. The results showed that the steel tube, PHC column, sandwich concrete can work well together subjected to bending moment. The change process of moment-curvature curve of specimen could be divided into three stages: elastic stage, elastic-plastic stage and hardening stage. The ultimate bearing capacity of the member increases with the increase of thickness of steel tube. The ultimate bearing capacity of member reinforced with deformed bars is higher than that of non-reinforcement. In addition, the three-dimensional finite element model was established by using ABAQUS software to analyze the behavior of members. Based on the experimental and numerical results, the simplified formula for calculating the flexural capacity of members was proposed. The calculated results are consistent well with the experimental results.

ARTICLE HISTORY

Received: 8 April 2024
Revised: 20 April 2024
Accepted: 5 June 2024

KEYWORDS

Reinforced hollow concrete filled square steel tube;
High strength concrete;
Flexural behavior;
Load sharing

1. Introduction

Concrete filled steel tube (CFST) is composed of filled concrete and steel tube with the advantages of high bearing capacity, good ductility and fire resistance, which is widely used in high-rise building, long-span bridges [1, 2]. In actual engineering, concrete-filled steel tube columns will bear bending moment under wind load and horizontal earthquake [3, 4], so it is necessary to study their flexural performance.

A lot of research about the flexural behavior of CFST members had been done in recent years. Elchalakani et al [5] presented the experimental results of the flexural behavior of circular concrete filled tubes under pure bending, which showed that the filled concrete enhances strength, ductility and energy absorption especially for thinner sections. Han et al [6, 7] conducted pure pending tests on 36 specimens, and four kinds of different parameters were considered, and the calculation formulae of moment versus curvature curves and the flexural stiffness were presented. Elchalakani and Zhao [8] investigated the cyclic flexural behavior of concrete-filled cold-formed circular steel tubes. Moon et al [9] used numerical models to predict the confinement effects, composite action, and flexural behavior of concrete-filled steel tubes, and proposed a simplified model. Wang et al [10] presented a FEA modeling to study the flexural behavior of rectangular concrete filled steel tubular members with compact, non-compact or slender element sections. Zhan et al [11] proposed prestressed concrete-filled steel tube to increase its enhancement as subjected to flexure. Javed et al [12] carried out numerical investigations to study the flexural behavior of square and rectangular steel tubes filled with normal and high strength concrete. Chen et al [13] reported the pure bending test results of 28 circular concrete-filled aluminum alloy tubes, which demonstrated that the large wall thickness of aluminum alloy tube improved the bearing capacity, the bending deformation capacity and the ductility of specimens. AL-Shaar and Gogus et al [14] reported the test results of flexural behavior of lightweight concrete and self-compacting concrete filled square steel tube beams. Liu et al [15] investigated the failure mechanism of concrete-filled steel circular tube support, and proposed welding steel at the vault and the spring line to improve flexural bearing capacity. Al Zand et al [16] conducted experimental and numerical investigations on the flexural performance of concrete-filled square steel tube stiffened with V-shaped grooves. Li et al [17] reported the test and numerical analysis results of high-strength concrete filled high-strength square steel tubes subjected cyclic pure bending, which indicated that the members had excellent energy dissipation capacity and ductility. Li et al [18] investigated the flexural performance of UHPC filled high-strength steel tube and UHPC filled double skin high-strength steel tube, which indicated that the composite action between UHPC and high-strength steel tube was efficient. Wang et al [19] investigated the flexural behavior of high-strength rectangular concrete-filled steel tube members by test and FEM, which indicated that the members with high-strength steel tubes had lower ductility compared with conventional-strength CFST member.

Hollow concrete filled steel tube (HCFST) is an important form of CFST, many researches have been conducted to study its behavior [20, 21, 22, 23, 24]. The bearing capacity, ductility and seismic performance of HCFST columns are lower than solid CFST columns. Therefore, the application scope of HCFST is limited, which is usually used in power transmission tower. To improve the behavior of HCFST, the reinforced hollow concrete filled steel tube (RHCFST) was proposed by Yang et al [25], which is composed by steel tube, PHC column and sandwich concrete. The flexural behavior of RHCFST members was studied by experiment, finite element analysis and theoretical analysis. A general method for calculating the flexural bearing capacity of members is proposed.

2. Experimental investigation

2.1. Specimen design

Six reinforced hollow high-strength concrete-filled square steel tube beams with varying parameters like steel tube thickness and deformed steel bars were designed. The cross section of the specimen is 400mm×400mm, and its length is 2800mm, as shown in Fig. 1. Q235 steel was used to make the tube. C80 and C60 are the compressive strengths of prestressed high strength concrete (PHC) column concrete and sandwich concrete, respectively. Table 1 shows the detailed parameters of the specimens.

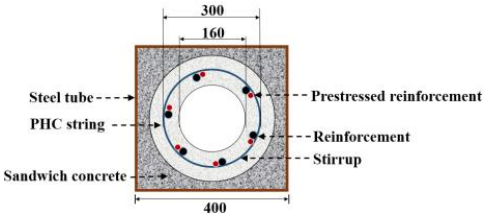

Fig. 1 Cross section of specimen

Table 1
Specimen parameters

Specimen	*t*/mm	Prestressed bars	Deformed steel bars	L_0/mm	ξ
BRHCFST-1	5	6A7.1	6B16	2400	0.234
BRHCFST-2	5	6A7.1	--	2400	0.234
BRHCFST-3	6	6A7.1	6B16	2400	0.284
BRHCFST-4	6	6A7.1	--	2400	0.284
BRHCFST-5	8	6A7.1	6B16	2400	0.386
BRHCFST-6	8	6A7.1	--	2400	0.386

2.2. Material properties

The properties of steel were determined in accordance with Metallic Materials-Tensile testing-Part 1: Method of test at room temperature (GB/T288.2010), which are detailed in Table 2. Commercial concrete was used to create sandwich concrete. The PHC column was prefabricated in factory. The concrete strength was determined using the GB/T 50081-2019 Standard for Test Methods of Concrete Physical and Mechanical Properties. The compressive strength was tested using three 150mm×150mm×150mm cubic standard test blocks. The cubic compressive strengths of PHC columns and sandwich concrete are 77.7MPa and 71.3MPa, respectively.

Table 2
Properties of the bars and steel tube

	t/mm	*d*/mm	f_y/MPa	f_u/MPa	*Es*/GPa
Prestressed bar	-	7.1	1465	1536	208.2
Deformed bar	-	16	459	650	199.5
Stirrup	-	4	631	692	215.5
Steel tube	5	-	358	503	189.7
	6	-	454	493	172.7
	8	-	363	484	190.7

Note: t is the thickness of steel tube, d is the diameter of reinforcement, fy is the yield strength, fu is tensile strength, and Es is elastic modulus

2.3. Test setup

The load was applied by the NYL-5007T testing machine with three-point loading method, as shown in Fig. 2. The deflection was recorded using three displacement transducers. As shown in Fig. 2(b), two displacement transducers (W-4 and W-5) were placed at the positions of the supports to measure their displacement. As shown in Fig. 2(c), twenty-four strain gauges were pasted on the steel tube to record the change in strain. The grading loading system was used in the test, and the load of each stage is about 1/15 of the ultimate bearing capacity, with each load lasting 2 minutes..

(a) Photo of loading device

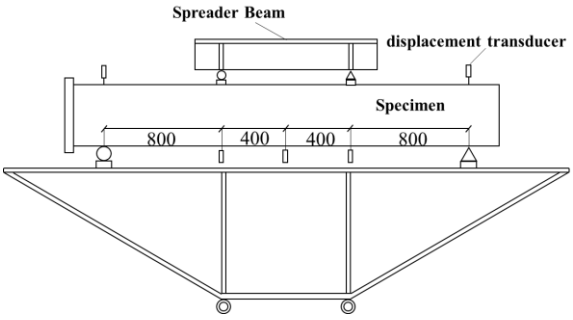

(b) Diagrammatic view

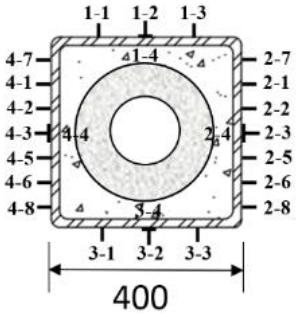

(c) Location of strain gauges

Fig. 2 Layout of loading device

2.4. Test results and discussions

2.4.1. Test phenomenon

At the beginning of the test, the load-deflection curve of specimen BRHCFST-1 grew linearly, suggesting that the specimen was in the elastic stage and had undergone no noticeable deformation. When the load reached 270.1kN, the specimen made a small noise and the concrete in the tension zone fractured. When loaded to 810.2kN, the steel tube in the tension zone reached yield strength. As the load grew, the transverse deformation of the concrete started to exceed that of the steel tube, and the confinement effect could be seen in the local buckling that started to occur in the compression zone of the steel tube's mid-span section. The specimen had reached the stage of elastic-plasticity. When loaded to 1348kN, the concrete made a continual cracking sound. When the load is greater than the specimen's ultimate bearing capacity of 1352.2kN, the load-deflection curve exhibits a decreasing trend. Fig. 3 depicts the overall failure mode and local buckling of BRHCFST-1 at the middle span.

(a) Over all failure mode

(b) Local buckling

Fig. 3 Failure mode of specimen BRHCFST-1

2.4.2. Failure mode

As loaded to 0.7P, the specimens began to appear obvious bending deformation gradually, and the deflection in the mid-span increased rapidly. When loaded to the ultimate bearing capacity, the steel tube on the compression surface appeared local buckling, as shown in Fig. 3(b). The test was terminated when the deflection reached L/50. After the mid-span deflection reached 48mm (L_0/50), the flexural bearing capacity of the specimen was still increasing, which indicates that the specimen has good ductility.

To further investigate the crack development and failure of the concrete of the typical specimen, the steel tube of the specimen BRHCFST-5 was removed, as shown in Fig. 4. The sandwich concrete was crushed at the position of steel tube buckling, the buckling near the loading point is obvious. There are several cracks in the tension zone of the pure bending section of the specimen, extending from the tension zone to the compression zone, about 3/4 of the height. The crack width of the core concrete is about 1~2mm, which is uniformly distributed, and the largest crack is about 5mm near the mid-span section. It could be found that reinforcement has obvious confinement effect on crack propagation of concrete. The larger the reinforcement ratio is, the slower the crack propagation is.

(a) Tensile side of sandwich concrete

(b) Compression side of sandwich concrete

(c) Side face of core concrete

(d) Tensile side of core concrete

Fig. 4 Failure mode of concrete

2.4.3. Distribution of the deflection curves

Fig. 5 shows the deflection distribution curves of specimens along the length. The solid line depicts the deflection curves of specimens subjected to various loads, the abscissa L represents the distance from the left end hinge, and the ordinate represents the deflection value. As shown in Fig. 5, the deflection of each measurement point increases as the load grade increases, and the shape of the deflection curve of the specimen under each load level is essentially a sinusoidal half-wave curve. Throughout the whole loading phase, the specimen deformation is essentially symmetrical and in good accord with the standard sine half-wave curve.

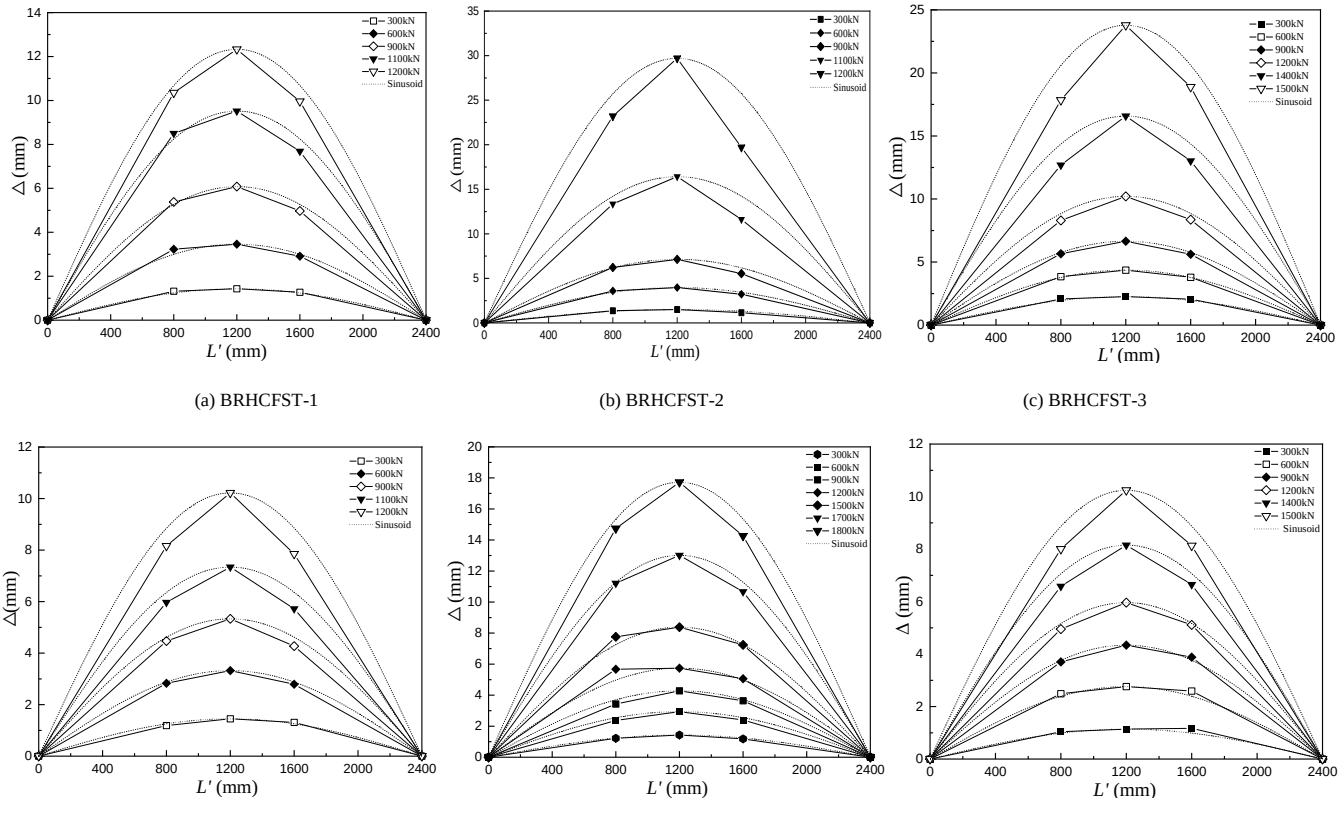

(a) BRHCFST-1 (b) BRHCFST-2 (c) BRHCFST-3

(d) BRHCFST-4 (e) BRHCFST-5 (f) BRHCFST-6

Fig. 5 Distribution of the deflection curves.

2.4.4. Load-strain curves

The specimen load-strain curves are shown in Fig. 6. In the first stage of loading, the longitudinal strain of the compression zone and the tension zone of the steel tube are comparable, and the strain grows essentially linearly. Because the concrete in the compression zone and the steel tube together support the load, when the concrete in the tension zone fractures, the rate of strain change in the tension zone is greater than in the compression zone. The steel tube in the tension zone initially reaches the elastic-plastic stage as the load increases, and the strain growth rate accelerates. After the steel tube in the compression zone has yielded, it enters the elastic-plastic stage and the entire portion of the specimen begins to deform plastically.

2.4.5. Longitudinal strain distribution

The longitudinal strain curves of the specimens at various load levels along the height of the mid-span section are shown in Fig. 7. F is the specimen's ultimate bearing capacity when the tension strain of the steel tube reaches 10000. As seen in Fig. 7, the strain connection is roughly a straight line during the whole loading procedure. Therefore, the deformation of the pure bending section conforms to the assumption of the plane section. The neutral axis is located at the junction of the strain distribution curve and the point X=0 under different loads. Prior to applying load, the neutral axis of the specimen's mid-span section coincides with the section's centroidal axis. When the load reaches 0.2F, the height of the neutral axis moves 0.08~0.1h higher than that of the centroidal axis, and the neutral axis rises at a quicker rate. As the load increases, the neutral axis begins to migrate much higher within the compression zone. When the load reaches about 0.6F, the neutral axis rises about 0.11~0.18h, but the rate of ascent slows. With the continuous increase of load, the rising speed of neutral axis tends to be stable. As the load continues to increase, the rising speed of the neutral axis tends to remain stable. When the load exceeds F, the neutral axis increases between 0.25 and 0.31h.

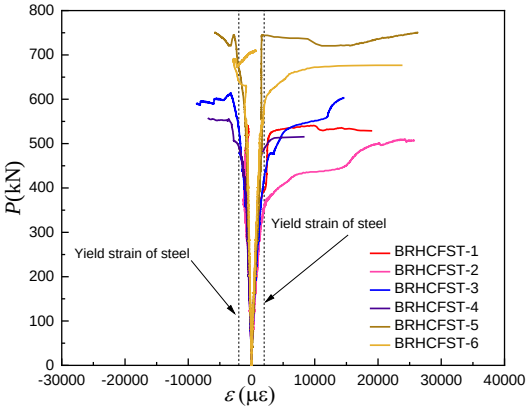

Fig. 6 Load - strain curves of specimens

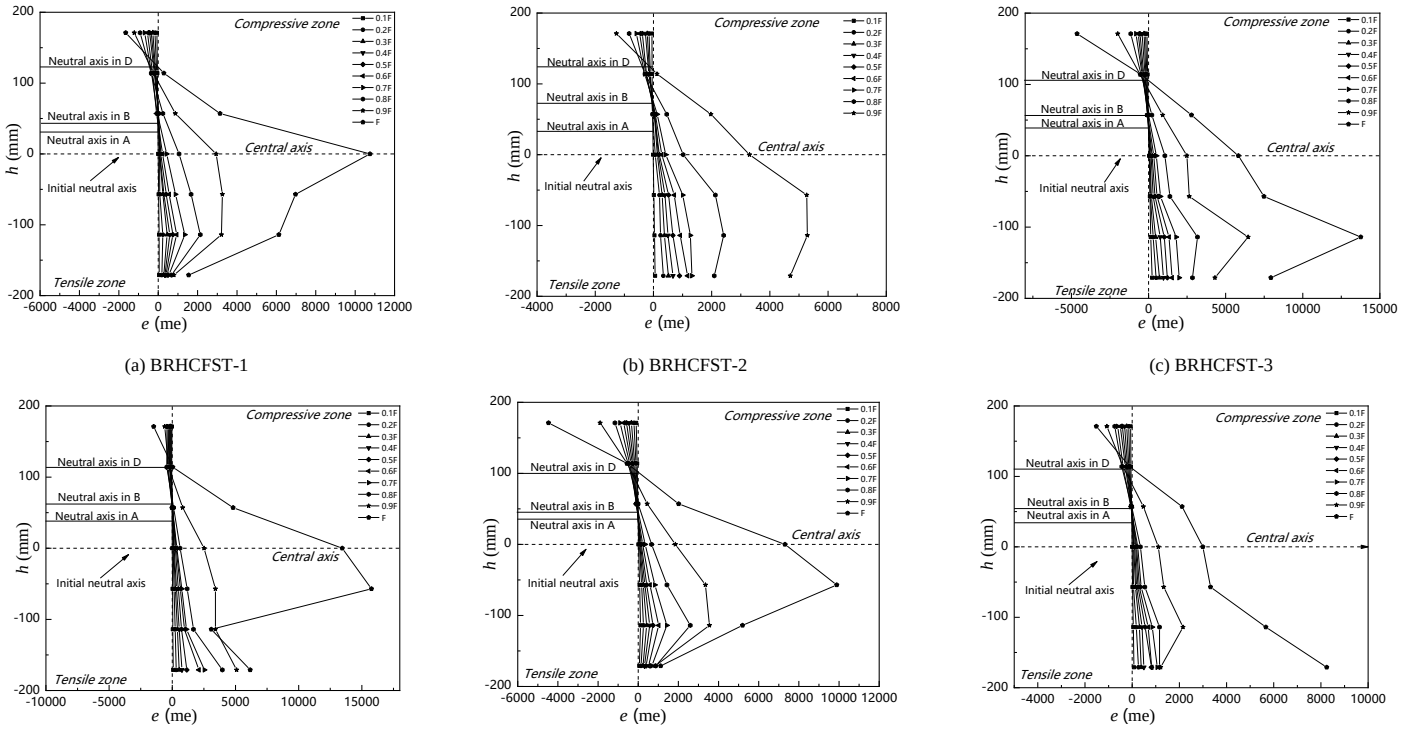

(a) BRHCFST-1 (b) BRHCFST-2 (c) BRHCFST-3

(d) BRHCFST-4 (e) BRHCFST-5 (f) BRHCFST-6

Fig. 7 Longitudinal strain distribution at mid-span

2.4.6. Bending moment-curvature curves

The curvature of the specimen can be calculated by Equ (1). Where Δ_m is the deflection of middle-span, x is the distance from the mid-span section to the support, and l0 is the effective span of the specimen.

$$\phi = (\pi^2 / l_0^2)\Delta_m \sin(\pi x / l_0) \quad (1)$$

Fig. 8 illustrates the moment-curvature curve of the specimen. When the bending moment reaches point A (M_A=0.2M_{ue}), the stiffness changes slightly, the concrete in the tensile zone of the specimen occurs cracks, and the bending stiffness decreases slightly. At point B (M_B=0.6M_{ue}), the tension zone of steel tube yields. At point C (M_C=0.8M_{ue}), compression zone of the steel tube yields. The specimen reaches the ultimate bending moment at Point D (M_D=M_{ue}) is the ultimate bearing capacity. After exceeding the ultimate bearing capacity, the bearing capacity of the member is continuing increasing, but the deformation is too large, so it is unloaded at point E and the test is ended.

Fig. 8 shows that moment-curvature curves can be divided into three stages: elastic stage, elastic-plastic stage and hardening stage. The behavior of each stage is as follows:

Elastic stage (OB): There is no visible change in the specimen during the initial stage of loading. Steel tube and concrete are both in the elastic stage, and their interaction is minimal. The concrete is compressed biaxially in the compression zone, while the transverse deformation of the steel tube is constrained. Bending moment growth is obviously faster than curvature growth, specimen flexural deformation is smaller, and the neutral axis rises slowly. The specimen reaches the proportional limit when the bending moment reaches M_A=0.2M_{ue}, and the concrete in the tension zone cracks when it reaches the ultimate tensile strain of concrete. As a result, the tensile strength of concrete has little effect on the overall mechanical behavior of specimens. Only the effect of tensile stress on steel tube is considered in the tension area, while the effect of concrete is ignored.

Elastic-plastic stage (BD): The maximum tensile stress of steel tube reaches

the yield strength when the bending moment reaches M_B=0.6M_{ue}. The longitudinal compressive stress of concrete continues to rise, and because steel tube has a lower transverse deformation coefficient than concrete, the hoop stress caused by deformation between steel tube and concrete rises as well. The stress in the steel tube greatly exceeds the proportional limit in the tension zone until the steel tube yields. When the bending moment reaches M_C=0.8M_{ue}, the yield strength of the steel tube in the compression zone is reached. The neutral axis rises obviously, but at a slower rate than in the elastic stage, and the rate of curvature growth is faster than the rate of bending moment.

Hardening stage (DE): The specimen enters the hardening stage when the ultimate bending moment M_D=M_{ue} is reached. The hoop stress between steel tube and concrete increases as transverse deformation increases. The bending moment of the specimen does not show a downward trend, the deflection of the specimen increases, and the specimen has undergone obvious large deformation. The specimens exhibit good ductility without brittle fracture due to the good cooperation between steel tube and concrete. Bending moment increases at a slower rate than curvature.

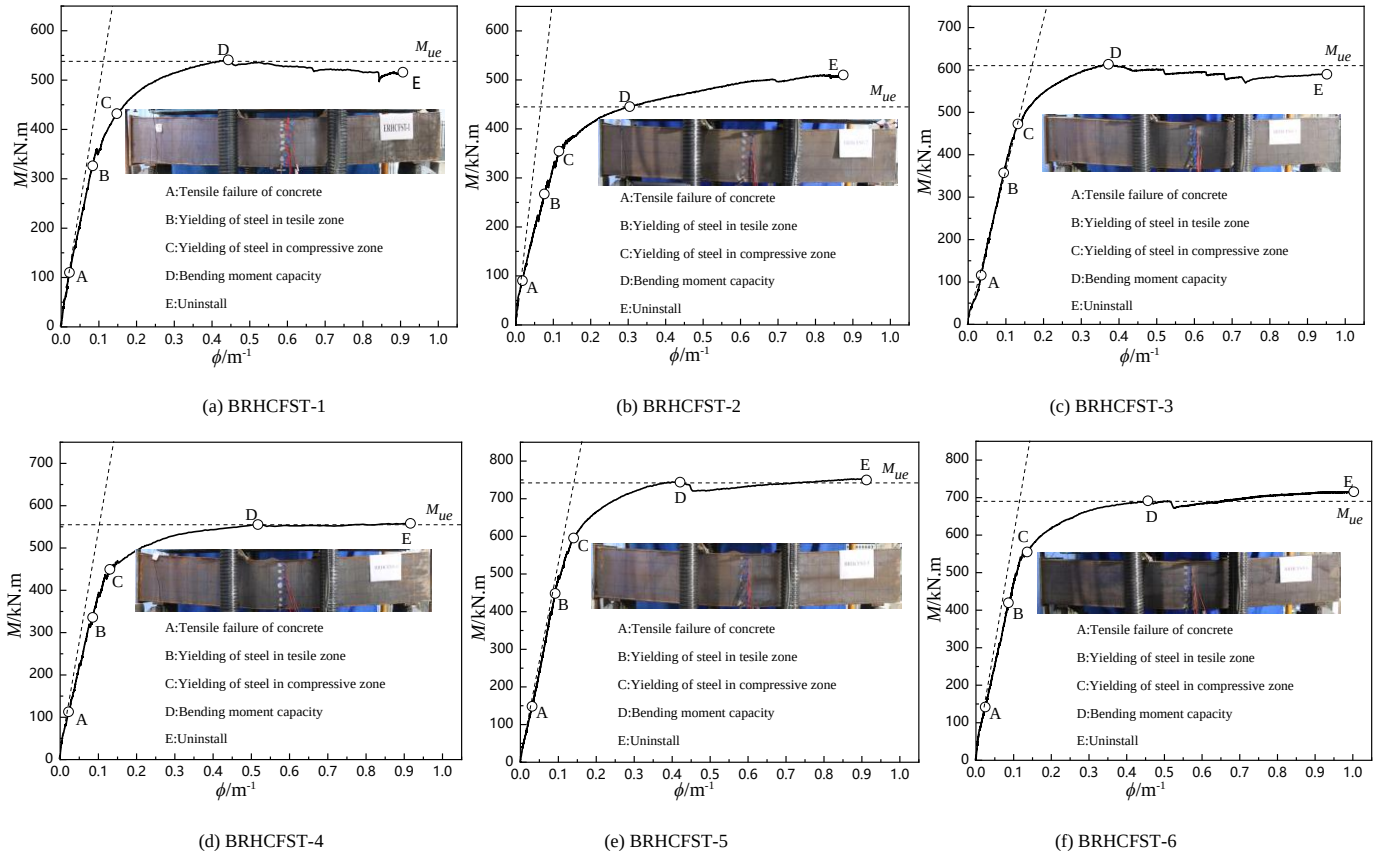

(a) BRHCFST-1 (b) BRHCFST-2 (c) BRHCFST-3

(d) BRHCFST-4 (e) BRHCFST-5 (f) BRHCFST-6

Fig. 8 Bending moment-curvature curves

3. Finite element analysis

3.1. Material constitutive model

3.1.1. Steel

Steel tube stress-strain relationship curve used the five fold line model, and the modulus of strengthening section is 0.01E_s. The bilinear model was used for deformed bars, prestressed bars, and spiral stirrups.

3.1.2. Concrete

The PHC column concrete used the compressive stress-strain relationship of concrete proposed by Guo [26] The modified simplified model considering confinement effect coefficient was adopted in the constitutive model of sandwich concrete [27]. Prestress of PHC column was applied by decreasing temperature method.

3.2. Model establishment

The steel tube, concrete and the endplate adopted a three-dimensional solid element (C3D8R) with 8-node reduction integral format. Surface-to-surface contact was used for the interaction between steel tube and concrete, the normal direction of the interface used hard contact, the tangential direction of the interface used the Coulomb friction model, and the friction coefficient was 0.6 [28]. Hard contact was adopted between endplate and concrete, tie contact was used between steel tube and endplate, and surface-to-surface contact was adopted between sandwich concrete and PHC column concrete. As shown in Fig. 9, the reference points were established at the third point on the upper surface of the specimen, and the displacement-controlled loading method was used to model the pure bending members.

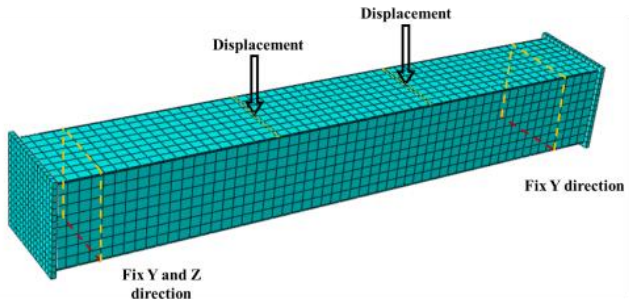

Fig. 9 Simulation boundary conditions.

3.3. Comparison between FEA and test results

Fig. 10 shows a comparison of the failure mode between finite element analysis and the test of specimen BRHCFST-1. The failure modes of the two are quite consistent, as shown in Fig. 10. The results of the finite element analysis are compared to the experimental moment-deflection curve shown in Fig. 11. The FEA results are in good agreement with the experimental bending moment and bending stiffness, as shown in Fig. 11. Table 3 shows that the maximum difference in bending moment is 8.06%. The findings demonstrate that the finite element model accurately simulates and analyzes the flexural behavior of a reinforced hollow high concrete filled square steel tube.

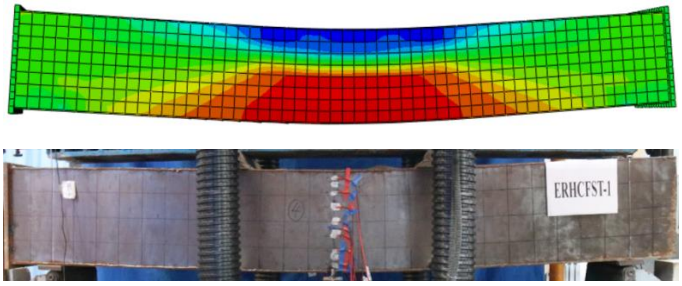

Fig. 10 Comparison of the failure mode

Table 3
Comparison of the ultimate bearing capacity and deflection

Specimen	FEA		TEST		M_s/M_u	Δ_s/Δ_u
	M_s(kN· m)	Δ_s(mm)	M_u(kN· m)	Δ_u(mm)		
BRHCFST-1	533.5	28.0	540.9	25.9	0.99	1.1
BRHCFST-2	484.0	26.0	445.0	17.7	1.08	1.5
BRHCFST-3	605.4	26.5	614.0	21.7	0.99	1.2
BRHCFST-4	550.9	31.5	556.0	30.6	0.99	1.0
BRHCFST-5	739.5	27.0	744.0	24.4	0.99	1.1
BRHCFST-6	678.9	31.8	691.5	26.6	0.98	1.2

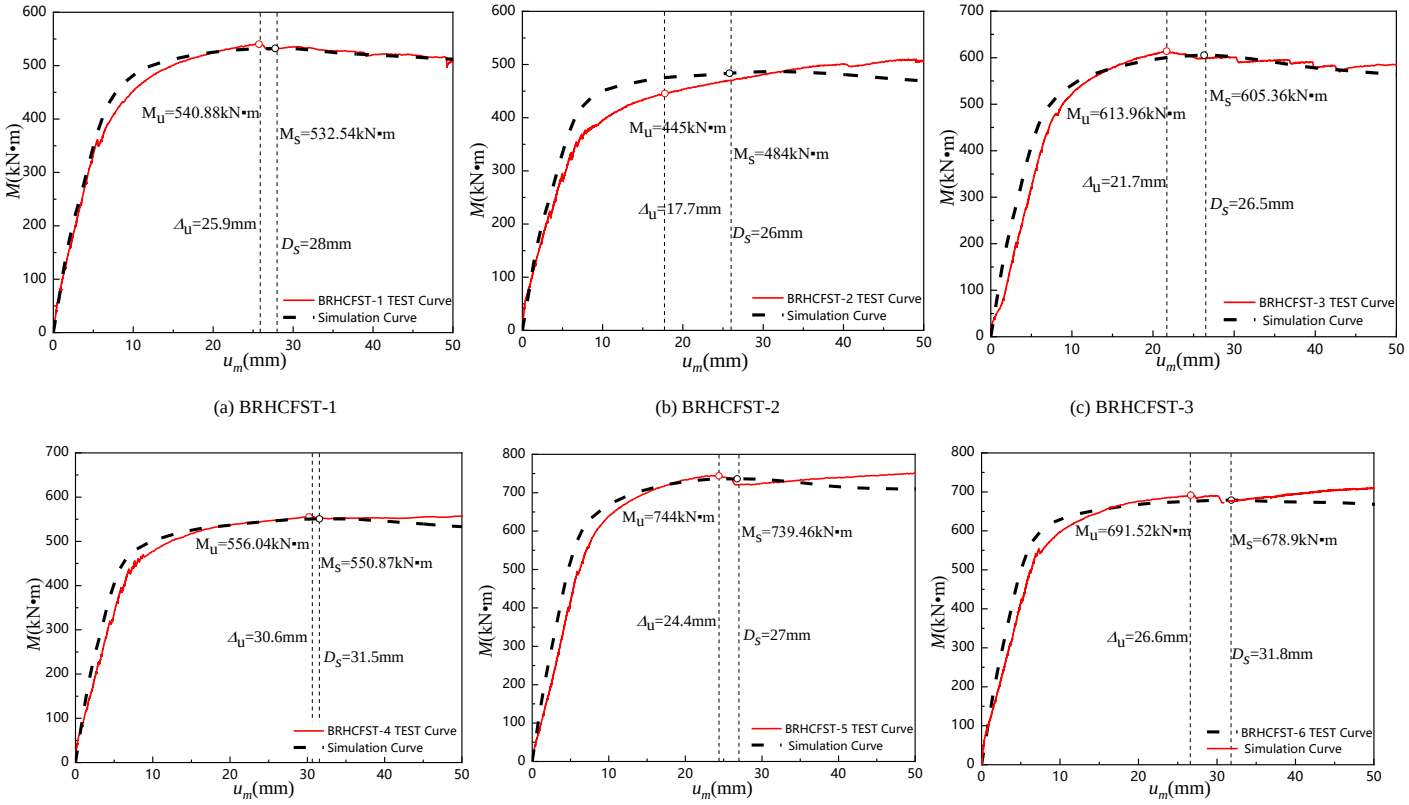

(a) BRHCFST-1 (b) BRHCFST-2 (c) BRHCFST-3

(d) BRHCFST-4 (e) BRHCFST-5 (f) BRHCFST-6

Fig. 11 Comparison of moment-deflection between simulation and test results.

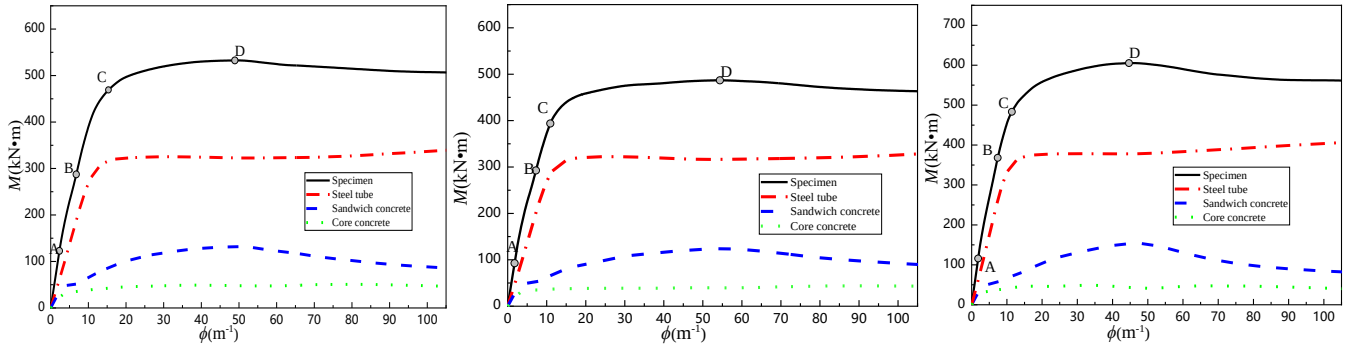

(a) BRHCFST-1 (b) BRHCFST-2 (c) BRHCFST-3

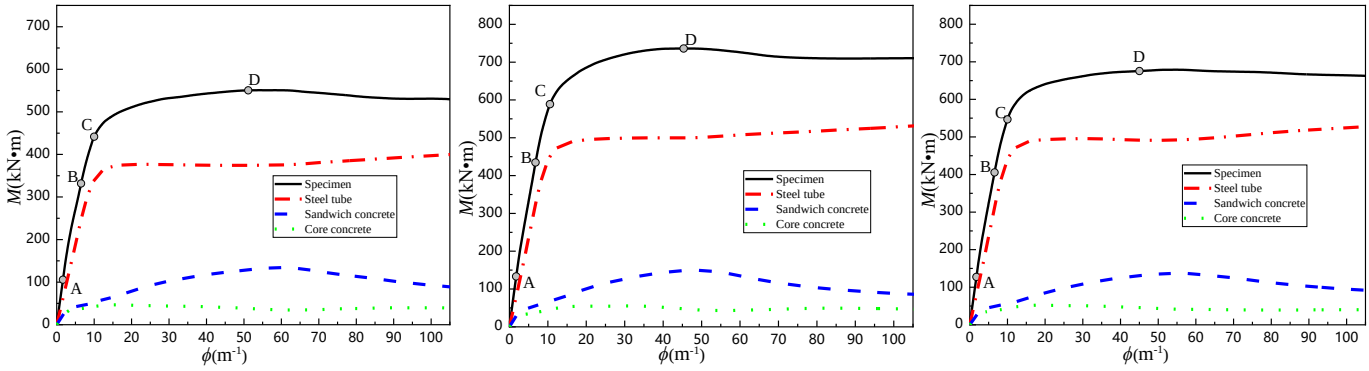

(d) BRHCFST-4 (e) BRHCFST-5 (f) BRHCFST-6

Fig. 16 The moment-deflection curve of each component

3.4. Load sharing of each component

Fig.16 show the bending moments of steel tube, sandwich concrete and PHC column concrete throughout the loading process. Before point A, the steel tube bears more than half of the bending moment, which is about 48.9%~63%, because at the initial stage of loading, the steel tube shares most of the load. The steel tube reaches the peak point after point C, and the bending moment is 67%~80%, and then decreases slowly. The bending moment of sandwich concrete at point D accounts for 19.4%~24.9% of the total bending moment. At this time, it reaches the peak point and then decreases. After the peak point, the curve of PHC column concrete tends to be smooth. Fig. 16 and Table 6 show that the load sharing ratio of steel tube decreases with the increase of deformed bar ratio and increases with the increase of thickness of steel tube.

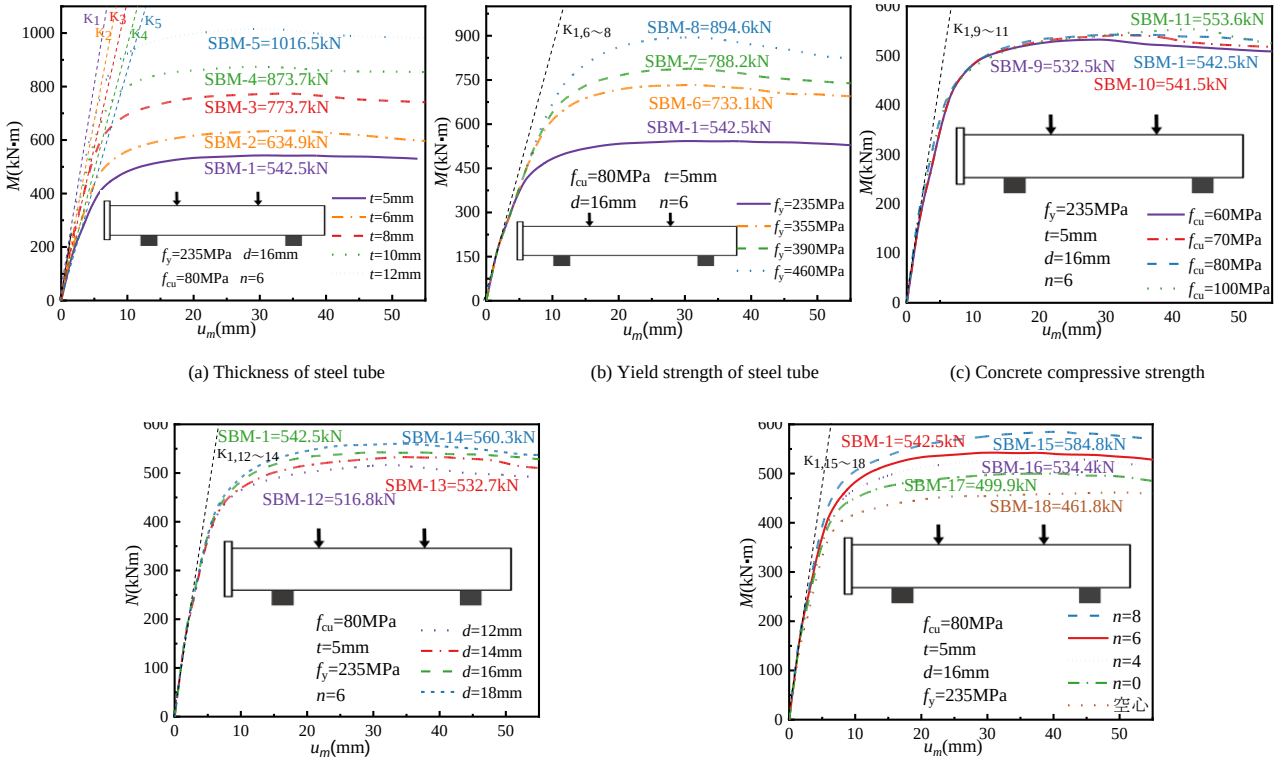

(a) Thickness of steel tube (b) Yield strength of steel tube (c) Concrete compressive strength

(d) Diameter of deformed bars (e) Number of deformed bars

Fig. 17 Moment-deflection curve of different parameters

4. Parameters analysis

To further analyze the influence of different parameters, the steel ratio, steel yield strength, compressive strength of sandwich concrete, the diameter of deformed bars, and number of deformed bars are taken as variables. The design parameters and corresponding results are shown in Fig. 17

4.1. Steel ratio

Fig. 17 (a) shows the moment-deflection curves of members with different steel ratio. The steel tube thickness of model SBM-1, 2, 3, 4 and 5 are 5, 6, 8, 10 and 12mm, respectively. The ultimate bending moments of model SBM-2, 3, 4 and 5 are 113.7%, 138.9%, 160.4% and 185.9% of SBM-1 respectively. The confinement coefficient increases with the increase of steel ratio. The change of steel ratio has a certain influence on the initial stiffness. At the initial stage of loading, the steel tube bears most of the bending moment, at this time, the role of concrete and reinforcement is relatively small, so changing the steel ratio has a great influence on the initial stiffness.

4.2. Steel yield strength

Fig. 17 (b) shows the moment-deflection curves of members with different steel yield strength. The yield strength of model SBM-1, 6, 7 and 8 is 235MPa, 345MPa, 390MPa and 550MPa, respectively. The ultimate bending moments of models SBM-6, 7 and 8 are 132%, 143.8% and 161.6% of SBM-1 respectively. The stiffness of the specimens with different steel strength is the same in the elastic stage. It can be seen from the bending moment distribution that the contribution of steel tube is greater, so when the yield strength of steel is

changed, the bearing capacity changes greatly. Changing the yield strength of steel has no effect on the initial stiffness.

4.3. Concrete compressive strength

Fig. 17 (c) shows the moment-deflection curves of members with different concrete compressive strength. The compressive strength of concrete of model SBM-1, 9, 10 and 11 is 60MPa, 70MPa, 80MPa and 100MPa respectively. The ultimate bending moments of models SBM-9, 10 and 11 are 101.7%, 102.7% and 103.8% of SBM-1, respectively. The change of the compressive strength of concrete has little influence on the bending moment, as shown in Fig. 17. Changing the compressive strength of concrete has no effect on the initial stiffness.

4.4. Diameter of deformed bars

Fig. 17 (d) shows the moment-deflection curves of members with different diameters of deformed bars. The steel diameters of model SBM-1, 12, 13 and 14 are 16mm, 14mm, 12mm and 10mm respectively. The ultimate bending moments of models SBM-12, 13 and 14 are 98.8%, 96.7% and 95.3% of SBM-1 respectively. The diameter of deformed bars has little effect on the ultimate bending moment of the members, and changing the diameter of deformed bars has no effect on the initial stiffness.

4.5. Diameter of deformed bars

Fig. 17 (e) shows the moment-deflection curves of members with different number of deformed bar. The number of deformed bar of model SBM-1, 15, 16 and 17 is 6, 4, 8 and 10 respectively. When the number of deformed bar is changing from 6 to 8, the bearing capacity of the members increases in turn. The member with 8 deformed bars has the highest bearing capacity, which shows a downward trend when it reaches the peak point, and develops steadily, showing good ductility. However, when the number of deformed bars is 10, the bearing capacity of the specimen decreases. The ultimate moment of model SBM-15, 16 and 17 is 97.1%, 105.7% and 103.7% of model SBM-1 respectively. Changing the number of deformed bars has little effect on the initial stiffness. It is recommended that the number of deformed bars to be arranged in the range of 6-8.

5. Calculation formula of flexural bearing capacity

The reinforced hollow high concrete filled square steel tube pure bending member can be regarded as the combination of hollow high concrete filled square steel tube and PHC column, and the two parts are superimposed. The calculation formula of bending bearing capacity is as follows:

$$M = M_{\mathrm{u}} + k_{\mathrm{d}} M_{\mathrm{p}} \tag{2}$$

$$M_u = \gamma_m W_{sc} f_{sc} \tag{3}$$

$$\gamma_m = (1-0.5\psi)(2.379\xi + 0.1819\sqrt{\xi}) \tag{4}$$

$$W_{sc} = \frac{\pi(r_0^{\,4} - r_{ci}^{\,4})}{4r_0} \tag{5}$$

$$f_{sc} = (1.212 + B\xi + C\xi^2) f_c \tag{6}$$

$$\xi = \frac{\mathrm{A_s} \cdot f}{\mathrm{A_c} \cdot f_c} \tag{7}$$

$$\begin{aligned} M_p = {} & (\alpha_1 f_{p\times k} A_{pc} (r_{pi} + r_{p0}) \frac{\sin \pi\alpha}{2\pi} + f_{pi}^{'} A_{pi} r_p \frac{\sin \pi\alpha}{\pi} \\ & + (f_{pit} - \sigma_{po}) A_{pi} r_p \frac{\sin \pi\alpha_1}{\pi} + f_{zi} A_{zz} r_z \frac{\sin \pi\alpha + \sin \pi\alpha_r}{2\pi}) \end{aligned} \tag{8}$$

$$\alpha = \frac{0.55\sigma_{po} + 0.45 f_{ptk} A_{py} + 0.5 f_{sy} A_{ss}}{\alpha_1 f_{pck} A_{pc} + f_{py}^{'} A_{py} + 0.45(f_{ptk} - \sigma_{po}) A_{py} + f_{sy} A_{ss}} \tag{9}$$

Where, M_{u} and M_{p} are the bending bearing capacity of hollow high concrete filled square steel tube and PHC column, respectively. γ_{m} is flexural strength index, W_{sc} is the section modulus of the composite section, f_{sc} is the nominal yield strength of the composite section, ψ is the hollow ratio, ξ is the confinement coefficient, r0 is the equivalent radius, r_{ci} is the hollow radius, f_y is the standard value of concrete compressive strength, B=0.039f/213+0.247, C=-0.006f_c/14.4+0.002, f is the standard value of compressive strength of steel. The symbols in Equ (7) can be found in reference [29].

The average value and standard deviation of the ratio between the calculated results of the bending capacity calculation formula and the simulated value of the finite element are 0.971 and 0.0016

The average value of the ratio of the calculated value of the bending bearing capacity formula to the finite element simulation value is 0.971, and the mean square deviation is 0.0016. Fig. 18 shows the comparison between the finite element analysis results and the bearing capacity calculation formula, and the error is less than 10%. The calculation formula is as follows:

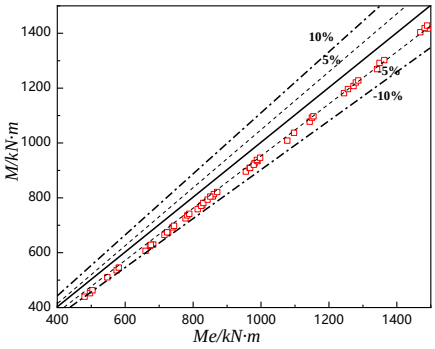

Fig. 18 Comparison of calculated and simulated values.

6. Conclusions

Through the analysis and discussion of the test results and finite element analysis results, the following conclusions can be drawn:

(1) The test results showed that the steel ratio and reinforcement ratio have important effects on the ultimate bearing capacity and ductility. The deflection curve was similar to the standard sinusoidal half wave curve, and the specimen appeared local buckling at the mid-span.

(2) Based on the reasonable constitutive model, a finite element model for simulating the mechanical behavior of reinforced hollow concrete filled square steel tubular beams was established. The finite element calculation results were in good agreement with the experimental results.

(3) In the whole process of stress, the steel tube resists most of the bending moment from beginning to end. The bending moment resistance of sandwich concrete is higher than that of tube column concrete. The pure bending specimen can be divided into elastic stage, elastic-plastic stage and hardening stage.

(4) The compressive strength of concrete, the yield strength of steel, the diameter of reinforcement and the number of reinforcements have a certain impact on the bearing capacity of the specimen. The ultimate bending moment of the specimen increases significantly with the increase of steel ratio and steel yield strength.

(5) The calculation formula of flexural capacity of reinforced hollow concrete filled square steel tubular member was proposed, and the accuracy of the calculation value of the formula is verified by the experimental data.

Acknowledgements

The research was supported by National Natural Science Foundation of China (52178148, 51808353), Excellent Youth Fund of Liaoning Province (2021-YQ-10), Xingliao Talent Program of Liaoning Province (XLYC2203109), Fundamental scientific research project of Liaoning Provincial Department of Education (LJKZ0598).

References

[1] Han L. H., Li W. and Bjorhovde R., “Developments and advanced applications of concrete-filled steel tubular (CFST) structures: Members”, Journal of Constructional Steel Research, 100, 211-228, 2014,

[2] Han, L.H., Li W., Wang W.D. and Tao, Z., Advanced composite and mixed structures: testing, theory and design approach (Second Edition), Science Press, Beijing, 2017.

[3] Kang J.Y., Choi E.S., Chin W.J. and Lee J.W., “Flexural behavior of concrete-filled steel tube members and its application”, International Journal of Steel Structures, 7, 319–324, 2007.

[4] Li G.C., Liu D., Yang Z.J. and Zhang, C.Y., “Flexural behavior of high strength concrete filled high strength square steel tube”, Journal of Constructional Steel Research, 128(1), 732-

744, 2017.
[5] Elchalakani M., Zhao X.L. and Grzebieta R.H., "Concrete-filled circular steel tubes subjected to pure bending", Journal of Constructional Steel Research, 57, 1141-1168, 2001.
[6] Han L.H., "Flexural behaviour of concrete-filled steel tubes", Journal of Constructional Steel Research, 60, 313-337, 2004,
[7] Han L. H., Lu H., Yao G.H. and Liao F.Y., "Further study on the flexural behaviour of concrete-filled steel tubes", Journal of Constructional Steel Research, 62, 554-565, 2006.
[8] Elchalakani M. and Zhao X. L., "Concrete-filled cold-formed circular steel tubes subjected to variable amplitude cyclic pure bending", Engineering Structures, 30, 287-299, 2008,
[9] Moon J., Roeder C.W. and Lee H.H., "Analytical modeling of bending of circular concrete-filled steel tubes", Engineering Structures, 42, 349-361, 2012.
[10] Wang R., Han L.H., Nie J.G. and Zhao X.L., "Flexural performance of rectangular CFST members", Thin-Walled Structures, 79, 154-165, 2014.
[11] Zhan Y.L., Zhao R.D., Ma John Z.G., Xu, T.F. and Song R.N., "Behavior of prestressed concrete-filled steel tube (CFST) beam", Engineering Structures, 122, 144-155, 2016.
[12] Javed, M.F., Sulong N.H.R., Memon S.A., Rehman S.K.Ur. and Khan N.B., "FE modelling of the flexural behaviour of square and rectangular steel tubes filled with normal and high strength concrete", Thin-Walled Structures, 119, 470-481. 2017.
[13] Chen Y., Feng R. and Gong W.Z, "Flexural behavior of concrete-filled aluminum alloy circular hollow section tubes", Construction and Building Materials, 165, 173-186, 2018.
[14] Al-shaar A.A.M. and Göğüş M.T., "Flexural behavior of lightweight concrete and self-compacting concrete-filled steel tube beams", Journal of Constructional Steel Research, 149, 153-164, 2018.
[15] Liu, D., Zuo J., Wang, J., Duan, K., Zhang, D.M. and Guo, S., "Bending failure mechanism and strengthening of concrete-filled steel tubular support", Engineering Structures, 2019, 198: 109449.
[16] Al Zand A.W. and Badaruzzaman W.H.W., "Flexural performance of square concrete-filled steel tube beams stiffened with V-shaped grooves", Journal of Constructional Steel Research, 166, 105930, 2020.
[17] Li G.C., Qiu Z.M., Yang Z.J., Chen B.W. and Feng Y.H., "Seismic performance of high strength concrete filled high strength square steel tubes under cyclic pure bending", Advanced Steel Construction, 16, 112-123, 2020.
[18] Li, J.Y., Deng, Z.C. and Sun, T., "Flexural behavior of ultra-high performance concrete filled high-strength steel tube", Structural Concrete, 22, 1688-1707, 2021.
[19] Wang Y., Lin, H., Lai Z.C., Li D., Zhou W,S. and Yang X.Q., "Flexural behavior of high-strength rectangular concrete-filled steel tube members", Journal of Structural Engineering, 148, 04021230, 2022.
[20] Kodur V.K.R. and MacKinnon D.H., "Simplified design of concrete-filled hollow structural steel columns for fire endurance", Journal of Constructional Steel Research, 46, 298, 1998.
[21] Song Y.L. and Chen J. F., "Structural behaviour of short steel—concrete composite spun tubular columns", Magazine of Concrete Research, 52, 411-418, 2000.
[22] Kvedaras A.K. and Kudzys A., "The structural safety of hollow concrete-filled circular steel members", 2006, 62(11), 1116-1122, Journal of Constructional Steel Research.
[23] Chen J., Jin W.L., Fu J., "Experimental investigation of thin-walled centrifugal concrete-filled steel tubes under torsion", Thin-Walled Structures, 46, 1087-1093, 2008,
[24] Zhao Y.G., Yan X.F. and Lin S.Q., "Compressive strength of axially loaded circular hollow centrifugal concrete-filled steel tubular short columns", Engineering Structures, 201, 109828, 2019.
[25] Yang Z.J., Han J.M., Lei Y.Q., Li G.C. and Liu S.Q., "A reinforced high-strength concrete-filled hollow steel tubes column", Chinese Patent, ZL 201821067732. 2, 2019.
[26] Guo, Z.H., "Strength and constitutive relationship of concrete - principle and application", China Construction Industry Press, Beijing, 1994.
[27] Han L.H., Yao G.H. and Tao, Z., "Performance of concrete-filled thin-walled steel tubes under pure torsion", Thin-Walled Structures, 45, 24-36, 2007.
[28] Han L.H.," Concrete filled tubular structure: theory and practice", Science Press, Beijing, 2016.
[29] Zhang S., "Mechanical behavior of reinforced hollow high strength concrete filled square steel tube members under pure bending", Shenyang Jianzhu University, MS Thesis, 2023.